MEASURED AND PREDICTED ROTOR-PAD TRANSFER FUNCTIONS FOR A ROCKER-PIVOT TILTING-PAD JOURNAL BEARING

A Dissertation

by

JASON CHRISTOPHER WILKES

Submitted to the Office of Graduate Studies of
Texas A&M University
in partial fulfillment of the requirements for the degree of

DOCTOR OF PHILOSOPHY

December 2011

Major Subject: Mechanical Engineering

Measured and Predicted Rotor-Pad Transfer Functions for a Rocker-Pivot Tilting-Pad
Journal Bearing

MEASURED AND PREDICTED ROTOR-PAD TRANSFER FUNCTIONS FOR A ROCKER-PIVOT TILTING-PAD JOURNAL BEARING

A Dissertation

by

JASON CHRISTOPHER WILKES

Submitted to the Office of Graduate Studies of
Texas A&M University
in partial fulfillment of the requirements for the degree of

DOCTOR OF PHILOSOPHY

Approved by:

Chair of Committee,	Dara W. Childs
Committee Members,	Paul Cizmas
	Alan Palazzolo
	Luis SanAndrés
Head of Department,	Jerald Caton

December 2011

Major Subject: Mechanical Engineering

ABSTRACT

Measured and Predicted Rotor-Pad Transfer Functions for a Rocker-Pivot Tilting-Pad Journal Bearing. (December 2011)

Jason Christopher Wilkes, B.S., Texas A&M University;
M.S., Texas A&M University
Chair of Advisory Committee: Dr. Dara W. Childs

Many researchers have compared predicted stiffness and damping coefficients for tilting-pad journal bearings (TPJBs) to measurements. Most have found that direct damping is consistently overpredicted. The thrust of this research is to explain the difference between measured and predicted stiffness and damping coefficients for TPJBs, and to provide some confidence to designers that TPJB dynamic coefficients can be accurately predicted.

Most analytical models for TPJBs are based on the assumption that explicit dependence on pad motion can be eliminated by assuming harmonic rotor motion such that the amplitude and phase of pad motions resulting from radial and transverse rotor motions are predicted by rotor-pad transfer functions. In short, these transfer functions specify the amplitude and phase of pad motion (angular, radial, translational, etc.) in response to an input rotor motion.

A new pad perturbation model is developed including the effects of angular, radial, and circumferential pad motion and changes in pad clearance due to pad bending compliance. Though all of these pad variables have previously been included in different analyses, there are no publications containing perturbations of all four variables. In addition, previous researchers have only perturbed the journal, while both the bearing and journal motions are perturbed in the present analysis, and the applicability of comparing rotor-perturbed bearing impedance predictions to impedances measured on a bearing-perturbed test rig is discussed. This perturbation model was

implemented in a Reynolds-based TPJB code to predict the frequency-dependent bearing impedances and rotor-pad transfer functions.

Direct measurements of pad motion during test excitation were recorded to produce measured transfer functions between rotor and pad motion, and a comparison between these measurements and predictions is given. Motion probes were added to the loaded pad (having the static load vector directed through its pivot) of a 5-pad TPJB to obtain accurate measurement of pad radial and tangential motion, as well as tilt, yaw, and pitch. Strain gages were attached to the side of the loaded pad to measure static and dynamic bending strains, which were then used to determine static and dynamic changes in pad curvature (pad clearance).

Good agreement was found between the amplitude of the measured and predicted transfer functions concerning radial and transverse pad motions throughout the range of speeds and loads tested, while pad tilt was moderately underpredicted.

For the bearing investigated, radial pad motions resulting from pivot compliance were as large as 60% of the radial component of shaft motion when operating at 4400 rpm under heavily loaded conditions. Hence, if a dynamic load applied to the shaft resulted in a shaft displacement of 25 microns (1 mil), the pad would displace radially 15 microns (0.6 mils), and the fluid film height would only decrease by 10 microns (0.4 mils). The consequence of this pad motion is that fluid film stiffness and damping forces produced by relative rotor-pad motions are significantly reduced, resulting in a bearing having significantly less direct stiffness and damping than predicted. A similar effect occurs when shaft motions produce significant changes in pad clearance due to pad compliance. For the pad tested here, the measurements show that predicting TPJB stiffness and damping coefficients without accounting for pad and pivot compliance will produce large errors, and is not advised.

Transverse pad motion was predicted and observed. Based on phase measurements, this motion is lightly damped, and appears to be caused by pivot deflection instead of slipping. Despite observing a lightly damped phase change, an increase in magnitude at this natural frequency was not observed.

Predicted direct stiffness and damping for unit loads from 0-3200 kPa (0-450 psi) fit through 1.5× running speed are within 18% of measurements at 4400 rpm, while predictions at 10200 rpm are within 10% of measurements. This is a significant improvement on the accuracy of predictions cited in literature.

Comparisons between predictions from the developed bearing model neglecting pad, pivot, and pad and pivot flexibility show that predicted direct stiffness and damping coefficients for a model having a rigid pad and pivot are overestimated, respectively, by 202% and 811% at low speeds and large loads, by 176% and 513% at high speeds and high loads, and by 51% and 182% at high speeds and light loads. While the reader is likely questioning the degree to which these predictions are overestimated in regard to previous comparisons, these predictions are based on measured operating bearing clearances, which are 20-30% smaller than the cold bearing clearances that previous comparisons were based on.

The effect of employing a full bearing model (retaining all of the pad degrees of freedom) versus a reduced bearing model (where only journal degrees of freedom are retained) in a stability calculation for a realistic rotor-bearing system is assessed. For the bearing tested, the bearing coefficients reduced at the frequency of the unstable eigenvalue (subsynchronously reduced) predicted a destabilizing cross-coupled stiffness coefficient at the onset of instability within 1% of the full model, while synchronously reduced coefficients for the lightly loaded bearing required 25% more destabilizing cross-coupled stiffness than the full model to cause system instability. This overestimation of stability is due to an increase in predicted direct damping at the synchronous frequency over the subsynchronously reduced value. This increase in direct damping with excitation frequency was also seen in highly loaded test data at frequencies below approximately 2×running speed, after which direct damping decreased with increasing excitation frequency. This effect was more pronounced in predictions, occurring at all load and speed combinations.

The same stability calculation was performed using measured stiffness and damping coefficients at synchronous and subsynchronous frequencies at 10200 rpm. It

was found that both the synchronously measured stiffness and damping and predictions using the full bearing model were more conservative than the model using subsynchronously measured stiffness and damping. This outcome contrasts with the comparison between models using synchronously and subsynchronously reduced impedance predictions, which showed the subsynchronously reduced model to be the most conservative. This contrast results from a predicted increase in damping with increasing excitation frequency at all speeds and loads, while this increase in damping with increasing excitation frequency was only measured at the most heavily loaded conditions.

DEDICATION

To My Wife, Monica,
for all her hard work at home with the kids while I put in my time at the lab.

ACKNOWLEDGEMENTS

First and foremost, I must thank my family for the support that they have shown me during the long and arduous task of pursuing my Ph.D. I could not have made it this far without you.

My sincerest gratitude goes out to Chris Kulhanek and Gustavo Vignolo for helping me get the test rig in its current condition. Without a capable test rig, this research would not have been possible.

I would like to thank Eddie Denk, Ray Matthews, Stephen Phillips, and all of the Turbomachinery Laboratory staff who help to make the Texas A&M Turbomachinery Laboratory successful, as well as the Turbomachinery Research Consortium (TRC) for sponsoring this research.

I would also like to thank my colleagues, Dara Childs, Luis SanAndrés, Alan Palazzolo, and Paul Cizmas for their advice on this subject and the manner in which it is presented.

To those students pursuing a PhD, I give the following advice: The path by which you arrive at a PhD is not a line, it is a vector ***AB***, having both a magnitude and a direction. This vector has two endpoints, the first (***A***) is your starting point, and the end (***B***) is determined by the quality, value, and scope of your research in its final form. To walk from ***A*** to ***B***, you will need to take a large number of steps. Each step you take will also have direction and magnitude, and the most efficient approach is to take large steps directly along the path from ***A*** to ***B***. At all cost, avoid steps perpendicular, or even against, the grain; these steps are not productive. Since the magnitude of ***AB*** is not defined at the start of your research, increasing the scope of your research will increase the length of your path; however, this choice may greatly improve the quality of your work, and should be made with care. When in doubt, keep your head down, and keep moving forward, even if the pace is slow. This will bring you to your goal.

TABLE OF CONTENTS

LIST OF TABLES

Page

LIST OF FIGURES

Page

Page

Page

Page

Page

CHAPTER I

INTRODUCTION

OVERVIEW OF THE TILTING PAD JOURNAL BEARING

As an elemental component of any rotating machine, bearings have a significant influence on rotor- bearing stability, reliability, and performance. The primary function of a bearing is to transmit reaction forces from one body to another while facilitating rotation between the two bodies. This rotation can be facilitated by several means, including rolling elements, mechanical contact, magnetic levitation, or fluid film lubrication. Each of these bearing types have strengths and weaknesses, but the current work will focus on the tilting-pad journal bearing, a specific type of fluid film bearing that is inherently stable, and has thus become a popular selection for commercial turbomachinery operating in high-speed, lightly-loaded conditions.

As stated, the primary function of a bearing is to support a shaft, or journal, by providing reaction forces. For motion about equilibrium, these bearing reaction force components are usually represented by one of the following forms: (1) a stiffness (k_{ij}) and damping (c_{ij}) (KC) model

$$-\begin{Bmatrix} f_{bx} \\ f_{by} \end{Bmatrix} = \begin{bmatrix} k_{xx} & k_{xy} \\ k_{yx} & k_{yy} \end{bmatrix} \begin{Bmatrix} x \\ y \end{Bmatrix} + \begin{bmatrix} c_{xx} & c_{xy} \\ c_{yx} & c_{yy} \end{bmatrix} \begin{Bmatrix} \dot{x} \\ \dot{y} \end{Bmatrix}, \tag{1}$$

where k_{ij}, c_{ij} can be constant (independent of excitation frequency) or frequency-dependent stiffness and damping coefficients, and x and y are relative rotor-stator motions, or (2) a stiffness, damping, and virtual-mass (m_{ij}) (KCM) model

$$-\begin{Bmatrix} f_{bx} \\ f_{by} \end{Bmatrix} = \begin{bmatrix} k_{xx} & k_{xy} \\ k_{yx} & k_{yy} \end{bmatrix} \begin{Bmatrix} x \\ y \end{Bmatrix} + \begin{bmatrix} c_{xx} & c_{xy} \\ c_{yx} & c_{yy} \end{bmatrix} \begin{Bmatrix} \dot{x} \\ \dot{y} \end{Bmatrix} + \begin{bmatrix} m_{xx} & m_{xy} \\ m_{yx} & m_{yy} \end{bmatrix} \begin{Bmatrix} \ddot{x} \\ \ddot{y} \end{Bmatrix}, \tag{2}$$

where k_{ij} and c_{ij} and m_{ij} are typically frequency-independent coefficients. The terms k_{xx}/k_{yy} and c_{xx}/c_{yy} in Eqs. (1) and (2) are commonly referred to as direct stiffness and

---

This dissertation follows the style of ASME Journal of Engineering for Gas Turbines and Power.

damping coefficients, and produce reaction forces that "directly" oppose displacement or velocity; the terms k_{xy}/k_{yx} and c_{xy}/c_{yx} are commonly referred to as cross-coupled stiffness and damping coefficients and provide reaction forces perpendicular to displacement and velocity, respectively. When k_{xy} and k_{yx} have different signs, the cross-coupled stiffness coefficients become destabilizing, producing forces that add energy to the shaft's orbit, which can result in large amplitude oil whirl/whip provided the bearing does not have enough direct damping to suppress this behavior.

Ideal TPJBs are inherently stable because they are composed of multiple pads, or shoes, that are free to tilt such that the net moment on each pad is zero at equilibrium; this reduces/eliminates the generation of destabilizing forces (destabilizing cross-coupled stiffness). Figure 1 shows a schematic of a pad's reaction force due to a displacement of the journal directed at the pad's pivot. If the pivot allows the pad to tilt freely (providing no reaction moment), then the pad's reaction force must be collinear with the journal's displacement, resulting in zero cross coupled stiffness.

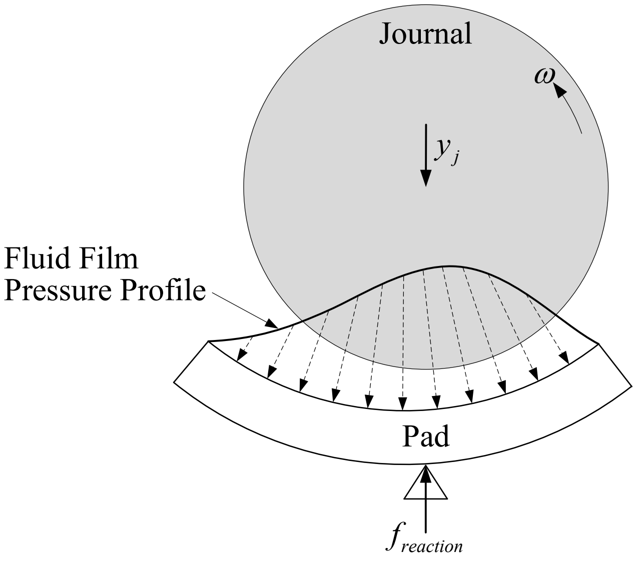

Figure 1: Tilting pad reaction force

Figure 2 shows some of the fundamental parameters that affect the operation of a TPJB. These parameters are defined formally in CHAPTER II, but they are introduced here to ensure that the reader is familiar with terms discussed in the literature review.

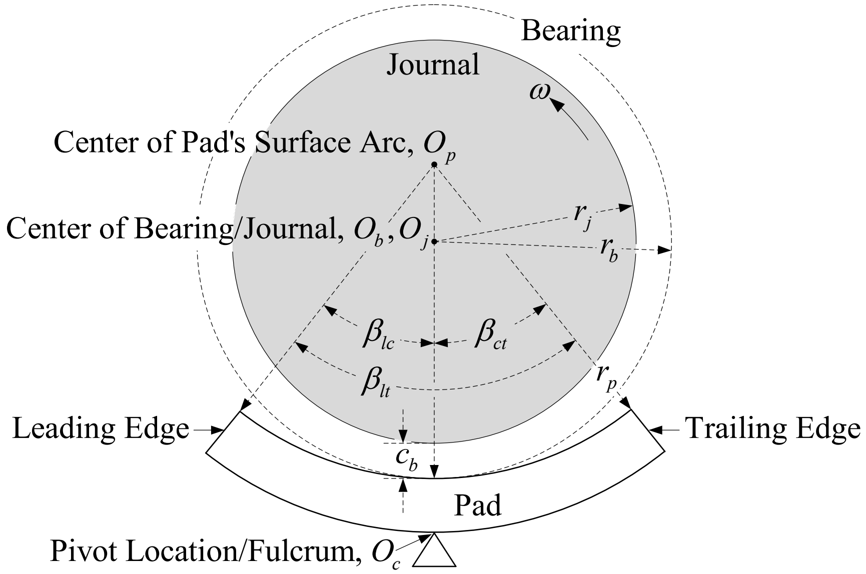

Figure 2: Fundamental parameters of the tilting pad

Figure 2 shows a journal having a radius r_j concentric in a bearing having a radius r_b with centers prescribed by O_j and O_b, respectively. The surface of the pad has a radius r_p about its geometric center O_p, and pivots about its fulcrum/pivot point O_c. β_{lc} and β_{ct} define the angular extent from the leading edge of the pad to the pivot (leading *segment* of the pad) and from the pivot to the trailing edge of the pad (trailing *segment* of the pad), respectively, and β_{lt} defines the angular extent of the pad. The location of the pivot relative to the leading and trailing edges of the pad is commonly referred to as the pad's offset, and is given by

$$Offset := \frac{\beta_{lc}}{\beta_{lc}+\beta_{ct}} = \frac{\beta_{lc}}{\beta_{lt}} . \tag{3}$$

Typical pad offsets range from 0.5-0.6, where 0.5 represents a centrally pivoted pad.

Figure 2 also shows the bearing clearance, c_b, defined as the difference between bearing and journal radii:

$$c_b = r_b - r_j . \tag{4}$$

Though not shown Figure 2, pad clearance is similarly defined as the difference between pad and journal radii:

$$c_p = r_p - r_j \tag{5}$$

The bearing and pad clearance are commonly related by a preload, a nondimensional parameter given by

$$Preload = 1 - \frac{c_b}{c_p} \tag{6}$$

Pad preloads are often positive, having typical values from 0-0.5. A positive preload tends to stiffen the bearing when unloaded, and reduces the likelihood of pad flutter, an instability that can occur in the unloaded pads in a tilting pad bearing.

At the back of each pad is a pivot that enables the pad to tilt, and applies the fluid film loads to the bearing housing, or shell. Figure 3 shows the three basic pivot types: rocker-pivot, sliding-pivot (ball-in-socket), and flexure-pivot, each differing in the manner in which pad rotation is facilitated.

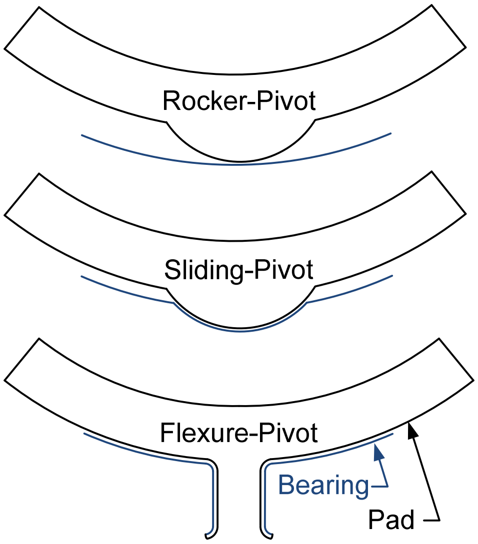

Figure 3: Three basic pivot types

A rocker-pivot, or "cylindrical" pivot, has a smaller radius than the surface of the bearing shell, and thus rocks with pad rotation, presumably rolling-without-slipping. The term "cylindrical" here can be misleading, as many rocker-back pivots contain a slight curvature in the axial direction. This feature results in a point contact between the pivot and housing that allows the pad to pitch to accommodate angular misalignment.

Rocker-pivots are usually retained by a loose fitting pin to prevent the pad from falling out during installation.

A sliding pivot, “ball-in-socket”, or “spherical pivot,” has a curvature only slightly smaller than the surface of the bearing in which it resides, allowing pad tilt primarily through relative sliding motion at the contact. This increase in contact area results in reduced contact stresses, but can be problematic if pad rotation is constrained by sliding friction. Ball-in-socket pivots are usually spherical, allowing for significant angular misalignment; however, sliding pivots may also be cylindrical in shape, thus the note of caution in referring to rocker-back pivots as “cylindrical” pivots.

Flexure pivots allow for pad rotation via a flexible web that supports the pad, reducing the likelihood of pivot contact fatigue that is possible in other pivot configurations. Although this web provides some angular stiffness to the pad, it is usually small in comparison to the stiffness of the fluid film, and nets little destabilizing cross-coupled stiffness [1]. Flexure-pivot TPJBs (FPTPJBs) are compact, usually made from a single piece with wire electron discharge machining (EDM), which reduces the tolerance stackup that can be problematic in other TPJB configurations.

Despite their inherent stability, calculating the stiffness and damping of TPJBs accurately is essential in predicting the stability or synchronous response of a larger system. Improving and validating the accuracy of these calculations has been a subject of interest in hydrodynamic lubrication for some time. The current work will propose several new theoretical and experimental concepts that may bring clarity to some of the controversial topics still at large in TPJB literature.

LITERATURE REVIEW

Few additions to literature have been as significant as Lund’s 1964 paper proposing a method for the calculation of stiffness and damping coefficients of a TPJB [2]. Procedurally, Lund solves for static equilibrium, perturbs the pad equation of motion, eliminates the system’s explicit dependence on pad motion by assuming harmonic rotor motion, and calculates direct and cross-coupled stiffness and damping coefficients for the bearing; these stiffness and damping coefficients are often called "reduced," or "frequency-reduced," bearing coefficients. Lund assumes that rotor motion is harmonic in the perturbation/reduction frequency Ω, and that running speed ω is an appropriate choice for Ω. This choice of reduction frequency, termed a "synchronous reduction," does not limit Lund's analysis to the determination of synchronous coefficients, and should not be portrayed as such. This frequency choice has been the subject of much discussion over the past few decades. Though Lund's work has been expanded to include pad and pivot compliance, more complicated fluid models, and used in unreduced/full bearing models (a bearing model explicitly containing all pad DOFs), the heart of Lund's analysis, writing equations of motion (EOMs) about the perturbed bearing equilibrium, remains the cornerstone of TPJB prediction.

Pad and Pivot Flexibility

In 1978, Nilsson addressed the influence of pad flexibility on the dynamic performance of radial oil films [3]. Pad flexibility refers to the flexibility of the pad relative to the pivot, which results in a change in curvature of the surface of the pad. Nilsson models the pads in a TPJB as curved beams, deflecting statically and dynamically under pressures from the oil film. He asserts that pad compliance having only a small impact on static characteristics can have a dramatic effect on dynamic characteristics, especially damping. Nilsson performs calculations on a pad having a 90° arc length supporting a journal with a static eccentricity ratio of 0.9, and concludes that damping can be reduced by as much as 40% in comparison to a rigid pad.

In 1987, Lund and Pederson [4] expand the work of Nilsson to include perturbations of film height due to *pivot flexibility* and *pad flexibility*. *Pivot flexibility*, or *pivot compliance*, refers to the flexibility of the pad relative to the bearing housing, and results from Hertzian contact stiffness in rocker-back and sliding pivots, or from stress-induced web deflections in flexure-pivots. Though the bearing tested in this work is a rocker-back TPJB whose pivot flexibility results from contact stiffness, statements concerning pivot stiffness/compliance will be used for the balance of this work to refer to compliance of the pad relative to the housing, which applies to all TPJB configurations. Lund and Pederson approximate pad deflections using curved beam theory such that fluid film pressures result in a change in pad radius. They conclude that both pad and pivot compliance severely reduce stiffness and damping of the bearing, especially the latter. In addition, Lund and Pederson reflect upon the choice of synchronous reduction frequency suggested in Lund's first work, and state that "In the special case of a damped eigenvalue calculation or a rotor stability calculation, the frequency term, $\tilde{j}\Omega$, *must* be replaced by the complex eigenvalue [of the unstable mode]: $\tilde{s} = \lambda + \tilde{j}\Omega$, where λ is the damping exponent." Bearing coefficients reduced at the frequency of the unstable mode were eventually termed "subsynchronously reduced" coefficients, a convention that will be used for the remainder of this work. In addition, 'tilde' will be used to denote that a variable is complex.

The notion that stability calculations should not be performed with synchronously reduced coefficients had previously been stated by Parsell et al. [5] in 1982 and Wilson and Barrett [6] in 1985. Parsell et al. noted that synchronously reduced bearing coefficients tend to be adequate for stability calculation except for the case of zero preload and large Sommerfeld numbers. However, Wilson and Barrett later showed significant differences between stability calculations employing full and synchronously reduced bearing models for an 8-stage compressor running on preloaded bearings; however, Wilson and Barrett did not have pivot flexibility in their model, and it is possible that using subsynchronously reduced bearing coefficients would have been more appropriate, considering the conclusion reached by Lund and Pederson in 1987. In 1988, Barrett et al. [7] retained the full damped eigenvalue $\tilde{s} = \lambda + \tilde{j}\Omega$ to determine system stability and suggested that using synchronously reduced coefficients will tend to overestimate stability, especially for a bearing operating at high Sommerfeld numbers and low preloads. These works inspired several papers in the late 1980s and 1990s investigating the effects of pad and pivot flexibility on the static and dynamic characteristics of TPJBs.

In 1988, Kirk and Reedy [8] presented analytical contact stiffness formulas for various pivot types using Hertzian-stress models. Although this work applies to some conventional pivots, contact stiffnesses for many pivot geometries remain to be defined, especially for mostly "cylindrical" pivots having a very slight radius of curvature, or crowning in the axial direction. Kirk and Reedy supported Lund and Pederson's conclusions concerning pivot stiffness, namely that it should be included in the calculation of bearing coefficients.

Brugier and Pascal [9] extended the analysis of Lund and Pederson in 1989 to include the effects of pivot flexibility and circumferential and axial pad flexibility on the static and dynamic performance of a TPJB. The hydrodynamic pressures and lubricant temperatures are computed with 2-dimensional models on the surface of the pad, and thermal and elastic pad and pivot deflections are obtained with a 3-dimensional finite element model. Brugier and Pascal conclude that "irrespective of the load, both pressure and temperature induced pad deflections must be taken into account in the calculation of dynamic bearing coefficients.

Earles et al. [10, 11] performed a similar analysis to Brugier and Pascal in 1990, investigating the effects of pad and pivot flexibility on bearing performance. Pad Flexibility was modeled using 2-dimensional finite elements, which allows for greater flexibility in modeling non-uniform pad geometries than Lund and Pederson's curved-beam approximation. Synchronously reduced stiffness and damping coefficients from the improved FEA pad model compare favorably to coefficients predicted with the simpler curved-beam approximation; however, Earles et al. noted that the pad surface does not remain circular when under the pressure of the fluid film as approximated by Lund and Pederson's simple model. Earles et al. predicted the stability of a flexible rotor having a destabilizing cross-coupled stiffness at mid-span sitting on two TPJBs using full and synchronously reduced models of a TPJB having rigid and compliant pivots. The full bearing model explicitly contained all of the pad degrees of freedom, while the reduced model consisted of 2×2 stiffness and damping matrices that resulted when the pad degrees of freedom were harmonically reduced from the model.

The TPJBs employed in the analysis had 5 spherically-pivoted pads with preloads of 0.4375 and offsets of 0.5. The stability of the system was assessed by comparing the rotor speed at which the system's eigenvalues became unstable using various bearing models. System stability was reduced with pad and pivot flexibility and with the full TPJB pad dynamics in the model; however, as with Wilson and Barrett, they did not include pivot flexibility in their synchronously reduced model. Though this analysis showed that it may be important to analyze system stability employing the full (unreduced) bearing dynamics, as noted by a 20% decrease in onset speed of instability relative to the synchronously reduced model, the reader is not instructed as to when employing a full bearing model in the system stability calculation will yield improved results over a synchronously reduced model. In addition, the accuracy of employing a model reduced at the frequency of the unstable mode is not discussed. The current work will attempt to address this shortcoming.

Kim et al. [12] extended the work of Earles et al. in 1995 to include multiple pad deflection modes. With only a few pad modes, they claim to predict stiffness and damping coefficients accurately for the experimental measurements presented by Brockwell et al. [13]; however, there is not a discussion on when the inclusion of additional pad bending modes in the model is warranted.

The notion that employing full or reduced bearing coefficients could have an impact on stability prediction was first suggested by Parsell et al. [5] in 1982 and was later echoed by Wilson and Barrett [6] in 1985, Lund and Pederson [4] in 1987, Barrett et al. [7] in 1988, Earles et al. [10, 11] in 1990, Qiao et al. [14] in 2007, and Dimond et al. [15] in 2010, who all concluded that using a reduced bearing model drastically overestimates system stability, yet the industrial community still resists this notion. What is the impetus for this resistance, and is it justified?

Recent publications by Kocur et al. [16], Childs [17], and Childs et al. [18] all address this question; unanimously, they conclude that there are significant differences in the frequency dependence of measured and predicted data, and that these differences have led to a lack of confidence in both measurements and predictions. It is the author's position that this lack of confidence must be resolved before the issue of the frequency dependence of TPJB dynamic coefficients can be resolved. The current work will attempt to address differences between measured and predicted frequency dependency in tilting pad journal bearings and the impact of using different bearing implementations in stability calculations.

Experimental Research and Frequency Dependency

Historically, bearing coefficients are measured on a floating-bearing test rig, where a stationary test-bearing (stator) is supported by a spinning rotor. The floating-bearing-test-rig concept was initially developed by Glienicke [19] in 1966, and has since become the dominant choice for testing fluid-film bearings; thus, the majority of experimental data contained in the literature, and in this work, were measured on floating-bearing test rigs.

As pad and pivot flexibility effects in TPJBs became more apparent, some researchers began to question whether test programs were adequately capturing the frequency dependent stiffness and damping coefficients of the TPJB given in Eq. (1). Though several excellent papers have presented experimental stiffness and damping coefficients for the TPJB, only a few key papers will be discussed.

In 1999, Ha and Yang [20] were the first to measure stiffness and damping coefficients for a TPJB as a function of excitation frequency. They reported a very slight increase in damping and little or no variation in stiffness with increasing excitation-frequency ratio. These effects were more pronounced at lower speeds and higher static loads; however, the following limited range of excitation frequencies was used in these tests: (1) excitation frequency ratios in the unloaded direction were 0.5 and 2.0, while (2) excitation frequency ratios in the loaded direction were 0.6, 0.7, 0.8, and 0.9.

Other researchers [21-26] have shown the frequency dependence of measured stiffness data is well approximated by a virtual-mass, initially proposed to fit hydrostatic bearing test data by Rouvas and Childs [27], which results in the frequency independent

(KCM) model given in Eq. (2) when damping is constant. This outcome does not imply that the parameter identification procedure used by researchers [21-26] cannot show frequency dependent stiffness and damping, just that the frequency dependent stiffness observed is proportional to Ω^2, which is adequately included by the addition of a "virtual-mass" term in the bearing reaction force model, and that damping is constant.

This virtual-mass captures the frequency dependence of measured stiffness data, and should not be mistaken for an added-mass, proposed by Reinhardt and Lund [28] to represent the effect of fluid inertia on bearing coefficients. The virtual-mass terms presented are usually relatively small (5-10kg), and typically have a softening effect; however, researchers [22, 25 and 26] have shown that virtual-mass terms can have a stiffening effect. Carter and Childs [22] observed this stiffening effect primarily at lower speeds, while Kulhanek [25] and Kulhanek and Childs [26] observed this stiffening effect at both low and high speeds. These same researchers have found damping to be constant with excitation frequency and static bearing load, while Dmochowski [29] shows a small decrease in damping with excitation frequency. Despite a large amount of scatter in his data, Dmochowski was the first researcher to obtain good agreement between experiments with variable excitation frequency and predictions using a model containing radial pivot flexibility for the pad, while researchers [21-26] consistently overpredicted damping.

Other notable experimental papers include those by Pettinato and De Choudhury [30,31] in 1999, who presented comparisons between theory and experiment for 5-pad cylindrical-seat and spherical-seat sliding-pivot bearings having similar pivot stiffnesses. Theoretical predictions were generated using an isoviscous Reynolds equation model and Lund's pad assembly method with rigid pads and pivots. They measured higher stiffness and damping for the cylindrical-seat bearing than the spherical-seat bearing. Stiffness was predicted well for the cylindrical-seat bearing and overpredicted for the spherical-seat bearing, while damping was uncharacteristically underpredicted for the cylindrical-seat bearing and overpredicted for the spherical-seat bearing.

Al-Ghasem and Childs [32] and Rodriguez [33] compared measured and predicted rotordynamic coefficients for a four pad FPTPJB in load-between-pad (LBP) and load-on-pad configurations in 2006. They show good agreement between measured and predicted stiffness and damping coefficients throughout a range of speeds and static bearing loads for a model neglecting radial pivot flexibility. This good agreement may result from increased radial pivot stiffness in comparison to the Hertzian-contact stiffness between the pads and housing in prior works. These tests include unit loads up to 988 kPa (143 psi), while researchers [22, 25, and 26] tested at unit loads up to 3200 kPa. This bearing was later retested by Hensley [34] in 2006 at higher unit loads, who found that the accuracy of the predictions using a rigid pivot decreased significantly at higher static bearing loads.

The test rig used by researchers [22, 25, 26, and 32-34] has also been used to test pressure dam and two-axial groove journal bearings by Al Jughaiman [35], who obtained good agreement between measurements and predictions throughout a range of unit loads using the same testing and data reduction techniques. Thus, there is no reason to suspect that the procedure used to test TPJBs is not valid.

It should be noted that claims by researchers [12] in 1995, [30,31] in 1999, and [29,32,33,35] in 2006 regarding good agreement between measurements and predictions do not specify whether cold-bearing or hot-bearing (operating) clearances were used to predict bearing coefficients. Since hot-bearing clearances were not stated in the experimental works cited by these researchers, it is likely that cold-bearing clearances were used for predictions. The current work notes significant reductions in bearing clearance at operating conditions, which significantly increases the magnitude of predicted bearing coefficients when included in the model.

Pad Motion

With a few exceptions, experimental measurement of *pad* motion has typically been limited to the observation of pad flutter on unloaded pads. Pad flutter, initially identified by Adams and Payandeh [36], is the self-excited vibration of statically unloaded pads in a TPJB. This vibration usually occurs at a frequency slightly less than 0.5 times the journal rotation speed, and can cause fatigue damage of the pad surface material. Pad flutter results from the absence of a stable static-equilibrium position of the pad, which can be suppressed by insuring that each pad operates with a positive preload.

Sabnavis [37] attempted to measure the pad motion of a spherical-seat TPJB, but failed to produce meaningful amplitude and phase measurements. This failure likely resulted from an inability to differentiate between pad tilt, radial pad motion, and other pad motions that may have been seen by the single proximity probe used to measure the motion of the pad.

Preliminary results from the current work were recently published by the author [38], which showed significant improvements in the ability to measure pad motion in a tilting pad journal bearing.

Thrust for This Research

Many researchers have compared predicted stiffness and damping coefficients for tilting-pad journal bearings to measurements; most have found that direct damping is overpredicted, and that the measured impedances are well approximated by frequency independent stiffness, damping, and mass (KCM) coefficients, while predictions made as early as 1975 suggest that this approach is not suitable [39]. This work aims to resolve discrepancies between measured and predicted bearing behavior by investigating, more closely, pad dynamics within a TPJB.

Most analytical models for TPJBs are based on the assumption that explicit dependence on pad degrees of freedom can be eliminated by assuming that rotor motion is harmonic such that the amplitude and phase of pad motions are predicted by rotor-pad transfer functions. Direct measurements of pad motion induced by harmonic rotor motion are needed to produce measured rotor-pad transfer functions, and a comparison between these measurements and predictions is needed to identify model discrepancies.

CHAPTER II

MATHEMATICAL MODEL

TPJB GEOMETRY

Figure 4 shows the journal, bearing, and k^{th} pad in the reference state (denoted by subscript '*o*'), defined such that the geometric center of the journal (O_{jo}) and bearing (O_{bo}) are located at the origin (O_o) of the inertial *X*-*Y* and η_k-ξ_k coordinate systems, and that the line $O_{po,k}$-$O_{co,k}$, connecting the center of the k^{th} pad's surface arc to the k^{th} pad's contact point (pivot location), passes through the origin. For all pivot configurations, O_c represents the pad's fulcrum, though it may be referred to as the contact point for the rocker-pivot pad shown in Figure 4. Variables corresponding to the k^{th} pad are denoted by a subscript '*k*' in the following analysis though this convention is omitted in Figure 4 for clarity.

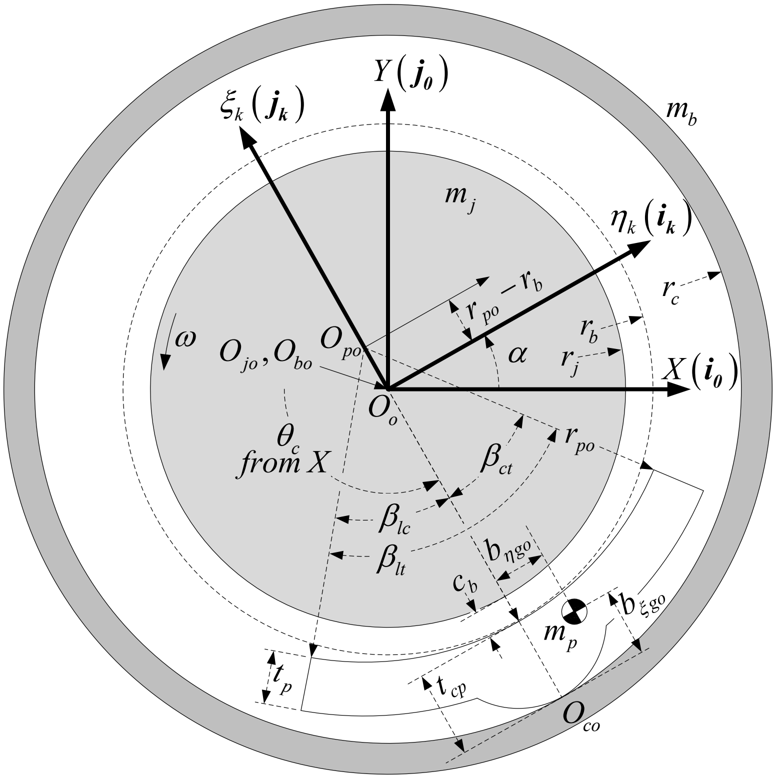

Figure 4: Schematic of the journal, bearing, and k^{th} pad in the reference state

The stationary *X-Y* coordinate system has unit vectors ($\boldsymbol{i_0},\boldsymbol{j_0}$), and the k^{th} pad's η_k-ξ_k reference coordinate system has unit vectors ($\boldsymbol{i_k},\boldsymbol{j_k}$); vectors in the two coordinate systems are related by the direction-cosine matrix $\mathbf{Q_k}$ according to

$$\begin{Bmatrix} b_{\eta,k} \\ b_{\xi,k} \end{Bmatrix} = \begin{bmatrix} \cos(\alpha_k) & \sin(\alpha_k) \\ -\sin(\alpha_k) & \cos(\alpha_k) \end{bmatrix} \begin{Bmatrix} b_X \\ b_Y \end{Bmatrix} = \mathbf{Q_k} \begin{Bmatrix} b_X \\ b_Y \end{Bmatrix}. \tag{7}$$

where $\alpha_k = \theta_{c,k} - 3\pi/2$ defines the angle from *X* to η_k about *Z* and $\theta_{c,k}$ is the angle from *X* to the k^{th} pad's contact location. For the remainder of this work, vectors will be ***bold-italic***, and matrices will be **bold**. The origin of the *X-Y-Z* coordinate system sits axially on the bearing centerline such that the axial extents of the pad are located at $Z = \pm L_{p,k}/2$, where $L_{p,k}$ is the length of the k^{th} pad.

The journal radius is r_j, while the bearing and contact radii of the k^{th} pad are $r_{b,k}$ and $r_{c,k}$, respectively. Radii $r_{b,k}$ and $r_{c,k}$ are related to the thickness of the k^{th} pad at the contact location ($t_{cp,k}$) by

$$r_{c,k} := r_{b,k} + t_{cp,k}. \tag{8}$$

Using these relations, the bearing clearance for the k^{th} pad describes the minimum film thickness *at the reference state*, which occurs along the line $O_{po,k}$-O_o-$O_{co,k}$, and is given by

$$c_{b,k} = r_{b,k} - r_j. \tag{9}$$

The surface of the k^{th} pad *at the reference state* is an arc of radius $r_{po,k}$ about its center, $O_{po,k}$, located at

$$\boldsymbol{e_{po,k}} = \left(r_{po,k} - r_{b,k}\right)\boldsymbol{j_k} = \left(c_{po,k} - c_{b,k}\right)\boldsymbol{j_k}, \tag{10}$$

where $c_{po,k}$ is the pad clearance *at the reference state* given by

$$c_{po,k} = r_{po,k} - r_j. \tag{11}$$

Pad clearance was included as a pad degree of freedom in Nilsson's analysis [3] to account for pad deflections resulting from moments applied to the pad by the fluid film, a practice continued in the current work. The pad degrees of freedom used in the present analysis will be discussed thoroughly in the following two sections.

In the reference state, the k^{th} pads center of gravity (CG) with the reference contact point ($O_{co,k}$) taken as a datum is given by

$$\boldsymbol{b_{cgo,k}} = b_{\eta go,k}\boldsymbol{i_k} + b_{\xi go,k}\boldsymbol{j_k}\,. \tag{12}$$

RIGID BODY PAD MOTIONS

Though facilitating tilt reduces the destabilizing cross-coupled stiffness provided by a TPJB, this feature customarily allows for rigid body radial and transverse pad motions and changes in pad radius/clearance resulting from fluid film pressures on the surface of the pad.

Figure 5 illustrates a pad's rigid body degrees of freedom (DOFs). The obvious DOF is pad tilt, which defines the rotation of the pad about its pivot point or fulcrum. The pivot point may be obvious for a rocker-pivot that pivots about its contact point, but this location may not be as well defined for sliding or flexure pivots.

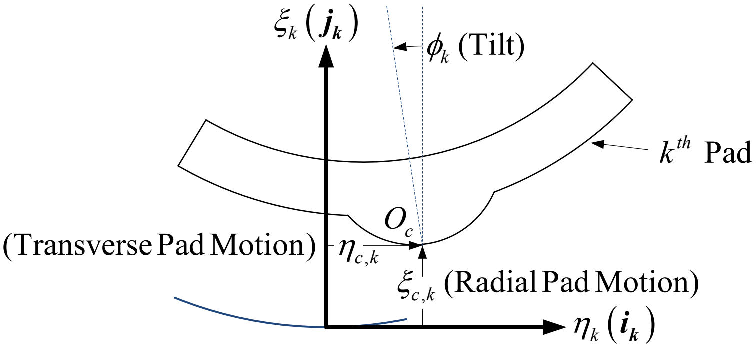

Figure 5: Rigid body degrees of freedom for a tilting pad

Two rigid body translations are shown in Figure 5, radial and transverse/ circumferential pad motion are defined as motion of the pad's pivot location (O_c) *relative to the housing* in the pad's radial (ξ_k) and transverse (η_k) directions. These rigid body pad motions occur because the forces transmitted to the pad via the fluid film must pass through the pivot, which is compliant. This *pivot flexibility*, or *pivot compliance*, refers to the flexibility of the pad relative to the bearing housing, and results from Hertzian contact stiffness in rocker-back and sliding pivots, or from stress-induced web deflections in flexure-pivots. Though the bearing tested in this work is a rocker-back TPJB whose pivot flexibility results from contact stiffness, statements concerning pivot stiffness/compliance will be used for the balance of this work to refer to compliance of the pad relative to the housing, which applies to all TPJB configurations.

Pivot Reaction Forces/Moments

Before discussing changes in pad clearance, we will classify the reaction forces/moments between the pivot and housing resulting from the relative pad-bearing motions illustrated in Figure 5. Figure 6 shows radial ($f_{c\xi,k}$) and transverse ($f_{c\eta,k}$) pivot reaction forces resulting from relative pad-bearing radial (ξ_k) and transverse (η_k) translations, and a reaction moment ($M_{cz,k}$) resulting from pad tilt (ϕ_k). In general, these reaction forces/moments may be nonlinear functions of relative pad-bearing translations and rotations; thus, they will be defined with zeroth (denoted by a subscript 0) and first order (denoted by a subscript 1) components, where the zeroth order component will represent the nonlinear reaction forces and moments corresponding to a guessed set of relative pad translations/rotations, and the first order components will represent linearized reaction forces and moments resulting from perturbations in displacements and velocities about the zeroth order state. When the guessed state results in a condition such that the forces and moments applied by fluid film are balanced by the reaction forces and moments provided by the pad's pivot (zero net force components and moment applied to the pad), the pad is said to be in equilibrium, and the linearized pivot reaction force coefficients resulting from first-order perturbations in displacement and velocity can be identified as stiffness and damping coefficients.

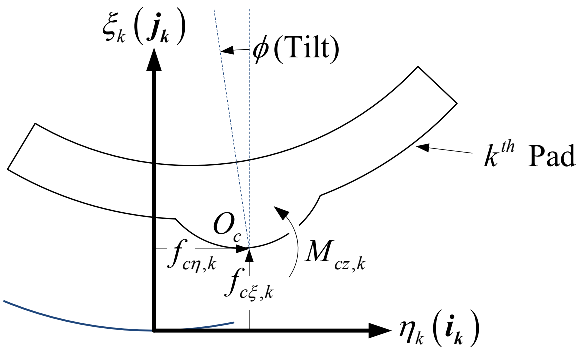

Figure 6: Pivot reaction forces

Although several TPJBs are likely to have negligible resistance to pad tilt, flexure-pivot TPJBs and some spherical seat bearings may resist pad angular motion; thus, reaction moments due to pad tilt will be included in this analysis for completeness. The pad reaction moment is

$$M_{cz,k} = M_{cz0,k} + M_{cz1,k} = M_{cz0,k}\left(\xi_{c0,k},\phi_{0,k}\right) + \left.\frac{\partial M_{cz,k}}{\partial \phi_{1,k}}\right| \phi_{1,k} + \frac{\partial M_{cz,k}}{\partial \dot{\phi}_{1,k}}\dot{\phi}_{1,k} \tag{13}$$

where $M_{cz0,k}\left(\xi_{c0,k},\phi_{0,k}\right)$ is permitted to be any function of pad radial or angular deflection. At equilibrium, the pivot's angular stiffness and damping coefficients are

$$k_{cz,k} = \left.\frac{\partial M_{cz,k}}{\partial \phi_{1,k}}\right|_0 ,\ c_{cz,k} = \left.\frac{\partial M_{cz,k}}{\partial \dot{\phi}_{1,k}}\right|_0 . \tag{14}$$

For sliding pivots, $c_{cz,k}$ may represent energy dissipation due to coulomb friction; this approach was taken by Wygant et al. [40] to model pivot friction in a spherical seat bearing.

The radial pivot reaction force between the k^{th} pad and bearing is

$$f_{c\xi,k} = f_{c\xi 0,k} + f_{c\xi 1,k} = f_{c\xi 0,k}\left(\xi_{c0,k}\right) + \left.\frac{\partial f_{c\xi,k}}{\partial \xi_{c1,k}}\right|_0 \xi_{c1,k} + \left.\frac{\partial f_{c\xi,k}}{\partial \dot{\xi}_{c1,k}}\right|_0 \dot{\xi}_{c1,k} \tag{15}$$

where $f_{c\xi 0,k}\left(\xi_{c0,k}\right)$, in general, may be a nonlinear function of the pad's radial deflection relative to the bearing. At equilibrium, the last two terms in Eq. (15) define the radial pivot stiffness and damping coefficients as

$$k_{c\xi,k} = \left.\frac{\partial f_{c\xi,k}}{\partial \xi_{c1,k}}\right|_0 , \quad c_{c\xi,k} = \left.\frac{\partial f_{c\xi,k}}{\partial \dot{\xi}_{c1,k}}\right|_0 . \tag{16}$$

Although there are analytical formulas used to describe the contact stiffness for cylindrical and spherical pivot/housing geometries [8], several TPJBs are "self-aligning," having pivots with complex curvatures that are not well modeled with analytical forms. For the rocker-pivot TPJB tested in this work, the load-versus-deflection curve was predicted numerically using the algorithm presented by Deeg [41] which agreed well with the experimentally determined load-versus-deflection curve as will be shown in the RESULTS section. In the bearing code, the load-versus-deflection curve was approximated using a fourth order polynomial, which performed adequately.

Similarly, the transverse pivot force may be given as

$$f_{c\eta,k} = f_{c\eta 0,k} + f_{c\eta 1,k} = f_{c\eta 0,k}\left(\xi_{c0,k}, \eta_{c0,k}\right) + \left.\frac{\partial f_{c\eta,k}}{\partial \eta_{c1,k}}\right|_0 \eta_{c1,k} + \left.\frac{\partial f_{c\eta,k}}{\partial \dot{\eta}_{c1,k}}\right|_0 \dot{\eta}_{c1,k} , \tag{17}$$

where $f_{c\eta 0,k}\left(\xi_{c0,k}, \eta_{c0,k}\right)$ yields the transverse pivot force at a guessed state. The inclusion of radial pivot deflection in this equation may be necessary if it is desired to approximate coulomb friction at the contact location, which varies with the radial contact force. At equilibrium, the partial derivatives in Eq. (17) yield the transverse pivot stiffness and damping coefficients

$$k_{c\eta,k} = \left.\frac{\partial f_{c\eta,k}}{\partial \eta_{c1,k}}\right|_0 , \quad c_{c\eta,k} = \left.\frac{\partial f_{c\eta,k}}{\partial \dot{\eta}_{c1,k}}\right|_0 . \tag{18}$$

The importance of the different contact stiffness and damping terms is likely to vary with different pivot designs; however, radial pivot stiffness in particular has been cited by many as detrimental to a pad's ability to transmit damping loads to the bearing housing; hence, various authors predict that damping can be significantly reduced due to radial pivot flexibility [4,8,11].

PAD BENDING DEFLECTIONS

The last pad degree of freedom to introduce is pad clearance. We will begin by considering the effect of a pressure distribution (*p*) on a pad with a uniform cross section as shown in Figure 7.

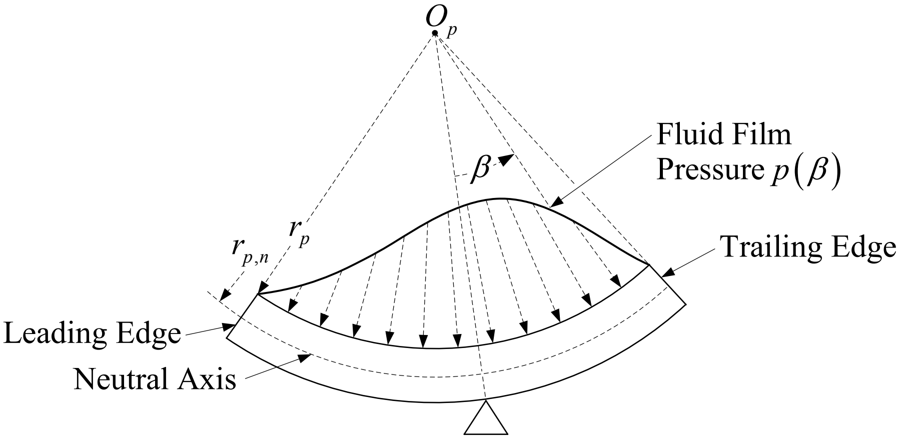

Figure 7: Pressure distribution on a tilting pad

Since there are no moments on the leading and trailing edges of the pad, $M_{c_p,n}$, the bending moment on the neutral axis of the pad (denoted by a subscript *n*) at any location along the pad is given by

$$M_{c_p,n}(\beta)=\begin{cases}-\int\limits_{-L_p/2}^{L_p/2}\int\limits_{-\beta_{lc}}^{\beta} p(\beta)r_{p,n}\sin(\beta)r_p d\beta dZ \ , \ \beta<0 \\ -\int\limits_{-L_p/2}^{L_p/2}\int\limits_{\beta}^{\beta_{ct}} p(\beta)r_{p,n}\sin(\beta)r_p d\beta dZ \ , \ \beta>0\end{cases}, \tag{19}$$

where $r_{p,n}$ is the radius of the neutral axis of the pad, β is the angle of a circumferential coordinate on the pad relative to the pivot, and Z defines an axial position on the pad relative to the pad's mid-plane.

When the pad is at static equilibrium, a state requiring that the forces and moments applied by fluid film are balanced by the reaction forces and moments provided by the pad's pivot (zero net force components and moment on the pad), the discontinuity in the bending moment on either side of the pivot at $\beta = 0^-$ and $\beta = 0^+$ is equal to the reaction moment applied by the pivot. Specifically,

$$M_{c_p,n}\left(0^-\right) + M_{cz} = M_{c_p,n}\left(0^+\right). \tag{20}$$

This condition is depicted in Figure 8.

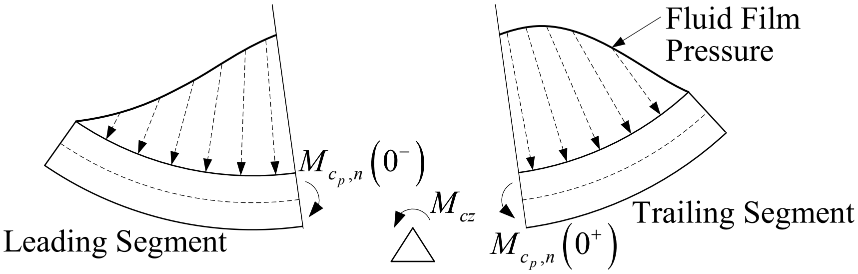

Figure 8: Balanced bending moments at the pivot location

Similar to Nilsson, Lund and Pederson [4] suggested that the effect of $M_{c_p,n}\left(\beta\right)$ on the pad's radius of curvature could be approximated by obtaining the average bending moment in the pad, and applying it as an end moment on a curved beam to determine the resulting change in pad radius. While this approach limits the deflection of a uniform cross-section pad to circular deflections, it permits an analytical perturbation in fluid film height due to pad clearance, which is advantageous. Earles et al. [10, 11] obtained results similar to Lund and Pederson using finite-elements to solve for pad deflections; this method is computationally expensive, but allows for more complex pad geometries. Note that pad clearance was formally defined in Eq. (5) as the difference between the radius of the pad and the radius of the journal; thus, for a constant journal radius, changes in pad clearance are equivalent to changes in pad radius.

Continuing with the assumption that the surface of the pad remains circular when deflected, $\bar{M}_{c_p,n}$, the average bending moment in the pad, is given by

$$\bar{M}_{c_p,n} = \frac{1}{\beta_{lt}} \int_{-\beta_l}^{\beta_t} M_{c_p,n}\left(\beta\right) d\beta \tag{21}$$

which results in a change in pad radius given by the approximation

$$\frac{1}{r_{p,n}} - \frac{1}{r_{p,n}+\delta_{c_p}} \simeq \frac{\delta_{r_p}}{r_{p,n}^{2}} = \frac{\bar{M}_{c_p,n}}{E_p I_{c_p}} \tag{22}$$

where δ_{r_p} is the change in pad radius resulting from the applied pressure field, E_p is the elastic modulus of the of the pad, and I_{c_p} is the pad's cross-sectional area moment of inertia. Since uniform changes in pad radius are equivalent to uniform changes in pad clearance (provided r_j is constant), δ_{r_p} in Eq. (22) may be exchanged with δ_{c_p} to yield changes in pad clearance due to an applied pressure profile. The change in pad radius, or pad clearance, resulting from an applied end moment $\bar{M}_{c_p,n}$ is shown in Figure 9.

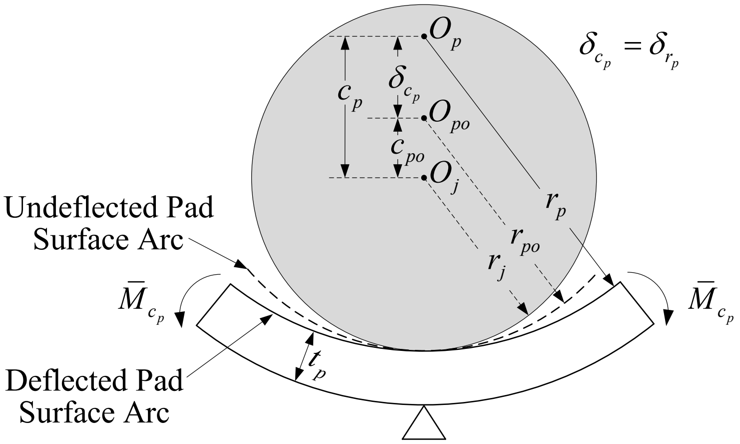

Figure 9: Change in pad curvature resulting from applied end moments

Figure 9 shows an undeflected pad surface arc having a radius r_{po} *at the reference state*, while the deflected pad surface resulting from the applied end moments has a radius r_p given by

$$r_p = r_{po} + \delta_{r_p}, \tag{23}$$

where $\delta_{r_p} = r_{p0} + r_{p1}$ is the sum of changes in pad radius due to zeroth order pressure profiles (denoted by a subscript 0) and perturbed pressure profiles (denoted by a subscript 1), respectively. The derivation of zeroth and first order pressure profiles is discussed in detail later. Similarly, pad clearance is given by

$$c_p = c_{po} + \delta_{c_p} \tag{24}$$

where $\delta_{c_p} = c_{p0} + c_{p1}$ represents the sum of changes in pad clearance resulting from zeroth and first order pressure fields, respectively. Note that substituting r_p from Eq. (23) and c_p from Eq. (24) into Eq. (5) and subtracting Eq. (11) nets

$$\delta_{c_p} = \delta_{r_p}, \tag{25}$$

an obvious outcome.

Though Eq. (20) is true for equilibrium conditions, dynamic pressure fields may require a dynamic pad bending model to account for the inertia of the pad; however this approach is not adapted in the current work.

Branagan and Barrett [42] used a slightly more general approach than Lund and Pederson. Taking Eq. (22) and writing it in a more general form yields

$$\delta_{c_p} = c_{p0} + c_{p1} = \frac{\bar{M}_{c_p,n}}{\bar{k}_{sc_p}}, \tag{26}$$

where $\bar{k}_{sc_p}$ represents the pad's structural bending stiffness (relating average bending moments in the pad to changes in pad clearance), and δ_{c_p} is again the change in pad clearance resulting from the average bending moment in the pad . In turn, Branagan and Barrett analyzed the accuracy of several analytical bending stiffness formulas by comparison with finite-element analysis (FEA) predictions, and suggested that the following formula by Deutschman et al. [43] is the most accurate:

$$\bar{k}_{sc_p,k} = \frac{E_{p,k} L_{p,k} t_{p,k}}{\Theta_k - 1} \frac{\left(\Theta_k^2 - 1\right)^2 - \left[2\Theta_k \ln\left(\Theta_k\right)\right]^2}{4\left\{1 - \Theta_k^2\left[1 - 2\ln\left(\Theta_k\right)\right]\right\}}, \tag{27}$$

where the subscript *s* implies that this is a structural pad stiffness, $\Theta_k = \left(r_{p,k} + t_{p,k}\right)/r_{p,k}$ is the ratio of outer to inner pad radii, and t_p is the thickness of the pad. Assuming that the pad has a uniform thickness of 18.16 mm (0.715 in), pad's in the current work have a bending stiffness of 11.0 MN (2.47×10^6 lbf).

Although the bending stiffness given in Eq. (27) assumes that the pad cross-section is uniform, the test bearing has pads with hardened pivot inserts to reduce wear, as shown in Figure 10.

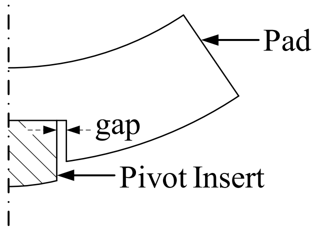

Figure 10: Illustration of a pad with a pivot insert

These hardened inserts are not press fitted into the pad, having a small gap on each side. This gap creates a discontinuity/nonlinearity in the pad's bending stiffness with increasing bending moments, and the effect of these bending moments on pad clearance is not approximated well with Eq. (26), which uses the average bending moment in the pad to calculate changes in pad clearance. Though the approach by Earles et al. [10, 11] is more flexible, it is not likely that this approach could easily be adapted to model the pads used in this work, whose structural model would have to vary with the bending moment on the pad.

The current work proposes a modified version of Eq. (26) given by

$$\delta_{c_p} = \frac{M_{c_p}}{k_{sc_p}}, \tag{28}$$

where $M_{c_p} = \frac{1}{2}\left[M_{c_p}\left(\beta^-\right) + M_{c_p}\left(\beta^+\right)\right]$ is the average of applied fluid-film moments (evaluated on the surface of the pad) directly on either side of the pad's pivot, and k_{sc_p} is a stiffness that relates this moment to a change in pad clearance. $M_{c_p}\left(\beta^-\right)$ and $M_{c_p}\left(\beta^+\right)$ are obtained using Eq. (19) after substituting r_p for $r_{p,n}$. This step eliminates the need to account for variations in the pad's neutral axis at different locations along the pad, which may not be practical input for a user friendly bearing code.

k_{sc_p} is obtained by the following procedure. A finite-element model of the pad is developed in ANSYS, Abaqus, etc., and a pressure distribution is applied to the surface of the pad. This distribution may be a uniform pressure distribution, or it could be more realistic. Ideally, a pressure profile similar to the pressure profile developed on a tilting pad should be used; however, a uniform pressure distribution was used in the current work and appears to work well. Regardless of the pressure distribution chosen, the resultant force created by the pressure distribution should pass through the pad's pivot to prevent rigid body rotation (tilt) of the pad. Next, calculate M_{c_p}, for the loading applied to the pad in the FEA, and determine the deflected pad radius by fitting the deflected pad's surface to a circle, or cylinder, using a least squares regression. The equivalent bending stiffness of the pad can then be obtained using

$$k_{sc_p} = \frac{M_{c_p}}{\delta_{c_p}} \tag{29}$$

where δ_{c_p} is the difference between deflected and undeflected pad radii.

JOURNAL, BEARING, AND PAD IN A GENERAL POSITION

Figure 11 illustrates the journal, bearing, and k^{th} pad in a general position. In this analysis, both the journal and bearing are free to translate, each pad is free to rotate (ϕ_k), and translate radially ($\xi_{c,k}$) and transversely ($\eta_{c,k}$) relative to the housing while maintaining continuous contact with the bearing. Only translations of the bearing in the XY plane are included in the present analysis; hence, structural modes of the bearing housing are not included in the present model. Previous researchers writing perturbed equations of motion for a TPJB have assumed that the bearing/stator is stationary; the applicability of this assumption to floating-bearing test rigs will be examined.

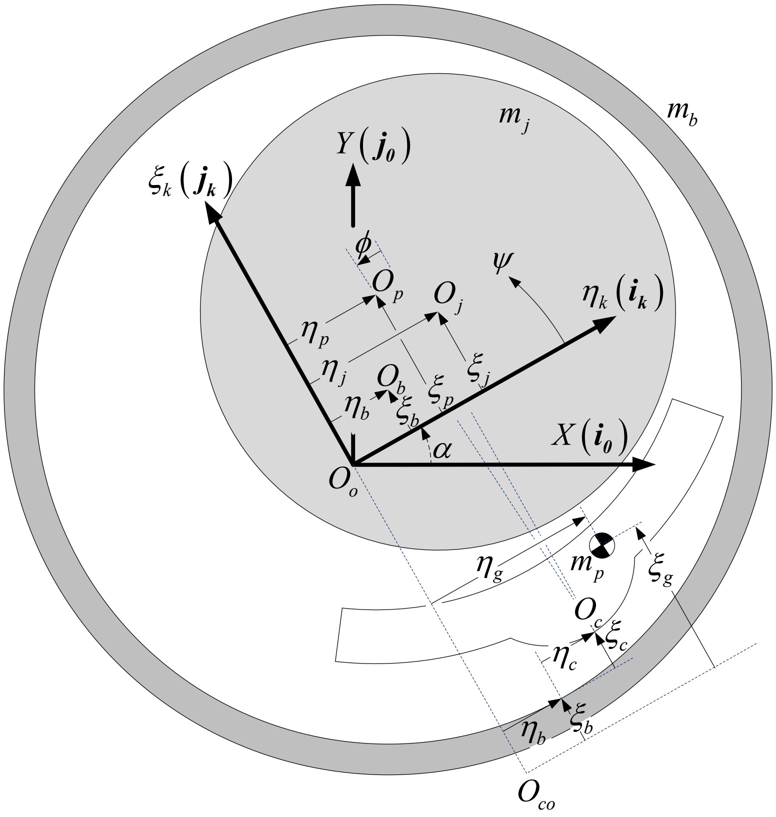

Figure 11: Schematic of the journal, bearing, and k^{th} pad in a general position

In a general position, the displacement of the journal (O_j) is

$$\boldsymbol{e_{j,k}} = \eta_{j,k}\boldsymbol{i_k} + \xi_{j,k}\boldsymbol{j_k}\,, \tag{30}$$

and the displacement of the bearing (O_b) is

$$\boldsymbol{e_{b,k}} = \eta_{b,k}\boldsymbol{i_k} + \xi_{b,k}\boldsymbol{j_k}\,. \tag{31}$$

Note that bearing displacements $\eta_{b,k}$ and $\xi_{b,k}$ in Figure 11 are duplicated from the reference state contact location to show the displacement of the pad's pivot due to bearing motion. Translation of the k^{th} pad's pivot at the contact point is given by the sum of bearing and relative pivot-bearing motion:

$$\boldsymbol{e_{c,k}} = \left(\eta_{b,k} + \eta_{c,k}\right)\boldsymbol{i_k} + \left(\xi_{b,k} + \xi_{c,k}\right)\boldsymbol{j_k}\,. \tag{32}$$

For small pad rotations ϕ_k, the translation of the center of the pad's surface arc relative to the contact point due to pad tilt is $-r_{cp,k}\phi_k\boldsymbol{i_k}$, where $r_{cp,k} = t_{cp,k} + r_{p,k}$ is the distance from

$O_{c,k}$ to $O_{p,k}$. Using this relation, the total displacement of the center of the pad's surface arc with respect to the inertial η_k-ξ_k reference coordinate system is

$$\boldsymbol{e_{p,k}} = \left(\eta_{b,k} + \eta_{c,k} - r_{cp,k}\phi_k\right)\boldsymbol{i_k} + \left(\xi_{b,k} + \xi_{c,k} + c_p - c_b\right)\boldsymbol{j_k} = \eta_{p,k}\boldsymbol{i_k} + \xi_{p,k}\boldsymbol{j_k} \,. \tag{33}$$

DEVELOPMENT AND PERTURBATION OF REYNOLDS EQUATION IN A TPJB

The following analysis was developed initially by Lund [2] in 1964, Lund and Thomsen [44] in 1978, and Lund and Pederson [4] in 1987, except that we will use the reference pad oriented η_k-ξ_k coordinate system instead of the global *X*-*Y* system. For most cases, Reynolds equation accurately characterizes the pressures developed in the fluid film. The Reynolds equation results when the Navier Stokes equations for the fluid film between two surfaces are simplified for the flow of an inertialess, isoviscous fluid in a thin film region. Under these circumstances, Reynolds equation, the partial differential equation governing the pressure of the oil film, is given by

$$\Re\left[p_k\right] := \frac{1}{r_j}\frac{\partial}{\partial\psi_k}\left\{\frac{h_k^3}{12\mu}\frac{\partial}{r_j\partial\psi_k}\right\} + \frac{\partial}{\partial z}\left\{\frac{h_k^3}{12\mu}\frac{\partial}{\partial z}\right\}\left[p_k\right] = \frac{\omega}{2}\frac{\partial h_k}{\partial\psi_k} + \frac{\partial h_k}{\partial t} \,, \tag{34}$$

where $\Re$ is a linear differential operator, $\psi_k = \theta - \alpha_k$ is the angle from η_k to a circumferential location on the pad, *Z* is the axial position from the pad's mid-plane, μ is the fluid viscosity, and h_k is the fluid film height on the k^{th} pad given by

$$h_k\left(\psi_k\right) = c_{p,k} - \left|\boldsymbol{e_{pj,k}}\right|\cos\left(\psi_k - \psi_{pj,k}\right), \tag{35}$$

where $\boldsymbol{e_{pj,k}} = \eta_{pj,k}\boldsymbol{i_k} + \xi_{pj,k}\boldsymbol{j_k} = \boldsymbol{e_{j,k}} - \boldsymbol{e_{p,k}}$ is the vector from O_p to O_j, and ψ_{pj} is the angle from η_k to $\boldsymbol{e_{pj,k}}$ about the positive *Z* axis, and $c_{p,k} = c_{po,k} + \delta_{c_p}$ represents the sum of installed pad clearance and changes in pad clearance due to fluid film pressures. For clarity, the subscripts '*pj*' will be dropped for the remainder of the analysis when referring to journal motion relative to the k^{th} pad, thus $\boldsymbol{e_{pj,k}} := \eta_k\boldsymbol{i_k} + \xi_k\boldsymbol{j_k}$

If we guess an initial state for the system such that a solution satisfying Eq. (34) may be found, the fluid film height can be written as the superposition of zeroth (guessed) and first (perturbed) order components as

$$h_k\left(\psi_k\right) = h_{0,k}\left(\psi_k\right) + h_{1,k}\left(\psi_k\right) \tag{36}$$

where

$$h_{0,k}\left(\psi_k\right) = c_{po,k} + c_{p0,k} - \left|\boldsymbol{e_{pj0,k}}\right|\cos\left(\psi_k - \psi_{pj0,k}\right) \tag{37}$$

describes the zeroth order (denoted by a subscript 0, not to be confused with the reference state) fluid film height on the k^{th} pad, and

$$h_{1,k}\left(\psi_k\right) = c_{p1,k} + \eta_{1,k}\cos\left(\psi_k\right) + \left(\xi_{1,k} - c_{p1,k}\right)\sin\left(\psi_k\right) \tag{38}$$

describes the first order (denoted by a subscript (1) fluid film height on the k^{th} pad. Note that $c_{p,k}$ is the sum of installed pad clearance $c_{po,k}$, and changes in pad clearance due to bending moments resulting from the guessed ($c_{p0,k}$) and perturbed ($c_{p1,k}$) pressure fields. If we assume that $\eta_{1,k}$, $\zeta_{1,k}$ and $c_{p1,k}$ are sufficiently small, a first order expansion of the fluid film pressures may be written as

$$p_k = p_{0,k} + p_{\eta 1,k}\eta_{1,k} + p_{\xi 1,k}\xi_{1,k} + p_{c_p 1,k}c_{p1,k} + p_{\dot{\eta}1,k}\dot{\eta}_{1,k} + p_{\dot{\xi}1,k}\dot{\xi}_{1,k} + p_{\dot{c}_p 1,k}\dot{c}_{p1,k} \tag{39}$$

where $p_{0,k}$ denotes the fluid film pressure at the zeroth order state, and ‘dot’ refers to differentiation with respect to time. Substituting Eqs. (36) and (39) into Eq. (34) and retaining only first order terms, seven differential equations governing the zeroth and first order pressure fields result. These are given by

$$\begin{array}{ll}
\Re\left[p_{0,k}\right]= & \dfrac{\omega}{2}\dfrac{\partial h_{0,k}}{\partial \psi_k} \\
\Re\left[p_{\eta 1,k}\right]= & -\dfrac{\omega}{2}\left(\sin\psi_k+3\dfrac{\cos\psi_k}{h_{0,k}}\dfrac{\partial h_{0,k}}{\partial \psi_k}\right)-\dfrac{h_{0,k}^3}{4r_j^2\mu}\dfrac{\partial p_{0,k}}{\partial \psi_k}\dfrac{\partial}{\partial \psi_k}\left(\dfrac{\cos\psi_k}{h_{0,k}}\right) \\
\Re\left[p_{\xi 1,k}\right]= & -\dfrac{\omega}{2}\left(-\cos\psi_k+3\dfrac{\sin\psi_k}{h_{0,k}}\dfrac{\partial h_{0,k}}{\partial \psi_k}\right)-\dfrac{h_{0,k}^3}{4r_j^2\mu}\dfrac{\partial p_{0,k}}{\partial \psi_k}\dfrac{\partial}{\partial \psi_k}\left(\dfrac{\sin\psi_k}{h_{0,k}}\right) \\
\Re\left[p_{c_p 1,k}\right]= & -\dfrac{\omega}{2}\left(\cos\psi_k+3\dfrac{1-\sin\psi_k}{h_{0,k}}\dfrac{\partial h_{0,k}}{\partial \psi_k}\right)-\dfrac{h_{0,k}^3}{4r_j^2\mu}\dfrac{\partial p_{0,k}}{\partial \psi_k}\dfrac{\partial}{\partial \psi_k}\left(\dfrac{1-\sin\psi_k}{h_{0,k}}\right) \\
\Re\left[p_{\dot{\eta} 1,k}\right]= & \cos\psi_k \\
\Re\left[p_{\dot{\xi} 1,k}\right]= & \sin\psi_k \\
\Re\left[p_{\dot{c}_p 1,k}\right]= & 1-\sin\psi_k
\end{array}. \tag{40}$$

To solve Eqs. (40), conditions must be specified for the zeroth ($p_{0,k}$) and first ($p_{\eta 1,k}$, *etc.*) order pressure fields on the boundary of the pad, that is

$$p_k=p_a \rightarrow p_{0,k}=p_a,\ p_{\eta 1,k}=p_{\xi 1,k}=p_{c_p 1,k}=p_{\dot{\eta} 1,k}=p_{\dot{\xi} 1,k}=p_{\dot{c}_p 1,k}=0: \begin{cases} \psi_k=\psi_{l,k} \\ \psi_k=\psi_{t,k} \\ Z=\pm L_{p,k}/2 \end{cases} \tag{41}$$

where p_a is ambient pressure, $\psi_{l,k}$ and $\psi_{t,k}$ are the leading and trailing edges of the pad, and $Z=\pm\frac{1}{2} L_{p,k}$ are the sides of the pad. Utilizing symmetry about the centerline of the pad, we may replace the conditions at $Z=-\frac{1}{2} L_{p,k}$ with

$$\frac{\partial p_k}{\partial Z}=0 \rightarrow \frac{\partial p_{0,k}}{\partial Z}=\frac{\partial p_{\eta 1,k}}{\partial Z}=\frac{\partial p_{\xi 1,k}}{\partial Z}=\frac{\partial p_{c_p 1,k}}{\partial Z}=\frac{\partial p_{\dot{\eta} 1,k}}{\partial Z}=\frac{\partial p_{\dot{\xi} 1,k}}{\partial Z}=\frac{\partial p_{\dot{c}_p 1,k}}{\partial Z}=0\ : Z=0 \tag{42}$$

If the pad is oriented such that there is a divergent wedge in the oil film, then it is likely that film rupture will occur. In this case, the boundary of film rupture, ψ_t, will become a function of Z such that oil pressure in the rupture region equals some cavitation pressure, and the gradient of the pressure normal to the curve is zero:

$$p_k=p_{cav},\ \frac{\partial p_k}{\partial n}=0 \rightarrow \frac{\partial p_k}{\partial \psi_k}=\frac{\partial p_k}{\partial Z}=0\ : \psi_k=\psi_{t,k}\left(Z\right). \tag{43}$$

where p_{cav} is the cavitation pressure of the fluid. If this result is applied to our perturbed pressure fields, one realizes that requiring the gradient of zeroth order pressure field to be zero on the cavitation boundary necessitates that the perturbed pressure fields are also identically zero on the rupture boundary. Thus, the following conditions apply at rupture.

$$\left.\begin{array}{c} p_{0,k} = p_{cav},\ \dfrac{\partial p_{0,k}}{\partial \psi_k} = \dfrac{\partial p_{0,k}}{\partial Z} = 0 \\ p_{\eta 1,k} = p_{\xi 1,k} = p_{c_p 1,k} = p_{\dot{\eta} 1,k} = p_{\dot{\xi} 1,k} = p_{\dot{c}_p 1,k} = 0 \end{array}\right. \quad : \ \psi_k = \psi_{t,k}\left(Z\right). \tag{44}$$

Utilizing the boundary conditions given in Eqs. (41-44), the zeroth and first order pressure fields given in Eq. (40) may be solved for using finite element or finite difference techniques.

Reaction Forces

At each step, these pressure fields may be integrated over the surface of the pad to yield the reaction force on the pad. Formally,

$$\begin{Bmatrix} f_{\eta,k} \\ f_{\xi,k} \end{Bmatrix} = \begin{Bmatrix} f_{\eta 0,k} \\ f_{\xi 0,k} \end{Bmatrix} + \begin{Bmatrix} f_{\eta 1,k} \\ f_{\xi 1,k} \end{Bmatrix} = -2 \int_0^{L_{p,k}/2} \int_{\psi_{l,k}}^{\psi_{t,k}} p_k \begin{Bmatrix} \cos\left(\psi_k\right) \\ \sin\left(\psi_k\right) \end{Bmatrix} r_{p0,k} \, d\psi_k \, dZ \tag{45}$$

where $f_{\eta 0,k}$ and $f_{\xi 0,k}$ are the guessed reaction force components on the journal, and the force components arising due to the perturbed pressure fields are

$$\begin{Bmatrix} f_{\eta 1,k} \\ f_{\xi 1,k} \end{Bmatrix} = -\begin{bmatrix} \dfrac{\partial f_{\eta 1,k}}{\partial \eta_{1,k}} & \dfrac{\partial f_{\eta 1,k}}{\partial \xi_{1,k}} & \dfrac{\partial f_{\eta 1,k}}{\partial c_{p1,k}} \\ \dfrac{\partial f_{\xi 1,k}}{\partial \eta_{1,k}} & \dfrac{\partial f_{\xi 1,k}}{\partial \xi_{1,k}} & \dfrac{\partial f_{\xi 1,k}}{\partial c_{p1,k}} \end{bmatrix} \begin{Bmatrix} \eta_{1,k} \\ \xi_{1,k} \\ c_{p1,k} \end{Bmatrix} - \begin{bmatrix} \dfrac{\partial f_{\eta 1,k}}{\partial \dot{\eta}_{1,k}} & \dfrac{\partial f_{\eta 1,k}}{\partial \dot{\xi}_{1,k}} & \dfrac{\partial f_{\eta 1,k}}{\partial \dot{c}_{p1,k}} \\ \dfrac{\partial f_{\xi 1,k}}{\partial \dot{\eta}_{1,k}} & \dfrac{\partial f_{\xi 1,k}}{\partial \dot{\xi}_{1,k}} & \dfrac{\partial f_{\xi 1,k}}{\partial \dot{c}_{p1,k}} \end{bmatrix} \begin{Bmatrix} \dot{\eta}_{1,k} \\ \dot{\xi}_{1,k} \\ \dot{c}_{p1,k} \end{Bmatrix}. \tag{46}$$

Expanding p_k by substitution of Eq. (39) into Eq. (45) and collecting like terms, we get

$$\begin{Bmatrix} f_{\eta 0,k} \\ f_{\xi 0,k} \end{Bmatrix} = -2 \int_0^{L_{p,k}/2} \int_{\psi_{l,k}}^{\psi_{t,k}} p_{0,k} \begin{Bmatrix} \cos\left(\psi_k\right) \\ \sin\left(\psi_k\right) \end{Bmatrix} r_{p0,k} \, d\psi_k \, dZ \tag{47}$$

to describe the guessed reaction force on the journal, and

$$\left\{ \begin{Bmatrix} \dfrac{\partial f_{\eta 1,k}}{\partial \eta_{1,k}} \\ \dfrac{\partial f_{\xi 1,k}}{\partial \eta_{1,k}} \end{Bmatrix}, \begin{Bmatrix} \dfrac{\partial f_{\eta 1,k}}{\partial \xi_{1,k}} \\ \dfrac{\partial f_{\xi 1,k}}{\partial \xi_{1,k}} \end{Bmatrix}, \begin{Bmatrix} \dfrac{\partial f_{\eta 1,k}}{\partial c_{p1,k}} \\ \dfrac{\partial f_{\xi 1,k}}{\partial c_{p1,k}} \end{Bmatrix}, \begin{Bmatrix} \dfrac{\partial f_{\eta 1,k}}{\partial \dot{\eta}_{1,k}} \\ \dfrac{\partial f_{\xi 1,k}}{\partial \dot{\eta}_{1,k}} \end{Bmatrix}, \begin{Bmatrix} \dfrac{\partial f_{\eta 1,k}}{\partial \dot{\xi}_{1,k}} \\ \dfrac{\partial f_{\xi 1,k}}{\partial \dot{\xi}_{1,k}} \end{Bmatrix}, \begin{Bmatrix} \dfrac{\partial f_{\eta 1,k}}{\partial \dot{c}_{p1,k}} \\ \dfrac{\partial f_{\xi 1,k}}{\partial \dot{c}_{p1,k}} \end{Bmatrix} \right\}$$
$$= 2 \int_{0}^{L_{p,k}/2} \int_{\psi_{l,k}}^{\psi_{t,k}} \left\{ p_{\eta 1,k}, p_{\xi 1,k}, p_{c_p 1,k}, p_{\dot{\eta} 1,k}, p_{\dot{\xi} 1,k}, p_{\dot{c}_p 1,k} \right\} \begin{Bmatrix} \cos(\psi_k) \\ \sin(\psi_k) \end{Bmatrix} r_{p0,k} d\psi_k dZ \tag{48}$$

describes the partial derivatives of the perturbed pressure fields with respect to perturbations in displacement and velocity.

Reaction Moments

In addition to reaction forces arising from the perturbed pressure fields, we must determine the bending moment applied to the pad by the fluid film. As previously stated, we will define the bending moment using $M_{c_p} = \frac{1}{2}\left[M_{c_p}\left(\beta^-\right) + M_{c_p}\left(\beta^+\right) \right]$, the average of bending moments resulting from the applied fluid-film pressures (evaluated on the surface of the pad) directly on either side of the pad's pivot, in conjunction with the pad's bending stiffness to determine changes in pad clearance. This allows us to write the applied bending moment using

$$M_{c_p,k} = M_{c_p 0,k} + M_{c_p 1,k} = -r_{p0,k} \int_{0}^{L_{p,k}/2} \int_{\psi_{l,k}}^{\psi_{c,k}} p_k \left| \cos(\psi_k) \right| r_{p0,k} d\psi_k dZ \tag{49}$$

where $M_{c_p 0,k}$ is the bending moment on the pad due to the zeroth order pressure field, and the applied bending moments arising from the perturbed pressure fields are

$$M_{c_p 1,k} = -\begin{bmatrix} \dfrac{\partial M_{c_p 1,k}}{\partial \eta_{1,k}} & \dfrac{\partial M_{c_p 1,k}}{\partial \xi_{1,k}} & \dfrac{\partial M_{c_p 1,k}}{\partial c_{p1,k}} \end{bmatrix} \begin{Bmatrix} \eta_{1,k} \\ \xi_{1,k} \\ c_{p1,k} \end{Bmatrix} - \begin{bmatrix} \dfrac{\partial M_{c_p 1,k}}{\partial \dot{\eta}_{1,k}} & \dfrac{\partial M_{c_p 1,k}}{\partial \dot{\xi}_{p1,k}} & \dfrac{\partial M_{c_p 1,k}}{\partial \dot{c}_{p1,k}} \end{bmatrix} \begin{Bmatrix} \dot{\eta}_{1,k} \\ \dot{\xi}_{1,k} \\ \dot{c}_{p1,k} \end{Bmatrix}. \tag{50}$$

Expanding p_k by substitution of Eq. (39) into Eq. (49) and collecting like terms, we get

$$M_{c_p 0,k} = -r_{p0,k} \int_{0}^{L_{p,k}/2} \int_{\psi_{l,k}}^{\psi_{c,k}} p_{0,k} \left| \cos(\psi_k) \right| r_{p0,k} d\psi_k dZ \tag{51}$$

to describe the guessed reaction moments on the journal, and

$$\left\{\frac{\partial M_{c_p1,k}}{\partial \eta_{1,k}},\frac{\partial M_{c_p1,k}}{\partial \xi_{1,k}},\frac{\partial M_{c_p1,k}}{\partial c_{p1,k}},\frac{\partial M_{c_p1,k}}{\partial \dot{\eta}_{1,k}},\frac{\partial M_{c_p1,k}}{\partial \dot{\xi}_{1,k}},\frac{\partial M_{c_p1,k}}{\partial \dot{c}_{p1,k}}\right\}$$
$$= r_{p0,k}\int_{0}^{L_{p,k}/2}\int_{\psi_{l,k}}^{\psi_{t,k}}\left\{p_{\eta 1,k},p_{\xi 1,k},p_{c_p1,k},p_{\dot{\eta}1,k},p_{\dot{\xi}1,k},p_{\dot{c}_p1,k}\right\}\left|\cos\left(\psi_k\right)\right| r_{p0,k}\,d\psi_k\,dZ \tag{52}$$

describes the partial derivatives of the bending moment on the pad with respect to perturbations in displacement and velocity.

Stiffness and Damping Coefficients

When the reaction forces resulting from the zeroth order solution and all other non fluid film reaction forces result in zero net force and moment on the shaft, bearing, and each pad, we say that our system is at static equilibrium and the stiffness and damping coefficients of the oil film due to relative rotor-pad displacements and changes in pad clearance are defined by

$$\left\{\begin{Bmatrix} k_{\eta\eta,k} \\ k_{\xi\eta,k} \\ k_{c_p\eta,k}\end{Bmatrix},\begin{Bmatrix} k_{\eta\xi,k} \\ k_{\xi\xi,k} \\ k_{c_p\xi,k}\end{Bmatrix},\begin{Bmatrix} k_{\eta c_p,k} \\ k_{\xi c_p,k} \\ k_{c_p c_p,k}\end{Bmatrix},\begin{Bmatrix} c_{\eta\eta,k} \\ c_{\xi\eta,k} \\ c_{c_p\eta,k}\end{Bmatrix},\begin{Bmatrix} c_{\eta\xi,k} \\ c_{\xi\xi,k} \\ c_{c_p\xi,k}\end{Bmatrix},\begin{Bmatrix} c_{\eta c_p,k} \\ c_{\xi c_p,k} \\ c_{c_p c_p,k}\end{Bmatrix}\right\}$$
$$= \int_{0}^{L_{p,k}/2}\int_{\psi_{l,k}}^{\psi_{t,k}}\left\{p_{\eta 1,k},p_{\xi 1,k},p_{c_p1,k},p_{\dot{\eta}1,k},p_{\dot{\xi}1,k},p_{\dot{c}_p1,k}\right\}\begin{Bmatrix} 2\cos\left(\psi_k\right) \\ 2\sin\left(\psi_k\right) \\ r_{p0,k}\left|\cos\left(\psi_k\right)\right|\end{Bmatrix} r_{p0,k}\,d\psi_k\,dz \quad . \tag{53}$$

TPJB STATIC EQUILIBRIUM

The resulting forces and moments acting on the bearing, journal, and pads are shown in the free-body diagram in Figure 12.

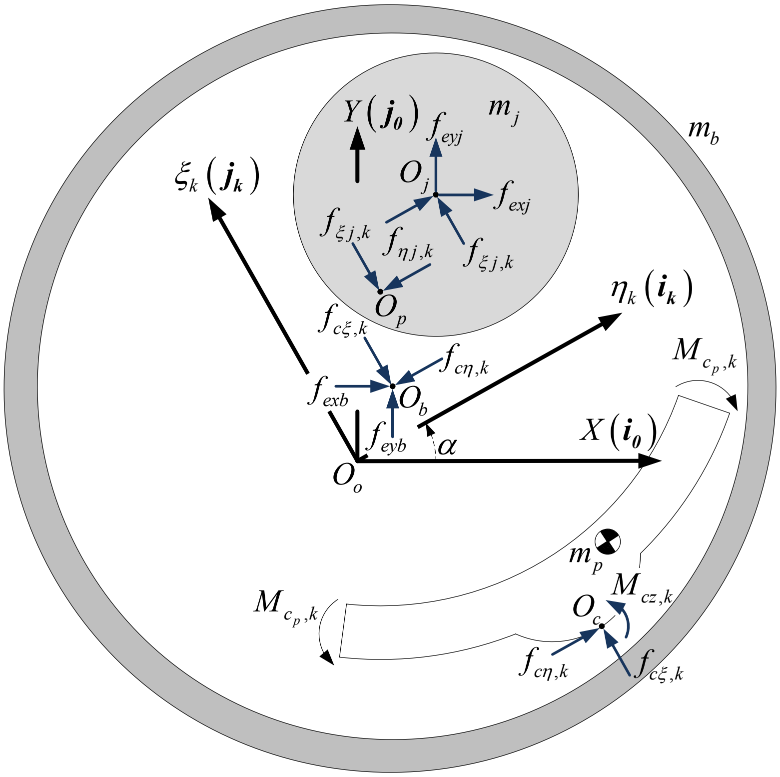

Figure 12: Free body diagram of the forces/moments acting on the pad, journal, and bearing due to the k^{th} pad and applied bearing and journal loads

Note that gravity forces (weights) are not included in Figure 12. In general, these forces are significantly smaller than the fluid film and pivot reaction forces, and will not be included in the analysis. Having classified the forces acting within our TPJB system, we must formally satisfy requirements for static equilibrium. To find equilibrium, we set all velocities and accelerations to zero and write the force balance for the journal, bearing, and each pad in the current (i^{th}) state. For each pad, we have

$$\left.\begin{array}{l} \sum M_{zc0,k} = 0 = r_{cp0,k} f_{\eta 0,k} + M_{cz0,k} \\ \sum F_{\eta g0,k} = 0 = -f_{\eta 0,k} + f_{c\eta 0,k} \\ \sum F_{\xi g0,k} = 0 = -f_{\xi 0,k} + f_{c\xi 0,k} \\ \sum M_{c_p 0,k} = 0 = M_{c_p 0,k} - k_{sc_p 0,k} c_{p0,k} \end{array}\right|_i , \tag{54}$$

where the first equation describes the summation of moments about the pad's pivot, the next two equations describe the summation of forces in the pad's transverse and radial directions, and the last equation describes the equilibrium equation for bending moments in the pad.

For the journal and bearing,

$$\begin{aligned}\sum_{k=1}^{n_p}\begin{Bmatrix}F_{xj0,k}\\F_{yj0,k}\end{Bmatrix}&=0=\sum_{k=1}^{n_p}\mathbf{Q_k}^T\left.\begin{Bmatrix}f_{\eta0,k}\\f_{\xi0,k}\end{Bmatrix}\right|_i+\begin{Bmatrix}f_{exj0}\\f_{eyj0}\end{Bmatrix}\\ \sum_{k=1}^{n_p}\begin{Bmatrix}F_{xb0,k}\\F_{yb0,k}\end{Bmatrix}&=0=\sum_{k=1}^{n_p}\mathbf{Q_k}^T\left.\begin{Bmatrix}-f_{c\eta0,k}\\-f_{c\xi0,k}\end{Bmatrix}\right|_i+\begin{Bmatrix}f_{exb0}\\f_{eyb0}\end{Bmatrix}\end{aligned}, \tag{55}$$

where f_{exj0}/f_{eyj0} and f_{exb0}/f_{eyb0} are static force components applied to the journal and bearing in the x/y directions, respectively, and $\mathbf{Q_k}$ is the coordinate transformation from the k^{th} pad fixed coordinate frame to the global X-Y coordinate frame given in Eq. (7).

Writing Eqs. (54) and (55) in matrix form and employing a Newton Raphson scheme yields

$$\mathbf{\Delta U_i}=\begin{bmatrix}\dfrac{\partial f_1}{\partial u_1}&\cdots&\dfrac{\partial f_1}{\partial u_n}\\ \vdots&\ddots&\vdots\\ \dfrac{\partial f_n}{\partial u_1}&\cdots&\dfrac{\partial f_n}{\partial u_n}\end{bmatrix}_{\mathbf{i}}^{-1}\mathbf{F_{0,i}}, \tag{56}$$

where $\mathbf{\Delta U_i}$ are the corrections needed to reduce the net force on all bodies to zero. Thus,

$$\mathbf{U_{i+1}}=\mathbf{U_i}+\mathbf{\Delta U_i} \tag{57}$$

is iteratively solved until the relative change from state i to $i+1$ is sufficiently small. In the bearing analyzed in this research, the circumferential position of each pivot was constrained to zero transverse movement during the determination of static equilibrium. This was done because pivots are restricted circumferentially by loose fitting pins, requiring assumptions to be made on the manner in which circumferential loads are transmitted through the pivot. As the author does not want to make assumptions on the mechanism supporting the circumferential shear load at each pivot, the transverse compliance of the pivot was included in the dynamic analysis, but not in the static analysis.

STIFFNESS AND DAMPING COEFFICIENTS AT EQUILIBRIUM

Figure 13 shows the lateral and angular stiffness and damping coefficients acting between the k^{th} pad and bearing housing and the fluid film stiffness and damping coefficients between the journal and k^{th} pad for perturbations about the equilibrium solution. Note that the fluid film moment coefficients are not shown in Figure 13; however, they are included in the analysis.

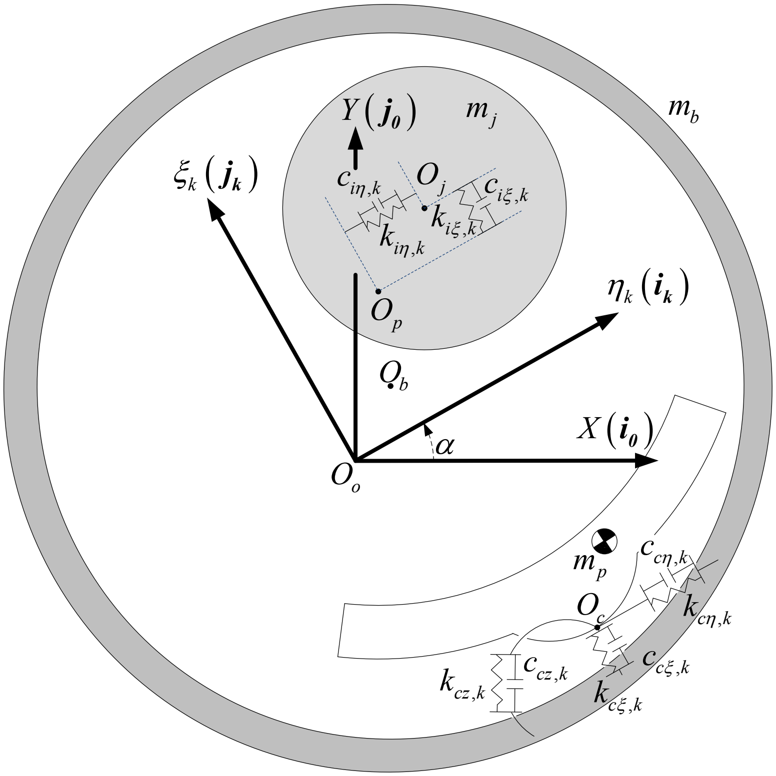

Figure 13: Schematic of the dynamic forces acting on the k^{th} pad in a TPJB

TPJB PERTURBED EQUATIONS OF MOTION

Having formally satisfied equilibrium requirements, let us develop equations of motion (EOMs) for our journal, k^{th} pad, and bearing using Newton's second law in the k^{th} pads η_k-ξ_k reference coordinate system. This approach means that we will be considering the dynamics of only a single pad in the preliminary stages of this development to eliminate the complexity arising from multiple coordinate transformations, and will discuss the inclusion of multiple pads into the model later.

Lund [2] was the first to perturb the journal and pads and write EOMs from an equilibrium state in a TPJB, producing a set of linear differential equations that were reduced by harmonic analysis to produce frequency dependent stiffness and damping coefficients for a single pad. Lund then assembled the contributions from each pad within the bearing to determine the total stiffness and damping for the bearing. Though this process has been enhanced by others, the fundamental process remains unchanged. Notable contributions to the process were the inclusion of pad compliance by Nilsson [3] in 1978, the inclusion of pivot compliance by Lund and Pederson [4] in 1987, and the inclusion of transverse pad motion by Jeng [1] for FPTPJBs in 1995. Jeng allows for tilt, radial, and circumferential pad motions in his development, but does not explicitly state the governing EOMs. None of the previous approaches perturb the position of the journal and bearing, and none of the previous approaches include all four pad degrees of freedom included here.

From Figures 4 and 11 we may write the displacement of the pad's CG located in the inertial frame, with the reference contact point ($O_{co,k}$) taken as a datum, as

$$\begin{aligned}
\eta_{g,k} &= \eta_{b,k} + \eta_{c,k} + b_{\eta go,k} - b_{\xi go,k}\sin(\phi) & \xi_{g,k} &= \xi_{b,k} + \xi_{c,k} + b_{\xi go,k} + b_{\eta go,k}\sin(\phi) \\
\dot{\eta}_{g,k} &= \dot{\eta}_{b,k} + \dot{\eta}_{c,k} - b_{\xi go,k}\cos(\phi)\dot{\phi}_k & \dot{\xi}_{g,k} &= \dot{\xi}_{b,k} + \dot{\xi}_{c,k} + b_{\eta go,k}\cos(\phi)\dot{\phi}_k \\
\ddot{\eta}_{g,k} &= \ddot{\eta}_{b,k} + \ddot{\eta}_{c,k} - b_{\xi go,k}\left[\cos(\phi)\ddot{\phi}_k - \sin(\phi)\dot{\phi}_k^2\right] & \ddot{\xi}_{g,k} &= \ddot{\xi}_{b,k} + \ddot{\xi}_{c,k} + b_{\eta go,k}\left[\cos(\phi)\ddot{\phi}_k - \sin(\phi)\dot{\phi}_k^2\right]
\end{aligned} \tag{58}$$

where $b_{\eta go,k}$ and $b_{\xi go,k}$ describe the distance from the contact location to the pad's center of mass in the pad's reference state. If we assume that motions are small such that $\sin(\phi) \simeq \phi$ and $\cos(\phi) \simeq 1$, Eq. (58) may be linearized as

$$\begin{aligned}
\eta_{g,k} &= \eta_{b,k} + \eta_{c,k} + b_{\eta go,k} - b_{\xi go,k}\phi_k & \xi_{g,k} &= \xi_{b,k} + \xi_{c,k} + b_{\xi go,k} + b_{\eta go,k}\phi_k \\
\dot{\eta}_{g,k} &= \dot{\eta}_{b,k} + \dot{\eta}_{c,k} - b_{\xi go,k}\dot{\phi}_k & \dot{\xi}_{g,k} &= \dot{\xi}_{b,k} + \dot{\xi}_{c,k} + b_{\eta go,k}\dot{\phi}_k \\
\ddot{\eta}_{g,k} &= \ddot{\eta}_{b,k} + \ddot{\eta}_{c,k} - b_{\xi go,k}\ddot{\phi}_k & \ddot{\xi}_{g,k} &= \ddot{\xi}_{b,k} + \ddot{\xi}_{c,k} + b_{\eta go,k}\ddot{\phi}_k
\end{aligned} \quad . \tag{59}$$

Applying Newton's second law to the pad yields the following perturbed EOMs for the k^{th} pad:

$$\begin{aligned}
&\sum M_{zc,k} = I_{c,k}\ddot{\phi}_k + m_{p,k}\left(\boldsymbol{b}_{\boldsymbol{cgo,k}} \times \ddot{\boldsymbol{e}}_{\boldsymbol{c,k}}\right) = r_{cp,k} f_{\eta,k} + M_{cz,k} \\
&\sum F_{\eta g,k} = m_{p,k}\ddot{\eta}_{g,k} = -f_{\eta,k} + f_{c\eta,k} \\
&\sum F_{\xi g,k} = m_{p,k}\ddot{\xi}_{g,k} = -f_{\xi,k} + f_{c\xi,k} \\
&\sum M_{c_p,k} = m_{c_p,k}\ddot{c}_{p1,k} = M_{c_p1,k} - k_{sc_p,k}c_{p1,k}
\end{aligned} \quad , \tag{60}$$

where the first equation is the summation of moments about the pivot (affecting pad tilt), the next two equations are the summation of forces in the pad's transverse and radial directions, and the last equation is the summation of bending moments (affecting pad clearance). The mass of the pad is $m_{p,k}$, $I_{c,k}$ is the pad's mass moment of inertia about the pivot, and $m_{cp,\mathrm{k}}$ represents the modal mass associated with changes in pad clearance. Though a modal analysis was not performed in the current work to determine $m_{cp,k}$, it is included here for completeness.

The second term in the pad tilt equation $m_{p,k}\left(\boldsymbol{b}_{\boldsymbol{cgo,k}} \times \ddot{\boldsymbol{e}}_{\boldsymbol{c,k}}\right)$ is required because moments are summed about the contact point which has radial and transverse translations given in Eq. (32) and Figure 11 that result from bearing motions and relative pad-bearing motions. This requirement was overlooked by previous researchers who included vertical pivot translation in the pad perturbation model. Overlooking this requirement may result in inaccurate coupling of pad tilt and bounce modes, which could produce erroneous results, depending on the mass of the pad and the vector $\boldsymbol{b}_{\boldsymbol{cgo,k}}$. For the bearing investigated, neglecting this term had no discernable impact on predicted bearing characteristics.

Proceeding with the sum of reaction forces due to the k^{th} pad on the journal and bearing, we have the following perturbed EOMs for the journal,

$$\begin{aligned}
&\sum F_{\eta j,k} = m_j\ddot{\eta}_{j,k} = f_{\eta,k} \\
&\sum F_{\xi j,k} = m_j\ddot{\xi}_{j,k} = f_{\xi,k}
\end{aligned} \quad , \tag{61}$$

where m_j represents the journal mass within the bearing, and the following perturbed EOMs for the bearing,

$$\begin{aligned}
&\sum F_{\eta b,k} = m_b\ddot{\eta}_{b,k} = -f_{c\eta,k} \\
&\sum F_{\xi b,k} = m_b\ddot{\xi}_{b,k} = -f_{c\xi,k}
\end{aligned} \quad . \tag{62}$$

Substituting the displacements from Eqs. (30-33), fluid film reaction forces from Eqs. (53), and pivot reaction forces from Eqs. (15, 17, and 13) into Eqs. (60-62), and writing them in matrix notation, we get

$$\begin{bmatrix} \mathbf{M_{jj}} & \mathbf{0} & \mathbf{0} \\ \mathbf{0} & \mathbf{M_{pp,k}} & \mathbf{M_{pb,k}} \\ \mathbf{0} & \mathbf{0} & \mathbf{M_{bb}} \end{bmatrix} \begin{Bmatrix} \mathbf{\ddot{U}_{j1,k}} \\ \mathbf{\ddot{U}_{p1,k}} \\ \mathbf{\ddot{U}_{b1,k}} \end{Bmatrix} + \begin{bmatrix} \mathbf{C_{jj,k}} & \mathbf{C_{jp,k}} & \mathbf{C_{jb,k}} \\ \mathbf{C_{pj,k}} & \mathbf{C_{pp,k}} & \mathbf{C_{pb,k}} \\ \mathbf{C_{bj,k}} & \mathbf{C_{bp,k}} & \mathbf{C_{bb,k}} \end{bmatrix} \begin{Bmatrix} \mathbf{\dot{U}_{j1,k}} \\ \mathbf{\dot{U}_{p1,k}} \\ \mathbf{\dot{U}_{b1,k}} \end{Bmatrix} + \begin{bmatrix} \mathbf{K_{jj,k}} & \mathbf{K_{jp,k}} & \mathbf{K_{jb,k}} \\ \mathbf{K_{pj,k}} & \mathbf{K_{pp,k}} & \mathbf{K_{pb,k}} \\ \mathbf{K_{bj,k}} & \mathbf{K_{bp,k}} & \mathbf{K_{bb,k}} \end{bmatrix} \begin{Bmatrix} \mathbf{U_{j1,k}} \\ \mathbf{U_{p1,k}} \\ \mathbf{U_{b1,k}} \end{Bmatrix} = \begin{Bmatrix} \mathbf{F_{j0,k}} \\ \mathbf{F_{p0,k}} \\ \mathbf{F_{b0,k}} \end{Bmatrix} \tag{63}$$

or more compactly

$$\mathbf{M_k \ddot{U}_{1,k}} + \mathbf{C_k \dot{U}_{1,k}} + \mathbf{K_k U_{1,k}} = \mathbf{F_{0,k}} = \mathbf{0}, \tag{64}$$

where the state vector $\mathbf{U_{1,k}}$ is given by

$$\mathbf{U_{1,k}} = \left\{ \begin{array}{c} \eta_{j1,k} \\ \xi_{j1,k} \\ \hline \phi_{1,k} \\ \eta_{c1,k} \\ \xi_{c1,k} \\ c_{p1,k} \\ \hline \eta_{b1,k} \\ \xi_{b1,k} \end{array} \right\} = \left\{ \begin{array}{c} \mathbf{U_{j1,k}} \\ \hline \mathbf{U_{p1,k}} \\ \hline \mathbf{U_{b1,k}} \end{array} \right\} \tag{65}$$

and the remaining terms in Eq. (64) are defined explicitly in Appendix A. In addition, Appendix B includes a derivation of the moment resulting from the application of a rolling-without-slipping constraint between a rocker-pivot and its housing.

INCORPORATING A BEARING INTO A DYNAMIC SYSTEM

At this time, we have two options to incorporate the structural model for each pad provided by Eqs. (63) into a global system model; we may: (1) include the full, unreduced, model provided by Eqs. (63) for each pad into the system model as suggested by Earles et al., or (2) assume that all motions can be characterized by vibrations of the form $\left(\tilde{\xi}_i, \tilde{\eta}_i\right) = \left(\tilde{\xi}_i, \tilde{\eta}_i\right) e^{\tilde{s}t} = \left(\tilde{\xi}_i, \tilde{\eta}_i\right) e^{(-\lambda + \tilde{j}\Omega)t}$, where $\tilde{s} = \lambda + \tilde{j}\Omega$ is the complex root of the assumed solution, and solve for pad motions as a function of rotor and bearing motions to reduce the bearing reaction force model to two rotor and two bearing DOFs as initially suggested by Lund [2].

Full (Unreduced) TPJB Model

If one wishes to explicitly include each pad's DOFs into the system dynamic model, a total of $4+4n_p$ equations are needed, where n_p represents the number of pads in the bearing. We will structure the state matrix as follows. Journal and bearing motions will be represented in the global X-Y coordinate frame, and each pad will retain its reference η_k-ξ_k coordinate system. The first two rows of the state matrix will be reserved for journal motions ($\mathbf{U_{j1}}=\{x_{j1}\ \ y_{j1}\}^{\mathrm{T}}$) and the last two rows will be reserved for bearing motions ($\mathbf{U_{b1}}=\{x_{b1}\ \ y_{b1}\}^{\mathrm{T}}$), while the remaining $4n_p$ rows will be broken into n_p groups of four, each containing a pad's DOFs ($\mathbf{U}_{\mathbf{p1},\boldsymbol{k}}=\{\phi_{1,k}\ \ \eta_{c1,k}\ \ \xi_{c1,k}\ \ c_{p1,k}\}^{\mathrm{T}}$). For the rotor and bearing, we have

$$\begin{aligned}
&\mathbf{M_{jj}}\ddot{\mathbf{U}}_{\mathbf{j1}}+\sum_{k=1}^{n_p}\mathbf{Q}_{\mathbf{k}}^{\mathbf{T}}\left(\mathbf{C_{jj,k}}\mathbf{Q_k}\dot{\mathbf{U}}_{\mathbf{j1}}+\mathbf{C_{jp,k}}\dot{\mathbf{U}}_{\mathbf{p1,k}}+\mathbf{C_{jb,k}}\mathbf{Q_k}\dot{\mathbf{U}}_{\mathbf{b1}}\right)\\
&\qquad\qquad+\sum_{k=1}^{n_p}\mathbf{Q}_{\mathbf{k}}^{\mathbf{T}}\left(\mathbf{K_{jj,k}}\mathbf{Q_k}\mathbf{U_{j1}}+\mathbf{K_{jp,k}}\mathbf{U_{p1,k}}+\mathbf{K_{jb,k}}\mathbf{Q_k}\mathbf{U_{b1}}\right)=\mathbf{F_{j1}}\\
&\mathbf{M_{bb}}\ddot{\mathbf{U}}_{\mathbf{b1}}+\sum_{k=1}^{n_p}\mathbf{Q}_{\mathbf{k}}^{\mathbf{T}}\left(\mathbf{C_{bj,k}}\mathbf{Q_k}\dot{\mathbf{U}}_{\mathbf{j1}}+\mathbf{C_{bp,k}}\dot{\mathbf{U}}_{\mathbf{p1,k}}+\mathbf{C_{bb,k}}\mathbf{Q_k}\dot{\mathbf{U}}_{\mathbf{b1}}\right)\\
&\qquad\qquad+\sum_{k=1}^{n_p}\mathbf{Q}_{\mathbf{k}}^{\mathbf{T}}\left(\mathbf{K_{bj,k}}\mathbf{Q_k}\mathbf{U_{j1}}+\mathbf{K_{bp,k}}\mathbf{U_{p1,k}}+\mathbf{K_{bb,k}}\mathbf{Q_k}\mathbf{U_{b1}}\right)=\mathbf{F_{b1}}
\end{aligned}\quad. \tag{66}$$

Likewise, for the k^{th} pad, we obtain

$$\begin{aligned}
&\mathbf{M_{pp,k}}\ddot{\mathbf{U}}_{\mathbf{p1,k}}+\mathbf{M_{pb,k}}\mathbf{Q_k}\ddot{\mathbf{U}}_{\mathbf{b1}}+\mathbf{C_{pj,k}}\mathbf{Q_k}\dot{\mathbf{U}}_{\mathbf{j1}}+\mathbf{C_{pp,k}}\dot{\mathbf{U}}_{\mathbf{p1,k}}+\mathbf{C_{pb,k}}\mathbf{Q_k}\dot{\mathbf{U}}_{\mathbf{b1}}\\
&\qquad\qquad+\mathbf{K_{pj,k}}\mathbf{Q_k}\mathbf{U_{j1}}+\mathbf{K_{pp,k}}\mathbf{U_{p1,k}}+\mathbf{K_{pb,k}}\mathbf{Q_k}\mathbf{U_{b1}}=\mathbf{0}\ \ ,\ k=1\ldots n_p
\end{aligned}\quad. \tag{67}$$

Thus, our system may be written in matrix form as

$$\begin{bmatrix} \mathbf{M_{jj}} & \mathbf{0} & \cdots & \mathbf{0} \\ \mathbf{0} & \mathbf{M_{pp,k}} & \cdots & \mathbf{M_{pb,k}Q_k} \\ \vdots & \vdots & \ddots & \vdots \\ \mathbf{0} & \mathbf{0} & \cdots & \mathbf{M_{bb}} \end{bmatrix} \begin{Bmatrix} \ddot{\mathbf{U}}_{\mathbf{j1}} \\ \ddot{\mathbf{U}}_{\mathbf{p1,k}} \\ \vdots \\ \ddot{\mathbf{U}}_{\mathbf{b1}} \end{Bmatrix} + \begin{bmatrix} \sum_{k=1}^{n_p} \mathbf{Q_k^T C_{jj,k} Q_k} & \mathbf{Q_k^T C_{jp,k}} & \cdots & \sum_{k=1}^{n_p} \mathbf{Q_k^T C_{jb,k} Q_k} \\ \mathbf{C_{pj,k} Q_k} & \mathbf{C_{pp,k}} & \cdots & \mathbf{C_{pb,k} Q_k} \\ \vdots & \vdots & \ddots & \vdots \\ \sum_{k=1}^{n_p} \mathbf{Q_k^T C_{bj,k} Q_k} & \mathbf{Q_k^T C_{bp,k}} & \cdots & \sum_{k=1}^{n_p} \mathbf{Q_k^T C_{bb,k} Q_k} \end{bmatrix} \begin{Bmatrix} \dot{\mathbf{U}}_{\mathbf{j1}} \\ \dot{\mathbf{U}}_{\mathbf{p1,k}} \\ \vdots \\ \dot{\mathbf{U}}_{\mathbf{b1}} \end{Bmatrix}$$

$$+ \begin{bmatrix} \sum_{k=1}^{n_p} \mathbf{Q_k^T K_{jj,k} Q_k} & \mathbf{Q_k^T K_{jp,k}} & \cdots & \sum_{k=1}^{n_p} \mathbf{Q_k^T K_{jb,k} Q_k} \\ \mathbf{K_{pj,k} Q_k} & \mathbf{K_{pp,k}} & \cdots & \mathbf{K_{pb,k} Q_k} \\ \vdots & \vdots & \ddots & \vdots \\ \sum_{k=1}^{n_p} \mathbf{Q_k^T K_{bj,k} Q_k} & \mathbf{Q_k^T K_{bp,k}} & \cdots & \sum_{k=1}^{n_p} \mathbf{Q_k^T K_{bb,k} Q_k} \end{bmatrix} \begin{Bmatrix} \mathbf{U_{j1}} \\ \mathbf{U_{p1,k}} \\ \vdots \\ \mathbf{U_{b1}} \end{Bmatrix} = \begin{Bmatrix} \mathbf{F_{j1}} \\ \mathbf{0} \\ \vdots \\ \mathbf{F_{b1}} \end{Bmatrix} \tag{68}$$

and linked to a global system model for imbalance response, stability analysis, or time transient simulations.

Reduced TPJB Model

To employ the reduced coefficients for each pad into the global system model, we use the following method. First, we assume that all motions can be characterized by vibrations of the form $\left(\tilde{\xi}_i, \tilde{\eta}_i\right) = \left(\tilde{\xi}_i, \tilde{\eta}_i\right) e^{\tilde{s}t} = \left(\tilde{\xi}_i, \tilde{\eta}_i\right) e^{(-\lambda + \tilde{j}\Omega)t}$, where $\tilde{s} = \lambda + \tilde{j}\Omega$ is the complex root of the assumed solution. For clarity, complex variables will be denoted with a “tilde.” Making this substitution, we rewrite Eq. (64) for a single pad as

$$\left(\mathbf{M_k}\tilde{s}^2 + \mathbf{C_k}\tilde{s} + \mathbf{K_k}\right)\tilde{\mathbf{U}}_{\mathbf{1,k}} = 0, \tag{69}$$

where the vector $\tilde{\mathbf{U}}_{\mathbf{1,k}}$ includes journal, pad and bearing motions in the k^{th} pad’s η_k-ξ_k reference coordinate system given by

$$\tilde{\mathbf{U}}_{\mathbf{1,k}} = \left\{ \begin{array}{c} \tilde{\mathbf{U}}_{\mathbf{j1,k}} \\ \hline \tilde{\mathbf{U}}_{\mathbf{p1,k}} \\ \hline \tilde{\mathbf{U}}_{\mathbf{b1,k}} \end{array} \right\} \tag{70}$$

where $\tilde{\mathbf{U}}_{\mathbf{j1,k}} = \left\{\tilde{\eta}_{j1,k}\ \tilde{\xi}_{j1,k}\right\}^T$, $\tilde{\mathbf{U}}_{\mathbf{p1,k}} = \left\{\tilde{\phi}_{1,k}\ \tilde{\eta}_{c1,k}\ \tilde{\xi}_{c1,k}\ \tilde{c}_{p1,k}\right\}^T$, and $\tilde{\mathbf{U}}_{\mathbf{b1,k}} = \left\{\tilde{\eta}_{b1,k}\ \tilde{\xi}_{b1,k}\right\}^T$. Eq. (69) can be expanded as

$$\begin{bmatrix} \tilde{\mathbf{I}}_{\mathbf{jj,k}} & \tilde{\mathbf{I}}_{\mathbf{jp,k}} & \tilde{\mathbf{I}}_{\mathbf{jb,k}} \\ \tilde{\mathbf{I}}_{\mathbf{pj,k}} & \mathbf{M}_{\mathbf{pp,k}}\tilde{\mathbf{s}}^2+\mathbf{I}_{\mathbf{pp,k}} & \mathbf{M}_{\mathbf{pb,k}}\tilde{\mathbf{s}}^2+\tilde{\mathbf{I}}_{\mathbf{pb,k}} \\ \tilde{\mathbf{I}}_{\mathbf{bj,k}} & \tilde{\mathbf{I}}_{\mathbf{bp,k}} & \tilde{\mathbf{I}}_{\mathbf{bb,k}} \end{bmatrix} \begin{Bmatrix} \tilde{\mathbf{U}}_{\mathbf{j1,k}} \\ \tilde{\mathbf{U}}_{\mathbf{p1,k}} \\ \tilde{\mathbf{U}}_{\mathbf{b1,k}} \end{Bmatrix} = \begin{bmatrix} \tilde{\mathbf{A}}_{\mathbf{jj,k}} & \tilde{\mathbf{A}}_{\mathbf{jp,k}} & \tilde{\mathbf{A}}_{\mathbf{jb,k}} \\ \tilde{\mathbf{A}}_{\mathbf{pj,k}} & \tilde{\mathbf{A}}_{\mathbf{pp,k}} & \tilde{\mathbf{A}}_{\mathbf{pb,k}} \\ \tilde{\mathbf{A}}_{\mathbf{bj,k}} & \tilde{\mathbf{A}}_{\mathbf{bp,k}} & \tilde{\mathbf{A}}_{\mathbf{bb,k}} \end{bmatrix} \begin{Bmatrix} \tilde{\mathbf{U}}_{\mathbf{j1,k}} \\ \tilde{\mathbf{U}}_{\mathbf{p1,k}} \\ \tilde{\mathbf{U}}_{\mathbf{b1,k}} \end{Bmatrix} = \begin{Bmatrix} -\mathbf{M}_{\mathbf{jj}}\tilde{\mathbf{s}}^2\tilde{\mathbf{U}}_{\mathbf{j1,k}} \\ \mathbf{0} \\ -\mathbf{M}_{\mathbf{bb}}\tilde{\mathbf{s}}^2\tilde{\mathbf{U}}_{\mathbf{b1,k}} \end{Bmatrix} \tag{71}$$

where $\tilde{\mathbf{I}}_{\mathbf{ij,k}} = \mathbf{C}_{\mathbf{ij,k}}\tilde{\mathbf{s}} + \mathbf{K}_{\mathbf{ij,k}}$, and $\mathbf{M_{jj}}/\mathbf{M_{bb}}$ are diagonal journal/bearing mass matrices that are defined explicitly in Appendix A. Expanding the second set of relations in Eq. (71) and solving for pad motion ($\tilde{\mathbf{U}}_{\mathbf{p1,k}} = \left\{\tilde{\phi}_{1,k}\ \tilde{\eta}_{c1,k}\ \tilde{\xi}_{c1,k}\ \tilde{c}_{p1,k}\right\}^T$) yields

$$\tilde{\mathbf{U}}_{\mathbf{p1,k}} = -\tilde{\mathbf{A}}^{\mathbf{-1}}_{\mathbf{pp,k}}\tilde{\mathbf{A}}_{\mathbf{pj,k}}\tilde{\mathbf{U}}_{\mathbf{j1,k}} - \tilde{\mathbf{A}}^{\mathbf{-1}}_{\mathbf{pp,k}}\tilde{\mathbf{A}}_{\mathbf{pb,k}}\tilde{\mathbf{U}}_{\mathbf{b1,k}} = \tilde{\mathbf{\Gamma}}_{\mathbf{pj,k}}\tilde{\mathbf{U}}_{\mathbf{j1,k}} + \tilde{\mathbf{\Gamma}}_{\mathbf{pb,k}}\tilde{\mathbf{U}}_{\mathbf{b1,k}} \tag{72}$$

where the *pad-journa*l, or *pad-rotor*, transfer function matrix is

$$\tilde{\mathbf{\Gamma}}_{\mathbf{pj,k}} = \begin{bmatrix} \tilde{\Gamma}^{\eta_j}_{\phi_k} & \tilde{\Gamma}^{\xi_j}_{\phi_k} \\ \tilde{\Gamma}^{\eta_j}_{\eta_{c,k}} & \tilde{\Gamma}^{\xi_j}_{\eta_{c,k}} \\ \tilde{\Gamma}^{\eta_j}_{\xi_{c,k}} & \tilde{\Gamma}^{\xi_j}_{\xi_{c,k}} \\ \tilde{\Gamma}^{\eta_j}_{c_{p,k}} & \tilde{\Gamma}^{\xi_j}_{c_{p,k}} \end{bmatrix} = -\tilde{\mathbf{A}}^{\mathbf{-1}}_{\mathbf{pp,k}}\tilde{\mathbf{A}}_{\mathbf{pj,k}} \equiv \begin{bmatrix} \tilde{\phi}^{\eta_j}_{1,k} & \tilde{\phi}^{\xi_j}_{1,k} \\ \tilde{\eta}^{\eta_j}_{c1,k} & \tilde{\eta}^{\xi_j}_{c1,k} \\ \tilde{\xi}^{\eta_j}_{c1,k} & \tilde{\xi}^{\xi_j}_{c1,k} \\ \tilde{c}^{\eta_j}_{p1,k} & \tilde{c}^{\xi_j}_{p1,k} \end{bmatrix} \begin{bmatrix} \tilde{\eta}^{-1}_{j1,k} & 0 \\ 0 & \tilde{\xi}^{-1}_{j1,k} \end{bmatrix}, \tag{73}$$

and the *pad-bearing* transfer function matrix is

$$\tilde{\mathbf{\Gamma}}_{\mathbf{bj,k}} = \begin{bmatrix} \tilde{\Gamma}^{\eta_b}_{\phi_k} & \tilde{\Gamma}^{\xi_b}_{\phi_k} \\ \tilde{\Gamma}^{\eta_b}_{\eta_{c,k}} & \tilde{\Gamma}^{\xi_b}_{\eta_{c,k}} \\ \tilde{\Gamma}^{\eta_b}_{\xi_{c,k}} & \tilde{\Gamma}^{\xi_b}_{\xi_{c,k}} \\ \tilde{\Gamma}^{\eta_b}_{c_{p,k}} & \tilde{\Gamma}^{\xi_b}_{c_{p,k}} \end{bmatrix} = -\tilde{\mathbf{A}}^{\mathbf{-1}}_{\mathbf{pp,k}}\tilde{\mathbf{A}}_{\mathbf{pb,k}} \equiv \begin{bmatrix} \tilde{\phi}^{\eta_b}_{1,k} & \tilde{\phi}^{\xi_b}_{1,k} \\ \tilde{\eta}^{\eta_b}_{c1,k} & \tilde{\eta}^{\xi_b}_{c1,k} \\ \tilde{\xi}^{\eta_b}_{c1,k} & \tilde{\xi}^{\xi_b}_{c1,k} \\ \tilde{c}^{\eta_b}_{p1,k} & \tilde{c}^{\xi_b}_{p1,k} \end{bmatrix} \begin{bmatrix} \tilde{\eta}^{-1}_{b1,k} & 0 \\ 0 & \tilde{\xi}^{-1}_{b1,k} \end{bmatrix}. \tag{74}$$

Here, superscripts (η, ξ) indicate that pad motions correspond to η_k, ξ_k motions of the journal/bearing. Essentially, these transfer functions define the amplitude and phase of pad motions due to radial and transverse journal/bearing motions. For example, $\tilde{\Gamma}^{\xi_j}_{\xi_{c,k}}$ specifies the ratio of radial pad motion relative to the bearing housing to radial rotor motion (i.e. $\tilde{\xi}_{c1} = \tilde{\Gamma}^{\xi_j}_{\xi_{c,k}}\tilde{\xi}_{j1}$).

Consider the impact of the *pad-rotor* transfer function $\tilde{\Gamma}^{\xi_j}_{\xi_{c,k}}$ on radial rotor motions of unit amplitude. If the pad has a rigid pivot, $\tilde{\Gamma}^{\xi_j}_{\xi_{c,k}} = 0$ for example, the pad may rock back and forth to balance tilting moments, but there will be no radial translation of the pad relative to the bearing housing. This lack of radial pad motion will result in changes in fluid film thickness equal to the magnitude of journal motion, which will maximize the impact of fluid film stiffness and damping on the journal.

If the pad has a softer pivot stiffness (similar to the bearing tested in this work), $\tilde{\Gamma}_{\xi_{c,k}}^{\xi_j} = 0.5$ for example, this implies that radial rotor motions of unit amplitude will produce radial pad motions given by $\tilde{\xi}_{c1} = \tilde{\Gamma}_{\xi_{c,k}}^{\xi_j} \tilde{\xi}_{j1} = 0.5$. Thus, unlike the previous case, changes in the fluid film height due to radial rotor motions of unit amplitude will only be ½ of the amplitude of rotor's motion. Since the pivot of the pad likely has very little damping, the effective fluid film stiffness and damping between the rotor and ground would be significantly reduced.

If the pad has a very soft pivot, or a very stiff fluid film, resulting in $\tilde{\Gamma}_{\xi_{c,k}}^{\xi_j} = 1$, the pad will move with the same amplitude and phase as the journal, resulting in zero change in fluid film height; hence, the impact of fluid film stiffness and damping on the journal are eliminated by the flexibility of the pivot.

Though these scenarios may be gross exaggerations of the impact of pad-rotor transfer functions defined in Eq. (73) and (74), they should serve as a starting point in illuminating the impact of the pad-rotor and pad-bearing transfer functions on the stiffness and damping of a bearing. To predict the correct reduced coefficients for a TPJB, the relations in Eqs. (73) and (74) must be accurate. Validating these relations by comparison of measured and predicted pad-rotor or pad-bearing transfer functions is a primary goal of this research.

To obtain reduced stiffness and damping coefficients, $\tilde{\mathbf{U}}_{\mathbf{p1,k}}$ is substituted from Eq. (72) into the top and bottom set of relations in Eq. (71) to yield

$$\begin{bmatrix} \tilde{\mathbf{A}}_{\mathbf{jj,k}} + \tilde{\mathbf{A}}_{\mathbf{jp,k}} \tilde{\boldsymbol{\Gamma}}_{\mathbf{pj,k}} & \tilde{\mathbf{A}}_{\mathbf{jb,k}} + \tilde{\mathbf{A}}_{\mathbf{jp,k}} \tilde{\boldsymbol{\Gamma}}_{\mathbf{pb,k}} \\ \tilde{\mathbf{A}}_{\mathbf{bj,k}} + \tilde{\mathbf{A}}_{\mathbf{bp,k}} \tilde{\boldsymbol{\Gamma}}_{\mathbf{pj,k}} & \tilde{\mathbf{A}}_{\mathbf{bb,k}} + \tilde{\mathbf{A}}_{\mathbf{bp,k}} \tilde{\boldsymbol{\Gamma}}_{\mathbf{pb,k}} \end{bmatrix} \begin{Bmatrix} \tilde{\mathbf{U}}_{\mathbf{j1,k}} \\ \tilde{\mathbf{U}}_{\mathbf{b1,k}} \end{Bmatrix} = \begin{bmatrix} \tilde{\mathbf{H}}_{\mathbf{jj,k}} & \tilde{\mathbf{H}}_{\mathbf{jb,k}} \\ \tilde{\mathbf{H}}_{\mathbf{bj,k}} & \tilde{\mathbf{H}}_{\mathbf{bb,k}} \end{bmatrix} \begin{Bmatrix} \tilde{\mathbf{U}}_{\mathbf{j1,k}} \\ \tilde{\mathbf{U}}_{\mathbf{b1,k}} \end{Bmatrix} = \begin{Bmatrix} -\mathbf{M}_{\mathbf{jj}} \tilde{\mathbf{s}}^{\mathbf{2}} \tilde{\mathbf{U}}_{\mathbf{j1,k}} \\ -\mathbf{M}_{\mathbf{bb}} \tilde{\mathbf{s}}^{\mathbf{2}} \tilde{\mathbf{U}}_{\mathbf{b1,k}} \end{Bmatrix} \quad (75)$$

where the elements of $\tilde{\mathbf{H}}_{\mathbf{ij,k}}$ are commonly referred to as impedances or complex dynamic stiffnesses. Though the term impedance technically refers to the ratio of a force to a velocity, it appears to be the preferred choice in hydrodynamic bearing literature, and will be used for the remainder of this work. Thus from Eq. (75), reduced pad stiffness and damping coefficients are given by the real and imaginary parts of $\tilde{\mathbf{H}}_{\mathbf{ij,k}}$ as

$$\mathbf{K}_{\mathbf{ij,k}}(\Omega)=\mathrm{Re}\left\{\tilde{\mathbf{H}}_{\mathbf{ij,k}}\right\},\ \mathbf{C}_{\mathbf{ij,k}}(\Omega)=\frac{\mathrm{Im}\left\{\tilde{\mathbf{H}}_{\mathbf{ij,k}}\right\}}{\Omega},\ \tilde{\mathbf{H}}_{\mathbf{ij,k}}(\Omega)=\begin{bmatrix}\tilde{H}_{\eta\eta,k} & \tilde{H}_{\eta\xi,k}\\ \tilde{H}_{\xi\eta,k} & \tilde{H}_{\xi\xi,k}\end{bmatrix}_{ij,k}, \tag{76}$$

where the subscripts η, ξ indicate that an impedance acts on motions in the pad-fixed η_k-ξ_k frame. Rotating $\tilde{\mathbf{H}}_{\mathbf{ij,k}}$ into the global *X-Y* coordinate system and summing impedances across all pads, we obtain the net bearing impedances for the journal and bearing motions as

$$\begin{bmatrix}\tilde{\mathbf{H}}_{\mathbf{jj}} & \tilde{\mathbf{H}}_{\mathbf{jb}}\\ \tilde{\mathbf{H}}_{\mathbf{bj}} & \tilde{\mathbf{H}}_{\mathbf{bb}}\end{bmatrix}=\begin{bmatrix}\sum_{k=1}^{n_p}\mathbf{Q}_{\mathbf{k}}^{\mathbf{T}}\tilde{\mathbf{H}}_{\mathbf{jj,k}}\mathbf{Q}_{\mathbf{k}} & \sum_{k=1}^{n_p}\mathbf{Q}_{\mathbf{k}}^{\mathbf{T}}\tilde{\mathbf{H}}_{\mathbf{jb,k}}\mathbf{Q}_{\mathbf{k}}\\ \sum_{k=1}^{n_p}\mathbf{Q}_{\mathbf{k}}^{\mathbf{T}}\tilde{\mathbf{H}}_{\mathbf{bj,k}}\mathbf{Q}_{\mathbf{k}} & \sum_{k=1}^{n_p}\mathbf{Q}_{\mathbf{k}}^{\mathbf{T}}\tilde{\mathbf{H}}_{\mathbf{bb,k}}\mathbf{Q}_{\mathbf{k}}\end{bmatrix} \tag{77}$$

The results of this pad-perturbation model are applicable to the reduction of stiffness and damping terms for both damped and undamped (harmonic) motions of the rotor or bearing given the proper selection of $\tilde{s}$.

Root Employed in Bearing Reduction

Historically, coefficients in Eq. (77) are calculated for purely harmonic solutions with $\tilde{s}=\tilde{j}\Omega,(\lambda=0)$ over a range of frequencies, but some researchers have stated that using a damped eigenvalue ($\lambda\neq 0$) in the calculation of reduced coefficients is more appropriate than using a harmonic solution, especially for stability calculations [4]. This argument is not justified, however, because $\lambda\to 0$ at the threshold of instability.

The frequency range and type of solution employed in the calculation of reduced bearing coefficients has been a controversial topic over the past few decades [16-18]. This work will continue to discuss these issues; however, the author's position is that the choice of solution and method of incorporating a bearing into a system model are irrelevant if the EOMs governing rotor, journal, and pad motion in Eq. (63) are not correct.

Selection of Method - Full versus Reduced Bearing Coefficients

Adding the full bearing dynamics given in Eq. (68) into the system model requires significantly more effort than incorporating a reduced coefficient model. When is this effort justified? The answer to this question depends on the type of analysis being performed.

For the prediction of system response to imbalance or pseudorandom harmonic excitations, no justification can be made to include the full model; both full and reduced coefficients will yield the same result.

For the prediction of system stability, the choice to employ a full or reduced bearing model is more complicated. A system becomes unstable if the real part of one of its eigenvalues becomes positive. The need to incorporate a full bearing model into a system's dynamic model arises when vibration modes eliminated during the bearing reduction affect the stability of the system. Since the eigenvalues of the pads are typically significantly higher in frequency than the unstable mode or critically damped [15], most researchers assume that the pad DOFs can be reduced from the model without a significant reduction in accuracy. Consider the following Jeffcott rotor systems supported by tilting pad bearings with a destabilizing cross-coupled stiffness applied at the mid-span. "System A" consists of a short shaft having a rigid-body cylindrical mode at the lowest natural frequency, while "System B" consists of a long flexible shaft having a pinned-pinned mode at the lowest natural frequency. When using a full bearing model to analyze these systems, $2+4n_p$ eigenvalues would exist, where the reduced system would only contain 2; thus, the system's eigenvalues for the full and reduced bearing models would not be the same. This statement alone is not justification for using the full bearing model to determine stability.

Answering this question requires us to ask whether the mode that becomes unstable is the same for both full and reduced models. For "System A," having large modal amplitudes at the bearing in the fundamental mode, it is likely that the dynamics within the bearing would have more impact on the stability of the fundamental mode; thus a full bearing model might yield a more accurate stability prediction. For "System B," having negligible modal amplitudes at the bearing in the fundamental mode, it is likely that the dynamics within the bearing would have little or no impact on the stability of the bending mode; thus a full model would not likely yield any improvement over the reduced model. For the prediction of system stability, the choice to employ a full or reduced bearing model depends on the relative impact of bearing dynamics on the dynamics of the overall system, and should be determined on a case by case basis. The effect of using full or reduced bearing models in stability calculations is discussed more thoroughly in the RESULTS section.

ROTOR VERSUS BEARING/STATOR PERTURBATION

During this analysis, transfer functions explicitly defining pad motion as a function of rotor and bearing/stator motions were found. If the pad-rotor and pad-bearing transfer functions given in Eqs. (73) and (74) differ significantly enough to cause differences in predicted bearing impedances for rotor-only or bearing-only motions, the predicted bearing impedances will depend on whether the rotor or bearing is perturbed; hence, previous comparisons between bearing impedances measured on floating bearing test rigs to predictions using a journal perturbed model would not be valid. Differences in these transfer functions result solely from the proper application of Newton's second law in writing the equation of motion for each pad; thus, if the inertia of the pads is insignificant, both rotor and bearing perturbations will yield the same impedance coefficients.

How can the issue of rotor-perturbed motion versus bearing-perturbed motion be resolved? There are several options. The logical starting point is to assume that the bearing is fixed, and predict coefficients for rotor perturbed motions. Next, fix the journal and predict coefficients for bearing perturbed motion. If the coefficients predicted for the bearing and journal perturbations are the same, then we may assume that the rotor or stator is fixed during tests, and use measured relative rotor-stator motion to generate transfer functions between the rotor/bearing and the pad.

If the coefficients predicted for the bearing-excited and journal-excited perturbations differ, then we must proceed with caution in comparing measured and predicted transfer functions. This would require that both absolute rotor and stator motions were known during experiments. Because relative rotor-stator motion is measured accurately by proximity probes during experiments, either absolute (inertial) rotor or stator motion would need to be measured. This could approximated for the bearing using

$$\tilde{\mathbf{U}}_{\mathbf{b1}} = -\Omega^{-2}\tilde{\mathbf{A}}_{\mathbf{b1}}, \tag{78}$$

where $\tilde{\mathbf{A}}_{\mathbf{b1}} = \{\tilde{A}_{xb}\ \tilde{A}_{yb}\}^T$ are the absolute stator/bearing acceleration components measured during experiments. This method might produce accurate stator motions at higher excitation frequencies, but quality may be reduced at low frequencies due to increased noise in the accelerometer signal at low frequencies.

UTILITY OF PAD-JOURNAL AND PAD-BEARING TRANSFER FUNCTIONS

What can be gained by the comparison of pad-journal and pad-bearing transfer functions over conventional testing methods? Answering this question requires that we first understand the product of a conventional bearing test.

A conventional bearing test produces the real and imaginary parts of $\tilde{\mathbf{H}}_{\mathbf{xx}}, \tilde{\mathbf{H}}_{\mathbf{xy}} \ldots$ for a bearing from measured relative rotor-stator motion components, bearing acceleration components, and applied external excitation force components over a range of frequencies. The results are frequency-dependent complex impedances that may be used to estimate stiffness, damping, or virtual-mass coefficients. Comparisons between measured and predicted stiffness, damping, or virtual-mass coefficients are then made, upon which conclusions are drawn concerning the accuracy of the prediction model. Historically, this process has led to many questions, and though it has provided many answers, continuing to test TPJBs in the same manner is not likely to resolve some of the questions that still remain.

For example, consider a conventional (stiffness, damping, or virtual-mass coefficient) comparison between measurements and predictions for a model having a rigid pivot where the stiffness is predicted fairly well and the virtual-mass is smaller than predicted, but the damping is overpredicted by a factor of 2. Translating this information into useful feedback to determine modeling or experimental shortcomings is no more than a guessing game.

Now consider comparing measured and predicted $\tilde{\Gamma}_{\xi_{c,k}}^{\xi_j}$ (defining radial pad motion due to radial rotor motion) for a model having a rigid pivot. Upon first inspection of the measured and predicted $\tilde{\Gamma}_{\xi_{c,k}}^{\xi_j}$, it would be obvious that radial pad translation was observed in tests, while no radial pad motion was predicted. This would imply that pivot flexibility must be included in the model to accurately predict the pad's motion. Furthermore, consider comparing measured and predicted $\tilde{\Gamma}_{\xi_{c,k}}^{\xi_j}$ for a model containing pivot flexibility. If measured $\tilde{\Gamma}_{\xi_{c,k}}^{\xi_j}$ is significantly larger in magnitude than predicted $\tilde{\Gamma}_{\xi_{c,k}}^{\xi_j}$, the pivot stiffness used in the prediction is likely too large, while overpredicted radial pad motion might suggest that the pivot stiffness in the model is too small. Thus, comparing measured and predicted rotor-pad transfer functions can provide significantly more feedback than a conventional bearing test.

Information that can be gained from measured rotor-pad transfer functions includes the following:

(1) $\tilde{\Gamma}_{\xi_{c,k}}^{\xi_j}$ (radial pad motion due to radial rotor motion) can be used to verify pivot stiffness.

(2) $\tilde{\Gamma}_{\xi_{c,k}}^{\xi_j}$ (radial pad motion due to transverse rotor motion) if observed, indicates that the transverse position of the rotor has an impact on the radial force applied to the pad, which results in cross coupled stiffness. This observation may indicate that the pivot is locked up, preventing the pad from tilting, or that the pad's

contact point translates due to a rolling-without-slipping motion. Inclusion of the latter effect in the model is discussed in Appendix B.

(3) $\tilde{\Gamma}^{\eta_j}_{\phi_k}$ (pad tilt due to transverse rotor motion) can be used to verify that the pivot allows the pad to tilt freely to track the motion of the pad; this ensures that the bearing is not providing significant cross coupled forces. $\tilde{\Gamma}^{\eta_j}_{\phi_k}$ can also be used to identify the location of the pivot point, which may be in question for a sliding pivot.

(4) $\tilde{\Gamma}^{\xi_j}_{\eta_{c,k}}$ and $\tilde{\Gamma}^{\eta_j}_{\eta_{c,k}}$ (transverse pad motion due to radial and transverse rotor motion) could be used to identify whether the back of the pad is slipping at the contact point, or translating excessively. This observation may be pertinent to avoid fretting at the contact surface.

(5) $\tilde{\Gamma}^{\xi_j}_{c_{p,k}}$ (changes in pad clearance due to radial rotor motion) can be used to verify the structural stiffness of the pad and the pad bending model.

These uses are discussed on a case-by-case basis in the RESULTS section.

In addition to validating the fundamental assumptions on pad motion used in predicting TPJB dynamic coefficients, comparing measured and predicted pad-rotor and pad-bearing transfer functions may also provide more detail concerning the relative importance of pad DOFs and vibration modes on bearing performance, reduce dependence on stator force and acceleration measurements, and provide insights into frequency dependent pad behavior such as natural frequencies, pad flutter, and pivot friction effects.

CHAPTER III

BEARING AND TEST RIG DESCRIPTION

TEST RIG DESCRIPTION

A drawing of the test rig is shown in Figure 14. A thorough description of this test rig is given in [21-23,25], and will not be discussed in detail here. The test rig is a floating-bearing test rig modeled after Glienicke [19], in which a bearing mounted in a stator (labeled bearing retainer in Figure 14) floats on an oil film supported by a "rigid rotor." The bearing, or stator, is excited by means of hydraulic actuators at various frequencies while components of applied force, absolute stator acceleration and relative rotor-stator motion vectors are recorded. In addition to dynamic excitations, a static load up to 22 kN (5k lbf) can be applied.

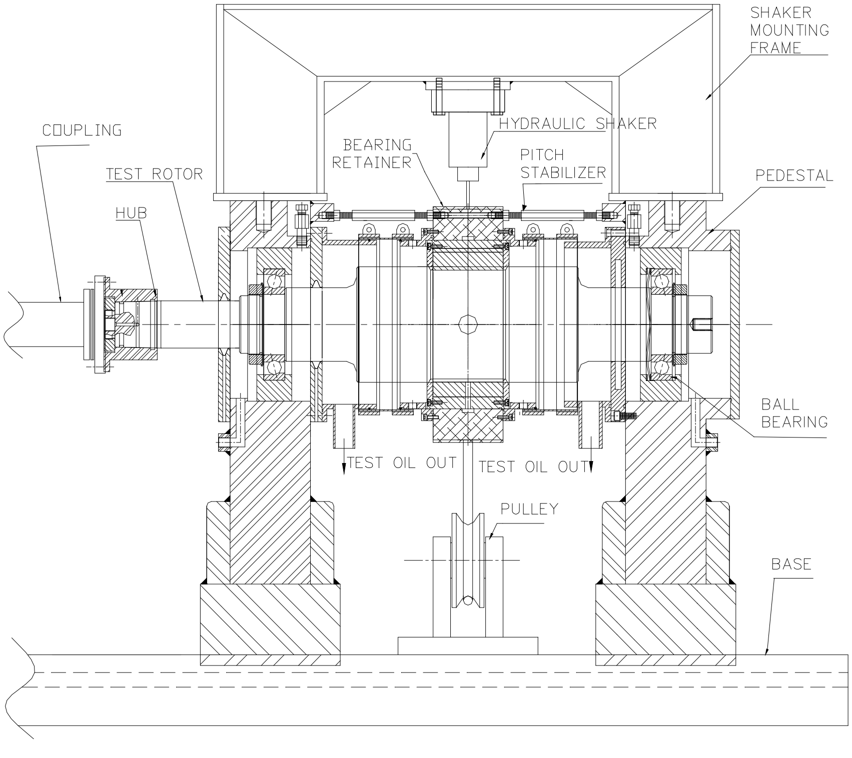

Figure 14: Drawing of the test rig [25]

Figure 15 shows a picture of the stator with a bearing installed. This picture shows two locations for the proximity probes, one set adjacent to the stinger connections, and another set 180° away from the stinger connection. Previously [21-23, 32-35], the proximity probes were located 180° from the stinger connections. Tests showed that they did not move with the same amplitude and phase as the stinger during the application of dynamic loads due to stator flexibility. The effect of relative motion between the top and bottom was confirmed by the reduction of data simultaneously recorded by probes in both locations. Because most of the dynamic load is carried by the statically loaded pad, more accurate impedance coefficients and loaded pad transfer functions should be obtained by mounting the proximity probes adjacent to the stingers. The current tests were conducted with accelerometers and proximity probes mounted in this configuration, as were full bearing tests by Kulhanek [25] and Kulhanek and Childs [26]. This change in probe orientation has a notable effect on measured impedances, quantified by a 10%-15% decrease in stiffness and a reduction in virtual-mass.

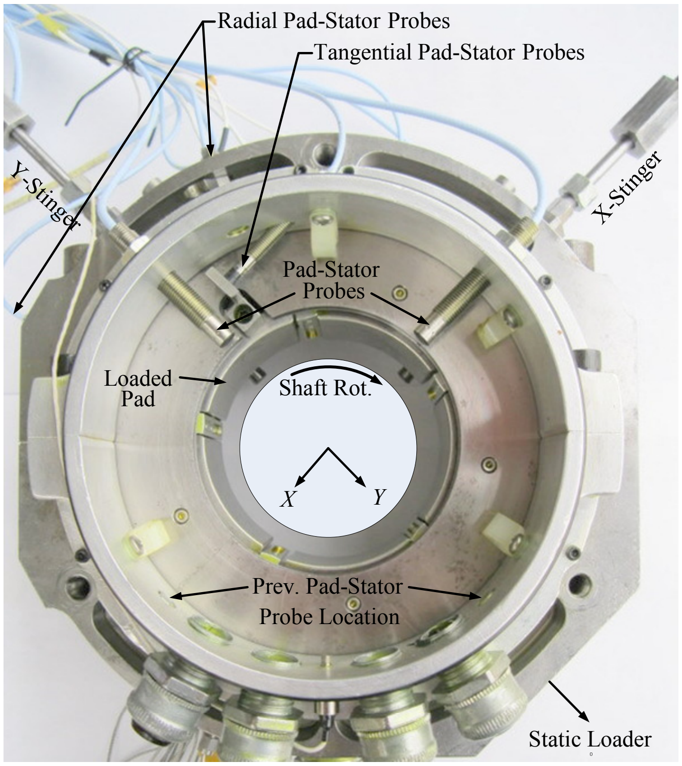

Figure 15: Stator and test bearing viewed from the non-drive end

TEST BEARING

A description of the test bearing configuration is given in Table 1. A rocker pivot similar to the one shown in Figure 4 is used. Pads are retained by a loose fitting pin, which allows the pivot to tilt, slide and bounce.

Table 1: Properties of the bearing at room temp. (24 °C)

Number of Pads	5
Loading Configuration	Load on pad (LOP)
Pad Arc Length (β_{lt})	58.9°
Rotor Diameter	101.587 mm (3.9995 in)
Pad Axial Length	55.88 mm (2.200 in)
Cold Bearing Radial Clearance[1]	68 µm (2.67 mils)
Cold Pad Radial Clearance[1]	120.65 µm (4.75 mils)
Cold Bearing Preload[1]	0.44
Pad Offset	0.50
Pad Mass (m_p)	0.385 kg (0.849 lb)
Pad Inertia about O_c ($I_{c,k}$)	1.807e-4 kg-m^2 (0.851 lb-in^2)
Pad C.G ($b_{\eta go}$,$b_{\xi go}$)	(0,0.0127) m, (0,0.5) in
Bearing Lubricant	DTE 797, ISO VG-32

Note 1: The cold bearing clearance describes the dimensions of the bearing at room temperature, not at operating conditions. Measurements of bearing and pad clearance during operation are discussed in the RESULTS section. Oil inlet temperatures and other static data can be found in Appendix C.

TEST SERIES

Testing was performed at the operating conditions prescribed in Table 2. Data were taken at 10-350 Hz, in 10 Hz increments.

Table 2: Operating conditions

Static Load	Speed [rpm], (Flow-rate [L/min] @ 96 °C)			
kPa (psi)	4400, (32)	7300, (32)	10200, (38)	13100 (38)
0	x	x	x	x
783 (113.6)	x	x	x	x
1567 (227.2)	x	x	x	x
2350 (340.9)	x	x	x	x
3134 (454.5)	x	x	x	x

PAD PROBE INSTRUMENTATION

The degrees of freedom to be measured on the loaded pad, whose pivot sits nominally on the static load line, are shown in Figure 16, and correspond to the coordinates given in Figures 5 and 11. Two additional degrees of freedom shown in Figure 16 are measured during tests, but were not included in the model. Pad yaw ($\phi_{\xi c,k}$) is defined as the rotation from the pad reference axis Z_0 to the perturbed axis $Z_{1,k}$ about the positive ξ_k -axis, and pad pitch ($\phi_{\eta c,k}$) is defined as the rotation from the pad reference axis Z_0 to the perturbed axis $Z_{1,k}$ about the positive η_k - axis.

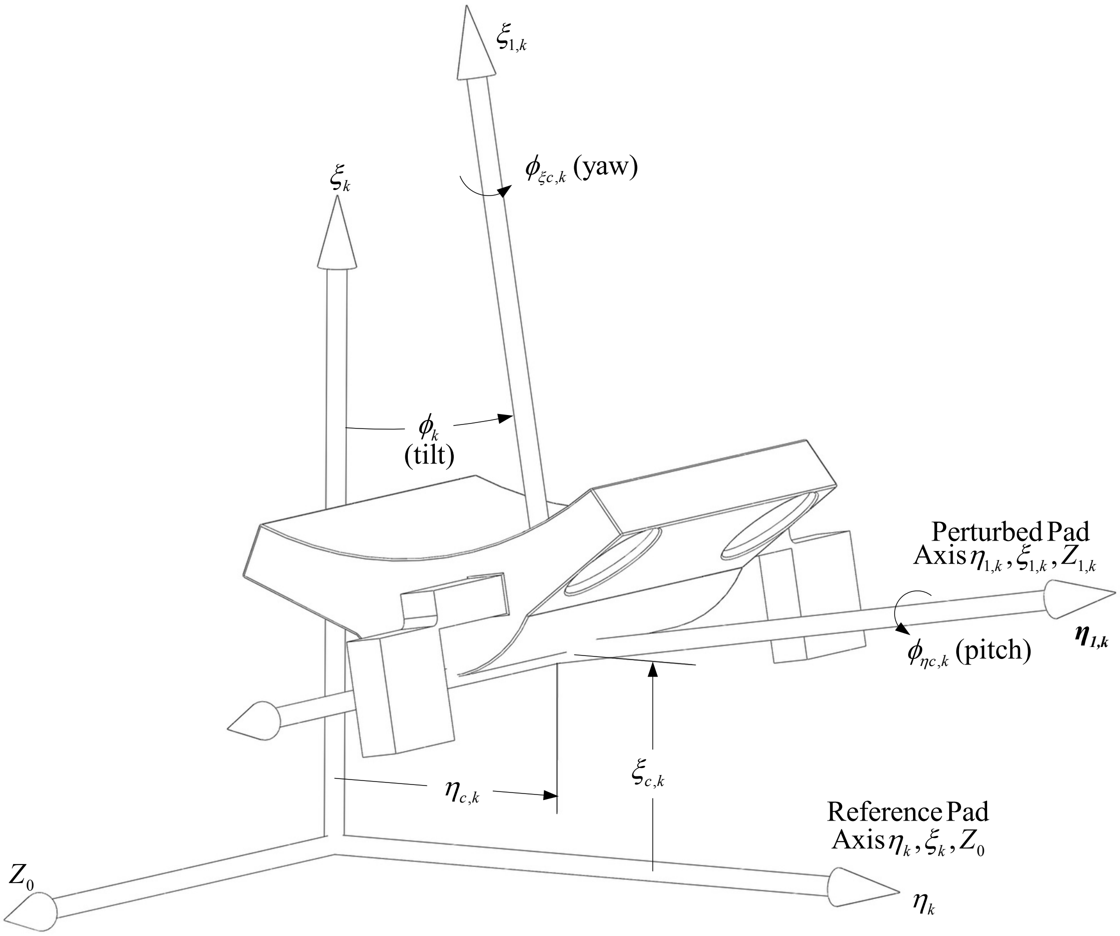

Figure 16: Primary pad degrees of freedom

The orientations of the proximity probes used to measure motion on the loaded pad are illustrated in Figure 17. Each of the five probes (M_{11}-M_{15}) is oriented in the η_k-ξ_k plane shown in Figure 16. Three radial probes (M_{11}-M_{13}) were added in a triangular pattern to observe the tilt, bounce, and pitching motion of the pads, while extensions were added to the sides of the pad to enable two transverse probes (M_{14}, M_{15}) to measure pad slip and yaw motions.

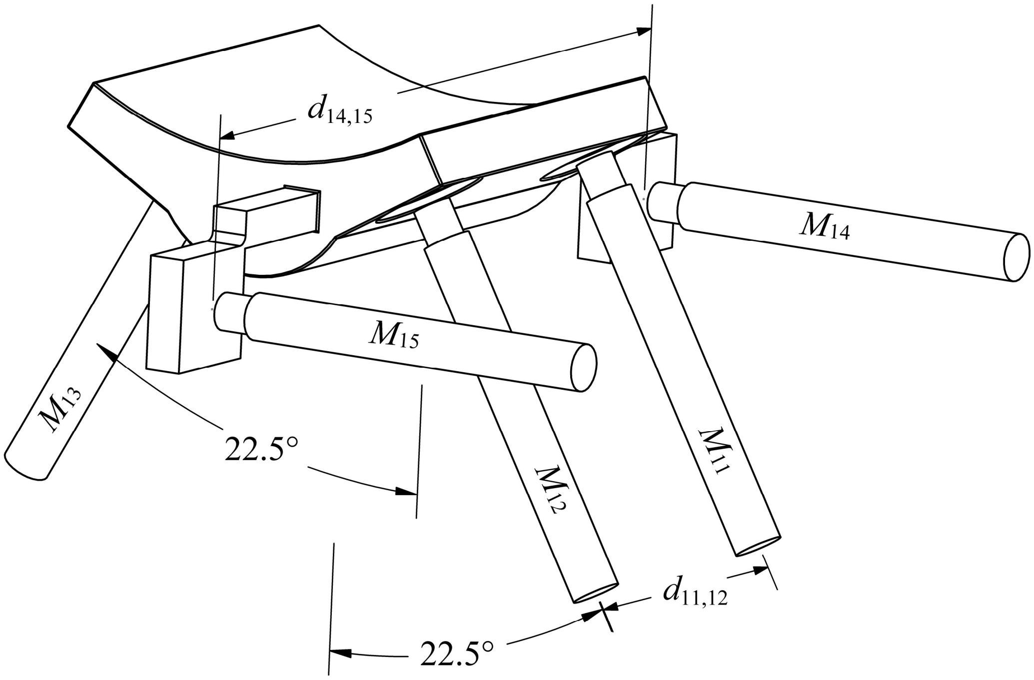

Figure 17: Proximity probe orientation on loaded pad

For the remainder of this work, the subscript k will be omitted when appropriate for variables pertaining to the instrumented pad. The total range of motion seen by the pad probes is 0.46 mm (18 mils); thus, small angle assumptions are applied to the geometric relations relating probe measurements to pad degrees of freedom as follows. The tangential motion of the pad is given by

$$\eta_c = \frac{\left(M_{14} + M_{15}\right)}{2} \tag{79}$$

because the centerline of the proximity probes lies on the contact surface. Their configuration was designed so that pad tilt does not affect probe output. The other motion observed by the tangential probes is pad yaw $\phi_{\xi c}$, defined as a rotation about the positive ξ_k axis according to

$$\phi_{\xi c} = \frac{M_{15} - M_{14}}{d_{14,15}} \tag{80}$$

where the assumption of small motion is justified by the total possible range of motion of the proximity probes. Because the radial pad probes are oriented at an angle of 22.5°

from the ξ_k axis, special care must be taken in deriving equations for pad tilt (ϕ), radial pivot motion (ξ_c), and pitch ($\phi_{\eta c}$). Radial motion (ξ_c) is defined as the average of vertical motion seen on each side of the pad plus the relative deflection due to a change in pad clearance and is

$$\xi_c = \frac{-\left(\frac{M_{11}+M_{12}}{2}+M_{13}\right)}{2}\cos\left(22.5°\right)+\delta_{c_p}\left[1-\cos\left(22.5°\right)\right]. \tag{81}$$

Measurement of pad clearance change (δ_{c_p}) with strain gages will be discussed in detail later, but note that changes in pad clearance must be accounted for when measuring radial pivot motion at a location other than the pivot.

Pad pitch is

$$\phi_{\eta c} = \left[\frac{M_{12}-M_{11}}{d_{11,12}} - \phi_{\xi c}\sin\left(22.5°\right)\right]\cos\left(22.5°\right) \tag{82}$$

where $\phi_{\xi c}$ negates the effect of yaw on the motion seen by M_{11} and M_{12}; hence, pure yaw may produce changes in the measurement M_{12}-M_{11}, but the effect of yaw will be nullified using measured yaw defined in Eq. (80). Lastly, pad tilt is

$$\phi = \frac{\left[M_{13}-\frac{M_{11}+M_{12}}{2}+2\eta_c\sin\left(22.5°\right)\right]}{2r_{11}\sin\left(22.5°\right)}\cos\left(22.5°\right) \tag{83}$$

where $2r_{11}$sin(22.5°) is the distance from probes M_{11} and M_{12} to M_{13} parallel to the η_k axis, and $2\eta_c$sin(22.5°) negates the effect of circumferential pivot motion (η_c) on the relative vertical motion at $M_{11,12}$ and M_{13} similar to the manner in which yaw was negated in the measurement of pad pitch.

PAD STRAIN INSTRUMENTATION

In addition to measuring pad translations and rotations, strain gages were applied to the side of the instrumented pad to measure static and dynamic bending strain as shown in Figure 18.

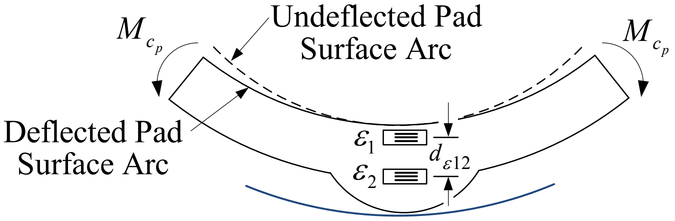

Figure 18: Configuration of strain gages applied to the loaded pad

The distance ($\delta_{\varepsilon 12}$) between the strain gages is approximately 7 mm (0.275 in), and the strain gages will be connected in series using a Wheatstone bridge configuration as shown in Figure 19.

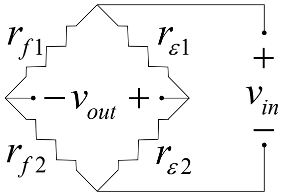

Figure 19: Strain gage monitoring circuit

The voltage output resulting from this measurement configuration is

$$v_{out} = v_{in}\left(\frac{r_{\varepsilon 2}}{r_{\varepsilon 1}+r_{\varepsilon 2}} - \frac{r_{f2}}{r_{f1}+r_{f2}}\right) \tag{84}$$

where r_{f1} and r_{f2} are high precision resistors having very low temperature sensitivity coefficients, and $r_{\varepsilon 1}$ and $r_{\varepsilon 2}$ are the resistances of strain gages 1 and 2, respectively. The benefit of this configuration is that the output voltage from the circuit is proportional to the difference

$$\varepsilon_{12} = \varepsilon_1 - \varepsilon_2 = \left(v_{out} - v_o\right) k_{\varepsilon 12} \tag{85}$$

where $k_{\varepsilon 12}$ relates the change in strain of gages 1 and 2 to a change in resistance, v_o is the output voltage at the reference state, and $\varepsilon_{12} = \varepsilon_{120} + \varepsilon_{121}$ represents the sum of static and perturbed strains as measured relative to the differential strain ε_{12_o} at the reference state. Eq. (85) can then be calibrated to directly calculate the change in pad curvature arising from the differential strain ε_{12} using

$$\delta_{c_p} = k_{c_p \varepsilon_{12}} \varepsilon_{12} \tag{86}$$

where $k_{cp\varepsilon 12}$ will be determined by analyzing the change in pad clearance relative to normal strains at the strain gage locations using finite element analysis (FEA). This process will be explained in the RESULTS section.

DATA ANALYSIS

To measure rotordynamic-coefficients on a floating bearing test rig, we assume that the stator, or bearing, can be modeled as a two degree of freedom system governed by the following EOMs:

$$\begin{Bmatrix} m_{bx} a_{bx} \\ m_{by} a_{by} \end{Bmatrix} = \begin{Bmatrix} f_{ex} \\ f_{ey} \end{Bmatrix} + \begin{Bmatrix} f_{bx} \\ f_{by} \end{Bmatrix}, \tag{87}$$

where a_{bx} and a_{by} are the absolute stator acceleration components, f_{ex} and f_{ey} are the excitation force components, and f_{bx} and f_{by} are the bearing reaction force components in the X and Y directions, respectively. Usage of bearing/stator here physically represents the bearing installed in the bearing housing and all attached peripheral components that move with the bearing housing. The effective masses m_{bx} and m_{by} are modal masses corresponding to X and Y translations of the stator, and their values are chosen such that the curvature of $\mathrm{Re}\{H_{xx}\}$ and $\mathrm{Re}\{H_{yy}\}$ is zero for baseline measurements. Baseline measurements are taken when the bearing is dry (having no oil in the bearing), and represent the dynamic characteristics of all non fluid film reaction forces. Ultimately, the baseline is subtracted from the dynamic bearing impedances to yield only the reaction force components provided by the bearing.

Taking the discrete-fourier transform (DFT) of the components in Eqs. (87) yields

$$\begin{Bmatrix} m_{bx} \tilde{A}_{bx} \\ m_{by} \tilde{A}_{by} \end{Bmatrix} = \begin{Bmatrix} \tilde{F}_{ex} \\ \tilde{F}_{ey} \end{Bmatrix} + \begin{Bmatrix} \tilde{F}_{bx} \\ \tilde{F}_{by} \end{Bmatrix} \tag{88}$$

where $\tilde{A}_{bx}$ and $\tilde{A}_{by}$ are the absolute stator acceleration components, $\tilde{F}_{ex}$ and $\tilde{F}_{ey}$ are the excitation force components, and $\tilde{F}_{bx}$ and $\tilde{F}_{by}$ are the bearing reaction force components.

Rewriting Eq. (88) with the bearing reaction force components given in Eqs. (1) or (2) represented as impedances yields

$$\begin{Bmatrix} \tilde{F}_{ex} - m_{bx}\tilde{A}_{bx} \\ \tilde{F}_{ey} - m_{by}\tilde{A}_{by} \end{Bmatrix} = \begin{bmatrix} \tilde{H}_{xx} & \tilde{H}_{xy} \\ \tilde{H}_{yx} & \tilde{H}_{yy} \end{bmatrix} \begin{Bmatrix} \tilde{U}_x \\ \tilde{U}_y \end{Bmatrix}, \tag{89}$$

where $\tilde{U}_x$ and $\tilde{U}_y$ are relative rotor-stator motions in the *X* and *Y* directions, respectively. To solve Eq. (89) for the bearing impedances ($\tilde{H}_{ij}$), we apply two independent excitations, typically chosen as the orthogonal *X, Y* pair, which provides us with an invertible motion matrix such that the impedances are given by

$$\begin{bmatrix} \tilde{H}_{xx} & \tilde{H}_{xy} \\ \tilde{H}_{yx} & \tilde{H}_{yy} \end{bmatrix} = \begin{bmatrix} \tilde{F}_{ex}^{x} - m_{bx}\tilde{A}_{bx}^{x} & \tilde{F}_{ex}^{y} - m_{bx}\tilde{A}_{bx}^{y} \\ \tilde{F}_{ey}^{x} - m_{by}\tilde{A}_{by}^{x} & \tilde{F}_{ey}^{y} - m_{by}\tilde{A}_{by}^{y} \end{bmatrix} \begin{bmatrix} \tilde{U}_{x}^{x} & \tilde{U}_{x}^{y} \\ \tilde{U}_{y}^{x} & \tilde{U}_{y}^{y} \end{bmatrix}^{-1} \tag{90}$$

If the real portion of $\tilde{H}_{ij}$ is quadratic in Ω and the imaginary portion of $\tilde{H}_{ij}$ is linear, then the bearing in question can accurately be described by a KCM model such that

$$\mathrm{Re}(\tilde{H}_{ij}) = k_{ij} - \Omega^2 m_{ij},\ \mathrm{Im}(\tilde{H}_{ij}) = \Omega c_{ij},\ \ i,j = x,y \tag{91}$$

where c_{ij} and m_{ij} are determined by the slope of a linear regression in Ω and Ω^2, respectively, and k_{ij} is the intercept of the latter.

To evaluate the measured *pad-rotor*/*pad-journal* transfer functions from the recorded pad and relative rotor-stator motions, we use the same technique used to solve Eq. (89), independent tests consisting of orthogonal rotor-stator motions. This yields a slightly expanded version of Eqs. (73) and (74), including the additional pad pitch and yaw motions.

$$\tilde{\mathbf{\Gamma}}_{\mathbf{p,k}} = \left[\begin{array}{cc} \tilde{\Gamma}_{\phi_k}^{\eta_j} & \tilde{\Gamma}_{\phi_k}^{\xi_j} \\ \tilde{\Gamma}_{\eta_{c,k}}^{\eta_j} & \tilde{\Gamma}_{\eta_{c,k}}^{\xi_j} \\ \tilde{\Gamma}_{\xi_{c,k}}^{\eta_j} & \tilde{\Gamma}_{c_{p,k}}^{\xi_j} \\ \tilde{\Gamma}_{c_{p,k}}^{\eta_j} & \tilde{\Gamma}_{\phi_{\xi c1,k}}^{\xi_j} \\ \hline \tilde{\Gamma}_{\phi_{\eta c1,k}}^{\eta_j} & \tilde{\Gamma}_{\phi_{\eta c1,k}}^{\xi_j} \\ \tilde{\Gamma}_{\phi_{\xi c1,k}}^{\eta_j} & \tilde{\Gamma}_{\phi_{\xi c1,k}}^{\xi_j} \end{array}\right] = \left[\begin{array}{cc} \tilde{\phi}_{1,k}^{\eta_j} & \tilde{\phi}_{1,k}^{\xi_j} \\ \tilde{\eta}_{c1,k}^{\eta_j} & \tilde{\eta}_{c1,k}^{\xi_j} \\ \tilde{\xi}_{c1,k}^{\eta_j} & \tilde{\xi}_{c1,k}^{\xi_j} \\ \tilde{c}_{p1,k}^{\eta_j} & \tilde{c}_{p1,k}^{\xi_j} \\ \hline \tilde{\phi}_{\eta_{c1,k}}^{\eta_j} & \tilde{\phi}_{\eta_{c1,k}}^{\xi_j} \\ \tilde{\phi}_{\xi_{c1,k}}^{\eta_j} & \tilde{\phi}_{\xi_{c1,k}}^{\xi_j} \end{array}\right] \mathbf{Q}_{\mathbf{k}} \begin{bmatrix} \tilde{U}_{x}^{x} & \tilde{U}_{x}^{y} \\ \tilde{U}_{y}^{x} & \tilde{U}_{y}^{y} \end{bmatrix}^{-1}, \tag{92}$$

where the partition in Eq. (92) separates the previously defined transfer functions that were included in the model, and the additional pad pitch and yaw transfer functions. Minimal pad pitch and yaw motions were observed during tests, which is to be expected since these motions are not heavily excited during experiments. These transfer functions are not discussed in the RESULTS section.

During dynamic bearing tests a harmonic waveform is sent to the hydraulic shakers, resulting in a harmonic excitation force. When this single frequency excitation force is repeated, the recorded motion can be divided into several sets of independent test data to yield multiple impedance measurements. The repeatability of these impedance measurements can then be assessed by the method given by Kulhanek [25], and displayed as 95% confidence bounds on bearing impedance plots. The same method was used in this work, and 95% confidence bounds are displayed on impedance plots in the RESULTS section.

Note that the confidence bounds for the majority of impedance data presented in this dissertation are extremely small, which suggests that the impedance measurements are highly repeatable. On average the confidence bounds for rotor-pad transfer-function measurements are less than 1% of the measured transfer-function amplitudes; hence, they are not displayed on figures due to a very high degree of repeatability.

CHAPTER IV

NUMERICAL PREDICTION

A finite-difference code was developed to solve for the steady-state and dynamic characteristics of a TPJB using the Reynolds equation. Pad and rotor position are determined using a Newton-Raphson algorithm that employs the analytically perturbed fluid-film stiffness and damping matrices. The code allows for each pad's properties to be defined irrespective of the other pads characteristics. This feature includes, but is not limited to, bearing clearance, pad clearance, pad thickness, pad length, offset, oil viscosity, etc.

The code does not include a thermal model to determine bearing fluid temperatures and viscosities. To reduce thermal uncertainties, pad surface temperature measurements for each test are used to estimate the circumferential fluid temperature profile on a given pad. This temperature profile is then used to calculate fluid viscosities at each node in the finite-difference grid. Similar measurements showing radial variations in pad temperature are used to estimate thermal bow in the pad, affecting a change in preload and pad radius. An option is also available to account for the temperature-dependent change in bearing clearance due to the mean temperature rise within a given pad.

At 10,000 rpm, the circumferential flow Reynolds number ($\frac{\rho\omega r_j c_b}{\mu}$) is 384; hence, laminar flow can be assumed in the numerical model [45].

The code allows for the input of a polynomial load-versus-deflection curve whose derivative describes the static nonlinear stiffness of the pivot. The load-dependent pivot stiffness is used initially to solve for the static equilibrium of the pad, then subsequently in the reduction of dynamic coefficients. A similar procedure was used to describe the nonlinear pad bending stiffness.

CHAPTER V

RESULTS

PLOTTING CONVENTIONS

Unless otherwise stated, the following conventions apply to figures in the RESULTS section of this dissertation.

- Measured data will be denoted by markers/symbols, and will be referred to as "Meas." in legends. These data markers may be connected by straight lines to aid in tracking the curves.
- Predicted data will be represented by solid or dashed lines, and referred to as "Pred." in legends. Unless otherwise stated, this data is predicted using the model discussed in CHAPTER II.

PIVOT STIFFNESS

To predict pivot stiffness, Hertzian contact stresses, deflections, etc. were evaluated numerically using the algorithm given by Deeg [41]. To apply the algorithm, the geometrical and mechanical properties of the pivot and housing must be known. The circumferential and transverse radii of the pivot and housing (about the pad's $Z_{0,k}$ and η_k axes, respectively) were obtained using a coordinate measuring machine (CMM) and are given in Table 3 along with the estimated mechanical properties of the pivot and housing based on typical bearing materials.

Table 3: Parameters used to determine Hertzian contact stiffness

	Pivot	**Housing**
Circumferential Radius[2]	62.13 mm (2.446 in)	-69.85 mm (-2.750 in)
Transverse Radius	1270 mm (50 in)	∞
Elastic Modulus	212 GPa (30.75 Msi)	206 GPa (29.88 Msi)
Poisson's Ratio	0.29	0.288

Note 2: A negative radius implies that the housing contact is concave.

Figure 20 shows a comparison of the measured and predicted load-versus-deflection curves for the pivot in the radial direction. These measurements were obtained by pressing the rotor into the pad along the pad's ξ_k axis with increasing force applied by the static loader.

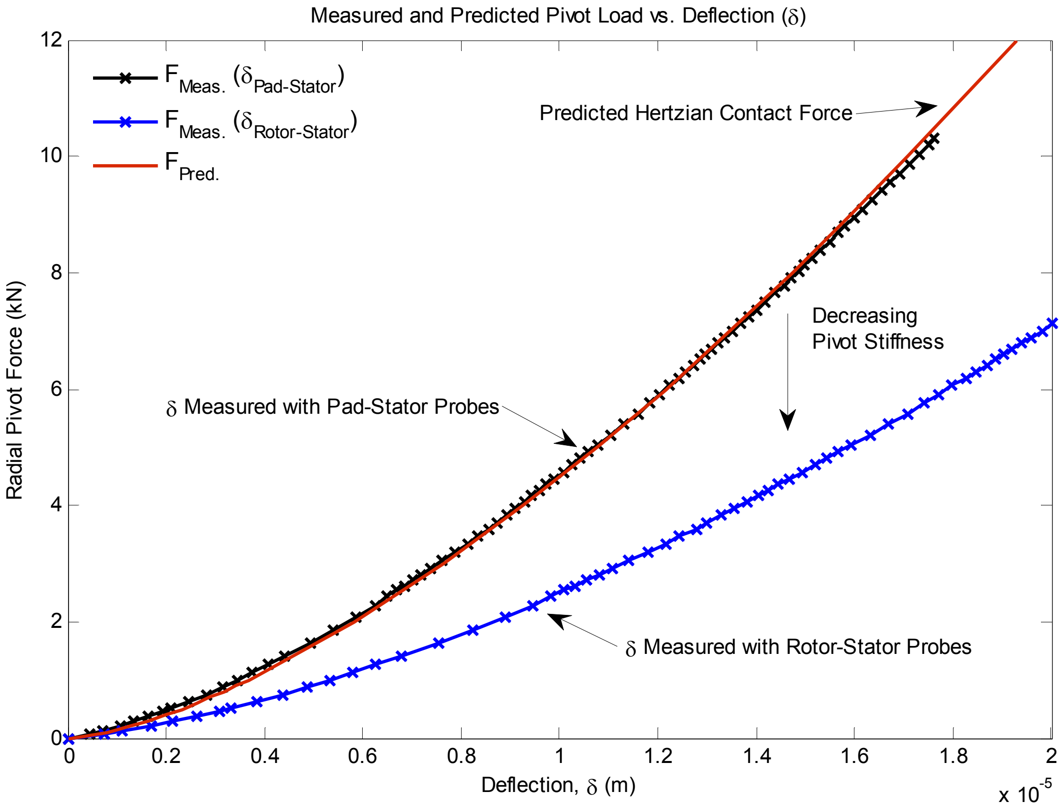

Figure 20: Comparison of measured and predicted pivot load versus deflection

During the experiment, two load-versus-deflection curves were obtained: (1) The black crosses represent the pivot deflection as seen by the pad-stator probes, while (2) the blue crosses represent the pivot deflection as seen by the relative rotor-stator probes (which corresponds to the approach taken by Harris and Childs [23]). The rotor-stator load-versus-deflection curve shows the pivot to be significantly softer than the pad-stator load-versus-deflection curve. This observation is logical because the rotor-stator load-deflection curve includes the compliance of the pivot in series with the compliance of the pad, Babbitt, and rotor as suggested by Harris and Childs. Since only the stiffness of the pad relative to the housing is desired, the stiffer pad-stator load-versus-deflection curve will be used in the bearing predictions. Figure 20 also shows the predicted load-versus-deflection curve using Hertzian contact theory [41], which agrees very well with the stiffer pad-stator load-versus-deflection curve.

Figure 21 shows the measured and predicted pivot stiffness versus pivot deflection. The measured stiffness values were calculated by taking the derivative of a fifth order polynomial fit of the measured load-versus-deflection curves shown in Figure 20. A fifth order polynomial fits the measured load-versus-deflection curves very well, and its derivative should accurately represent pivot stiffness.

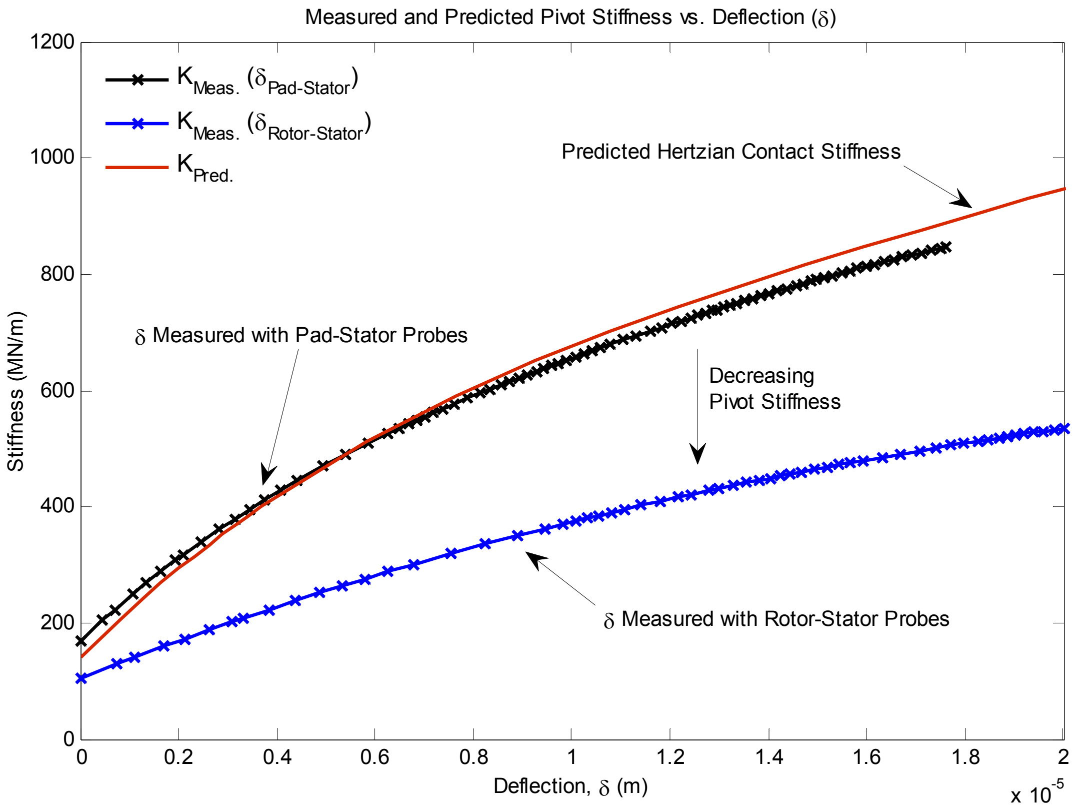

Figure 21: Comparison of measured and predicted pivot stiffness versus deflection

Note that the pivot stiffness measured using the rotor-stator probes is almost half the stiffness obtained by the pad-stator probes. Employing the rotor-stator measured pivot stiffness in numerical predictions would greatly underestimate dynamic coefficients. This raises an interesting question, how should the measured load-versus-deflection curve be implemented in a bearing code? Though other options may exist, the current work approximates the pivot's load-versus-deflection curve with a polynomial. Since a polynomial is continuous and differentiable, the stiffness is easily determined as a function of pivot deflection; however, this approach does require caution in selecting the order of polynomial used to approximate the pivot's load-versus-deflection curve.

Figure 22 shows the stiffness determined from a quadratic approximation of the measured pad-stator load-versus-deflection curve in comparison to the stiffness determined from a higher order approximation.

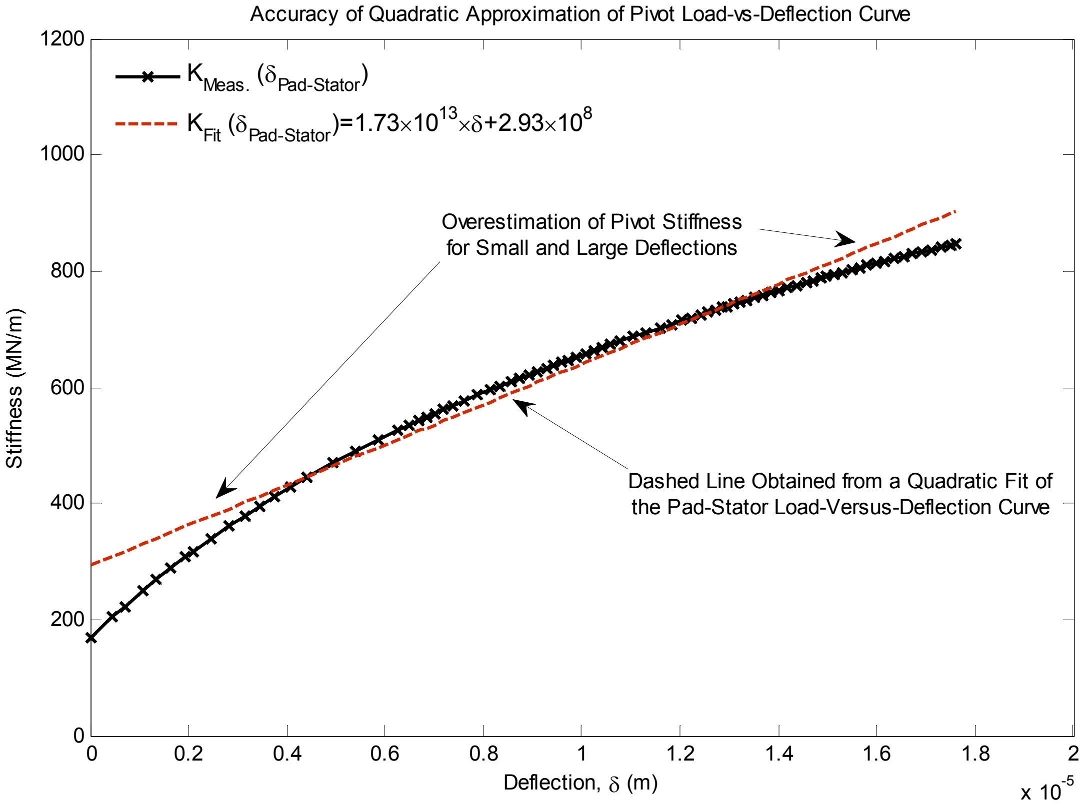

Figure 22: Accuracy of pivot stiffness obtained from a quadratic approximation of pivot load-versus-deflection curve

With the exception of small and large pivot deflections, the quadratic does a decent job of approximating the measured pivot stiffness; hence, one might suggest that better agreement may be obtained using a higher order polynomial. This is true;

however, using a higher order polynomial outside of the range of deflections used to fit the polynomial can lead to erroneous results and difficulty in convergence. Because the maximum loads applied to the pad in these experiments is approximately 17 kN, using a higher order polynomial to approximate the measured load-versus-deflection curve given in Figure 20 is not acceptable. This said, due to the excellent agreement between measured and predicted pivot stiffnesses, a fourth order approximation of the predicted Hertzian pivot stiffness for a larger range of loads will be used to approximate the pivot load-versus-deflection curve employed in numerical predictions. This is given by

$$f_{c\xi} = 7.321\times10^{21}\delta^4 - 6.653\times10^{17}\delta^3 + 3.339\times10^{13}\delta^2 + 1.773\times10^8\delta - 64.44, \qquad (93)$$

where $f_{c\xi}$ is in Newtons, and δ is in meters.

BENDING MOMENTS, BENDING STRAIN, AND PAD CLEARANCE

Though pictures cannot be shown of the pads used in this work for proprietary reasons, Figure 23 is a schematic for a tilting pad having a pivot insert similar to the pads tested in this work. The pivot insert is used to enable adjustment of pad thickness and thus bearing clearance, as well as to reduce pivot wear by using harder materials.

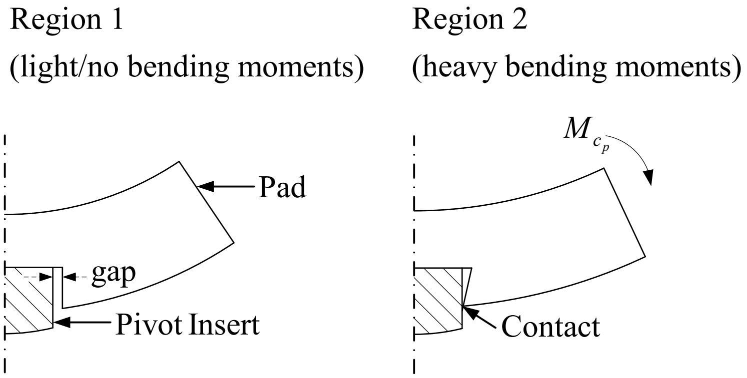

Figure 23: Schematic of a typical tilting pad with pivot insert showing Region 1, where the pivot insert is not in compression, and Region 2, where the bending moment is large enough to result in contact between the back of the pad and the pivot insert

The pad shown in Figure 23 has a gap between the pivot insert and the inside of the slot that it resides in when little or no load is applied. Though this gap is enlarged for clarity, it is on the order of 12 μm (0.5 mils) for the bearing studied; it greatly affects the pad's ability to resist bending moments, and results in a nonlinear bending stiffness for the pad.

To characterize this nonlinear behavior, the deflection of the pad is divided into two distinct regions: Region 1, where the bending moments on the pad are insufficient to eliminate the gap between the pivot and the insert, and Region 2, where the pad deflection is large enough to cause contact between the pad and the pivot as shown in Figure 23. A pad operating in Region 1 will have a much lower bending stiffness than a pad operating in Region 2. The extents of these regions were determined by a simple experiment, whose schematic is shown in Figure 24.

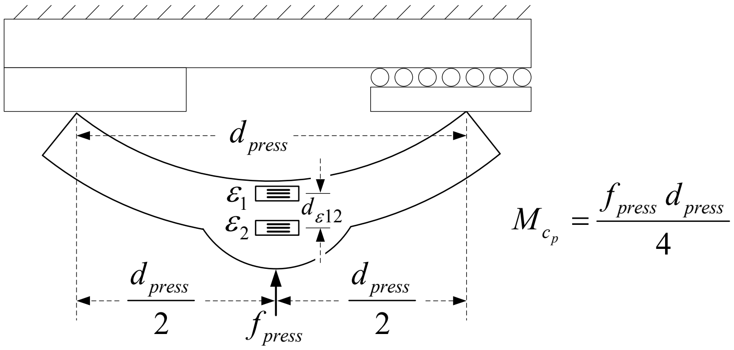

$$M_{c_p} = \frac{f_{press}\, d_{press}}{4}$$

Figure 24: Schematic of strain gage verification experiment

The pad was placed on a flat plate, supported on one end by a pinned support and the other with a rolling support. A press was then used to apply a load to the pivot of the pad, passing though a load cell to measure the force (and thus the applied bending moment), while the pad's strain gages were used to measure bending strains at the middle of the pad. The results from this experiment may also be used to correlate measurements of bending strain to changes in pad clearance by comparison with finite element (FE) predictions. Figure 25 shows the load dependent strain resulting from the experiment, as well as linear trends corresponding to deflections in Regions 1 and 2, and predictions resulting from finite element (FE) analysis in ANSYS.

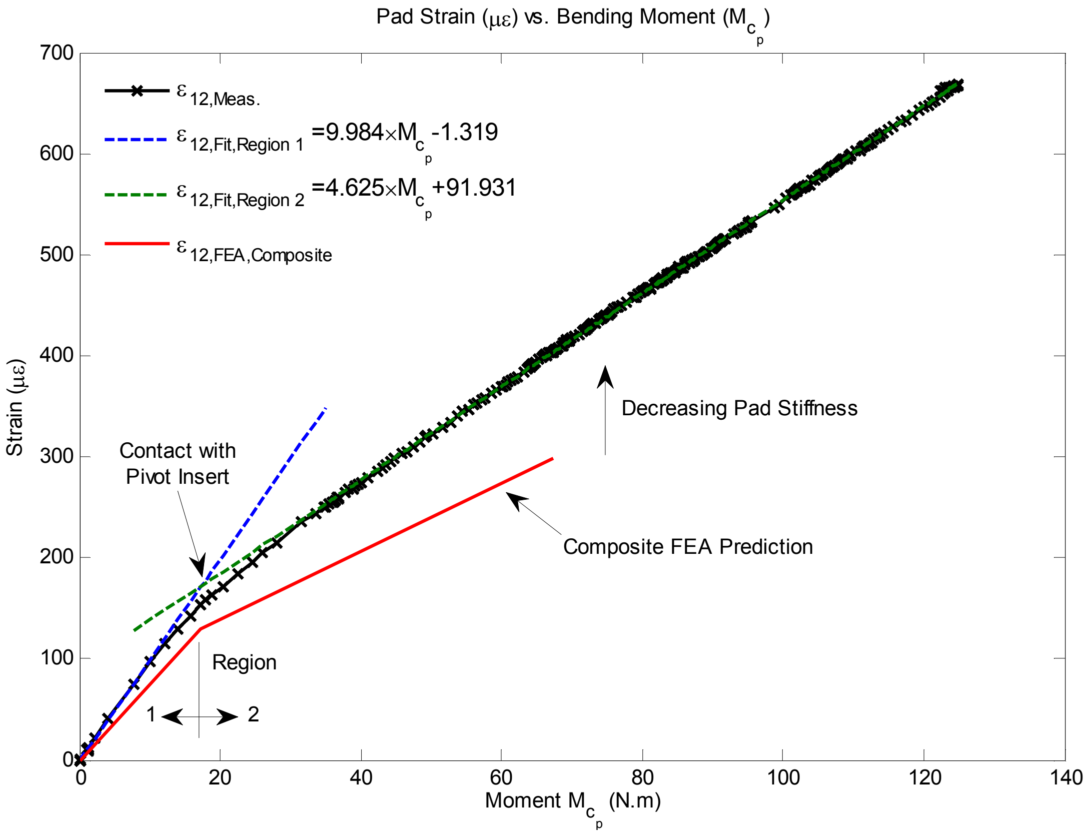

Figure 25: Differential pad strain versus applied moment

Figure 25 shows that there are two distinct linear regions of constant bending stiffness, separated by a transition region. Region 1 consists of a constant bending stiffness, fit by the blue line in Figure 25. As the pad begins to contact the pivot as shown in Figure 23, the pad's bending stiffness is gradually increased by the contact forces. After the pad is fully in contact with the pivot, the contact stiffness becomes constant, and the pad deforms linearly with applied bending moment. The green curve is a fit of the pad's bending stiffness in Region 2. These results suggest that constant bending stiffnesses may be used to model pad flexibility in Regions 1 and 2, provided that the correct stiffness is used for the given bending moment applied to the pad.

The red curve in Figure 25 is a composite of FE results consisting of analysis of a pad model in Regions 1 and 2. Analysis in Region 1 is performed with a model having no contact between the pad and pivot at the back of the pad, and analysis in Region 2 is performed with a model having contact at the location shown in Figure 23.

The top 1.78 mm (0.071 mils) of the pad's surface is Babbitt, which has approximately ¼ the elastic modulus of steel. The interaction of the pad and Babbitt is modeled as a bonded connection, while the interaction between the pad and pivot are modeled using a frictionless connection. Overall, the predicted bending stiffness of the pad is roughly 25% larger than the measurements suggest, but behaves very similarly to the behavior observed in the experiment. This overestimation of bending stiffness may be due to differences in pad/pivot materials, geometric properties such as thermocouple holes, or deficiencies in strain gage mounting and calibration techniques. It is the author's perspective that the last reason is the most plausible; therefore, a conservative approach was taken such that strains measured using Eq. (85) were reduced by 33% before calculating changes in pad clearance.

Having obtained a FE model that agrees reasonably with measured strains during the simple experiment shown in Figure 24, we will apply a uniform pressure (p_{unif}) to the surface of the pad, then determine the effect of measured pad strain and applied bending moments on pad clearance. A uniform pressure distribution will be used to approximate fluid film pressures, and pad clearance will be estimated from numerical results by fitting the surface of the deflected pad to a circle, then subtracting the original radius.

Figure 26 shows the radial deflection of the pad normalized by the applied moment obtained by FEA in Regions 1 and 2 as well as the predicted change in clearance for the point load applied in the experiment, $c_{p,exp}$, and for the uniform pressure $c_{p,p_{unif}}$ that will be used to approximate pad deflections due to moments in numerical predictions.

Though the pad's surface does not remain circular for the loading applied in the experiment, the application of a uniform pressure resulted in a more circular deflection of the pad's surface. Despite approximating that the pad's surface arc remains circular when deflected, Earles et al. [10, 11] conclude that differences in predictions assuming that the pad's surface remains circular and predictions using a more accurate FE formulation are minor; however, the validity of this assumption for the pads in this work could be in question. The pad's bending stiffnesses (k_{sc_p}) for the uniform pressure and experimental point loads in Regions 1 and 2 are given by the applied moment divided by the change in clearance, and the results are displayed in the legend in Figure 26.

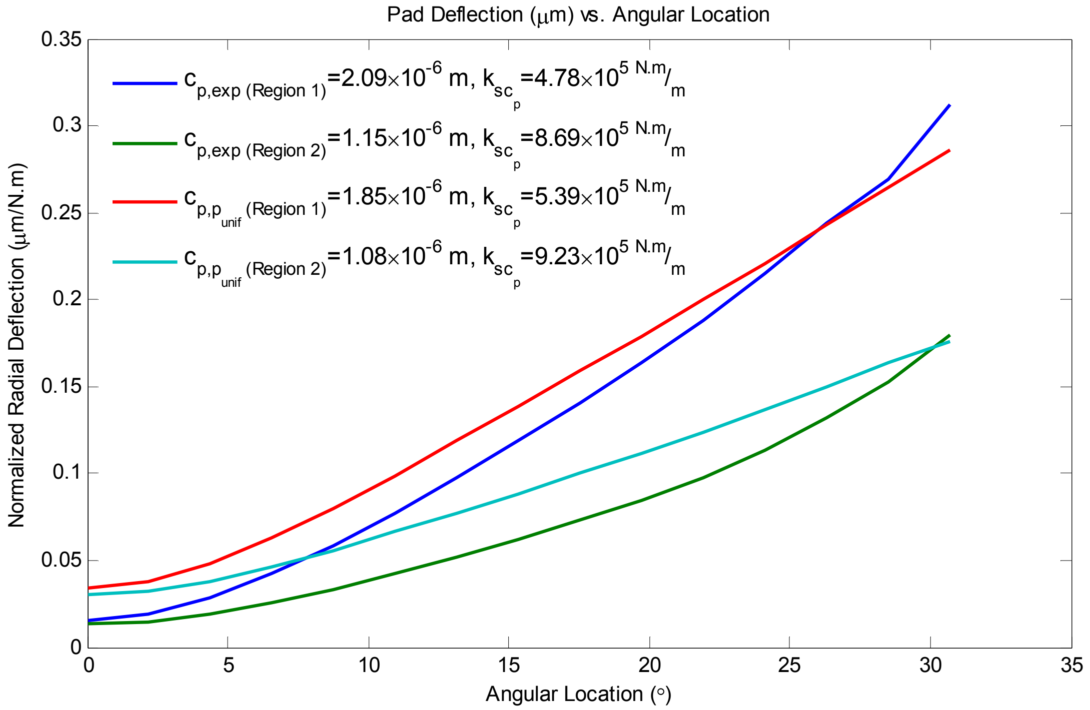

Figure 26: Predicted pad surface deflection normalized by applied bending moment as a function of angular distance from pivot location for structural models in Regions 1 and 2 for the different loading conditions

In comparison to the analytical pad stiffness given by Deutschman et al. [43] in Eq. (27) for a uniform cross section having the full thickness of the pad (including the Babbitt layer), the FE stiffness in Region 2 is 5-6 times softer. This is understandable due to the substantial reduction in bending stiffness associated with the pivot insert contact flexibility and additionally the top 1.78 mm (0.071 mils) of the pad's surface is Babbitt, which has approximately ¼ the elastic modulus of steel.

Table 4 gives the change in pad clearance corresponding to a change in bending strain measured at the strain gage locations in Regions 1 and 2 from FEA of the two load configurations analyzed.

Table 4: Change in clearance relative to a change in bending strain

Loading	$k_{cp\varepsilon 12}$ (μm/με)
Experiment (Region 1)	0.2787
Experiment (Region 2)	0.3397
Uniform Pressure (Region 1)	0.2560
Uniform Pressure (Region 2)	0.2782

The results show that despite the manner that loads are applied to the pad and the region that it is operating in, the relationship between predicted strain and predicted changes in pad clearance is relatively constant. Due to the similarity in pad bending strain factors due to a uniform fluid pressure in Regions 1 and 2, the mean of the two factors in Regions 1 and 2,

$$k_{c_p\varepsilon_{12}} = 0.2671\,\mu m / \mu\varepsilon\,, \tag{94}$$

will be used to convert measured bending strains into changes in pad clearance.

Using the pad bending strain factor given in Eq. (94), we may determine another bending stiffness for the pad to use in dynamic bearing predictions by correlating the change in predicted bending moment on the pad due to test excitations at low frequencies to measured changes in pad clearance recorded during those same test excitations. This may be necessary to account for changes in the pad/pivot fit that may occur with the thermal gradients present at the time of a test, and/or the addition of thermal moments in conjunction with pressure induced bending moments.

Figure 27 shows the pad bending stiffness obtained by applying Eq. (29) to determine measured changes in pad clearance during dynamic test excitations and dynamic bending moments predicted from simulations of the test cases at various static operating conditions.

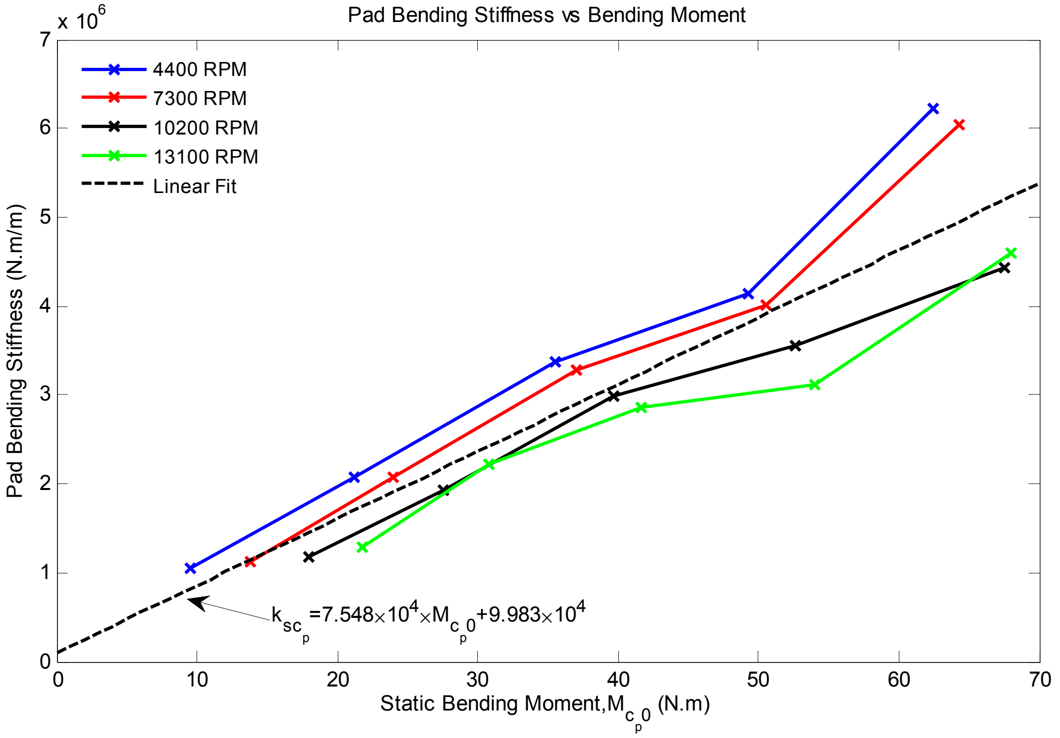

Figure 27: Pad Bending stiffness at various operating conditions as determined from measured changes in pad strain and predicted bending moments

Figure 27 shows that the pad's bending stiffness calculated using this method is primarily a function of the static bending moment applied to the pad, which increases with increasing static load. These stiffness values are significantly higher for large static bending moments than predicted by FEA and the simple pad experiment, suggesting that it may be necessary to account for thermal gradients/thermal bending moments present during dynamic tests. In fact, using the pad bending stiffness obtained with FEA led to very poor prediction of bearing characteristics (largely underpredicted). Thus the following bending stiffness (N.m/m) will be used in predictions

$$k_{sc_p} = 7.548\times10^4 \times M_{c_p 0} + 9.983\times10^4 , \tag{95}$$

where $M_{c_p 0}$ is the static bending moment (N.m) applied to the pad by the fluid film.

Though this value was larger than obtained during the static experiment, FEA predictions show the bending stiffness of a solid pad having the same shape as the pads in the test bearing to be several times stiffer than the formulation given in Eq. (95).

BEARING CLEARANCE

Figure 28 shows pentagonal bearing clearance measurements at taken by slowly precessing the stator around the non-rotating shaft with a circular force. These measurements consist of cold bearing clearances, taken at room temperature, as well as a few hot bearing clearances, taken at a few of the operating conditions given in Table 2.

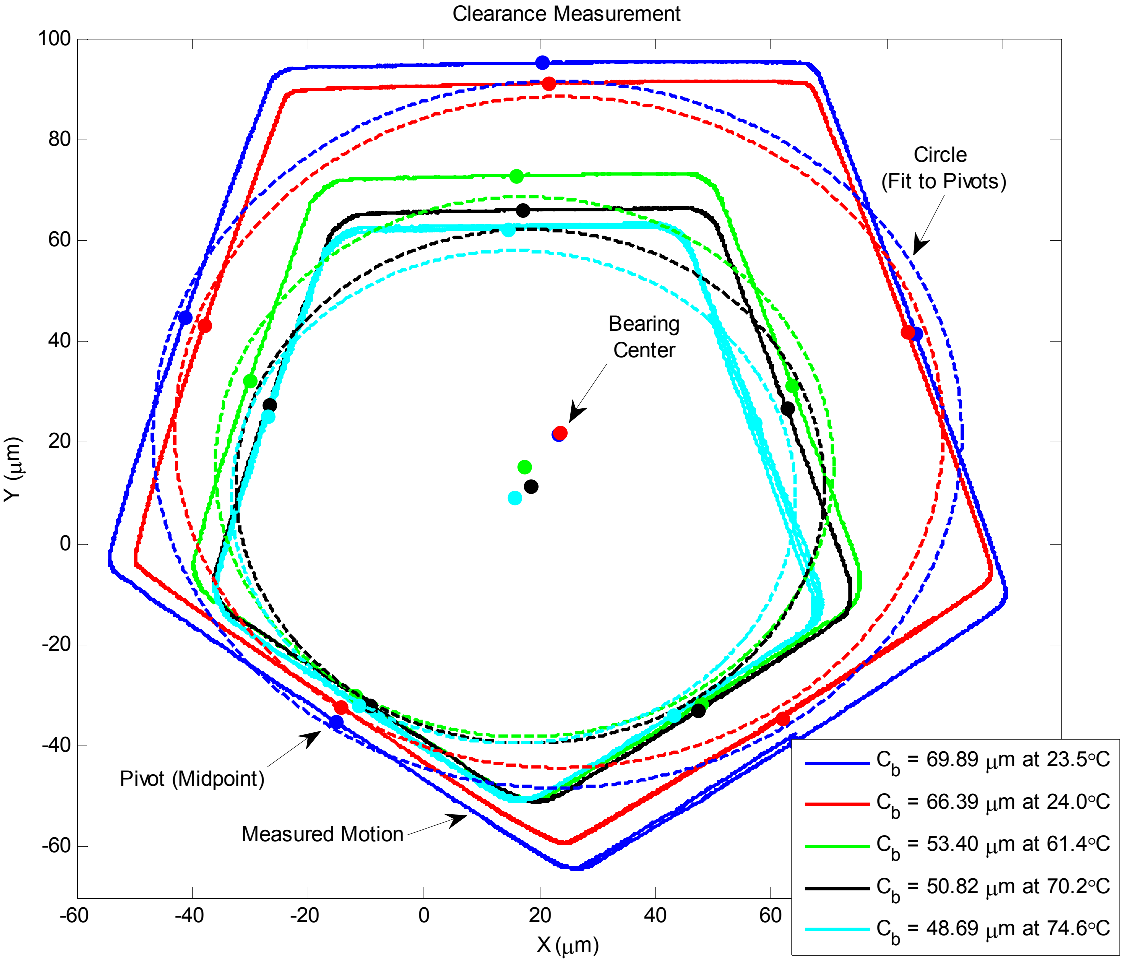

Figure 28: Pentagonal clearance measurement at a variety of temperatures (as determined by the mean of pad surface temperatures at the pivot location)

These clearance measurements are recorded while slowly precessing the stator about a non-rotating shaft using a circular force that is just large enough to initiate contact between the pads and rotor (to prevent significant pivot deflections). For a

TPJB, this generates a polygon, having n_p sides corresponding to the number of pads in the bearing.

Cold bearing clearances are taken when the test rig has not been operated for several hours, and the temperature given is the average of each pad's surface temperatures taken during the clearance measurement. The cold clearance measurements should accurately reflect the installed clearances provided by the manufacturer, where negligible thermal gradients are present in the system. The location of the pad surface thermocouples is given in Appendix C.

Hot bearing clearances are taken immediately (~15 sec) after shutting down the test rig after operating at steady state conditions for a given speed and load. For hot-clearance measurements, the temperature given consists of the average of pad surface temperatures at the pivot location, as determined by a spline fit of the temperatures along the surface, recorded at the steady state operating condition immediately prior to shutdown. The difference between using actual operating temperatures versus temperatures recorded during the clearance measurement only seconds later is probably slight, but the author feels that this procedure will yield a more useful approach to researchers who desire to adjust bearing clearance with pad surface temperatures measured during operation.

The bearing has five pads, corresponding to the number of sides in the clearance measurement. The top side represents the loaded pad, and shaft rotation is clockwise. At the center/midpoint of each side, a colored dot represents the pivot location for that pad. Fitting these points to a circle provides a good means of determining the average bearing clearance, which is indicated by the dashed line.

At room temperature the clearance is fit well by a circle, indicating that the installed bearing clearance for each pad is very consistent. The loaded pad, however, has a slightly larger (7 μm (0.28 mil)) bearing clearance, which probably resulted from permanent compression of the Babbitt surface during pivot-stiffness measurements. As the bearing gets hotter, the rotor, pads, and bearing expand. Assuming the bearing bore remains constant, a hotter pad will expand more, resulting in a decreased clearance;

therefore, the length of that pad's side of the clearance pentagon measurement will increase with respect to its peers. If the bearing bore expands more on the hotter side, however, it would tend to increase that pad's clearance and decrease the length of that pads side of the pentagonal clearance measurement.

In addition to these relative changes in clearances among the pads, there is significant reduction in the average bearing clearance. Figure 29 shows the measured bearing clearance versus the average of pad surface temperatures at the pivot location.

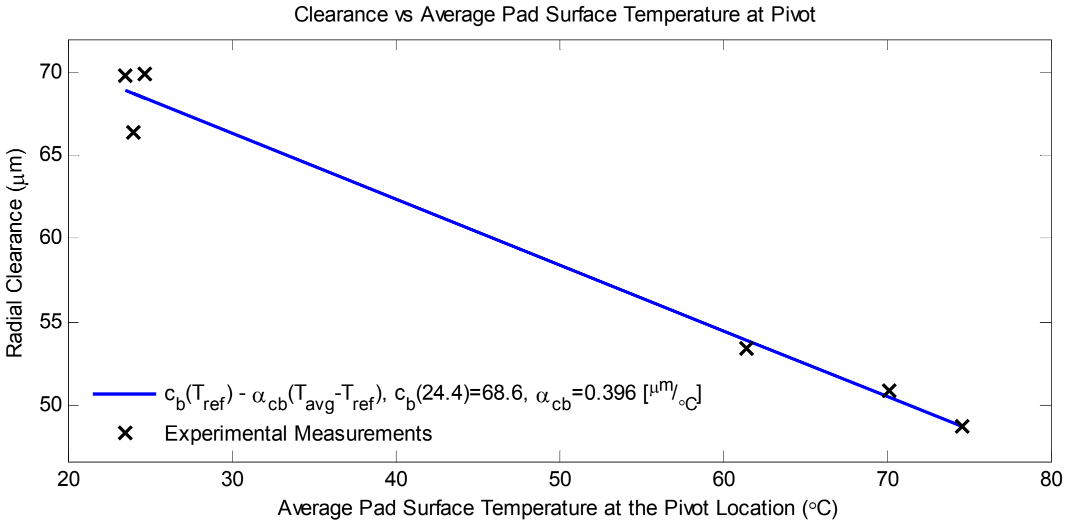

Figure 29: Bearing clearance as a function of the average of pad surface temperatures at the pivot location

Figure 29 shows that the bearing clearance decreases linearly in proportion to the average of pad surface temperatures at the pivot location, abiding by the relation

$$c_b = c_{b,ref} - \alpha_{c_b}\left(T_{avg} - T_{ref}\right) \tag{96}$$

where $c_{b,ref}$ is the reference bearing clearance at temperature T_{ref}, and α_{cb}, the slope of the fit in Figure 29, is similar to a thermal expansion coefficient. To place some perspective on α_{cb}, we will define the relation

$$l_{T,char} = \frac{\alpha_{c_b}}{\alpha_{mat}} = \frac{0.396\ ^{\mu m}/_{\circ C}}{11.4\ ^{\mu}/_{\circ C}} = 34.7\,\text{mm}\left(1.37\,\text{in}\right), \tag{97}$$

where $l_{T,char}$ is a characteristic thermal length of the system with respect to the mean of pad surface temperatures at the pivot locations.

This relation is useful because it provides a means of assessing the length of material expanding in the test rig (relative to an increase in pad surface temperature at the pivot). In their research, Branagan and Barrett [42] account for reductions in bearing clearance by calculating the thermal expansion of the pad using the difference between the pad at room temperature and at operating conditions (using the mean of pad temperatures at the surface and back of the pad), the pad's thermal expansion coefficient, and the thickness of the pad at the pivot. For the bearing investigated, employing this method results in a clearance reduction coefficient of

$$\alpha_{c_b} = 0.17 \, {}^{\mu m}/{}_{\circ C}, \tag{98}$$

which accounts for only ½ the change in clearance noted in the current work.

While it should be noted that the present temperature dependent bearing clearance was measured on a floating bearing test rig that may have larger thermal gradients than in commercial turbomachinery, it does indicate that previous comparisons between measured and predicted bearing coefficients on floating bearing tests rigs should be treated with caution if a temperature dependent bearing clearance was not included in the prediction model. It would be interesting to compare the characteristic thermal length for this bearing to other bearings tested on the TAMU oil-bearing test rig to see if this length is dominated by the test rig, the bearing, or a combination of the two.

Finally, note that the clearance measurements shown in Figure 28 seem to shift down and to the left with increasing temperature. This effect probably occurs because the proximity probes taking these measurements are expanding more than the housing that they are mounted on. Figure 15 shows the proximity probes extending approximately 38.1 mm (1.5 in) toward the shaft from their mounting location, which is fastened rigidly to the steel bearing housing at a radius of 17.7 cm (7 in). A simple calculation shows that a 20° temperature difference between the inboard portion of the proximity probes and the housing results in a 12 μm (0.45 mil) reduction in the gap between the probe and rotor. This temperature difference seems possible because the proximity probes may be directly hit by hot oil exiting the bearing, while the housing is cooled by both inlet oil and the ambient air. Since the shift in measured rotor positions are approximately 10-15 μm (0.39-.59 mil), as will be shown later, this explanation seems feasible.

This observation could be important because presenting static eccentricity measurements without accounting for probe expansion may result in errors in both eccentricity magnitude and attitude angle. The author believes this is the primary reason for the number of eccentricity measurements presented in literature with slight, but significant, attitude angles [22,23].

The effect of probe expansion could be accounted for taking clearance measurements at each operating condition, such that rotor eccentricities are measured relative to the center of a specific clearance measurement. This procedure, however, would be quite time consuming since a 10-15 minute period is required to reach steady state after a shutdown. Another option would be to use 8 proximity probes, mounted in pairs across the shaft. If the probes on both sides of the shaft expanded equally, they would offset one another, resulting in an accurate measurement of journal position. Difficulties with this approach may include differences in proximity probe temperatures on either side of the shaft, and relative motion of the proximity probes due to housing flexibility.

This is not the first attempt to measure operating bearing clearances. Wygant et al. [40] used in-rotor motion probes to measure fluid film heights while the shaft was rotating. This approach could yield valuable information on pad clearance and changes in bearing clearance due to centrifugal shaft expansion, but mechanical and electrical runout on the surface of the pads reduced the clarity of their clearance measurements, and did not allow for discussions on the variation of measured clearances with speed and temperature. It should also be noted that radial pad displacement due to pad compliance would also have to be accounted for when using this procedure.

STATIC DATA

Figures 30-34 show measured static results generated by slowly increasing the unit load applied to the bearing from 0-3132 kPa (454 psi) while keeping a constant rotor speed. Unit load is defined as the static load per cross-sectional area of the bearing. Due to the density of data points recorded in these tests, static measurements presented here are represented as solid curves. Additional static data such as thermocouple temperatures and locations, pressures, and oil flowrates can be found in Appendix C.

Figure 30 shows the locus of the bearing relative to a measured hot and cold bearing clearance with increasing load for a variety of rotor speeds. Note that these clearance measurements are the boundaries of the bearing when the pads have not deflected radially in response to fluid film loads.

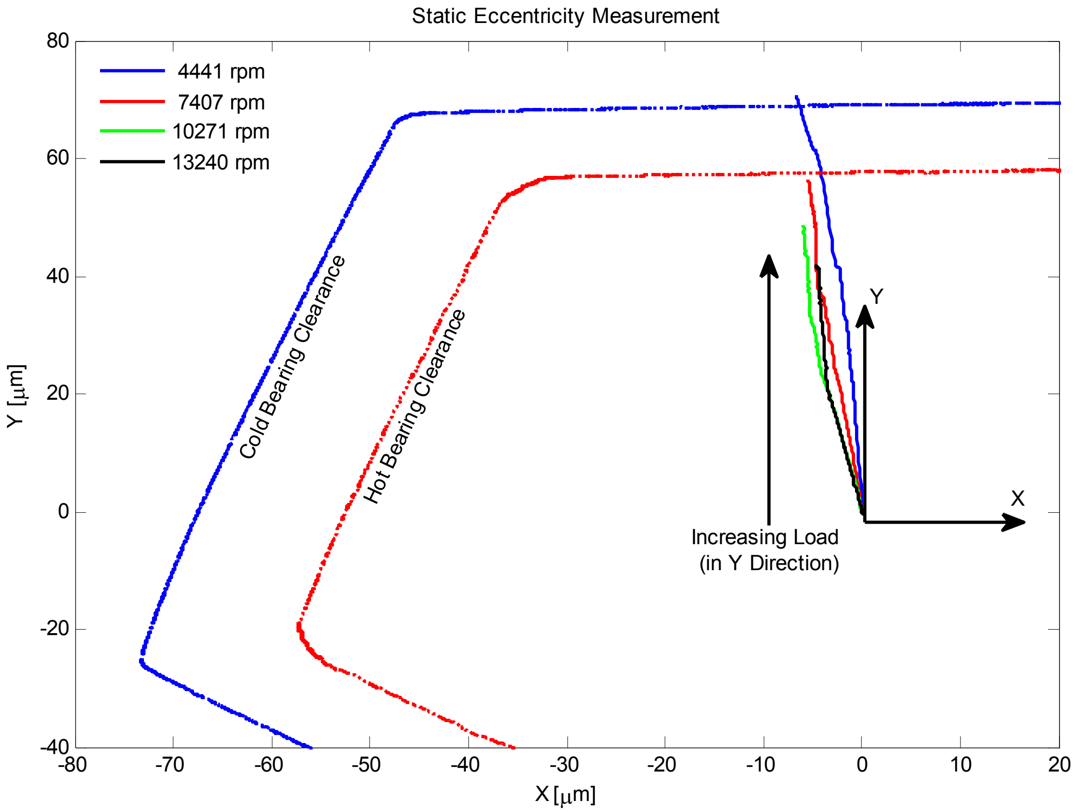

Figure 30: Measured static eccentricity at various speeds with unit loads in the Y-direction from 0-3132 kPa

Figure 30 shows that the difference in static eccentricity ratio, the static eccentricity divided by the bearing clearance, using the hot and cold bearing clearances is considerable. Comparing measured static eccentricities to predictions based on the cold bearing clearance is highly misleading and wrong. Comparing predicted and measured static eccentricity ratios using the cold-bearing clearance might agree well for a model with rigid pivots, while comparisons to the hot-bearing clearance reveals that the journal actually exceeds the hot-bearing clearance by 11-12 μm for heavily loaded operation at low speeds. This fact alone supports the notion that predicting static characteristics for this bearing requires a model containing pivot flexibility. As indicated earlier in discussing the measured hot-bearing clearances, the slight change in attitude angle with increasing load could be attributed probe expansion, and does not necessarily indicate the presence of cross-coupled stiffness coefficients.

Figure 31 shows a comparison between the measured and predicted eccentricities versus static load for a range of rotor speeds. While the relation between static eccentricity and load is predicted very well at the lowest speed, Figure 31 suggests that the model has slightly less load capacity than the bearing tested at higher speeds. Although there are a variety of input parameters that could affect this comparison, the author feels that adjusting inputs to more accurately reflect measured quantities is counterproductive when trying to assess the accuracy of the applied model.

Unless stated otherwise, note that predictions from this point forward are generated with the model given in CHAPTER II using the pivot load-versus-deflection curve given in Eq. (93), the load dependent pad bending stiffness given in Eq. (95), and the temperature dependent bearing clearance given in Eq. (96).

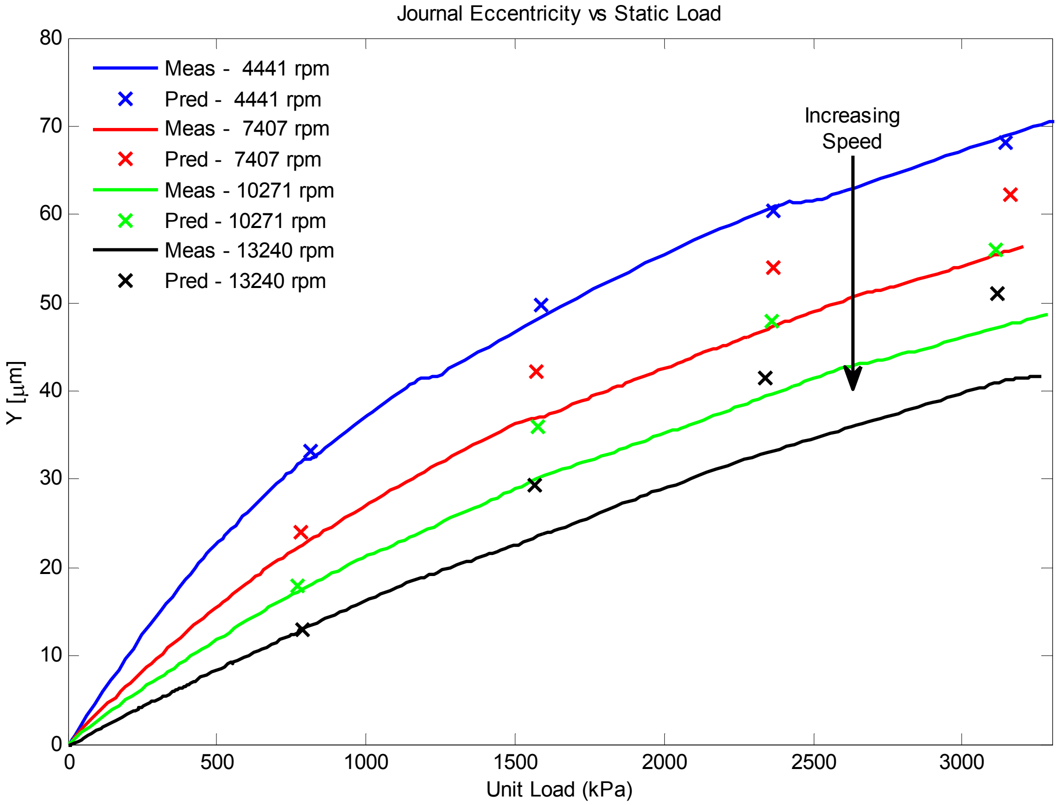

Figure 31: Measured and predicted journal eccentricity (along loaded Y axis) versus unit load at various operating speeds

Figure 32 shows the radial displacement of the loaded pad versus applied static load at different operating speeds. A radial displacement of ξ_c=0 denotes that the pivot is uncompressed, sitting on the surface of the bearing. The radial displacement of the loaded pad indicates how much radial load is supported by the loaded pad. As expected, the pad's positive preload results in an increase in centering force with increasing rotation speed for lightly loaded operating conditions. As the static load increases, however, the pads adjacent to the loaded pad support less load at lower speeds, requiring the loaded pad to bear a larger portion of the static load than observed at higher speeds.

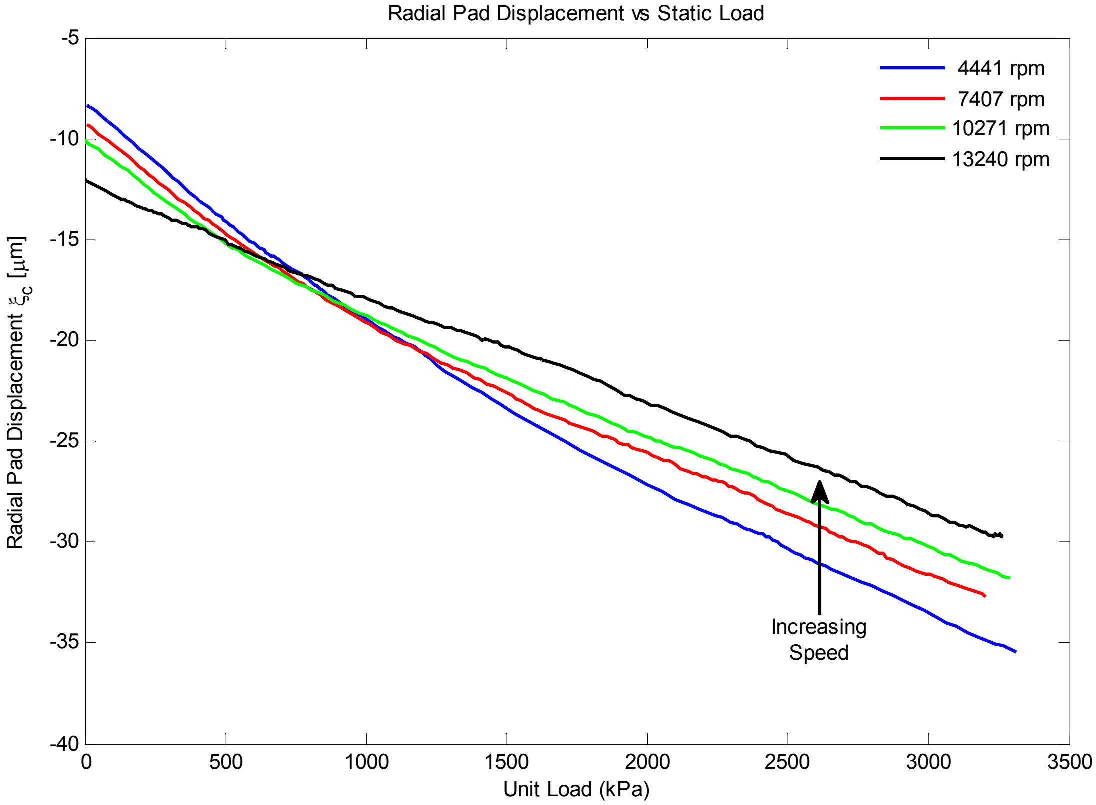

Figure 32: Measured radial displacement of the loaded pad versus applied unit load

In light of the 36 μm radial displacement of the loaded pad, the eccentricities extending 12 μm outside of the hot bearing clearance as reported in Figures 30 and 31 seem feasible. This statement may prompt the following question: How well is static eccentricity in the loaded direction predicted with a model having rigid pads and pivots that accounts for the reduction in hot bearing clearance at elevated temperatures?

Figure 33 shows that static eccentricities predicted using hot bearing clearances with rigid pads and pivots is approximately 33% lower than measured static eccentricities at large loads. Compare this error to the 17% error in static eccentricity predicted using cold bearing clearances and rigid pads and pivots shown by Hensley [34], and it should be apparent that previous comparisons between measurements and predictions not accounting for the change in bearing clearance at operating conditions need to be taken with caution.

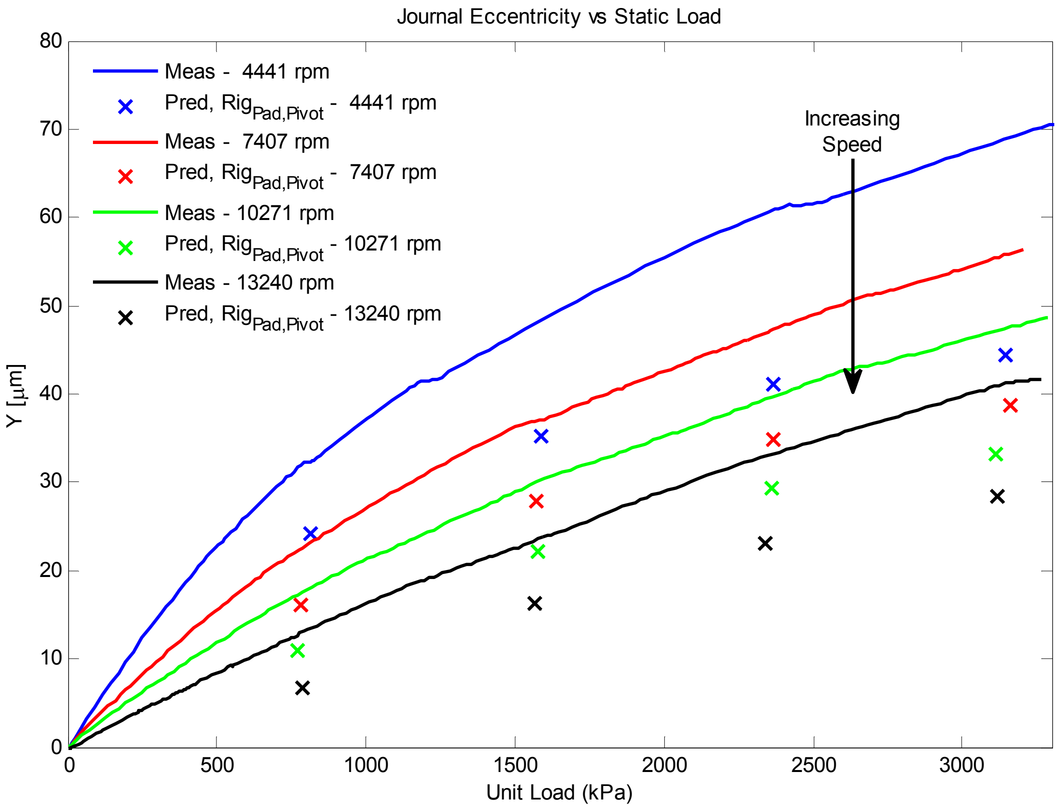

Figure 33: Measured and predicted journal eccentricity (along loaded Y axis) versus unit load at various rotor speeds using a model with rigid pads and pivots

Figure 34 shows measured pad clearance versus unit load at the different operating speeds. Measured pad clearance is the sum of the reference state pad clearance shown in Table 1 and measured changes in pad clearance given by Eq. (86), differential strain in Eq. (85) reduced by 33%, and $k_{c_p\varepsilon_{12}}$ in Eq. (94).

This figure is interesting for a number of reasons. For the bearing tested, the measured pad clearance can be as much as 160% of the installed pad clearance. This increase in pad clearance has a tendency to decrease the frequency dependence of predicted dynamic coefficients as stated by Parsell et al. [5], which may provide some resolution on the disparity between the measured and predicted frequency dependency of TPJB dynamic coefficients. These results include both structural and thermal changes in pad preload; however, predictions using the nonlinear bending stiffness given in Eq. (95)

suggest that the majority of the increase in pad clearance can be attributed to structural deflections for the bearing tested.

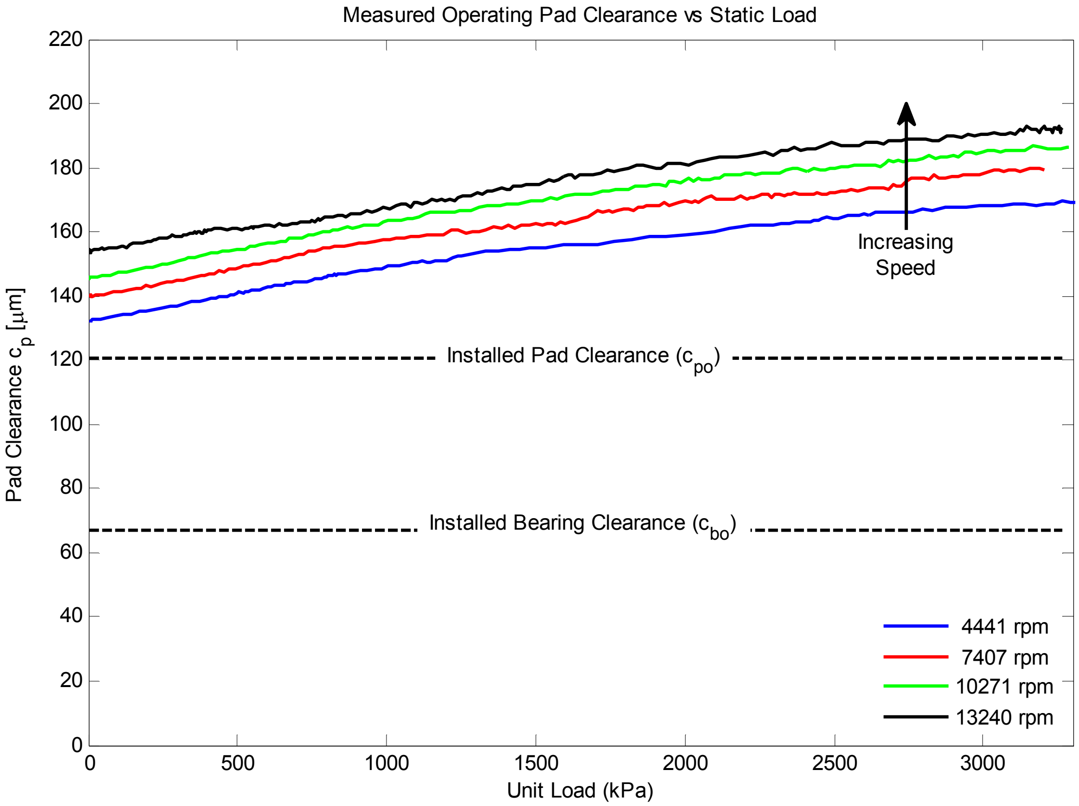

Figure 34: Measured loaded-pad clearance versus unit load at various rotor speeds

Figure 35 shows the static tilt angle ϕ of the loaded pad versus load at different operating speeds. This figure shows that the tilt angle of the loaded pad increases with increasing operating speed, and tends to decrease with increasing static load. There are exceptions in the low load and speed range, where the tilt appears to increase with static load. It is possible that this occurs with differential heating of the pads proximity probes during static load cases.

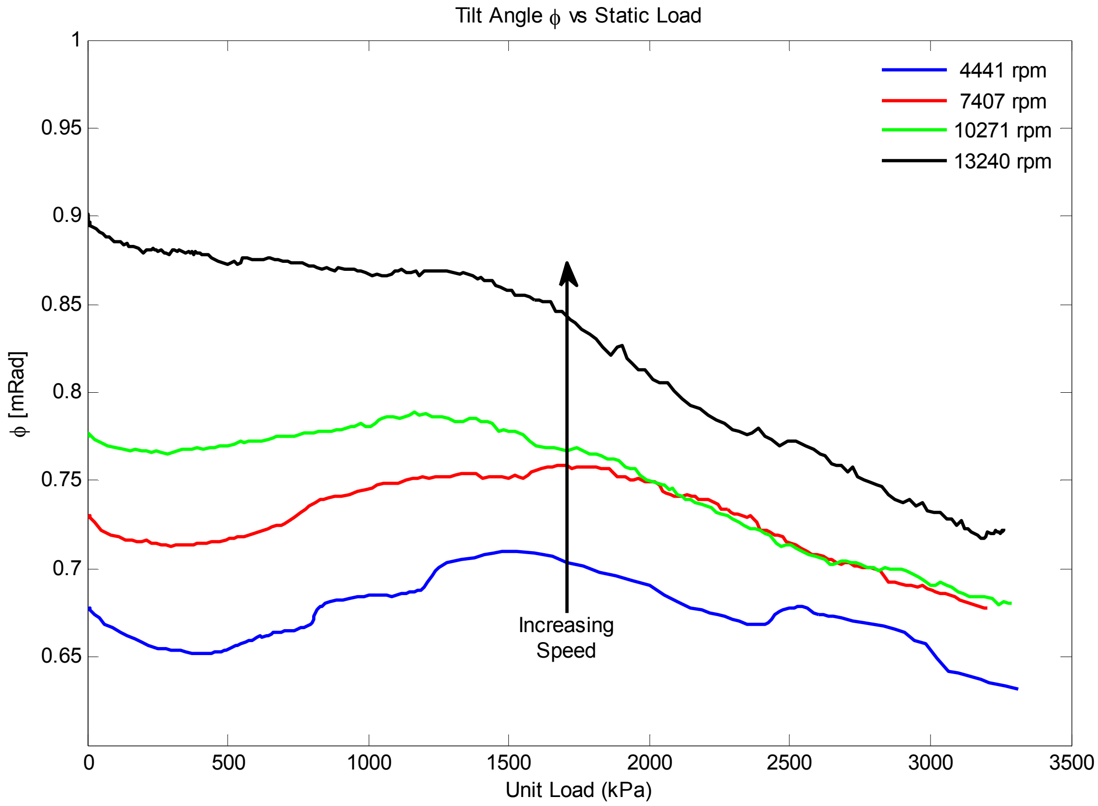

Figure 35: Measured loaded pad tilt angle versus unit load at various rotor speeds

To generate Figure 35, measured values of ϕ (defined by Eq. (83)) were compensated with an offset such that $\phi=0$ when the pad is located in the reference state shown in Figure 4. This occurs when the line $O_{po,k}$-$O_{co,k}$, connecting the center of the k^{th} pad's surface arc to the k^{th} pad's contact location passes through the center of the bearing. Though the offset needed to compensate measured values of ϕ (to satisfy $\phi=0$ at the reference state) may change slightly during tests due to changes in thermal equilibrium in the bearing, the following method should suffice in determining a reasonable offset.

During the clearance measurements shown in Figure 28, each pad tilts as the rotor traverses its side. Since pad motions are recorded during clearance measurements, tilt of the loaded pad versus transverse rotor motion can be obtained while the rotor traverses the top side of the clearance pentagon as shown in Figure 36.

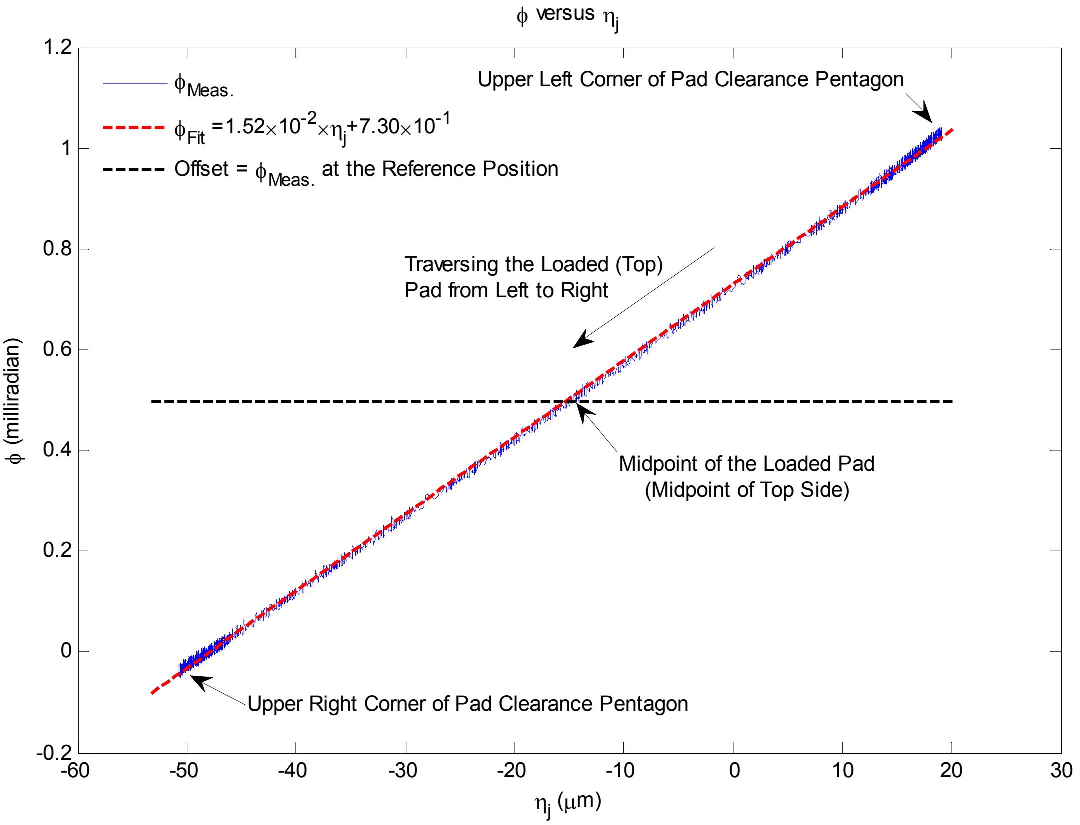

Figure 36: Pad tilt angle ϕ measured while traversing the loaded pad (top side of the clearance pentagon) during a clearance measurement

Figure 36 shows that the relationship between pad tilt and transverse rotor motion is linear while the rotor traverses the loaded pad, which suggests that the relative displacement between $O_{p,k}$ and O_j is constant. Since this relative displacement is constant, the extent that a pad tilts while the rotor transverses its side of the pentagon during a clearance measurement can be used to determine the pad tilt angle when the rotor is located transversely at the pad's pivot location (midpoints of each side are illustrated with dots in Figure 28). Thus, the loaded pad's tilt angle at the midpoint of the top segment of the clearance pentagon should correspond to the offset needed to compensate pad tilt measurements to represent angles relative to the reference state.

The linear relation between pad tilt and transverse rotor motion also yields an approximate means to verify Eq. (83) and the accuracy of the loaded pad's motion probes. Since the relative displacement between $O_{p,k}$ and O_j is constant, the ratio of pad tilt angle to transverse rotor motion should correspond to $1/r_{cp,k} = 14.4$ in rad/m, where $r_{cp,k}$ is the distance from the pivot point O_c to the center of the pad's surface arc O_p shown in Figure 2. This is in fact very close to 15.2 rad/m, the measured slope of the tilt angle versus transverse rotor motion curve shown in Figure 36. If this comparison is accurate, it would amount to a relative error of $\approx 6\%$ in the measured tilt angles.

Another important measure of bearing performance is power loss. Figure 37 shows measured hydraulic power loss versus speed and unit load. Hydraulic power loss is calculated using

$$P_{loss} = \dot{m}_{oil} c_{p,oil} \Delta T_{oil}, \tag{99}$$

where $\dot{m}_{oil}$, $c_{p,oil}$, and ΔT_{oil} are the mass flowrate, specific heat, and temperature change of the oil from the inlet to the outlet of the bearing, respectively. Figure 37 shows that power loss is primarily a function of rotor speed, but increases moderately with static bearing load.

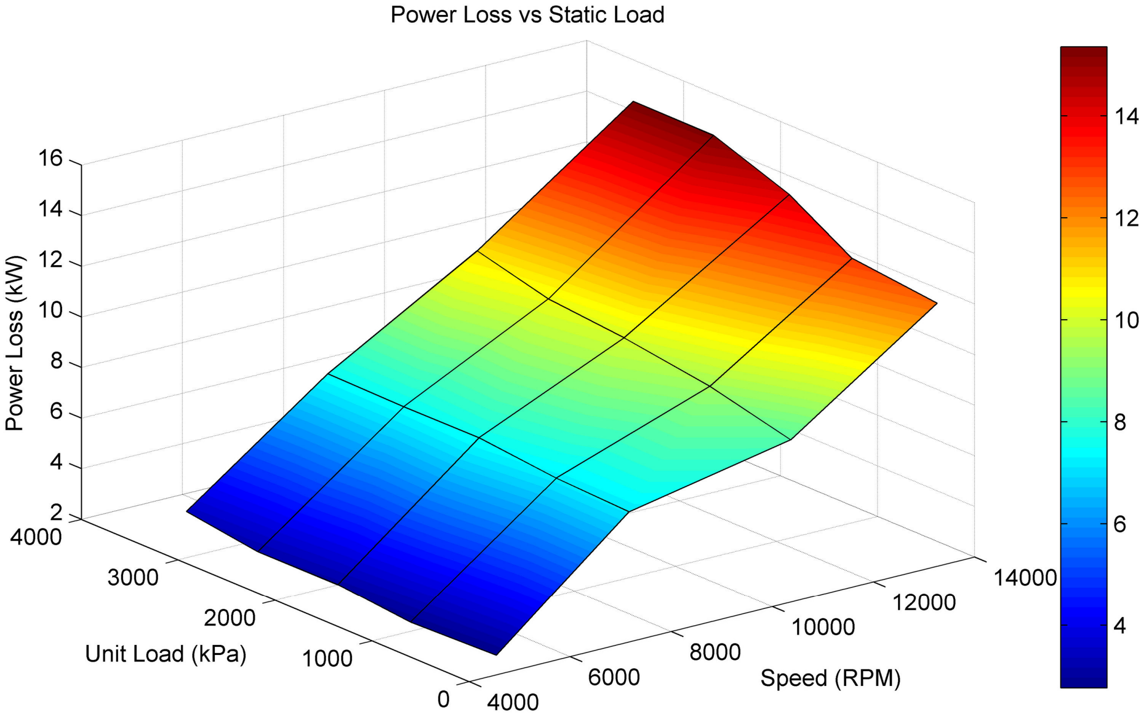

Figure 37: Estimated hydraulic power loss versus unit load and speed

JOURNAL VERSUS BEARING PERTURBED IMPEDANCE COEFFICIENTS

Figure 38 shows the difference between reduced real and imaginary bearing impedances predicted relative to perturbations of the rotor $\tilde{\mathbf{H}}_{\mathbf{jj,k}}$ and bearing $\tilde{\mathbf{H}}_{\mathbf{bb,k}}$ given in Eq. (75). Figure 38 shows that the impedances predicted for this bearing are not heavily dependent on whether they are predicted using journal or bearing perturbations. This suggests that the impedances measured on the test rig for the test bearing are independent of whether the bearing or rotor is perturbed.

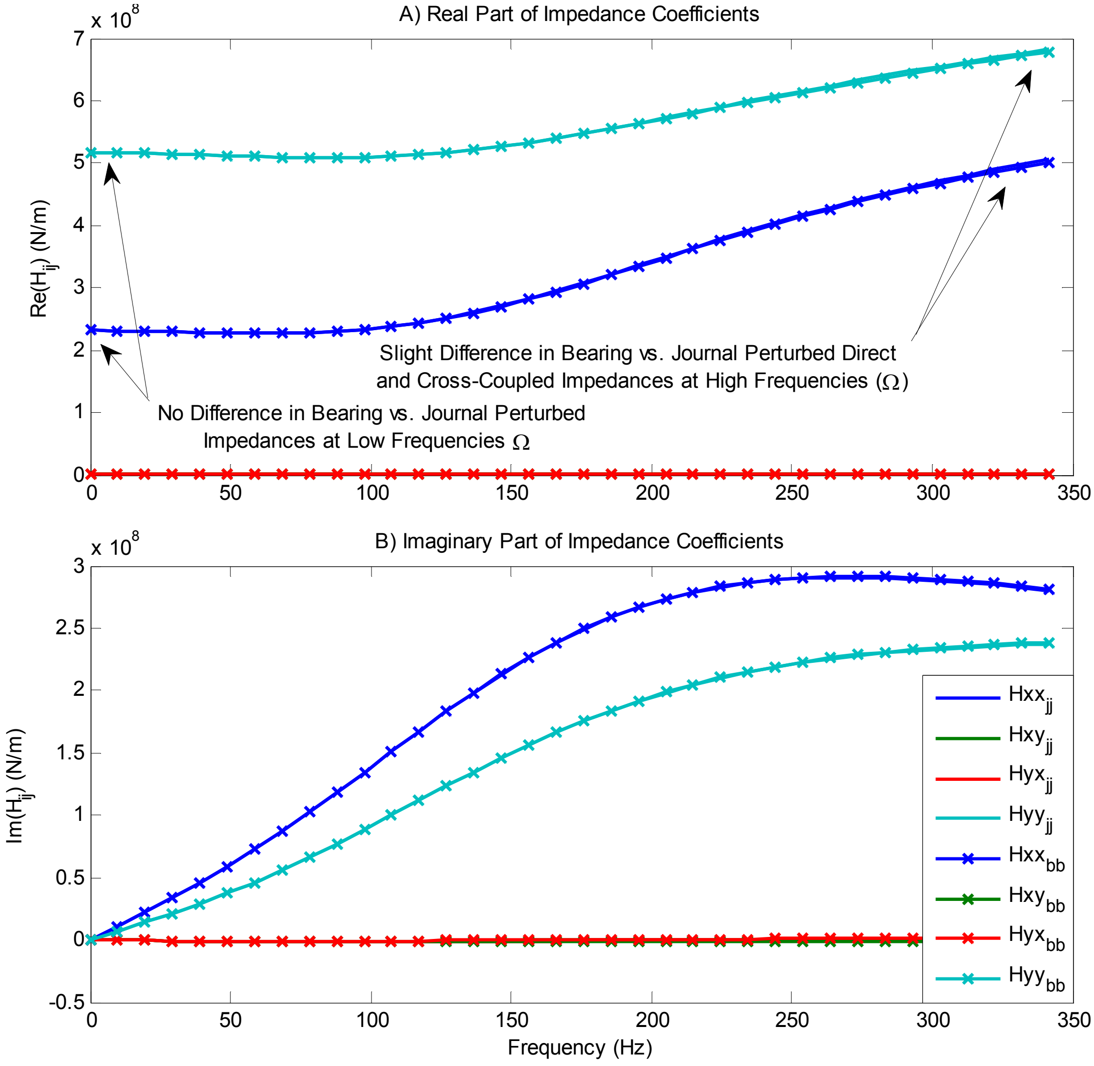

Figure 38: Real and imaginary bearing impedances predicted relative to perturbations of the journal (jj) and bearing (bb) at 4400 rpm and 3132 kPa unit load

Figure 38 shows a slight (almost imperceptible) difference in magnitude of the real and imaginary impedances at higher frequencies. This difference increases with the mass of the pads in the bearing as shown in Figure 39, which shows impedances for the same bearing having 10× denser (heavier) pads. Note that at high frequencies, the bearing perturbed stiffness tends to be smaller than the journal perturbed stiffness while the bearing perturbed damping tends to be larger than the journal perturbed.

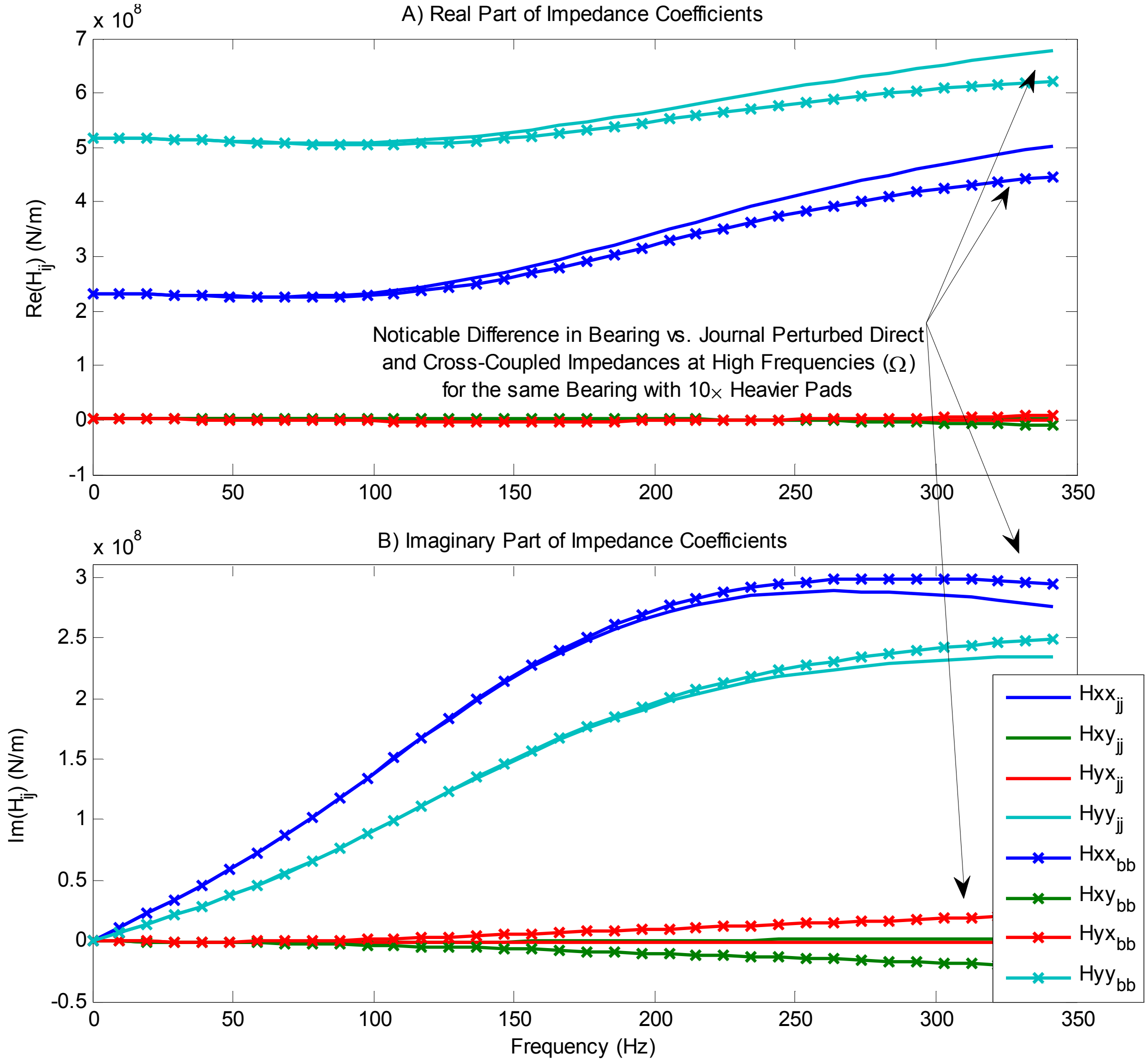

Figure 39: Real and imaginary bearing impedances predicted relative to perturbations of the journal (jj) and bearing (bb) at 4400 rpm and 3132 kPa unit load for the test bearing having 10× heavier pads

Figure 40 shows the predicted real and imaginary bearing impedances predicted relative to perturbations of the rotor $\tilde{\mathbf{H}}_{\mathbf{jj,k}}$ as well as the cross-impedances $\tilde{\mathbf{H}}_{\mathbf{jb,k}}$ given in Eq. (75) that prescribe forces on the rotor due to a displacements of the bearing.

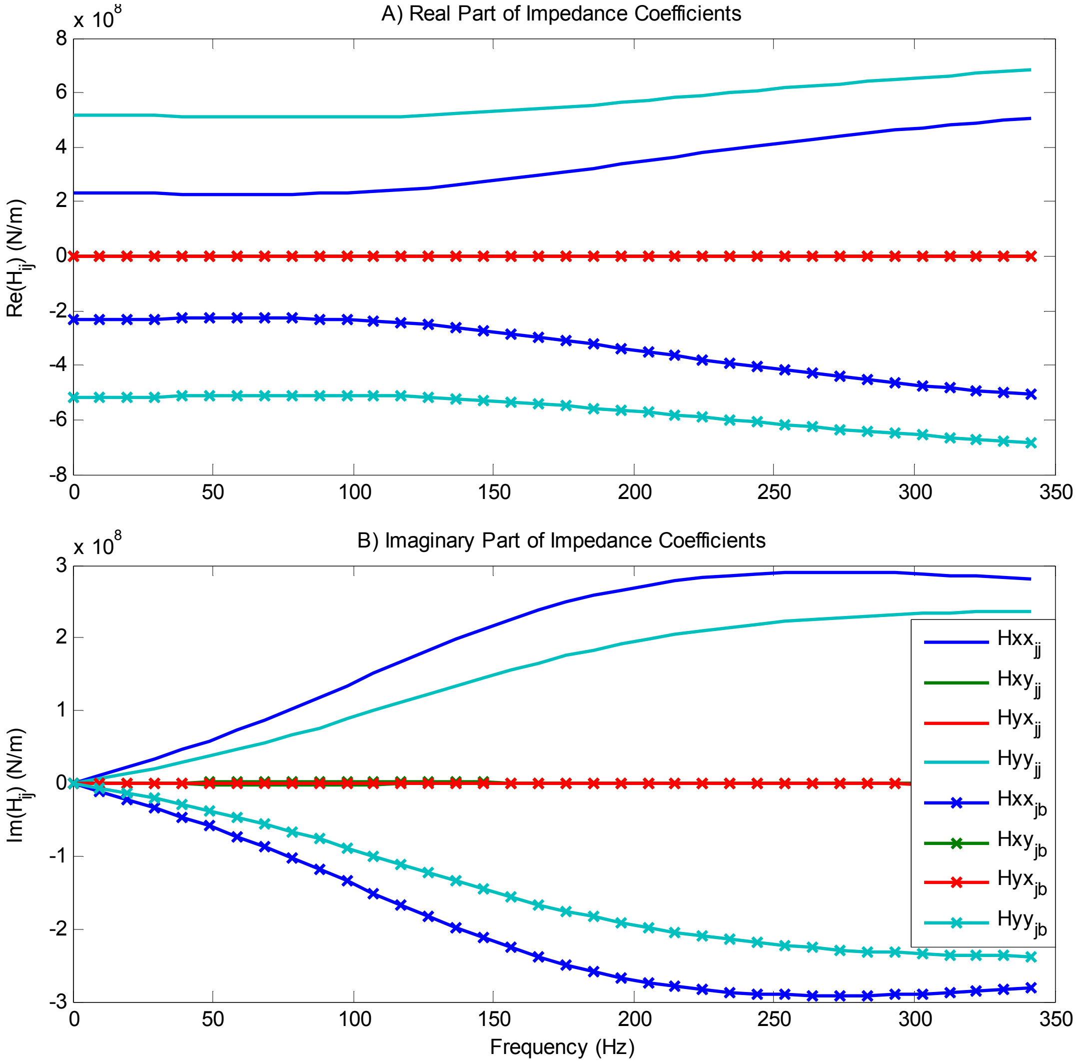

Figure 40: Predicted real and imaginary bearing impedances predicted relative to perturbations of the journal (jj) and journal-bearing (jb) at 4400 rpm and 3132 kPa (454 psi) unit load

Note that $\tilde{\mathbf{H}}_{\mathbf{jj,k}}$ and $\tilde{\mathbf{H}}_{\mathbf{jb,k}}$ are equal and opposite in magnitude. This implies that the bearing will not generate forces if both the journal and bearing are displaced the same amount (ie. if there is no relative motion between the journal and bearing). This is an obvious conclusion; however, it is included for the sake of completeness. Note that an additional comparison between journal and bearing reduced impedance predictions at 10200 rpm and 783 kPa (113 psi) is included in Appendix D.

ROTOR-PAD TRANSFER FUNCTIONS

Figure 41 shows measured rotor-pad transfer functions resulting from the application of Eq. (92) to dynamic pad measurements at 4400 rpm at a 1566 kPa (227 psi) unit load. Note that the legend shows Γ_ϕ, $\Gamma_{\xi c}$, and $\Gamma_{\eta c}$, which correspond to tilt, radial, and transverse pad motions, respectively, in both Figure 41 (A) and (B). Specifically, Figure 41-(A) shows tilt, radial, and transverse pad motions resulting from transverse rotor motion, denoted by Γ^η in the title, while Figure 41-(B) shows pad tilt, radial, and transverse pad motions resulting from radial (on pad) rotor motion, denoted by Γ^ξ in the figure title. The direction of shaft translation is also shown schematically in the depiction of transverse and radial rotor motions on the right hand side of Figure 41 (A) and (B), respectively. Note that $\tilde{\Gamma}_\phi$, $\tilde{\Gamma}_{\xi_c}$, and $\tilde{\Gamma}_{\eta_c}$ are complex numbers, despite being shown in the figures without a tilde.

In Figure 41 and the remaining figures, the pad tilt transfer function $\tilde{\Gamma}_{\hat{\phi}}$ is $\tilde{\Gamma}_\phi$ normalized by multiplying $\tilde{\Gamma}_\phi$ by the distance from the pivot to the leading edge of the pad (25.4 mm). This normalization emphasizes the relative importance of pad tilt ϕ on the fluid-film height at the leading/trailing edges of the pad as compared to horizontal and vertical pad motions ξ_c and η_c; hence, normalized pad tilt will be defined accordingly ($\hat{\phi} = 0.0254\text{m} \times \phi$).

A synopsis of the rotor-pad transfer functions and their implications on dynamic bearing characteristics was given in CHAPTER II immediately following the definition of the pad-rotor and transfer functions in Eq. (73) and in a discussion under the subheading UTILITY OF THE PAD-JOURNAL AND PAD-BEARING TRANSFER FUNCTIONS (pg. 46); nonetheless, a brief overview will be given here.

Essentially, the pad-rotor transfer functions define the amplitude and phase of pad motions resulting from radial and transverse journal/rotor or bearing motions. For example, $\tilde{\Gamma}^{\xi_j}_{\xi_{c,k}}$ specifies the ratio of radial pad motion relative to the bearing housing to radial rotor motion; i.e. relative radial pad-bearing motion resulting from harmonic rotor motion $\tilde{\xi}_j$ is given by $\tilde{\xi}_{c1} = \tilde{\Gamma}^{\xi_j}_{\xi_{c,k}} \tilde{\xi}_j$.

Figure 41-(A) shows pad-rotor transfer functions relating transverse shaft motion to pad tilt, and radial and transverse pivot motions. These transfer functions provide feedback on a pad's ability to track transverse shaft motion, which can yield valuable insights on cross-coupled bearing coefficients; reaction forces orthogonal to rotor displacements.

Consider the case of low frequency (10 Hz) shaft vibrations of unit magnitude along the transverse axis of the loaded pad (i.e. $\tilde{\eta}_j(\Omega = 10) = 1$). Figure 41 (A) can be used to directly calculate the tilt, and radial and transverse pad motion relative to the housing resulting from this perturbed rotor motion. For example, the magnitude of normalized pad tilt $\left|\tilde{\hat{\phi}}\right|$ would be given by $\left|\tilde{\hat{\phi}}\right| = \left|\tilde{\Gamma}^{\eta_j}_{\hat{\phi}} \tilde{\eta}_j\right| \approx 0.32$; thus, transverse pad motions of unit magnitude at 10 Hz excite normalized pad tilt motions having a magnitude of 0.32. In general, $\tilde{\Gamma}^{\eta_j}_{\hat{\phi}}$ provides valuable information on the ability of the pad to track transverse rotor motions. Since the ability of a pad to track the shaft is a key feature of the TPJB, $\tilde{\Gamma}^{\eta_j}_{\hat{\phi}}$ could be used to verify that angular pivot stiffness or angular pivot friction are not preventing the pad from tracking the rotor, which may result in the generation of destabilizing cross-coupled reaction forces. This procedure will be discussed in a case study later in the RESULTS section.

Figure 41-(A) also shows that $\tilde{\Gamma}^{\eta_j}_{\xi_c}$ and $\tilde{\Gamma}^{\eta_j}_{\eta_c}$, the effect of transverse shaft motion on radial (ξ_c) and circumferential (η_c) pad motions is small relative to $\tilde{\Gamma}^{\eta_j}_{\hat{\phi}}$, the effect of transverse shaft motion on normalized pad tilt ($\hat{\phi}$). The magnitude of $\tilde{\Gamma}^{\eta_j}_{\xi_c}$ indicates whether or not transverse rotor motion results in significant radial reaction forces, which

would produce significant radial displacements of the pad, while the magnitude of $\tilde{\Gamma}_{\eta_c}^{\eta_j}$ may indicate whether there is significant slipping at the contact surface. This could result in fretting of the contact surfaces, and ultimately fail the bearing.

(A) Magnitude of Pad Transfer Function Due to Transverse Rotor Motion $|\Gamma^{\eta}|$

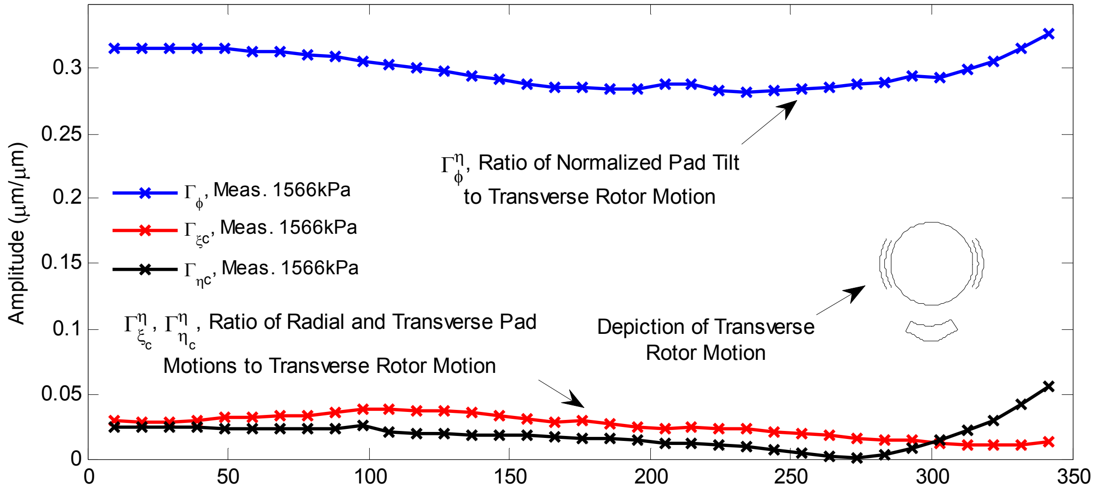

(B) Magnitude of Pad Transfer Function Due to Radial Rotor Motion $|\Gamma^{\xi}|$

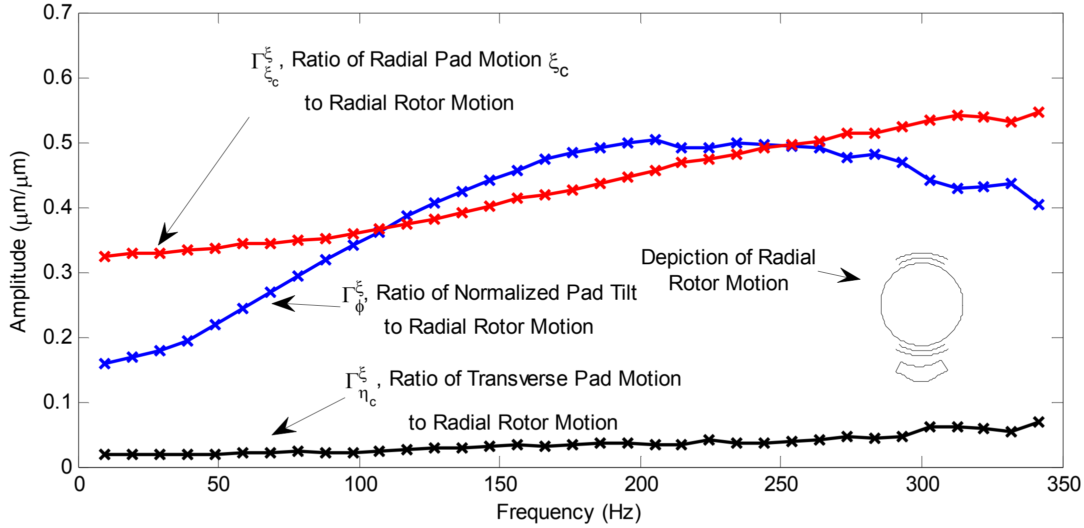

Figure 41: Properties of the measured transfer function amplitudes of the loaded pad due to (A) transverse (η_j) and (B) radial (ξ_j) rotor motions at 4400 rpm and 1566 kPa unit load

Figure 41-(B) shows the transfer functions resulting from shaft motion in the radial axis of the pad. These transfer functions provide valuable information on the

direct stiffness and damping provided by the pad, and a good understanding of these transfer functions and how they compare to predictions is vital to correcting modeling deficiencies relating to direct damping and stiffness.

Consider the case of low frequency (10 Hz) shaft vibrations of unit magnitude along the radial axis of the loaded pad (i.e. $\tilde{\xi}_j\left(\Omega=10\right)=1$). Figure 41 (B) can be used to directly calculate the tilt, and radial and transverse pad motion relative to the housing resulting from this perturbed rotor motion. For example, the magnitude of relative radial pad-bearing motion $\left|\tilde{\xi}_c\right|$ would be given by $\left|\tilde{\xi}_c\right| = \left|\tilde{\Gamma}_{\xi_c}^{\xi_j}\tilde{\xi}_j\right| \approx 0.33$; thus, a 10 Hz dynamic load applied to the shaft resulting in a shaft displacement of 25 microns (1 mil) would produce radial pad displacements of 8.3 microns (0.33 mils), and the fluid film height would only decrease by 16.7 microns (0.67 mils). The consequence of this pad motion is that fluid film stiffness and damping forces produced by relative rotor-pad motions are significantly reduced, resulting in a bearing having significantly less direct stiffness and damping than an otherwise equivalent bearing having a rigid pivot. A similar effect occurs when shaft motions produce significant changes in pad clearance due to pad compliance. For the bearing tested here, these pad-rotor transfer function measurements will show that predicting TPJB stiffness and damping coefficients without accounting for pad and pivot compliance will not result in an accurate prediction of pad motion.

Low Speed (4400 rpm) Rotor-Pad Transfer Functions

Figure 42 shows the measured rotor-pad transfer functions of the loaded pad for low, medium, and large unit loads at 4400 rpm.

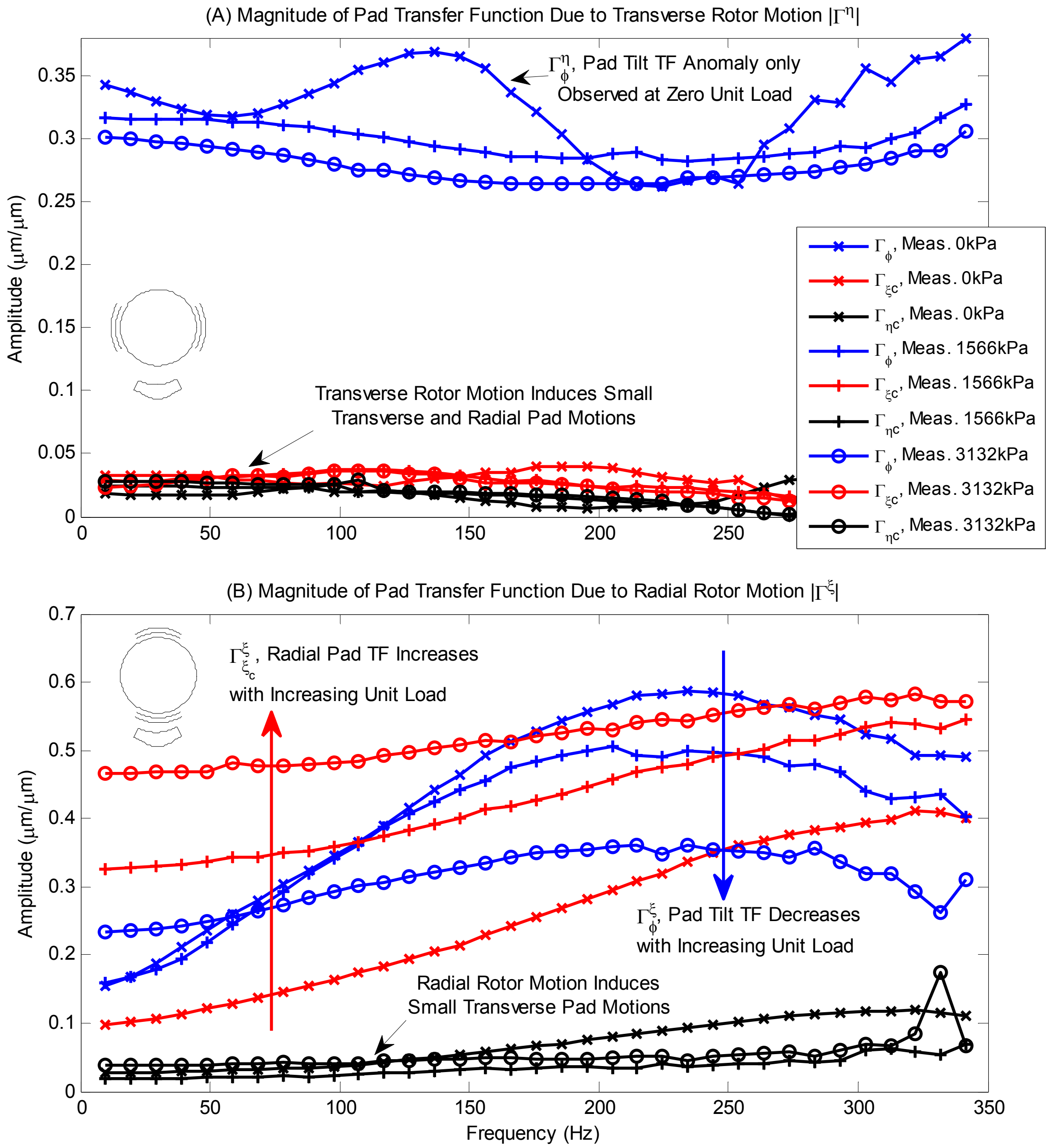

Figure 42: Measured transfer function amplitudes of the loaded pad due to (A) transverse (η_j) and (B) radial (ξ_j) rotor motions at 4400 rpm at zero, medium and high unit loads

Figure 42-(A) shows that the magnitude of radial (ξ_c) and circumferential (η_c) pad motions due to transverse rotor motions are not significantly affected by static load. In each case, $\tilde{\Gamma}^{\eta_j}_{\xi_c}$ and $\tilde{\Gamma}^{\eta_j}_{\eta_c}$ are significantly smaller than $\tilde{\Gamma}^{\eta_j}_{\hat{\phi}}$, pad tilt induced by

transverse rotor motion. $\tilde{\Gamma}^{\eta_j}_{\hat{\phi}}$ tends to decrease slightly with static load, which may result from the increase in pad clearance with increasing unit load noted in Figure 34. $\tilde{\Gamma}^{\eta_j}_{\hat{\phi}}$ also shows slightly different behavior at zero load than in the loaded cases. This undulating behavior was seen only in the unloaded cases at different speeds, and did not occur in any of the loaded tests. This effect might be attributed to the observation of higher-order pad bending modes with the pad proximity probes that were excited by transverse rotor motion at light unit loads, where the pad is significantly more flexible. This speculation could be investigated by including higher order bending modes in the pad's structural model using the method given by Kim et al. [12]. A recent publication by Varela and Santos [46] concludes that the effect of higher order pad bending modes are almost negligible in comparison the lowest bending mode; however, the pads in their analysis appear to be much stouter than the pads in the current work.

Figure 42-(B) shows some very interesting behavior concerning the load and frequency dependency of pad motion resulting from radial rotor motion. Starting with $\tilde{\Gamma}^{\xi_j}_{\xi_{c,k}}$, specifying the ratio of radial pad motion relative to the bearing housing to radial rotor motion, we note the following observations: (1) For the case of zero unit load, the magnitude of $\tilde{\Gamma}^{\xi_j}_{\xi_{c,k}}$ increases from approximately 0.1 at low frequencies, to about 0.4 at high frequencies. This observation implies that for low frequency perturbations of the unloaded shaft, assuming that the pivot is rigid may yield a satisfactory prediction of bearing stiffness and damping coefficients; however, at higher frequencies, Figure 42-(B) shows that vibrations of the statically unloaded shaft produce radial pad displacements having 40% of the magnitude of the radial shaft vibrations. This radial pad motion will result in significantly less relative pad-rotor motion at high frequencies, which will ultimately reduce the fluid film reaction forces due to relative motion between the rotor and ground. The other implication of the frequency dependency of $\tilde{\Gamma}^{\xi_j}_{\xi_{c,k}}$ is that the frequency dependency of direct bearing impedances predicted with and without pivot flexibility will be different; hence, predictions of direct stiffness for a

bearing with rigid pivots may decrease with frequency, while predictions of direct stiffness for a bearing with compliant pivots may increase with frequency. This scenario is just an example of what may occur; however, the difference between bearing stiffness and damping predictions for models with and without pad and pivot compliance will be discussed later in the RESULTS section.

Figure 42-(B) also shows that the magnitude of $\tilde{\Gamma}^{\xi_j}_{\xi_{c,k}}$ radial pad motion to radial shaft motion increases dramatically with applied unit load. In contrast to ratios of radial pad motion to radial shaft motion of 10%-40% for the unloaded shaft, this ratio increases to 50%-60% when the pad is heavily loaded. This observation suggests that the difference between predicted pad motion with rigid versus compliant pivot models will worsen with increasing static load on the pad; thus, the importance of using a model with pivot compliance to predict reaction force coefficients increases with the load on the bearing.

Figures 43-45 compare the measured and predicted rotor-pad transfer functions for low, medium, and high bearing static loads. Looking first at the transfer functions resulting from shaft motion in the transverse axis of the pad shown in Figures 43-45 (A), note the following observations. Figure 43-(A) shows relatively little radial and circumferential motion measured or predicted in comparison to the amount of pad tilt accommodating circumferential rotor motion. The ability of the model to predict the tracking behavior (tilting motion) of the pad is quite good; neither the predicted nor observed tilt transfer function amplitude changes significantly with load or excitation frequency.

One valuable piece of information can be obtained from this measurement; however, and it relates to the pivot location. Consider the differential force in the transverse direction ($f_{\eta 1}$) between the rotor and pad given in Eq (46). If our bearing acts as an ideal tilting pad bearing (one that provides no destabilizing cross-coupled forces), then $f_{\eta 1} = k_{\eta\eta}\ \eta_1 = 0$, where η_1 is the relative transverse motion between the center of the pad's surface arc and the journal, and $k_{\eta\eta}$ is the resulting fluid film stiffness. Since it will not generally be the case that $k_{\eta\eta} = 0$, η_1 must be zero (the pad will track the shaft).

Thus, subtracting Eq. (33) from Eq. (30), assuming that transverse pad motion is negligible, and taking the magnitude yields

$$\left|\eta_j - \eta_b\right| = \left|r_{cp}\phi\right| \tag{100}$$

where r_{cp} is again the distance from the pivot to the center of the pad's surface arc; therefore, the transfer function between the normalized pad tilt angle and transverse rotor motion should be the distance from the pivot to the leading edge of the pad divided by the distance from the pivot to the center of the pad. For the bearing in question,

$$\tilde{\Gamma}^{\eta}_{\hat{\phi}} = \frac{0.025}{r_{cp}} = 0.363 \tag{101}$$

which is very close to both the measured and predicted $\tilde{\Gamma}^{\eta}_{\hat{\phi}}$ in Figure 43-(A). While r_{cp} would be obvious for the pivot type tested, this simple insight may prove to be more useful for a ball-in-socket or cylindrical pivot, in which the actual pad-pivot location may be in question.

Figures 43-45 (B) show comparisons between the measured and predicted transfer functions resulting from shaft motion along the radial (vertical) axis of the pad. Figures 43-45 (B) show that at each static load, the model predicts radial pad motion amplitudes very accurately throughout the entire frequency range, but fails to reproduce the same accuracy in predicting the pad tilt transfer functions, which are increasingly under-predicted at larger static loads. Note that the agreement between the pad tilt transfer function measurements and predictions is better when pad flexibility is not included in the model [38]; however, neglecting pad flexibility also results in overpredicted radial pad transfer functions and direct bearing coefficients.

There are small amounts of circumferential (transverse) pad motion measured at all unit loads in Figures 43-45 (A) and (B), while the model predicts almost no transverse motion. The nature of this motion will be discussed further in regard to the comparison between measured and predicted transfer function phases shown in Figure 46.

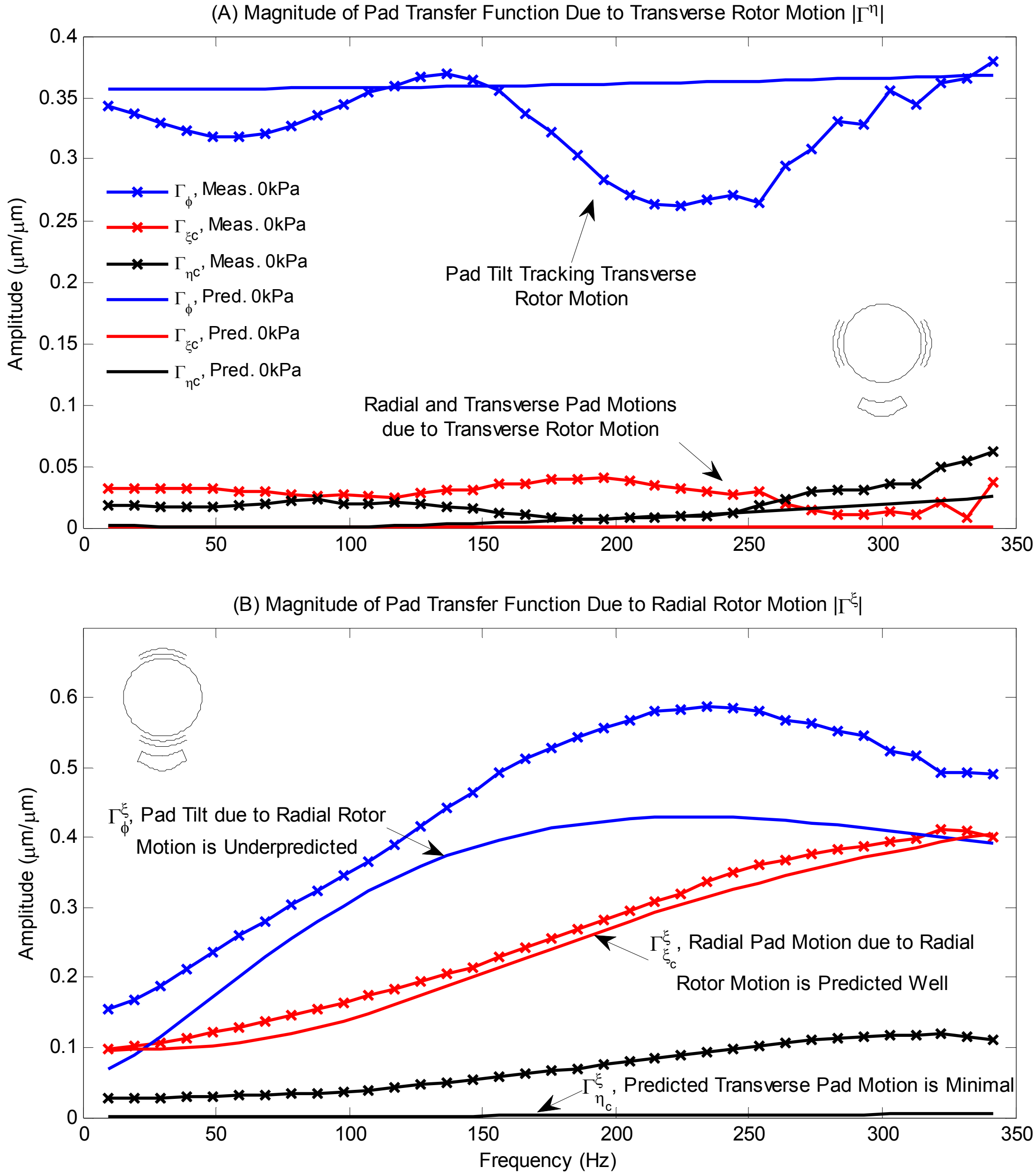

Figure 43: Measured and predicted pad-rotor transfer function amplitudes of the loaded pad due to (A) transverse (η_j) and (B) radial (ξ_j) rotor motions at 4400 rpm and 0 kPa (0 psi) unit load

(A) Magnitude of Pad Transfer Function Due to Transverse Rotor Motion $|\Gamma^{\eta}|$

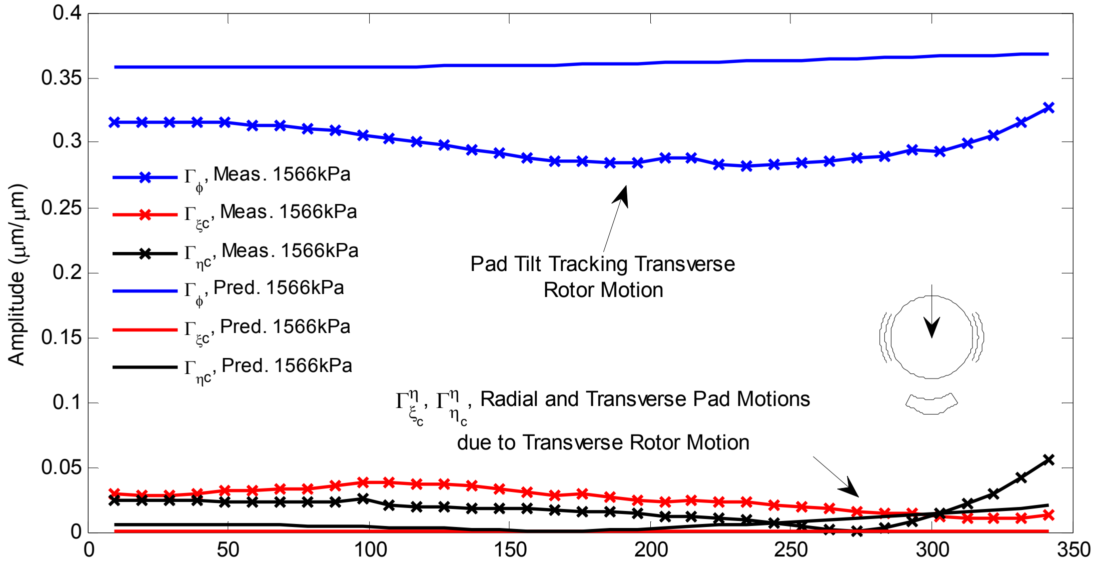

(B) Magnitude of Pad Transfer Function Due to Radial Rotor Motion $|\Gamma^{\xi}|$

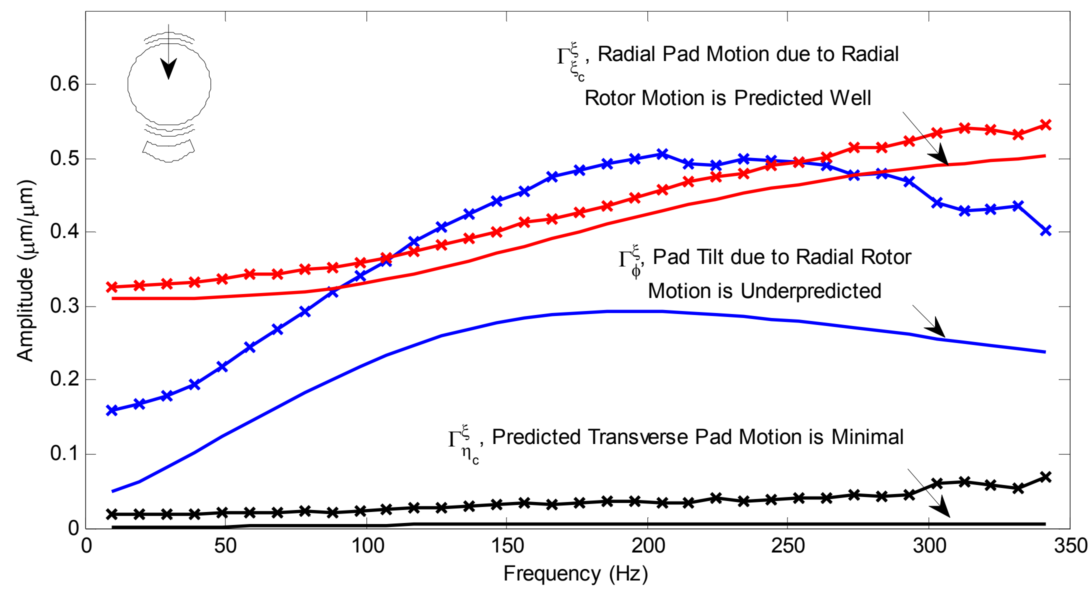

Figure 44: Measured and predicted pad-rotor transfer function amplitudes of the loaded pad due to (A) transverse (η_j) and (B) radial (ξ_j) rotor motions at 4400 rpm and 1566 kPa (227 psi) unit load

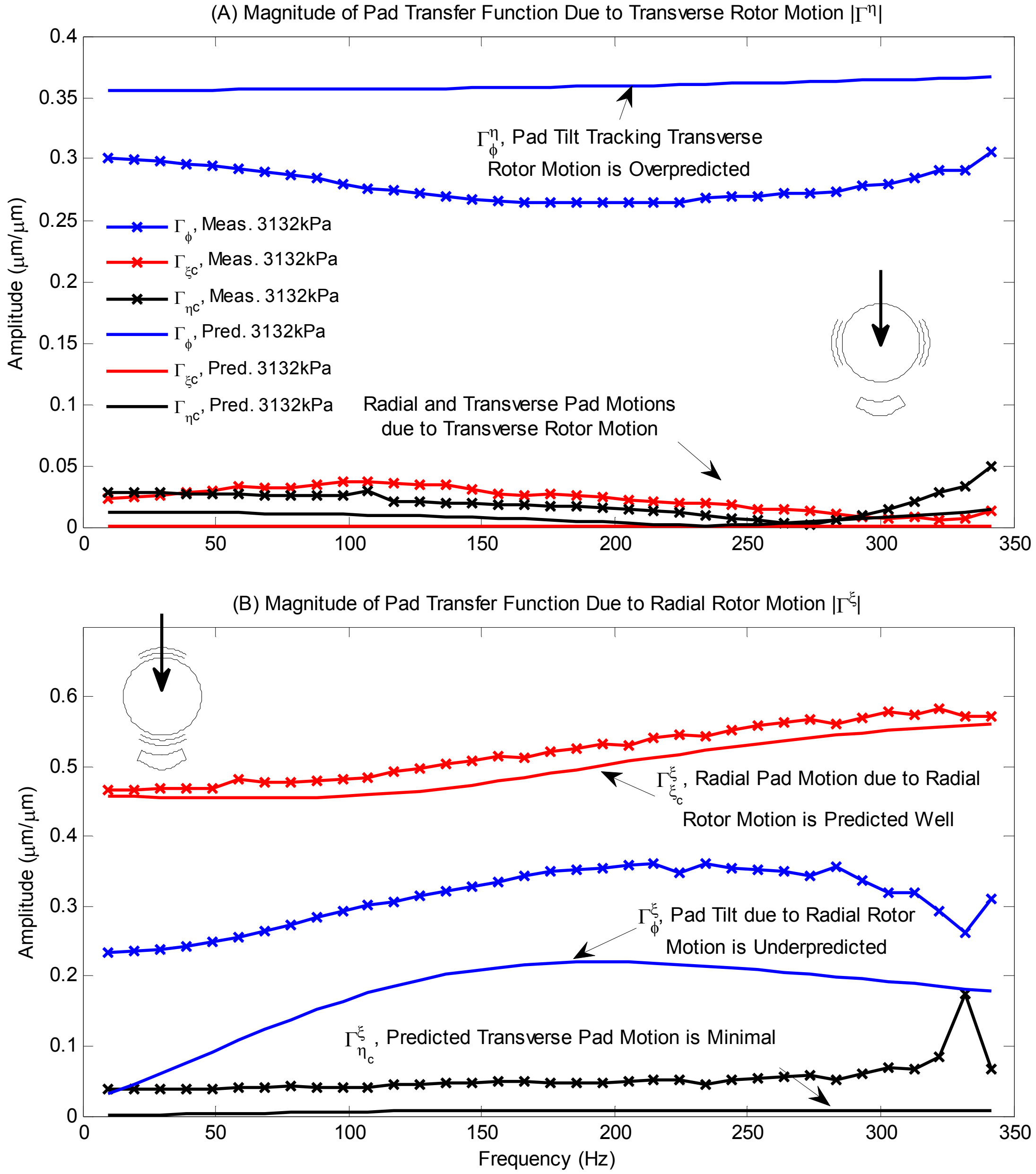

Figure 45 : Measured and predicted pad-rotor transfer function amplitudes of the loaded pad due to (A) transverse (η_j) and (B) radial (ξ_j) rotor motions at 4400 rpm and 3132 kPa (454 psi) unit load

Figure 46 compares the measured and predicted phase of the pad-rotor transfer functions at 4400 rpm with a 1566 kPa (227 psi) load. With the exception of predicted radial pad motion due to transverse rotor motion ($\tilde{\Gamma}^{\eta_j}_{\xi_c}$) and the transverse pivot transfer functions ($\tilde{\Gamma}^{\eta_j}_{\eta_c}, \tilde{\Gamma}^{\xi_j}_{\eta_c}$) the phases of the transfer functions are predicted quite well. This holds especially true for the prediction of tilting angle and radial motion due to radial rotor motion, which had very accurate amplitude predictions as shown in Figure 44.

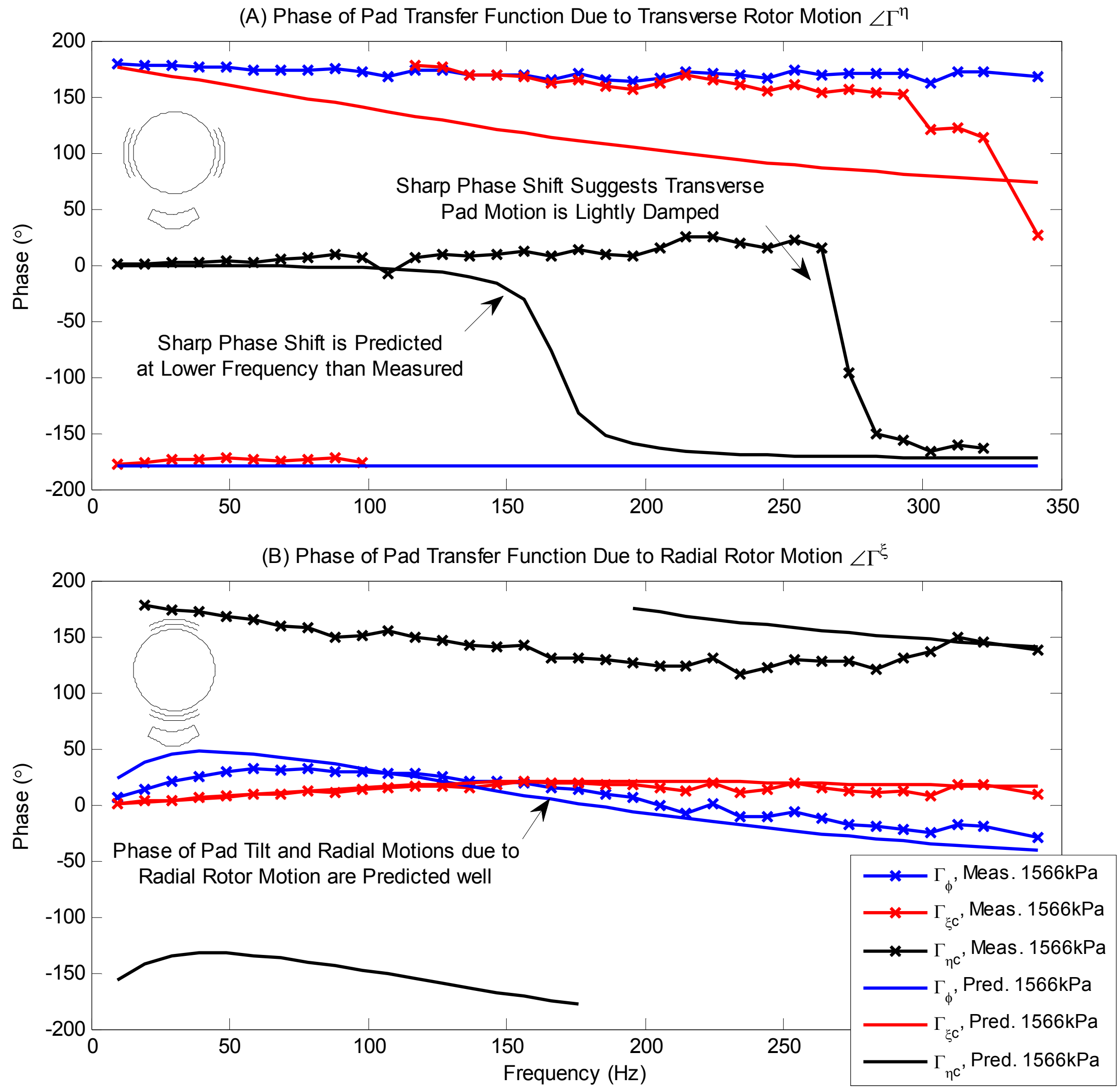

Figure 46: Measured and predicted pad-rotor transfer function amplitudes of the loaded pad due to (A) transverse (η_j) and (B) radial (ξ_j) rotor motions at 4400 rpm and 1566 kPa unit load

Note the 180° shift in the phase of $\tilde{\Gamma}^{\eta}_{\eta_c}$ shown in Figure 46-(A). This shift is predicted as well, but at a lower frequency than measured. This measured phase change suggests that at low excitation frequencies the pad translates in the same direction as the rotor; and then translates in the opposite direction of the rotor at higher frequencies. The sharp change in phase indicates the presence of a lightly damped "pad" vibration mode, and suggests that the circumferential motion observed is not due to sliding of the pivot, but actually transverse deflections of the support of the pad relative to the surface that it sits on. This compliance could arise from contact (Hertzian) related effects or possibly due to motion of the pivot insert relative to the body of the pad. While these observations may suggest that the pivot is rolling-without-slipping on the surface of the housing, there is not sufficient evidence to support this conclusion. It should be noted that Figure 44 (A) does not show a predicted nor observed increase in the magnitude of $\tilde{\Gamma}^{\eta}_{\eta_c}$ surrounding these phase shifts, but instead $\tilde{\Gamma}^{\eta}_{\eta_c}$ appears to approach a magnitude of zero at the frequency of these phase shifts. The reason for this peculiarity is not known at this time.

Figure 47 shows the measured pad-clearance transfer function for a range of unit loads at 4400 rpm. Figure 47 shows that changes in pad clearance due to transverse rotor motions are small, as was the case for radial and transverse pad motions. Unlike the radial pad transfer function, however, the magnitude of the pad-clearance transfer function due to radial rotor motion decreases with increasing unit load (except for the unloaded test, which has a $\tilde{\Gamma}^{\xi_j}_{c_p}$ of reduced magnitude). This trend may result from the drastic increase in pad bending stiffness with increasing moment applied to the pad. These changes in pad clearance are significant, and suggest that neglecting pad flexibility when modeling the subject bearing will not accurately predict the behavior of the pads in the bearing.

Figure 48 shows a comparison between the measured and predicted pad-clearance transfer function for heavily loaded operation at 4400 rpm. Figure 48-(A) shows that changes in pad clearance due to transverse rotor motion are predicted to be very small, substantiating the previous claim that predicted changes in the radial load on the pad are minimal due to transverse rotor motion, despite measurements showing larger, but likely insignificant $\tilde{\Gamma}_{c_p}^{\eta_j}$ magnitudes. Figure 48-(B) shows that changes in pad clearance due to radial rotor motion are slightly underpredicted, but has similar frequency characteristics to the measured values of $\tilde{\Gamma}_{c_p}^{\xi_j}$.

(A) Magnitude of Pad Transfer Function Due to Transverse Rotor Motion $|\Gamma^{\eta}|$

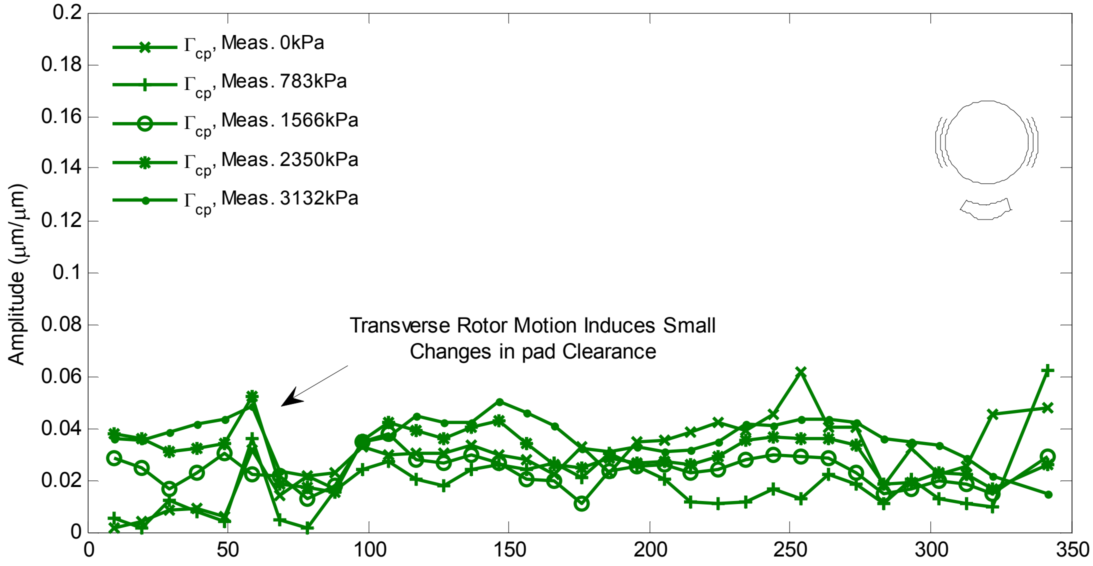

Transverse Rotor Motion Induces Small Changes in pad Clearance

(B) Magnitude of Pad Transfer Function Due to Radial Rotor Motion $|\Gamma^{\xi}|$

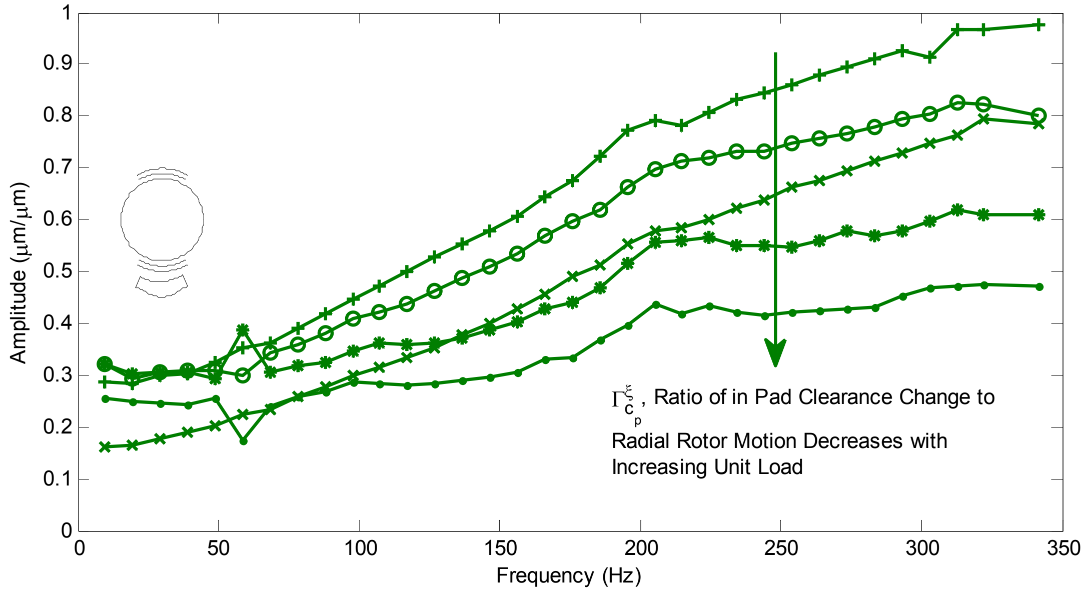

$\Gamma_{c_p}^{\xi}$, Ratio of in Pad Clearance Change to Radial Rotor Motion Decreases with Increasing Unit Load

Figure 47: Measured pad-clearance change transfer function amplitudes of the loaded pad due to (A) transverse (η_j) and (B) radial (ξ_j) rotor motions at 4400 rpm at various unit loads

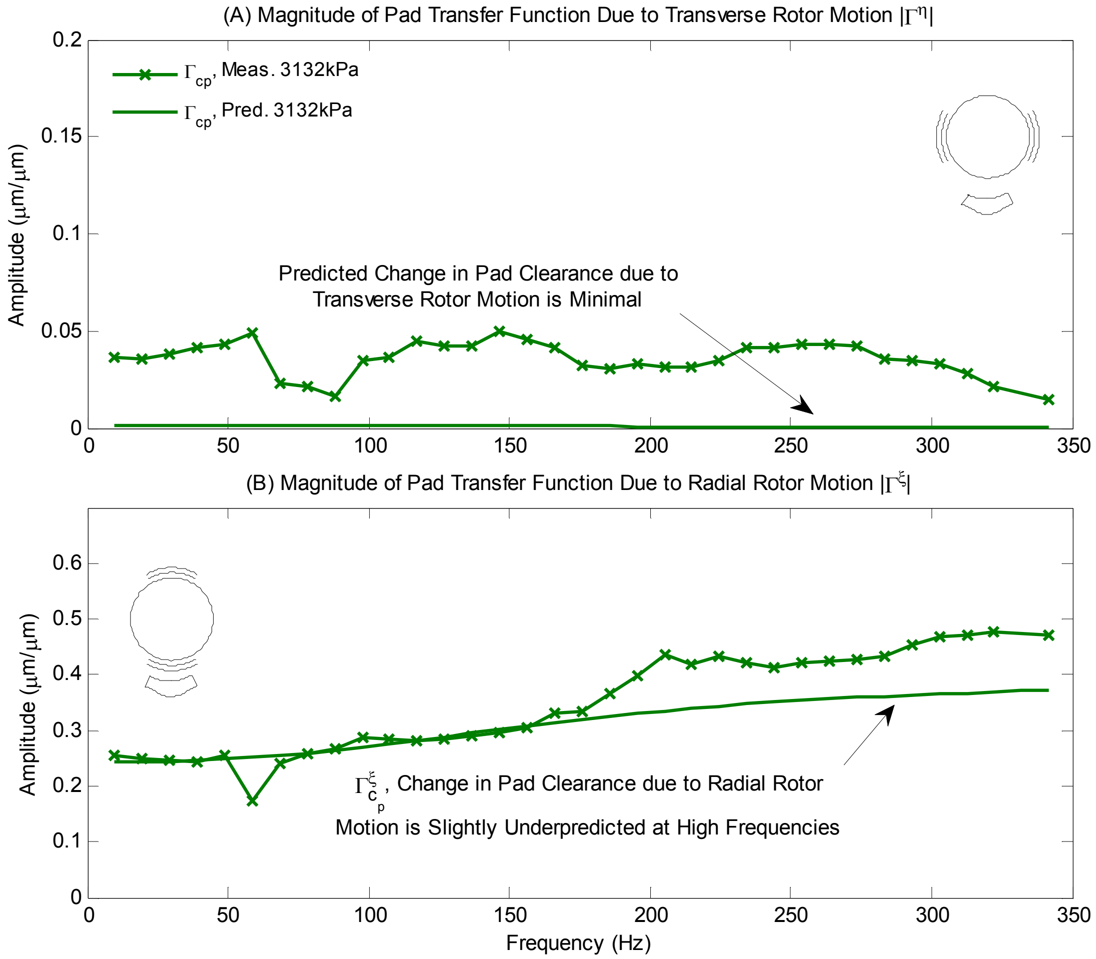

Figure 48: Measured and predicted pad-clearance change transfer function amplitudes of the loaded pad due to (A) transverse (η_j) and (B) radial (ξ_j) rotor motions at 4400 rpm and 3132 kPa (454 psi) unit load

Figure 49 shows a waterfall plot of normalized pad tilt frequency response due to input excitation frequencies at 4400 rpm (73 Hz) at 3132 kPa. The magnitude of the tilt response is normalized such that the magnitude of the response at the excitation frequency is equal to the magnitude of $\hat{\Gamma}_{\phi}^{\xi}$. Figure 49 shows that the majority of pad tilt occurs at the excitation frequency, despite slight 2× and 3× harmonics of excitation frequency, and 1×, 2×, and 3× synchronous frequencies.

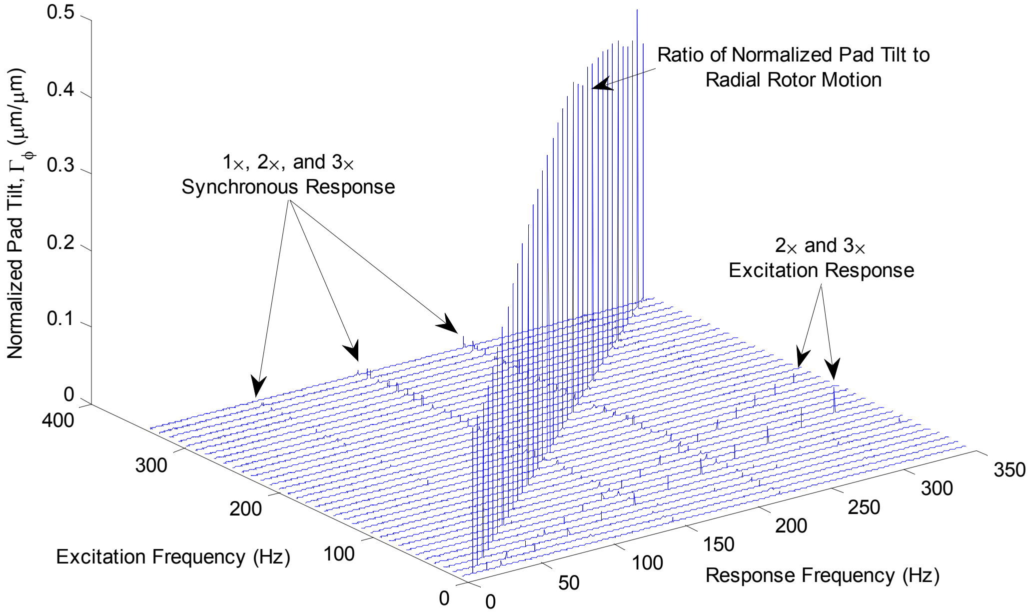

Figure 49: Waterfall plot of normalized pad tilt response due to test excitations at 4400 rpm and 3132 kPa unit load

High Speed (10200 rpm) Rotor-Pad Transfer Functions

Figure 50 shows the measured rotor-pad transfer functions of the loaded pad for low, medium, and large unit loads at 10200 rpm. In contrast to the transfer functions measured at 4400 rpm shown in Figure 42, the high speed transfer functions vary less with frequency, especially $\tilde{\Gamma}_{\phi}^{\xi}$. Figure 50 also shows that the magnitude of $\tilde{\Gamma}_{\phi}^{\xi}$ increases with increasing unit load, while lower speeds showed that pad tilt due to radial rotor motion decreased with increasing unit load. The radial pad transfer function due to radial shaft motion $\tilde{\Gamma}_{\xi_c}^{\xi}$ has similar frequency characteristics at both speeds; however, $\tilde{\Gamma}_{\xi_c}^{\xi}$ varies less with static unit load at the higher speed. This observation can likely be supported by the previous observation from Figure 32 that the radial load supported by the loaded pad for light loads increases with increasing speed, while heavily loaded operation showed the radial load supported by the loaded pad to decrease with increasing rotor speed. Figure 50 also shows that the magnitude of $\tilde{\Gamma}_{\phi}^{\xi}$ increases with increasing unit load, while lower speeds showed that pad tilt due to radial rotor motion decreased.

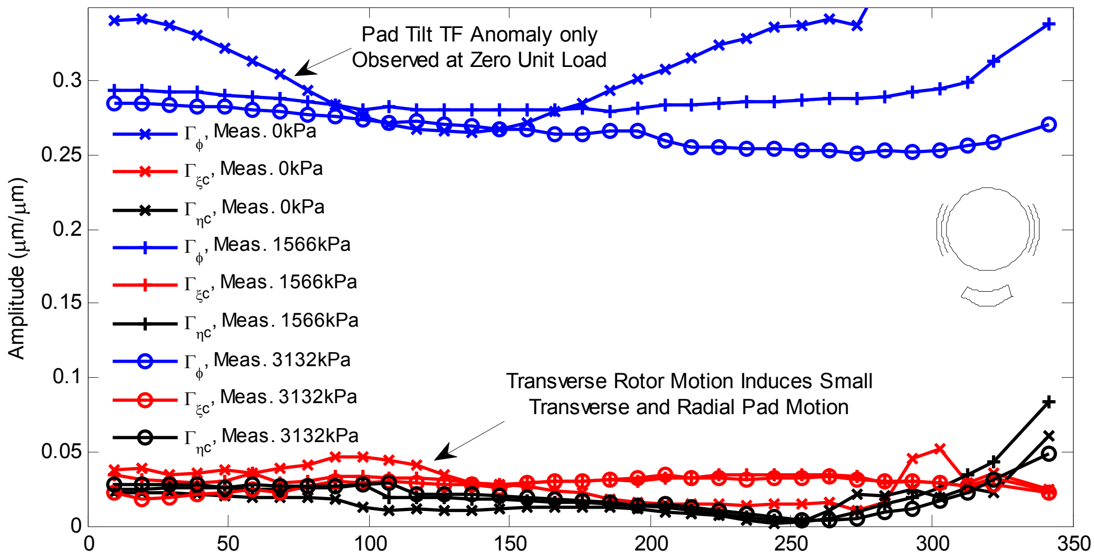
(A) Magnitude of Pad Transfer Function Due to Transverse Rotor Motion $|\Gamma^{\eta}|$

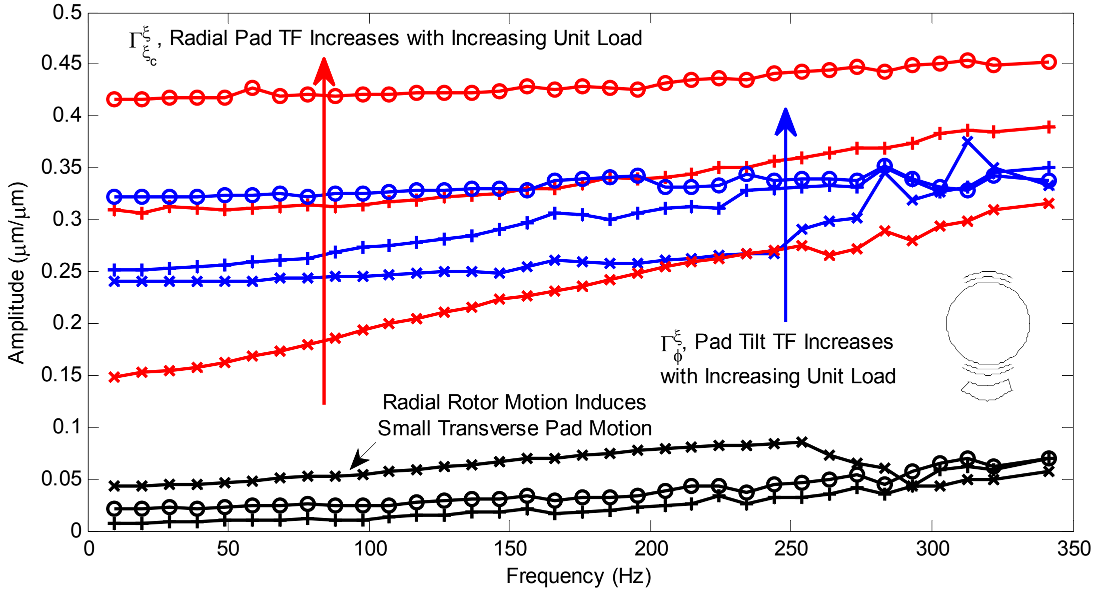
(B) Magnitude of Pad Transfer Function Due to Radial Rotor Motion $|\Gamma^{\xi}|$

Figure 50: Measured transfer function amplitudes of the loaded pad due to (A) transverse (η_j) and (B) radial (ξ_j) rotor motions at 10200 rpm at zero, medium and high unit loads

Figures 51 and 52 show comparisons between measured and predicted rotor-pad transfer functions at light and heavy unit loads at 10200 rpm. In general, the rotor-pad transfer functions are predicted quite well; however, radial pad motion is underpredicted for the low load case shown in Figure 51-(B), and the model still has a tendency to underpredict pad tilt due to radial rotor motion Γ_{ϕ}^{ξ} as shown in Figures 51 and 51 (B).

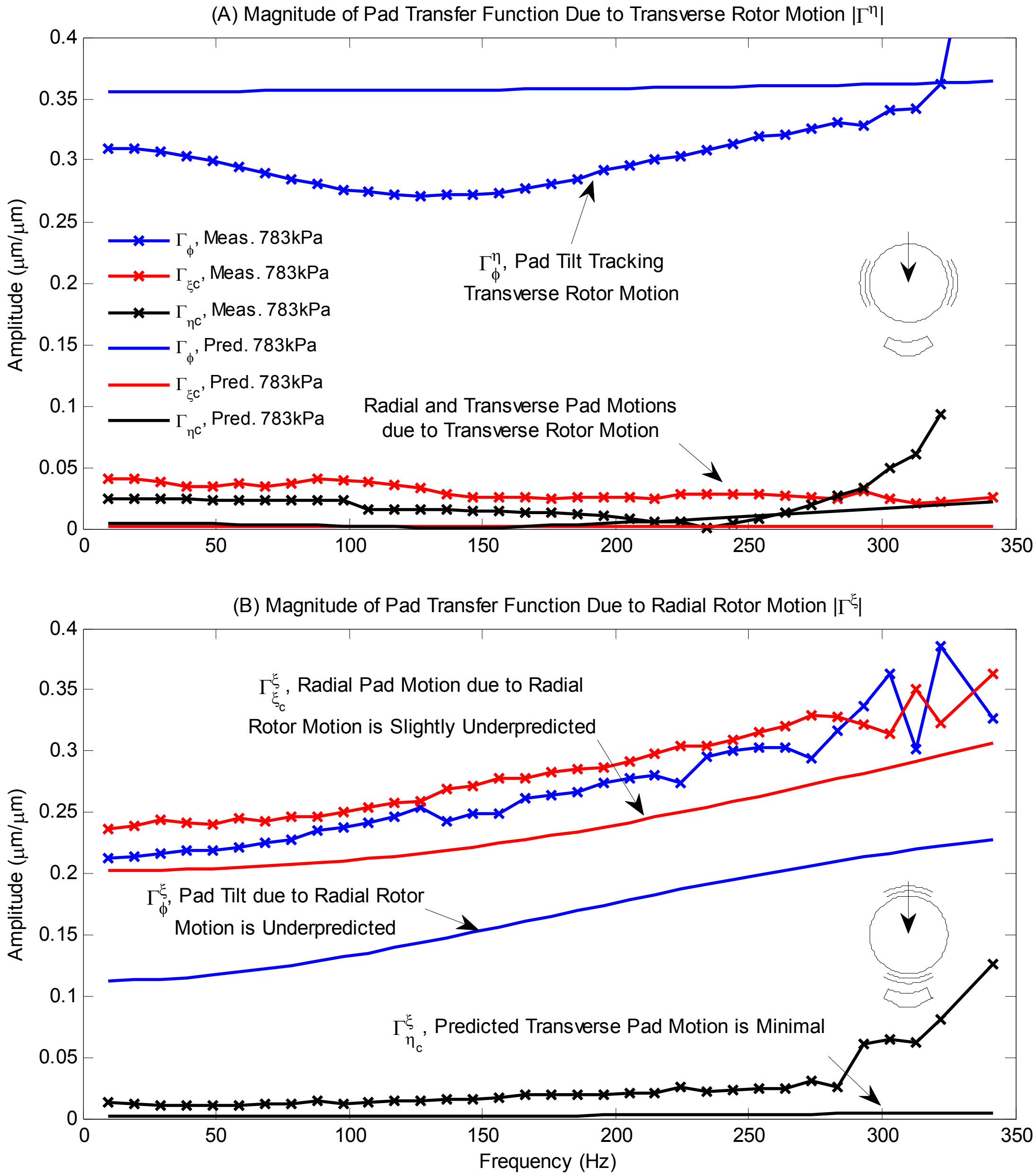

Figure 51: Measured and predicted rotor-pad transfer function amplitudes of the loaded pad due to (A) transverse (η_j) and (B) radial (ξ_j) rotor motions at 10200 rpm and 783 kPa (113 psi) unit load

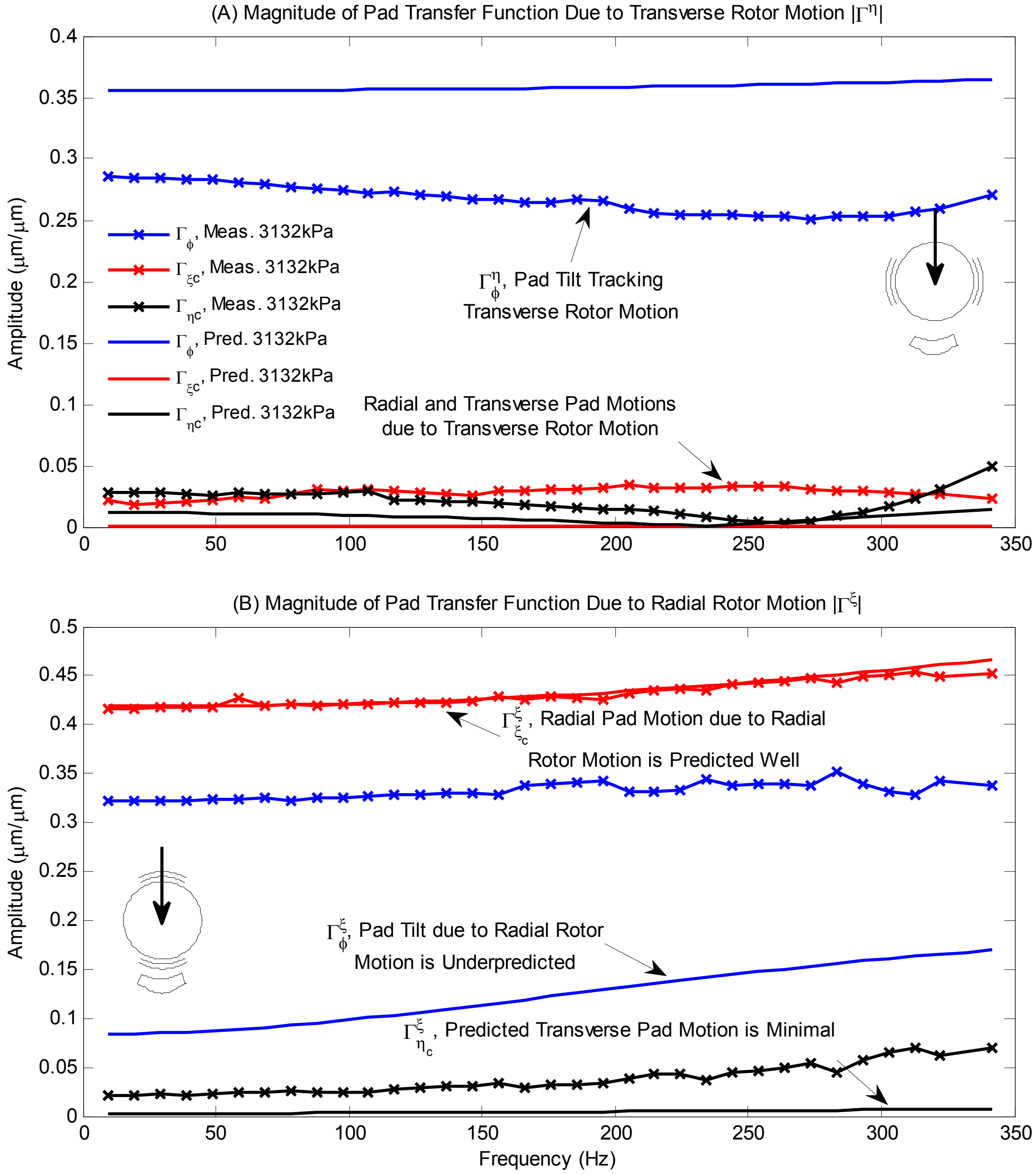

Figure 52 : Measured and predicted rotor-pad transfer function amplitudes of the loaded pad due to (A) transverse (η_j) and (B) radial (ξ_j) rotor motions at 10200 rpm and 3132 kPa (454 psi) unit load

REAL AND IMAGINARY PARTS OF BEARING IMPEDANCES

Low Speed (4400 rpm) Bearing Impedances

Figures 53 and 54 show the measured and predicted real and imaginary reduced bearing impedances as a function of excitation frequency at 4400 rpm at light (783 kPa) and heavy (3134 kPa) unit loads. Note that impedances ($\tilde{H}_{xx}$, $\tilde{H}_{xy}$ …) shown in the following figures are complex numbers, despite being represented without a tilde, and that the static load is applied in the *Y* direction. Measured impedances result from the application of Eqs. (88)-(91) to test data, while predictions were generated with the model given in CHAPTER II using the pivot load-versus-deflection curve given in Eq. (93), the load dependent pad bending stiffness given in Eq. (95), and the temperature dependent bearing clearance given in Eq. (96).

Figures 53 and 54 show that the model does well in stiffness and damping prediction at low and heavy loads out to the running speed of 73 Hz (4400 rpm), but deviates moderately in the prediction of frequency-dependent behavior for both the real and imaginary parts of H_{ij} after about 1.5× running speed. These frequency dependent differences include an overpredicted falloff in direct damping at higher frequencies and an overestimation of direct stiffness with increasing excitation frequency. If a KCM model were applied to the data, this overestimation of direct stiffness with increasing excitation frequency could be identified by an increase in the predicted magnitude of negative direct virtual-mass coefficients. The accuracy of the real and imaginary impedances for these cases out to 1.5× running speed are summarized in Table 5, which shows the relative error in predicted stiffness and damping coefficients through 100 Hz.

At 4400 rpm, the direct stiffness coefficients are predicted within 13% for light and heavy loads, while direct damping predictions are within 18% at light and heavy loads. At light loads, the coefficients tend to be overpredicted, while predicted coefficients at the heavy load are both high and low.

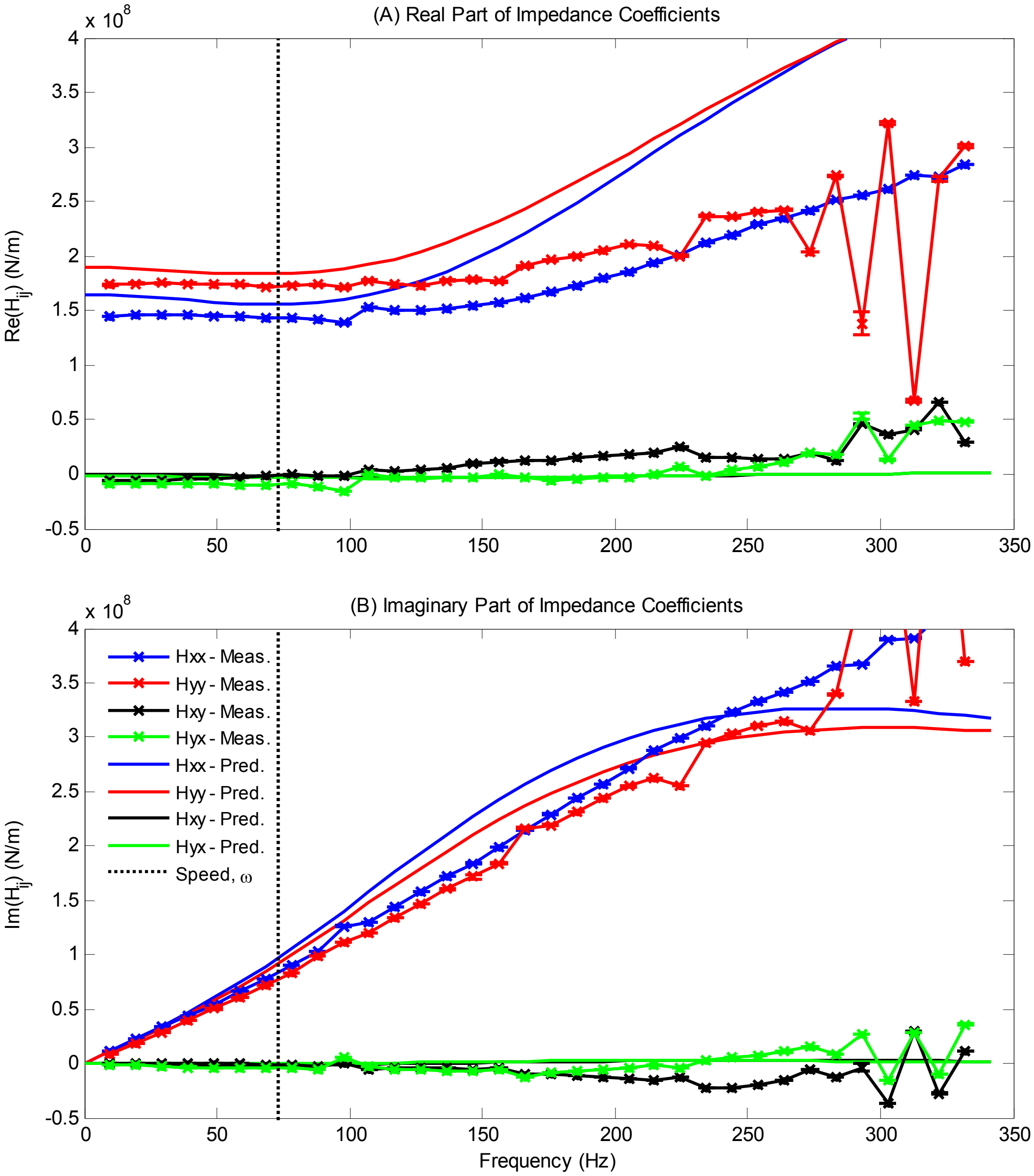

Figure 53: (A) Real and (B) imaginary components of measured and predicted bearing impedance coefficients at 4400 rpm and 783 kPa (114 psi) unit load

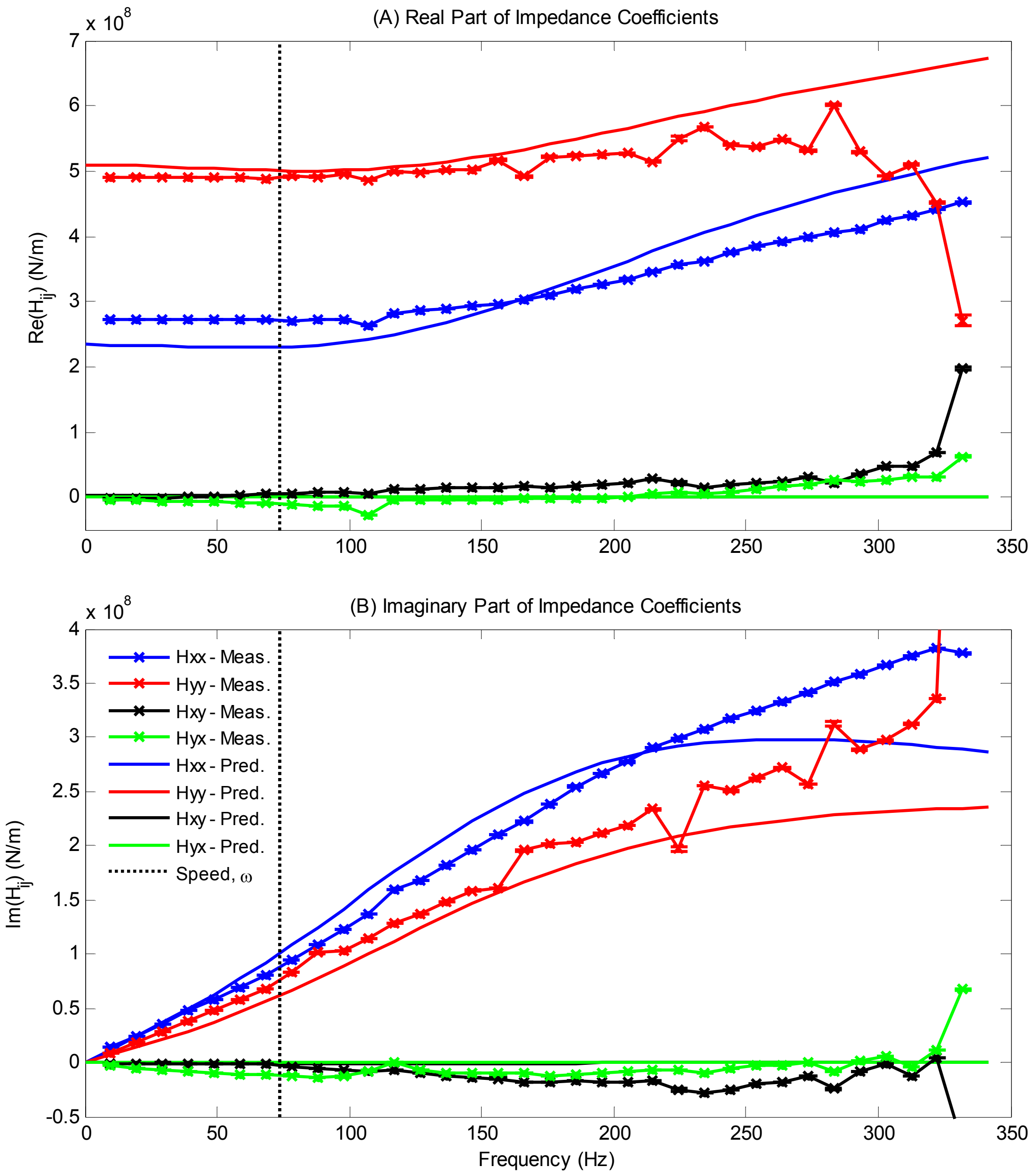

Figure 54: (A) Real and (B) imaginary components of measured and predicted bearing impedance coefficients at 4400 rpm and 3134 kPa (454 psi) unit load

Table 5: Percent relative error in principal stiffness and damping coefficients at 4400 rpm (fit through 1.5× running speed). Positive values indicate overpredicted coefficients

Unit Load kPa (psi)	$100\left(\frac{k_{xx,pred}}{k_{xx,meas}}-1\right)$	$100\left(\frac{k_{yy,pred}}{k_{yy,meas}}-1\right)$	$100\left(\frac{c_{xx,pred}}{c_{xx,meas}}-1\right)$	$100\left(\frac{c_{yy,pred}}{c_{yy,meas}}-1\right)$
783 (114)	8.15	6.77	15.10	18.14
3134 (454)	-13.42	0.95	15.94	-14.10

High Speed (10200 rpm) Bearing Impedances

Figures 55 and 56 show a comparison between measured and predicted bearing impedances at 10200 rpm (170 Hz) at low and high loads. In general, the accuracy of the bearing predictions are excellent. There is still a slight deviation in the frequency characteristics of the real part of $\tilde{H}_{xx}$ and $\tilde{H}_{yy}$ at low loads, but less than was noted for the 4400 rpm cases. Considering the nonlinearity of both the pad and pivot stiffness for this bearing, the author feels that the agreement is excellent, and notably better than previous comparisons between measured and predicted bearing coefficients.

The results of the bearing predictions are summarized in Table 6 which shows the relative error in predicted bearing coefficients at 10200 rpm. In general, predicted direct stiffness and damping coefficients in the loaded direction are within 5% of the measured values with the exception direct stiffness in the unloaded direction that is overpredicted by 10% for the heavily loaded case.

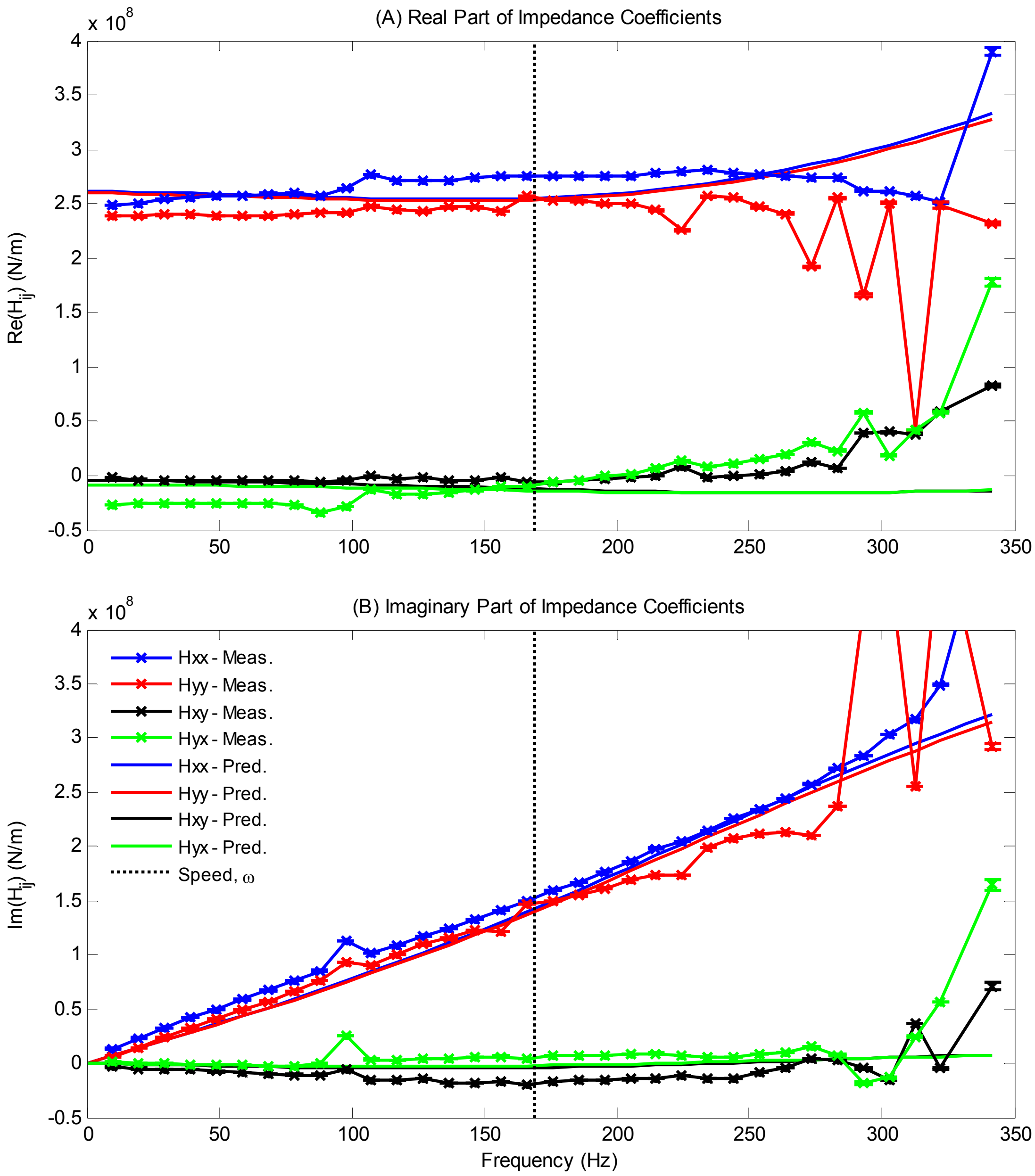

Figure 55: (A) Real and (B) imaginary components of measured and predicted bearing impedance coefficients at 10200 rpm and 783 kPa (114 psi) unit load

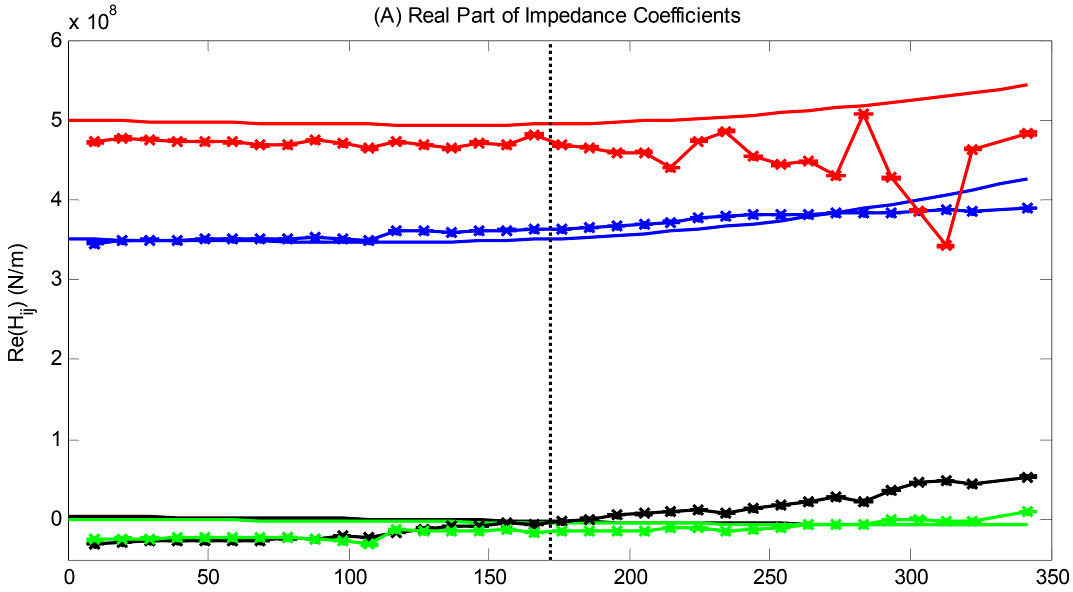

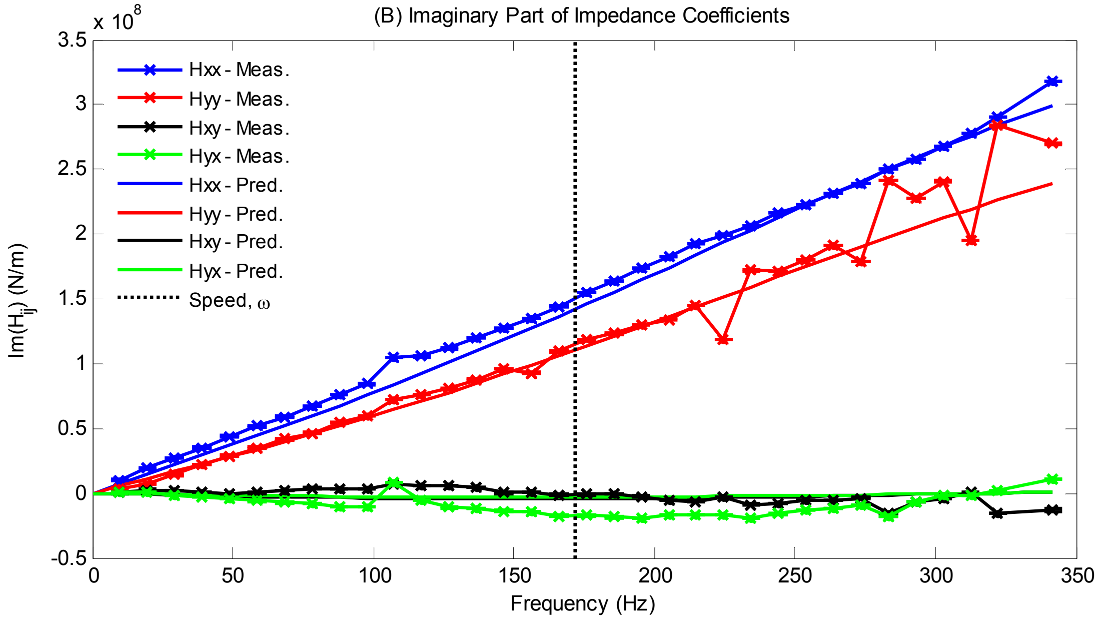

Figure 56: (A) Real and (B) imaginary components of measured and predicted bearing impedance coefficients at 10200 rpm and 3134 kPa (454 psi) unit load

Table 6: Percent relative error in principal stiffness and damping coefficients at 10200 rpm (fit through 1.5× running speed). Positive values indicate overpredicted coefficients

Unit Load kPa (psi)	$100\left(\frac{k_{xx,pred}}{k_{xx,meas}}-1\right)$	$100\left(\frac{k_{yy,pred}}{k_{yy,meas}}-1\right)$	$100\left(\frac{c_{xx,pred}}{c_{xx,meas}}-1\right)$	$100\left(\frac{c_{yy,pred}}{c_{yy,meas}}-1\right)$
783 (114)	-3.27	4.59	-0.85	5.41
3134 (454)	-3.61	10.63	-1.42	-2.15

IMPACT OF PAD AND PIVOT FLEXIBILITY ON BEARING IMPEDANCES

Figures 57 and 58 illustrate the importance of predicting bearing impedances with pad and pivot flexibility for operation at 4400 and 10200 rpm at 3132 kPa unit load, and Figure 59 shows similar results at 10200 rpm at 783 kPa unit load. These figures compare real and imaginary impedance measurements to predictions for models with and without pad, pivot, or pad and pivot flexibility. For example, the "$\text{Rigid}_{\text{pad,pivot}}$" cases represent bearing predictions for a model having a rigid pad and a rigid pivot in solving for static equilibrium and perturbing that equilibrium.

These results are tabulated in Tables 7 - 9 which clearly reveal the scope of error induced in calculations when not including pad and pivot compliance in TPJB predictions at both light and heavy loads. For the bearing tested, predicted principal direct stiffness and damping coefficients at heavy unit loads are impacted more by pivot flexibility than pad flexibility, while a rigid pad and pivot model yields an overestimation of direct stiffness by 202% and damping by 811% in the loaded direction at 4400 rpm and an overestimation of direct stiffness by 177% and damping by 513% in the loaded direction at 10200 rpm when heavily loaded. While the reader may be questioning the degree to which these predictions are overestimated in regard to previous comparisons, keep in mind that these predictions are based on measured operating clearances, which are 20-30% smaller than the cold bearing clearances that previous comparisons were based on. It should be noted that the importance of pad flexibility will increase with the arc length of the pad; hence, pad flexibility may be more important in larger bearings and bearings with fewer pads.

Though stiffness and damping are overpredicted more at heavy loads, Figure 59 and Table 9 show that not including pad and pivot compliance results in overpredicted direct stiffness and damping in the loaded direction by 51% and 182% at light unit loads.

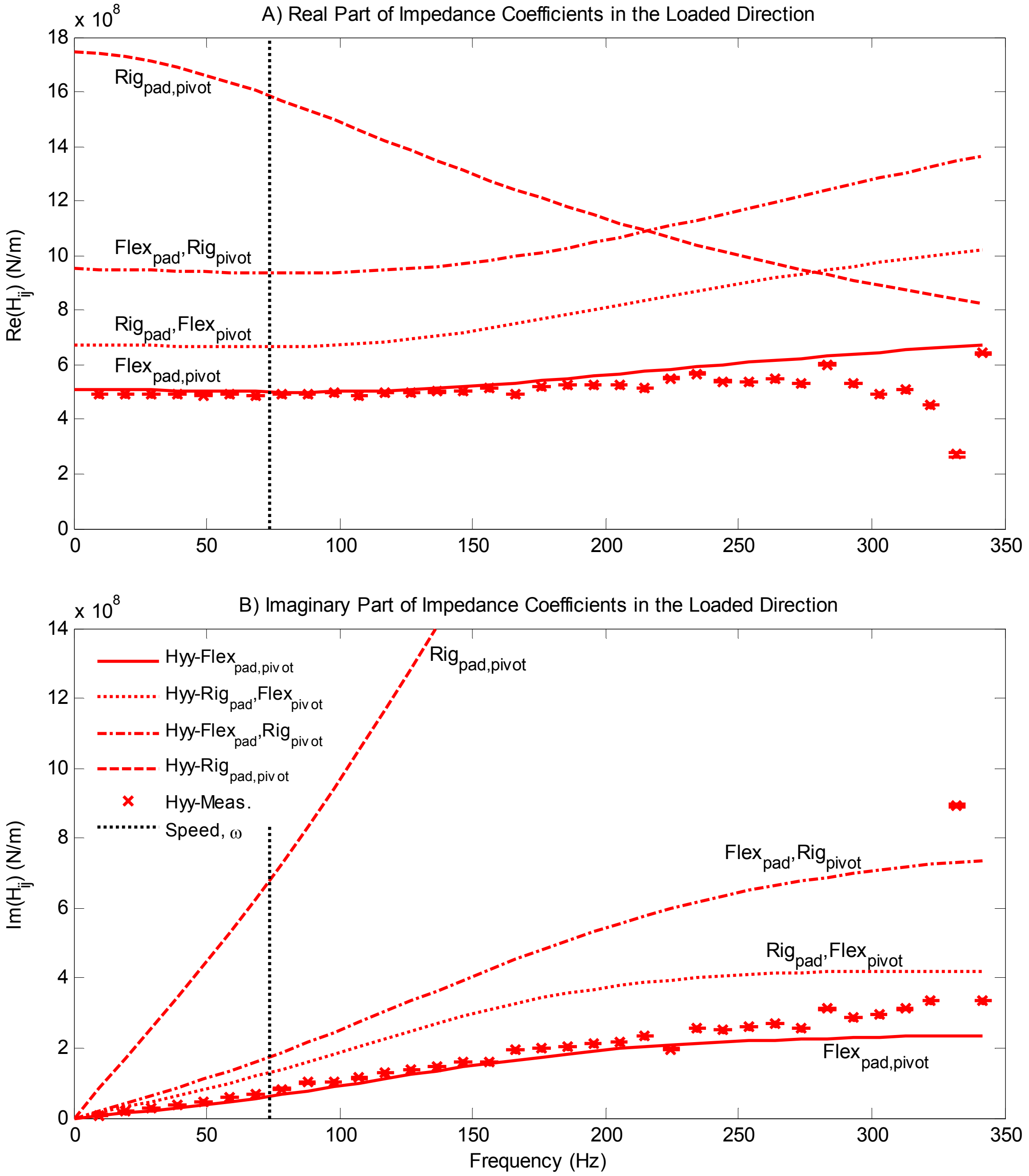

Figure 57: (A) Real and (B) imaginary components of principal bearing impedances in the loaded direction at 4400 rpm and 3132 kPa unit load showing the importance of pad and pivot flexibility

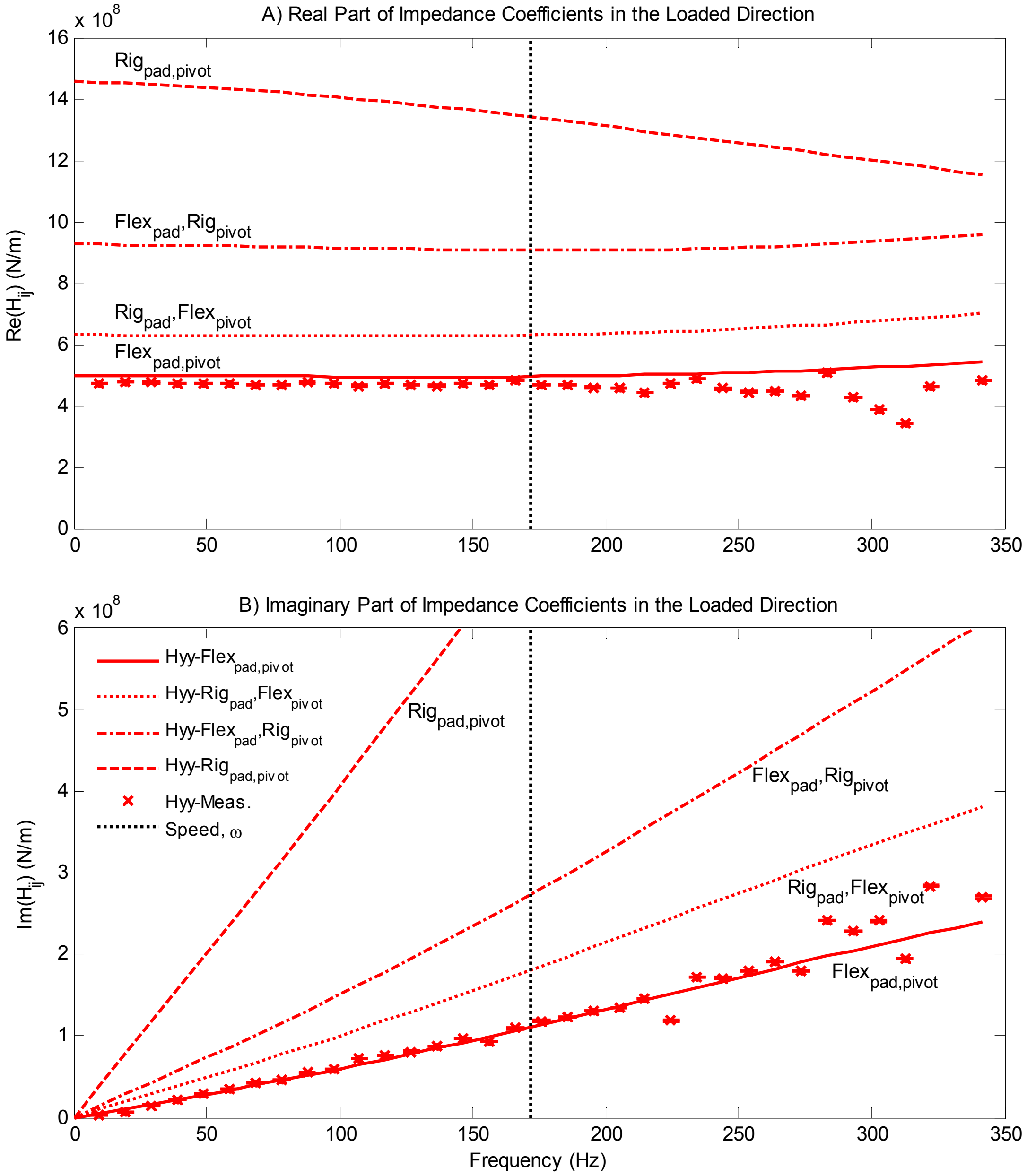

Figure 58: (A) Real and (B) imaginary components of principal bearing impedances in the loaded direction at 10200 rpm and 3132 kPa unit load showing the importance of pad and pivot flexibility

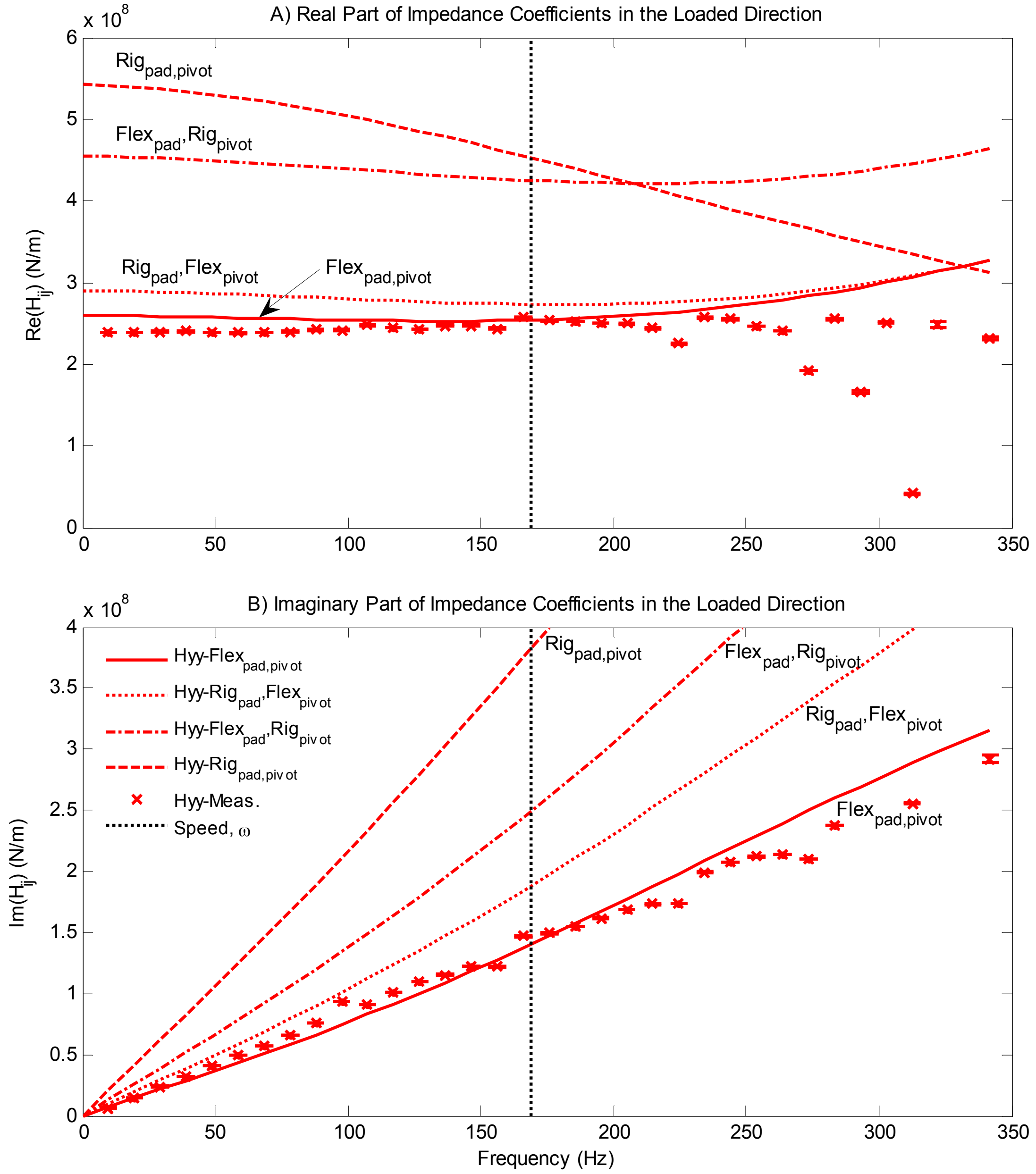

A) Real Part of Impedance Coefficients in the Loaded Direction

B) Imaginary Part of Impedance Coefficients in the Loaded Direction

Figure 59: (A) Real and (B) imaginary components of principal bearing impedances in the loaded direction at 10200 rpm and 783 kPa unit load showing the importance of pad and pivot flexibility at light loads

Table 7: Percent relative error in principal stiffness and damping coefficients at 4400 rpm and 3134 kPa for models with and without pivot/pad flexibility (fit through 1.5× running speed). Positive values indicate overpredicted coefficients

Pad Model Type	$100\left(\frac{k_{xx,pred}}{k_{xx,meas}}-1\right)$	$100\left(\frac{k_{yy,pred}}{k_{yy,meas}}-1\right)$	$100\left(\frac{c_{xx,pred}}{c_{xx,meas}}-1\right)$	$100\left(\frac{c_{yy,pred}}{c_{yy,meas}}-1\right)$
$\text{Flex}_{\text{pad,pivot}}$	-13.42	0.95	15.94	-14.10
$\text{Rigid}_{\text{pad}}$,$\text{Flex}_{\text{pivot}}$	-5.36	35.53	74.30	77.93
Flex_{pad}, $\text{Rigid}_{\text{pivot}}$	13.30	88.88	88.11	136.33
$\text{Rigid}_{\text{pad,pivot}}$	12.24	201.61	201.72	810.78

Table 8: Percent relative error in principal stiffness and damping coefficients at 10200 rpm and 3134 kPa for models with and without pivot/pad flexibility (fit through 1.5× running speed). Positive values indicate overpredicted coefficients

Pad Model Type	$100\left(\frac{k_{xx,pred}}{k_{xx,meas}}-1\right)$	$100\left(\frac{k_{yy,pred}}{k_{yy,meas}}-1\right)$	$100\left(\frac{c_{xx,pred}}{c_{xx,meas}}-1\right)$	$100\left(\frac{c_{yy,pred}}{c_{yy,meas}}-1\right)$
$\text{Flex}_{\text{pad,pivot}}$	-3.61	10.63	-1.42	-2.15
$\text{Rigid}_{\text{pad}}$,$\text{Flex}_{\text{pivot}}$	8.72	41.77	49.00	56.90
Flex_{pad}, $\text{Rigid}_{\text{pivot}}$	66.51	99.84	99.59	140.29
$\text{Rigid}_{\text{pad,pivot}}$	72.79	176.65	266.10	512.99

Table 9: Percent relative error in principal stiffness and damping coefficients at 10200 rpm and 783 kPa for models with and without pivot/pad flexibility (fit through 1.5× running speed). Positive values indicate overpredicted coefficients

Pad Model Type	$100\left(\frac{k_{xx,pred}}{k_{xx,meas}}-1\right)$	$100\left(\frac{k_{yy,pred}}{k_{yy,meas}}-1\right)$	$100\left(\frac{c_{xx,pred}}{c_{xx,meas}}-1\right)$	$100\left(\frac{c_{yy,pred}}{c_{yy,meas}}-1\right)$
$\text{Flex}_{\text{pad,pivot}}$	-3.27	4.59	-0.85	5.41
$\text{Rigid}_{\text{pad}}$,$\text{Flex}_{\text{pivot}}$	-1.88	8.49	35.37	42.27
Flex_{pad}, $\text{Rigid}_{\text{pivot}}$	58.00	64.34	78.55	88.09
$\text{Rigid}_{\text{pad,pivot}}$	41.28	51.16	172.65	181.93

In addition to quantifying the error in dynamic impedances fit through running speed, note that Figures 57 and 58 show the predicted frequency characteristics of the stiffness and damping to be completely different when pad and pivot flexibility are not included. Consider the implications of performing a stability analysis using reduced coefficients predicted by a model without pad and pivot flexibility. Most discussions concerning the proper frequency to use in reducing coefficients focus on the importance of obtaining accurate damping values [16-18] (despite having shown here that this is an unlikely outcome); however, a substantial reduction in bearing stiffness is noted in Figures 57 and 58 with increasing excitation frequency for models without pad and pivot flexibility, whereas models including pad and pivot flexibility have an increase in dynamic stiffness with excitation frequency. While bearing damping is arguably a dominant factor in determining system stability, bearing stiffness affects the location of the damped eigenvalue, as well as the mode shapes that determine how much energy can be dissipated by the bearing.

IMPACT OF FULL VERSUS REDUCED BEARING MODELS ON STABILITY

Figure 60 shows a schematic of the rotor-bearing system used to demonstrate the effect of calculating system stability using full versus reduced bearing models. The system consists of a symmetric rotor supported on either end by TPJBs with a destabilizing cross-coupled stiffness applied at the rotor's midspan. The radius of the shaft at the bearings corresponds to the rotor radius given in Table 1, and the rotor radius at midspan and total shaft length were adjusted for each case to place the first critical speed of the system at approximately 0.4-0.5 times the running speeds of 4400 and 10200 rpm, respectively.

The rotor was modeled using 8 Euler-Bernoulli finite-elements, and the model was validated by comparing free-free natural frequencies against predictions using XLTRC^2, a validated rotordynamic code. The bearings were modeled using the code used to predict the dynamic stiffness and damping coefficients of the experimental tests contained in this dissertation, which has been shown to be fairly accurate. Both reduced and full bearing models were assembled and connected to the rotor, and then stability was assessed by increasing the magnitude of the destabilizing cross-coupled stiffness at midspan until eigenvalue analysis showed the system to be unstable.

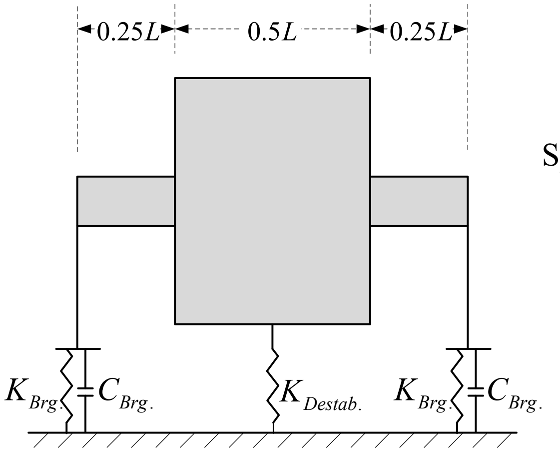

Speed(rpm)	4400	10200
L(m)	1.61	1.15
R_{mid}(m)	0.3	0.25

Figure 60: Rotor bearing system used to calculate the effect of employing full versus reduced bearing models on system instability

Reduced bearing coefficients were calculated at both the frequency of the unstable eigenvalue (subsynchronous) and at rotor speed (synchronous). The natural frequency of the unstable eigenvalue was determined iteratively by reducing coefficients at a guessed frequency, calculating stability, then using the frequency of the calculated unstable root to reduce coefficients for the next iteration. The reduction frequency converged after only a few iterations to the same value, which was typically very close to the natural frequency of the unstable mode predicted with the full bearing model.

Tables 10 and 11 show the percent relative error in magnitude of destabilizing cross-coupled stiffness required to cause instability with respect to the full bearing model using subsynchronously and synchronously reduced bearing coefficients, respectively. Despite showing several unit loads, the unit load of the model shaft on each bearing was 1556 kPa (225.6 psi) at 4400 rpm and 781 kPa (113.3 psi) at 10200 rpm. The **boldface** cases in Tables 10 and 11 correspond to scenarios where the weight of the shaft matches the unit load used to predict the bearing coefficients.

Table 10 shows that the relative error in magnitude of destabilizing cross-coupled stiffness required to cause instability using subsynchronously reduced bearing coefficients is less than 1.2% for all loads at 4400 and 10200 rpm, while Table 11 shows that the relative error in magnitude of destabilizing cross-coupled stiffness required to cause instability using synchronously reduced bearing coefficients were as large as 24%

and 17% for lightly loaded operation at 4400 rpm and 10200 rpm, respectively. For unit loads corresponding to the example model geometry, employing synchronously reduced coefficients overestimated the maximum allowable destabilizing cross-coupled stiffness by 7.6% and 16% at 4400 rpm and 10200 rpm, respectively.

Table 10: Percent relative error in destabilizing cross-coupled stiffness required to cause the system shown in Figure 60 to become unstable when employing subsynchronously reduced coefficients at speeds of 4400 and 10200 rpm at various unit loads. Boldface values indicate approximate unit loads matching model shaft geometry

	4400 rpm		10200 rpm	
Unit Load kPa (psi)	$100\left(\frac{K_{xy,red}}{K_{xy,full}}-1\right)$	$\frac{\omega_{unstable}}{\omega_{shaft}}$	$100\left(\frac{K_{xy,red}}{K_{xy,full}}-1\right)$	$\frac{\omega_{unstable}}{\omega_{shaft}}$
0	1.277	0.422	0.881	0.408
783 (114)	1.156	0.440	**0.716**	**0.409**
1566 (227)	**1.242**	**0.451**	0.868	0.420
2350 (340)	0.649	0.461	0.935	0.426
3132 (454)	0.714	0.464	1.198	0.432

Table 11: Percent relative error in destabilizing cross-coupled stiffness required to cause the system shown in Figure 60 to become unstable when employing synchronously reduced coefficients at speeds of 4400 and 10200 rpm at various unit loads. Boldface values indicate approximate unit loads matching model shaft geometry

	4400 rpm		10200 rpm	
Unit Load kPa (psi)	$100\left(\frac{K_{xy,red}}{K_{xy,full}}-1\right)$	$\frac{\omega_{unstable}}{\omega_{shaft}}$	$100\left(\frac{K_{xy,red}}{K_{xy,full}}-1\right)$	$\frac{\omega_{unstable}}{\omega_{shaft}}$
0	24.681	0.422	18.731	0.408
783 (114)	17.341	0.440	**16.714**	**0.409**
1566 (227)	**6.832**	**0.451**	12.724	0.420
2350 (340)	3.247	0.461	7.170	0.426
3132 (454)	2.857	0.464	2.996	0.432

Figure 61 shows the content in Tables 10 and 11graphically. Figure 61 shows using synchronously reduced coefficients leads to an overestimation of system stability when the shaft is lightly loaded, and a moderate overestimation of system stability at heavier unit loads.

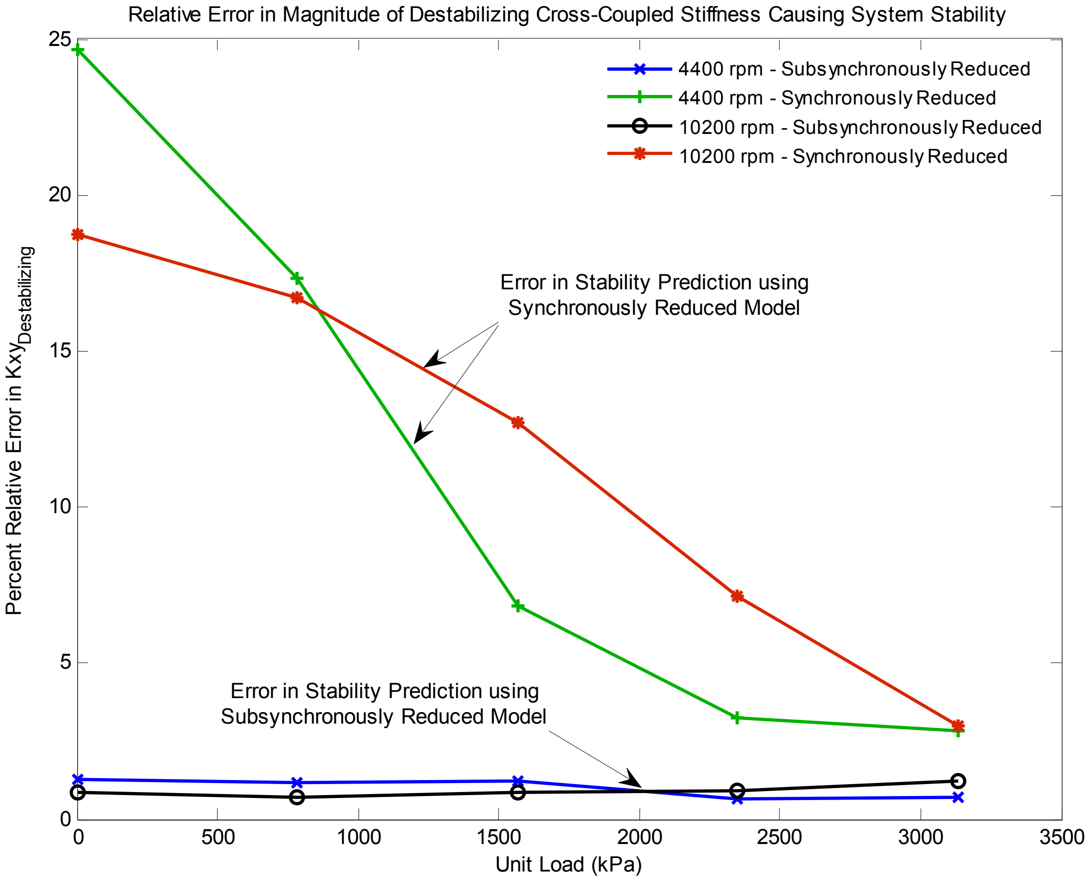

Figure 61: Percent relative error in destabilizing cross-coupled stiffness required to cause the system in Figure 60 to become unstable when employing synchronous and subsynchronous reductions at 4400 rpm and 10200 rpm at various unit loads

While this example does not cover all possible scenarios, it supports the use of asynchronously reduced coefficients for stability calculations, and refutes the notion that synchronously reduced bearing coefficients should be used for stability calculation. The reason that the pad modes can be reduced from the model at the frequency of the unstable mode is that the pad's vibration modes are either overdamped, or have a significantly higher damped natural frequency than the unstable mode. The vibration modes and damping ratios of the loaded pad at 10200 rpm (170 Hz) at 783 kPa unit load are shown in Table 12. The eigenvalues of the loaded pad were calculated with the journal and bearing fixed.

Table 12: Vibration modes of the loaded pad at 10200 rpm (170 Hz) and 783 kPa unit load

Damped Natural Frequency, ω_d (Hz)	Damping Ratio, ζ
0	∞
4565.86	0.027
2130.38	0.002
241.94	2.024

The obvious question is: Why is stability overestimated with a synchronously reduced model? Figure 62 shows the synchronously reduced direct stiffness and damping coefficients relative to their subsynchronously reduced counterpart. Synchronously reduced stiffness is moderately underestimated at 4400 rpm, and less so at 10200, while synchronously reduced damping is moderately overestimated at 4400 rpm and 10200 rpm. Both of these effects will tend to increase the effective damping of the synchronously reduced model, which will cause the synchronously reduced model to be more stable.

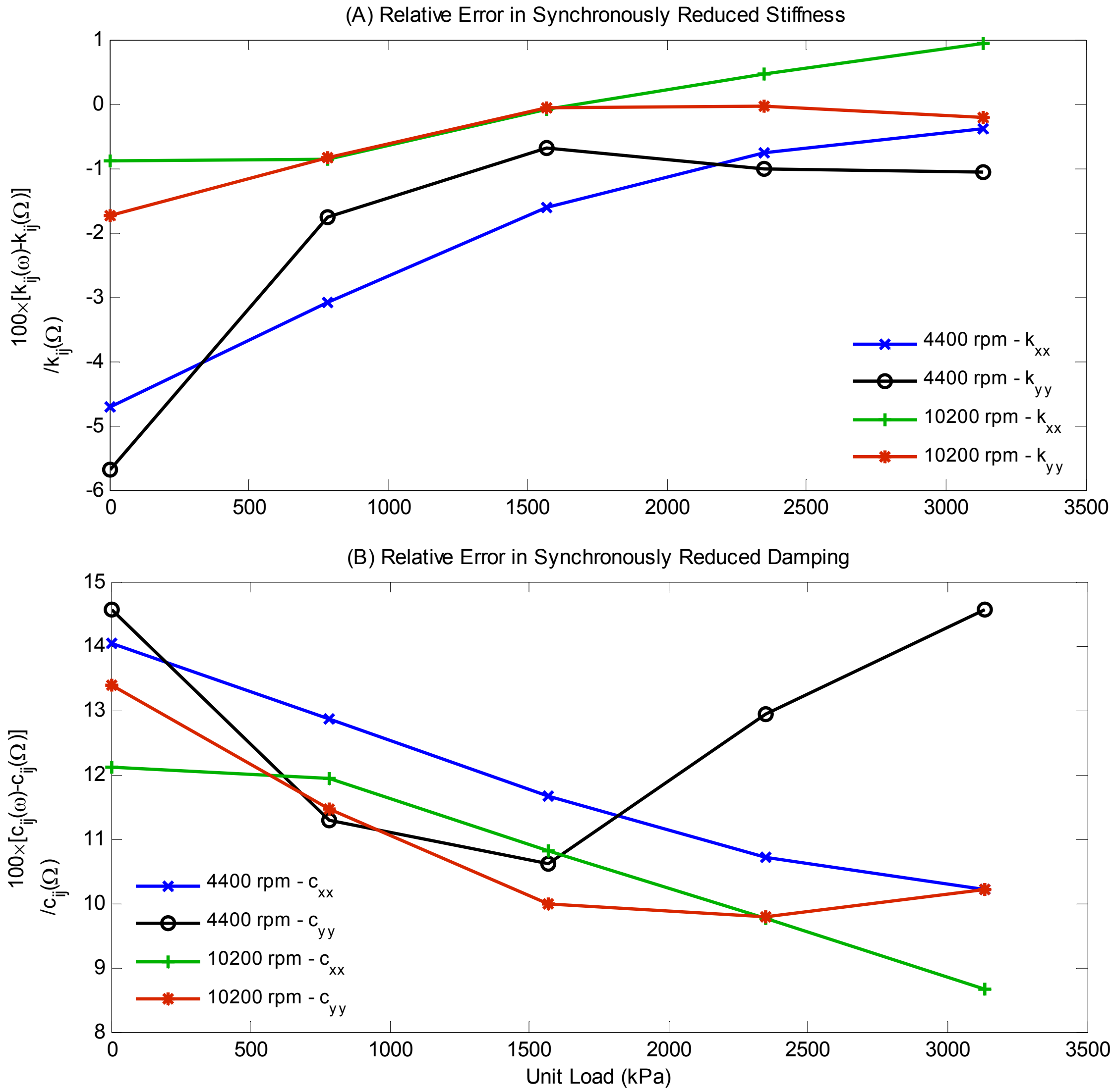

Figure 62: Relative error in synchronously reduced principal stiffness and damping coefficients relative to subsynchronously reduced stiffness and damping coefficients

While it may be possible to account for changes in stiffness with a frequency independent KCM model, damping would have to be constant. Since damping is not predicted to be constant using the developed code, a frequency dependent KCM model would be required for the bearing tested. This frequency dependent damping was measured as well, as shown in Figure 63 at low speed and high load and Figure 64 at high speed and high load. Both the measured and predicted damping coefficients have similar frequency characteristics, but the predicted damping tends to change more with frequency than the measured data.

Though the pads in this bearing have pad and pivot flexibility, Figure 63 shows the direct damping at 4400 rpm to increase from 0-150 Hz, at which point the damping begins to falloff. This high frequency falloff will not be predicted using a rigid pad/pivot model, but the increase in damping with frequency would still exist. Figure 64 shows an increase in measured and predicted damping with excitation frequency at 10200 rpm similar to the low speed case; however, this increase in damping with excitation frequency was only measured in the loaded direction, and the falloff frequency was predicted to be much higher.

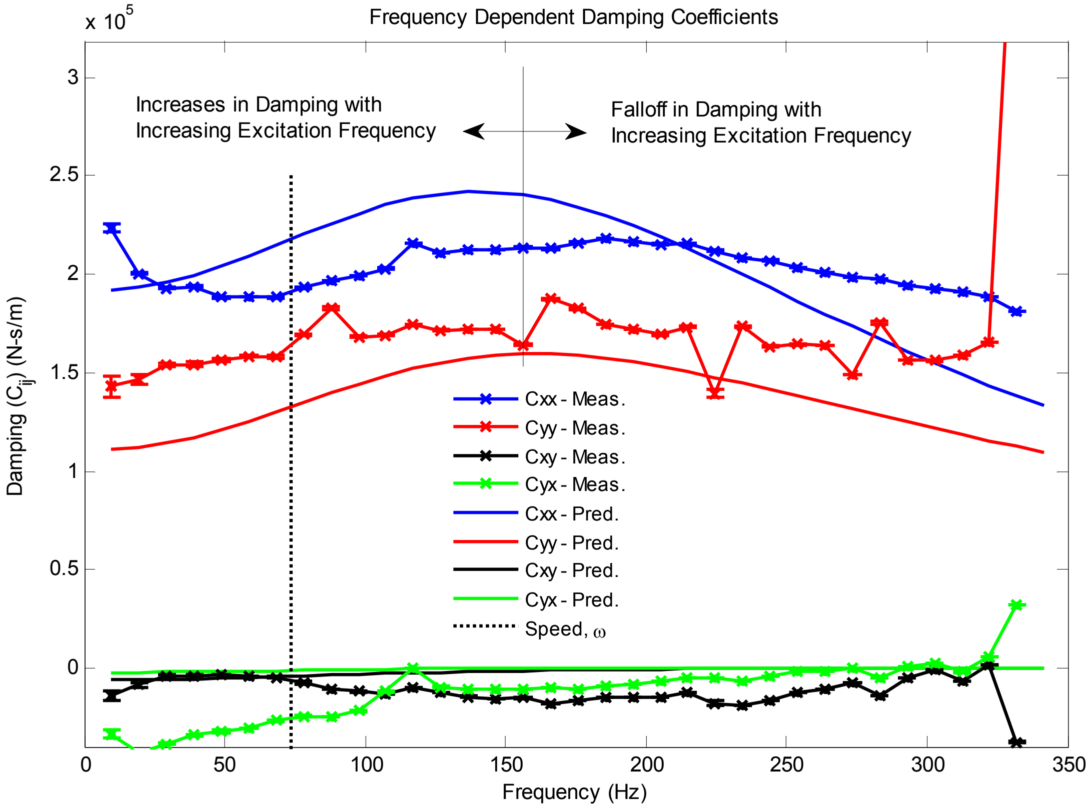

Figure 63: Frequency dependent damping coefficients at 4400 rpm and 3132 kPa unit load

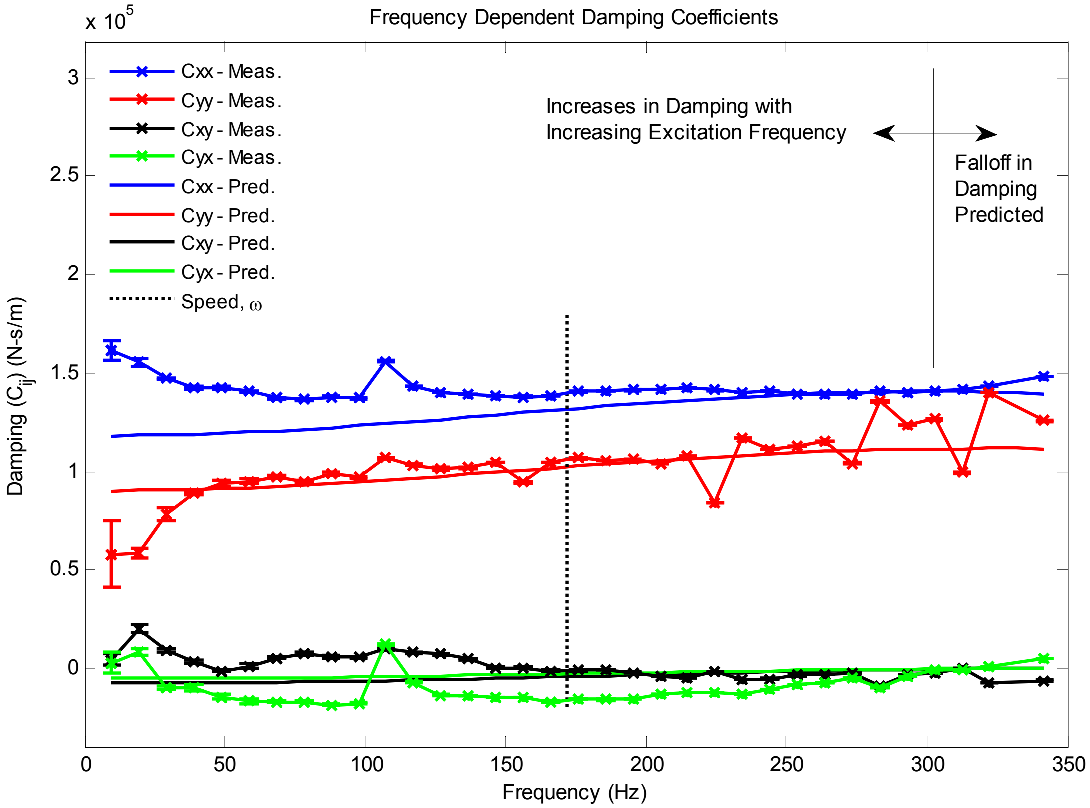

Figure 64: Frequency dependent damping coefficients at 10200 rpm, 3132 kPa unit load

This increase in damping with excitation frequency was predicted for most cases; however, it was only observed when the bearing was heavily loaded as shown in Figure 65, which shows measured and predicted damping with excitation frequency at 10200 rpm when the bearing is lightly loaded.

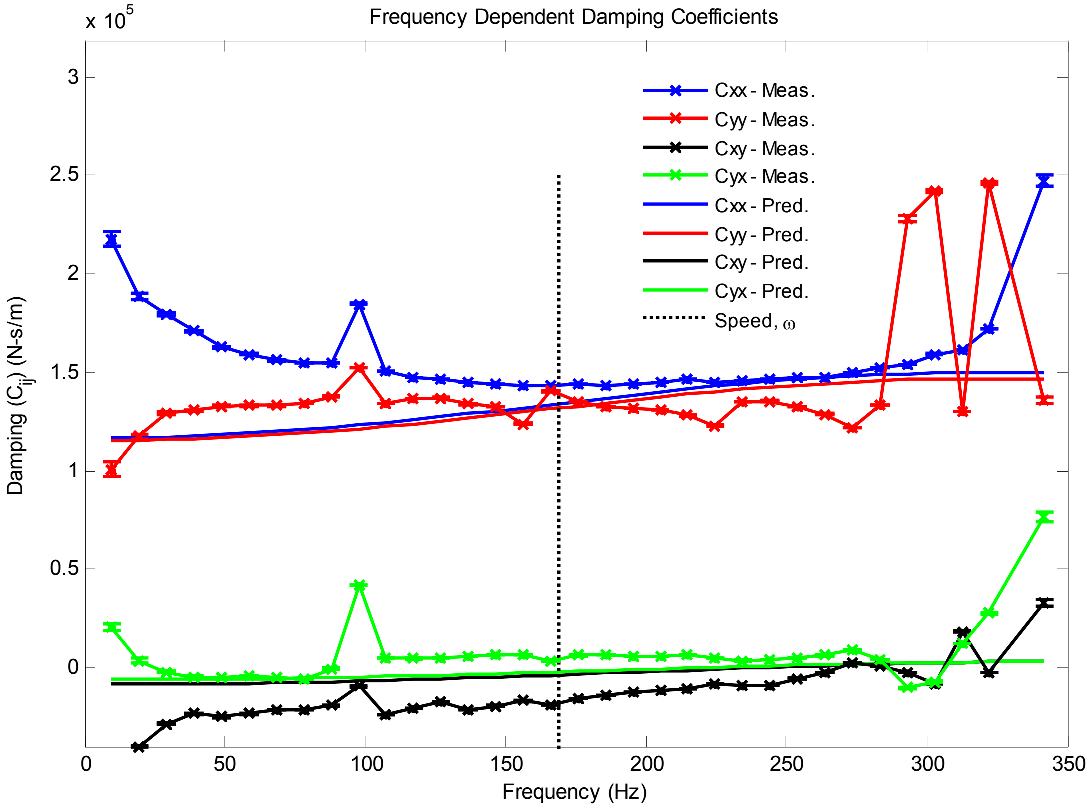

Figure 65: Frequency dependent damping coefficients at 10200 rpm, 783 kPa unit load

This discussion leads to additional questions. How well does the full bearing model predict the stability of the system shown in Figure 60, and would measured bearing coefficients at the synchronous or subsynchronous frequency yield a more conservative estimate of system stability? Figure 66 shows the magnitude of destabilizing cross-coupled stiffness needed to cause the system to become unstable using subsynchronously measured bearing impedances, synchronously measured bearing impedances, and predictions from a full bearing model. Note that the subsynchronously measured coefficients are the most conservative, followed by the synchronously measured coefficients, and then the full bearing prediction. This observation contrasts greatly with the results shown in Figure 61, which showed that using synchronously reduced predicted stiffness and damping coefficients were more conservative in estimating stability than the subsynchronously reduced coefficients.

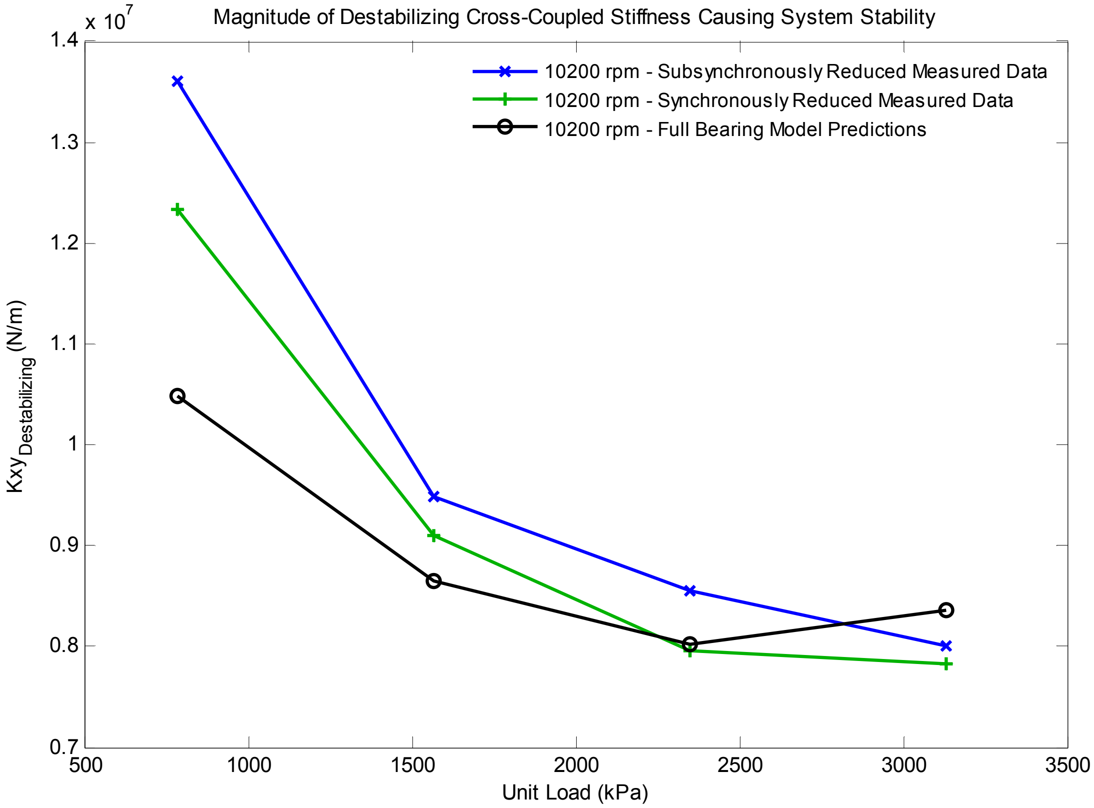

Figure 66: Magnitude of destabilizing cross-coupled stiffness required to cause the system in Figure 60 to become unstable using subsynchronously and synchronously measured coefficients and predictions using a full bearing model

CHAPTER VI

SUMMARY AND CONCLUSIONS

A new bearing perturbation model is proposed allowing for journal and bearing motions, as well as pad rotation, pad compliance, and radial and circumferential pivot flexibility. Perturbations of pad radial and tilting degrees of freedom follows from the analysis initially provided by Lund [2] in 1964 and Lund and Pederson [4] in 1987, pad clearance by Nilsson [3] in 1978, and transverse pad motion by Jeng [1] in 1995; however, unlike previous perturbations, the present analysis includes perturbation of all four variables and allows for an arbitrary pad center of gravity. The affect of including an arbitrary pad center of gravity is minimal for the bearing tested, but could prove to be important for larger tilting pad bearings, where pad inertias are significantly larger.

This perturbation model was implemented in a Reynolds-based TPJB finite-difference code to produce real and imaginary complex dynamic stiffness coefficients (impedances) by reducing the pad degrees of freedom from the model. During the reduction procedure, relations for pad motion as a function of rotor motion are determined, which results in frequency-dependent rotor-pad and pad-bearing transfer functions. Though many researchers have used the predicted pad motion (pad-rotor transfer functions) to obtain reduced bearing coefficients, this work explores the possibility of utilizing these transfer functions to obtain a more comprehensive outlook on the motion of pads in a TPJB. Specifically, this notion was exploited by comparing the amplitude and phase of these predicted rotor-pad transfer functions to experimentally measured rotor-pad transfer functions over a range of speeds and loads.

Though previous measurements of pad motion exist, they typically consist of pad tilt measurements using only one proximity probe. At most, these measurements have yielded information on pad flutter. The current work extends greatly on the previous capability of pad motion measurements. The motion of the loaded pad of a five pad tilting-pad journal bearing was measured using five proximity probes, while strain gages were used to measure changes in the radius of the pad. These measurements define six independent pad degrees of freedom: radial and circumferential pad motion, tilt, yaw, pitch, and pad clearance. These measurements were then used to determine rotor-pad transfer functions, which define the amplitude and phase of pad motions resulting from radial and transverse rotor motions.

In this work, clearance measurements were taken at a variety of temperature conditions by precessing the bearing about the non-rotating shaft with a circular force. This approach to measure bearing clearance is specific to this work, and yields a more accurate means of determining the bearing clearance at each pad, in comparison with a bump test that requires some assumptions to be made on the uniformity of bearing clearance. These clearance measurements show that hot bearing clearances can be as much as 30% smaller than the bearing clearance at room temperature (installed bearing clearance).

The relationship between bearing clearance and operating temperature was investigated, and showed that bearing clearances are inversely proportional to the average of pad surface temperatures at the pivot location. This correlation was later used to determine a thermal length for the bearing, which relates the temperature-clearance relation to the thermal expansion coefficient of the material in the bearing/housing. The current work shows that approximating the reduction in clearance by calculating the increase in pad thickness at elevated temperatures accounts for only 50% of the measured reduction in clearance, which would result in significantly lower predicted stiffness and damping coefficients than would be obtained by using the measured bearing clearances given here.

From the measured pad motion, static pad radial displacement, tilt angle, and pad clearance were presented. These pad degrees of freedom have not previously been measured. Static measurements show that pivot compliance results in radial pad motions as large as 36 μm (1.41 mils), while pad compliance results in pad clearances 60% larger than the installed pad clearance at large unit loads. Static eccentricity measurements show that the journal's locus exceeds the bearing clearance by almost 12 μm (0.5 mils) when heavily loaded. This outcome is explained by the pivot-contact flexibility, and confirms the necessity of utilizing a compliant pivot in the bearing model.

Excellent agreement is found between the amplitude of the measured and predicted radial pad transfer functions, while tilt is moderately underpredicted. Note that for pads on the test bearing, not thought to have “soft pivots,” radial journal motion at high loads produced radial pad motion having 60% of the amplitude of radial shaft motion. The magnitude of the loaded pad’s radial transfer function increases with load and excitation frequency. These measurements show that predicting TPJB characteristics without accounting for pad and pivot deflection will not accurately reflect the behavior of the pad in the bearing, regardless of the loading applied to the pivot.

Transverse pad pivot motion is predicted and observed; however, this motion appears to be lightly damped, which suggests that it is caused by transverse compliance of the pivot, not slipping. The author does not assert that the inclusion of a circumferential pad degree of freedom has a substantial impact on predicted coefficients for the bearing tested, but it may be more influential for a flexure-pivot TPJB. Relative to the bearing tested, this type of pivot would likely see larger transverse pivot forces resulting from increased angular pivot stiffness, while the effect of these forces would likely produce larger motions due to decreased transverse pivot stiffness.

Predicted direct stiffness and damping for unit loads from 0-3200 kPa (0-450 psi) fit through 1.5× running speed are within 18% of measurements at 4400 rpm, while predictions at 10200 rpm are within 10% of measurements. This is a significant improvement on the accuracy of predictions cited in literature.

Why are damping coefficients over-predicted for the majority of test data? There may be a number of contributing factors. First and foremost may be that most comparisons between measured and predicted bearing characteristics do not account for the reduction in bearing clearance at operating conditions, shown here to be 30% smaller than the cold bearing clearance. This oversight can lead to a decent prediction of stiffness and static eccentricity for models without support flexibility, which may lead to the assumption that pad and pivot compliance are not needed in the model, while damping is consistently overpredicted.

Comparisons between predictions from the developed bearing model without pad, pivot, and pad and pivot flexibility show that predicted direct stiffness and damping coefficients for a model having a rigid pad and pivot are overestimated, respectively, by 202% and 811% at low speeds and large loads, by 176% and 513% at high speeds and high loads, and by 51% and 182% at high speeds and light loads. While the reader may question the degree to which these predictions are overestimated in regard to previous comparisons, these predictions are based on measured operating bearing clearances, which are 20-30% smaller than the cold bearing clearances that previous comparisons were likely based on.

A realistic rotor-bearing model was developed to reinvestigate the assertions of previous researchers concerning the use of reduced versus full bearing models in stability calculations. In this discussion, reduced implies that the pad degrees of freedom have been eliminated from the model using a harmonic reduction, which reduces the bearing reaction force to a 2×2 stiffness and damping matrix, and full implies that the pad's degrees of freedom are included explicitly in the system model.

Though the author does not wish to discredit previous conclusions by researchers [4-7, 10, 11, 14, 15] that employing reduced bearing coefficients in stability calculations is erroneous, the author states the following on the subject. It does not matter what form of bearing model (full versus reduced) is used to predict system stability if the perturbation model is inaccurate. If one has an accurate perturbation model, and can accurately predict stiffness and damping for a TPJB, employing a full bearing model is always the most accurate means of assessing stability. If one wishes to use a reduced bearing reaction force model to predict stability, bearing coefficients should be reduced at the frequency of the unstable mode (subsynchronously reduced), which can be determined iteratively as shown here.

For the case investigated, the destabilizing cross-coupled stiffness coefficients required to cause system stability were predicted within 1% using stiffness and damping coefficients reduced at the unstable eigenvalue relative to the magnitude of destabilizing cross-coupled stiffness required with the full bearing model. If coefficients are reduced synchronously, however, the magnitude of destabilizing cross-coupled stiffness required to cause system instability is overestimated by as much as 24% when compared to the full-model prediction. If the frequency dependency of the bearing coefficients is well modeled by a KCM model, this method will also produce an accurate assessment of stability.

The same stability calculation was performed using measured stiffness and damping coefficients at synchronous and subsynchronous frequencies at 10200 rpm. It was found that both the synchronously measured stiffness and damping and predictions using the full bearing model were more conservative than the model using subsynchronously measured stiffness and damping. This outcome contrasts with the comparison between models using synchronously and subsynchronously reduced impedance predictions, which showed the subsynchronously reduced model to be the most conservative. This contrast results from a predicted increase in damping with increasing excitation frequency at all speeds and loads, while this increase in damping with increasing excitation frequency was only measured at the most heavily loaded conditions. Note that these observations pertain to a bearing that has an extremely compliant pad, caused by a loose-fitting hardened pivot insert on the pad installed to reduce fretting at the contact surface.

At the onset of this work, a question was posed regarding the industrial communities resistance in using a full bearing model to predict stability. Though there may be several answers to this question, the author’s position is that differences between the measured and predicted frequency dependence of TPJB stiffness and damping coefficients have led to a lack of confidence in the ability to accurately predict the dynamic characteristics of a TPJB. With this lack of confidence, it appears that researchers have become divided on the responsible course of action in performing stability calculations. The majority of experimental evidence suggests that the lack of frequency dependence in measured damping supports one course of action [16-18], while the majority of theoretical papers showing frequency dependent damping supports a different course of action [4-7,10,11, etc.]. Though some of these theoretical works suggest that a full bearing model is required to assess stability, the current work shows that a subsynchronously reduced bearing model predicted stability within 1% of the full bearing model. Hence, stability calculations employing predicted bearing coefficients should be performed with full or subsynchronously reduced models, while stability calculations performed with measured bearing coefficients should use subsynchronously measured bearing impedances or a KCM model when applicable. The real question that should be asked is the following: why is there a difference in the measured and predicted frequency dependence of TPJB dynamic coefficients?

Rotor-pad transfer functions can be useful in identifying deficiencies in the model or test setup, specifically in regard to obtaining more information from an experiment than determining bearing stiffness, damping, and mass. Future research in this area may even include a multivariable input-output parameter identification technique to directly measure the stiffness and damping of the fluid film on a single pad [47]. The transfer of measured and predicted transfer-function deviations into useful feedback could yield valuable information on current TPJB modeling deficiencies.

NOMENCLATURE

$\tilde{A}_{bi}^{j}$	FFT of absolute bearing/stator acceleration (e.g. $\bar{A}_{bi}^{j}$ is acceleration in the '*i*' direction, due to an excitation in the '*j*' direction)	[L/t^2]
$\tilde{\mathbf{A}}_{\mathbf{ij,k}}$	Matrix of fixed impedances including virtual-mass terms ($\tilde{\mathbf{A}}_{\mathbf{ij,k}} = \mathbf{M}_{\mathbf{ij,k}}\tilde{\mathbf{s}}^2 + \mathbf{C}_{\mathbf{ij,k}}\tilde{\mathbf{s}} + \mathbf{K}_{\mathbf{ij,k}}$)	[F/L]
$\mathbf{C_k}$	Damping matrix for the k^{th} pad	[F.t/L]
$E_{p,k}$	Pad modulus of elasticity	
$\mathbf{F_{0,k}}$	Vector of forces applied to the journal, pad, and bearing.	[F]
$\tilde{F}_{ei}^{j}$	FFT of applied excitation force (e.g. $\tilde{F}_{ei}^{j}$ is force in the '*i*' direction, due to an excitation in the '*j*' direction)	[F]
$\tilde{\mathbf{H}}_{\mathbf{ij,k}}$	Matrix of reduced impedances or complex dynamic stiffnesses	[F/L]
$I_{c,k}$	Pad mass moment of inertia about $O_{c,k}$	[M.L^2]
$\tilde{\mathbf{I}}_{\mathbf{ij,k}}$	Matrix of fixed impedances including stiffness and damping terms only ($\tilde{\mathbf{I}}_{\mathbf{ij,k}} := \mathbf{C}_{\mathbf{ij,k}}\tilde{\mathbf{s}} + \mathbf{K}_{\mathbf{ij,k}}$)	[F/L]
$\mathbf{K_k}$	Stiffness matrix for the k^{th} pad	[F/L]
$L_{p,k}$	Axial length of the k^{th} pad	[L]
M_{11}-M_{15}	Relative stator-pad displacements measured with proximity probes 11-15	[L]
$M_{c_p,n}$	Bending moment at the pad's neutral axis as a function of the circumferential location on the pad	[F.L]
$M_{cz,k}$	Pivot reaction moment	[F.L]
$\bar{M}_{ic_p,k}$	Average of the applied bending moment due to pressure p_i about the pad's neutral axis	[F.L]
$M_{ic_p,k}$	Average of the applied bending moment due to pressure p_i at the surface of the pad on either side of the pad's pivot	[F.L]
$\mathbf{M_k}$	Mass matrix for the k^{th} pad	[M]
O_c	Pad contact location	
O_j, O_b, O_p,	Center of the journal, bearing, and pad surface arc	
O_o	Origin of the inertial coordinate system	

$\mathbf{Q_k}$	Direction-cosine matrix relating vectors in inertial coordinates to a vector in the k^{th} pad's reference state coordinates	
$\mathbf{U_{1,k}}$	Vector of journal, bearing, and k^{th} pad displacements in the k^{th} pad's reference state coordinates	[L, -]
$\tilde{U}_i^j$	FFT of relative rotor-stator motion (e.g. $\tilde{U}_i^j$ is relative rotor-stator motion in the '*i*' direction, due to an excitation in the '*j*' direction)	[L]
$\mathbf{U_{j1,k}}$, $\mathbf{U_{p1,k}}$, $\mathbf{U_{b1,k}}$	Journal, pad, and bearing displacement vectors in the k^{th} pad's reference state coordinates	[L, -]
X-Y- Z	Inertial coordinate axes	
a_{bx}, a_{by}	Absolute bearing acceleration component in the x,y direction	[L/t^2]
$b_{\eta go,k}$, $b_{\xi go,k}$	Distance from $O_{co,k}$ to the k^{th} pad's CG in the η_k, ξ_k direction at the reference state	[L]
$c_{cj,k}$	k^{th} pad's pivot damping in the j^{th} direction	[F.t/L]
c_{ij}	Damping coefficient (e.g. reaction force in the '*i*' direction due to velocity in the '*j*' direction)	[F.t/L]
c_b	Bearing clearance	[L]
c_p	Pad clearance ($c_p = c_{po} + c_{p0} + c_{p1} = c_{po} + \delta_{c_p}$)	[L]
c_{po}	Installed pad clearance	[L]
c_{p0}	Change in pad clearance due to zeroth order pressure field	[L]
c_{p1}	Change in pad clearance due to perturbed pressure field	[L]
$d_{11,12}$	Axial distance between probes 11 and 12	[L]
$d_{14,15}$	Axial distance between probes 14 and 15	[L]
$d_{\varepsilon 12}$	Radial distance between strain gage 1 and 2	[L]
$\boldsymbol{e}_{c,k}$	Displacement of the k^{th} pad's pivot at the contact location relative to the bearing	[L]
$\boldsymbol{e}_j$, $\boldsymbol{e}_b$, ...	Displacement of journal, bearing, etc.	[L]
$\boldsymbol{e}_{pj,k}$	Relative pad-journal displacement (vector from O_p to O_j $\boldsymbol{e}_{pj,k} := \eta_k \boldsymbol{i}_k + \xi_k \boldsymbol{j}_k$)	[L]
f_{bx}, f_{by}	Bearing reaction force component in the x,y direction	[F]
$f_{c\eta,k}$	Transverse pivot reaction force	
$f_{c\xi,k}$	Radial pivot reaction force	
f_{ex}, f_{ey}	Bearing excitation force component in the x,y direction	[F]
$f_{i\eta,k}$, $f_{i\xi,k}$	Reaction forces in the η_k, ξ_k directions due to pressure p_i	[F]

h_k	Fluid film height of the k^{th} pad	[L]
$\boldsymbol{i_0}, \boldsymbol{j_0}$	Unit vectors in the X-Y directions	
$\boldsymbol{i_k}, \boldsymbol{j_k}$	Unit vectors in the k^{th} pad's reference η_k-ξ_k directions	
$\tilde{j}$	Imaginary unit ($\sqrt{-1}$)	
$k_{cj,k}$	k^{th} pad's pivot stiffness in the j^{th} direction	[F/L]
k_{ij}	Stiffness coefficient (e.g. reaction force in the 'i' direction due to displacement in the 'j' direction)	[F/L]
$k_{scp.k}$	k^{th} pad's structural bending stiffness	[F]
$k_{\varepsilon 12}$	Conversion factor from measured voltage to relative strain ε_{12}	[1/V]
$l_{T,char}$	Characteristic thermal length of the system with respect to average of pad surface temperatures at the pivot location	[L]
$m_{cp,k}$	Modal mass of the pads first bending mode	[M]
m_{ij}	Mass coefficient (e.g. reaction force in the 'i' direction due to acceleration in the 'j' direction)	[M]
m_{bx}, m_{by}	Modal mass of the test rig's bearing/stator in the X, Y dir.	[M]
m_j, m_b, $m_{p,k}$	Mass of the journal, bearing, and k^{th} pad	[M]
n_p	Number of pads in bearing	
$p_{0,k}$,	Zeroth order pressure field	[F/L^2]
p_a	Ambient pressure in the bearing	[F/L^2]
p_{cav}	Fluid cavitation pressure	[F/L^2]
$p_{\eta 1,k}, p_{\xi 1,k}, \ldots$	First order pressure field due to perturbations $\eta_{1,k}$, $\xi_{1,k}, \ldots$	[F/L^2]
r_{11}	Radius of surface on back of pad measured by probe 11	[L]
$r_{cp,k.}$	Distance from k^{th} pad's pivot point to the center of the k^{th} pad's surface arc	[L]
r_{f1}, r_{f2}, $r_{\varepsilon 1}$, r_{e2}	Resistance of components ($f1$, $f2$, etc.) in the strain gage circuit	[V/I]
r_j, r_b	Radius of the journal, bearing	[L]
r_p	Pad radius ($r_p = r_{po} + r_{p0} + r_{p1} = r_{po} + \delta_{r_p}$)	[L]
r_{po}	Installed pad radius	[L]
r_{p0}	Change in pad radius due to zeroth order pressure field	[L]
r_{p1}	Change in pad radius due to perturbed pressure field	[L]
$r_{p,k.}$	Radius of pad's neutral axis ($r_{p,n} = r_p + ½\, t_p$)	[L]
r_r, r_{rh}	Radius of the pad's rocker, housing mating with the rocker.	[L]

$\tilde{s}$	System eigenvalue or root of an assumed solution ($\tilde{s} = \lambda + \tilde{j}\Omega$)	
t_{cp}	Thickness of the pad at the contact location $t_{cp} = r_c - r_b$	[L]
t_p	Thickness of the pad	[L]
v_{in}, v_{out}	Voltage in/out from the strain gage Wheatstone bridge	[V]
$\Gamma_{i_k}^{\eta_b}, \Gamma_{i_k}^{\xi_b}$	Transfer function relating the i^{th} pad motion to η_k, ξ_k bearing motions	[L/L, 1/L]
$\Gamma_{i_k}^{\eta_j}, \Gamma_{i_k}^{\xi_j}$	Transfer function relating the i^{th} pad motion to η_k, ξ_k journal motions	[L/L, 1/L]
$\hat{\Gamma}_{\phi 1}^{\eta}, \hat{\Gamma}_{\phi 1}^{\xi}$	Pad tilt transfer function normalized by the distance from the pivot to the leading edge of the pad	
Θ_k	Ratio of outer to inner pad radii $\Theta = \left(R_p + t_p\right) / R_p$	
Ω	Reduction frequency or applied excitation frequency	[1/t]
∂	Partial differential operator	
$\psi_{pj,k}$	Angle from η_k to $\boldsymbol{e}_{pj,k}$ about the positive Z axis	
α_{cb}	Thermal expansion coefficient of the shaft/pad/bearing assembly	[L/T]
α_k	Angle from the X-axis to the k^{th} pad's η_k axis $\alpha_k = \theta_{c,k} + \pi / 2$	
α_{mat}	Thermal expansion coefficient of the shaft/pad/bearing assembly	[1/T]
β	Angular distance from the k^{th} pad's pivot to a location on the pad	
$\beta_{lc,k}$, $\beta_{ct,k}$	Angular distance from the k^{th} pad's leading edge to contact location, and from contact to the trailing edge	
β_{lt}	Angular extent of the k^{th} pad	
δ	Pivot deflection	[L]
δ_{c_p}	Change in pad clearance $\delta_{c_p} = c_{p0} + c_{p1}$	[M]
δ_{r_p}	Change in pad radius $\delta_{r_p} = r_{p0} + r_{p1}$	[M]
$\delta_{\varepsilon 12}$	Distance between center of strain gage 1 and 2	[M]
ε_1, ε_2	Strain measured by gage 1, 2	
ε_{12o}, ε_{120}, ε_{121}	Relative strain between gages 1 and 2 ($\varepsilon_{12} = \varepsilon_1 - \varepsilon_2$) at the reference, equilibrium, and perturbed state	

ϕ_k	k^{th} pad's tilt angle about the positive Z-axis	
$\hat{\phi}_k$	Pad tilt normalized by multiplying ϕ_k by the distance from the pivot to the leading edge of the pad	
$\phi_{\xi c,k}$	Pad yaw (rotation from the pad reference axis Z_0 to the perturbed axis $Z_{1,k}$ about the positive ξ_k -axis)	
$\phi_{\eta c,k}$	Pad pitch (rotation from the pad reference axis Z_0 to the perturbed axis $Z_{1,k}$ about the positive η_k axis)	
$\eta_{g,k}$, $\xi_{g,k}$	Distance from $O_{co,k}$ to the k^{th} pad's CG in the η_k, ξ_k direction	[L]
$\eta_{i,}$, ξ_i	Components of vector $\boldsymbol{e_i}$ in the η_k, ξ_k direction	[L]
η_k-ξ_k	k^{th} pad's reference state radial-circumferential coordinate axis	
λ	System damping exponent	
μ	Fluid viscosity	[F.t/M^2]
$\theta_{c,k}$	Angle from the X-axis to the k^{th} pad's contact location	
ω	Journal rotational speed	[1/t]
ψ_k	Angle from η_k to a circumferential location on the pad,	
$\psi_{l,k}$, $\psi_{t,k}$	Angle from η_k to the leading and trailing edges of the pad	

Subscript

0	b_0 refers to the zeroth order/guessed component of b
1	b_1 refers to the first order/perturbed component of b
b	Bearing
c	Contact
ij	Permute i,j with rotor coordinates ($i = x, y,\ j= x, y$)
ij,k	Permute i,j with pad coordinates ($i = \eta_k, \xi_k,\ j= \eta_k, \xi_k$)
j	Journal
k	b_k refers to the k^{th} pad
o	b_o refers to the reference state component of b

Superscript

x, y	Measured during x, y excitation of the stator
$\eta_{b,}$, ξ_b	Corresponds to motions of the bearing in the η_k, ξ_k direction
$\eta_{j,}$, ξ_j	Corresponds to motions of the journal in the η_k, ξ_k direction

Formatting

Bold	**B** is a matrix
bold-italic	***b*** is a vector
italic	b is real-valued
"tilde"	$\tilde{b}$ is complex

Acronyms

CG	Center of Gravity
DFT	Discrete-Fourier Transform
DOF	Degree of Freedom
EDM	Electron Discharge Machining
EOM	Equation of Motion
FE	Finite Element
FEA	Finite Element Analysis
FP	Flexure-Pivot
FPTPJB	Flexure-Pivot Tilting Pad Journal Bearing
KC	Stiffness and Damping Model
KCM	Stiffness, Damping, and Mass Model
LOP	Load On Pad
TAMU	Texas A&M University
TPJB	Tilting-Pad Journal Bearing

REFERENCES

[1] Jeng, W., 1995, “Bearing Dynamic Coefficients of Flexible-Pad Journal Bearings,” Trib. Trans., **38**(2), pp.253-260.

[2] Lund, J.W., 1964, “Spring and Damping Coefficients for the Tilting-Pad Journal Bearing,” ASLE Trans., **7**, pp. 342-352

[3] Nilsson, L., 1978, “The Influence of Bearing Flexibility on the Dynamic Performance of Radial Oil Film Bearings,” *Proc. 5th Leeds-Lyon Symposium on Tribology*, **5**, pp.311-319, Lyon, France, Mechanical Engineering Publications, London (September 1978).

[4] Lund, J.W., and Pedersen, L.B., 1987, "The Influence of Pad Flexibility on the Dynamic Coefficients of a Tilting Pad Journal Bearing," ASME J. Trib., **109**(1), pp. 65-70.

[5] Parsell, J. K., Allaire, P. E. & Barrett, L. E., 1982, “Frequency Effects in Tilting-Pad Journal Bearing Dynamic Coefficients,” ASLE Trans., **26**(2), pp. 222-227.

[6] Wilson, B. W., and Barrett, L. E., 1985, "The Effect of Eigenvalue-Dependent Tilt Pad Bearing Characteristics on the Stability of Rotor Bearing Systems," Report No. UVA/643092/MAE85/321, University of Virginia

[7] Barrett, L. E., Allaire, P. E., and Wilson, B. W., 1988, "The Eigenvalue Dependence of Reduced Tilting Pad Bearing Stiffness and Damping Coefficients," Trib. Trans., **31**(4), pp. 411-419.

[8] Kirk, R. G., and Reedy, S. W., 1988, "Evaluation of Pivot Stiffness for Typical Tilting-Pad Journal Bearing Designs," J. Vib. Acoust. Stress Reliab. Des., **110**(2), pp. 165-171.

[9] Brugier, D., and Pascal, M., 1989, “Influence of Elastic Deformations of Turbo-Generator Tilting Pad Bearings on the Static Behavior and on the Dynamic Coefficients in Different Designs,” ASME J. Trib., **111**, pp. 364-371.

[10] Earles, L., Palazzolo, A., and Armentrout, R., 1990, “A Finite Element Approach to Pad Flexibility Effects in Tilt Pad Journal Bearings: Part I - Single Pad Analysis,” ASME J. Trib., **112**, pp. 169-177.

[11] Earles, L., Palazzolo, A., and Armentrout, R., 1990, “A Finite Element Approach to Pad Flexibility Effects in Tilt Pad Journal Bearings: Part II - Assembled Bearing and System Analysis,” ASME J. Trib., **112**, pp. 178-182.

[12] Kim, J., Palazzolo, A., and Gadangi, R., 1995, “Dynamic Characteristics of TEHD Tilt Pad Journal Bearing Simulation Including Multiple Mode Pad Flexibility Model,” ASME J. Vib. Acoust., **117**(1), pp. 123-135.

[13] Brockwell, K., Kleinbub, D., and Dmochowski, W., 1990, “Measurement and Calculation of the Dynamic Operating Characteristics of the Five Shoe, Tilting Pad Journal Bearing,” Trib. Trans, **33**(4), pp. 481-492.

[14] Qiao, G., Wang, L., and Zheng, T., 2007. “Linear Stability Analysis of a Tilting-pad Journal Bearing System”. ASME J. Trib., **129**(2), pp. 348–353.

[15] Dimond, T.W., Younan, A. A., Allaire, P.E., and Nicholas, J.C., 2010, Modal Frequency Response of a Four-Pad Tilting Pad Bearing With Spherical Pivots, Finite Pivot Stiffness, and Different Pad Preloads,” *Proc. of ASME Turbo Expo 2010*, Paper GT2010-23609, June 14-18, Glasgow, UK.

[16] Kocur, J., Nicholas, J., and Lee, C., 2007, “Surveying Tilting Pad Journal Bearing and Gas Labyrinth Seal Coefficients and Their Effect on Rotor Stability,” *Proc. of the 36th Turbomachinery Symposium*, Houston, USA.

[17] Childs, D., 2010, “Tilting-Pad Bearings: Measured Frequency Characteristics of their Rotordynamic Coefficients,” *Proc. of the 8th IFToMM International Conference on Rotordynamics*, September 12-15, Seoul, Korea.

[18] Childs, D., Delgado, A., and Vannini, G., 2011, “Tilting-Pad Bearings: Measured Frequency Characteristics of their Rotordynamic Coefficients,” *Proc. of the 40th Turbomachinery Symposium*, September 12-15, Houston, USA.

[19] Glienicke, J., 1966, “Experimental Investigation of Stiffness and Damping Coefficients of Turbine Bearings and Their Application to Instability Predictions,” *Proc. of the International Mech. E.*, **181** (3B), pp. 116-129.

[20] Ha, H., and Yang, S., 1999, “Excitation Frequency Effects on the Stiffness and Damping Coefficients of a Five-Pad Tilting Pad Journal Bearing,” ASME J. Trib., **121**, pp. 517-522.

[21] Rodriguez, L., and Childs, D., 2006, “Frequency Dependency of Measured and Predicted Rotordynamic Coefficients for Load-on-Pad Flexible-Pivot Tilting-Pad Bearing,” ASME J. Trib., **128** (2), pp. 388-395.

[22] Carter, C., and Childs, D., 2008 “Measurements versus Predictions for the Rotordynamic Characteristics of a 5-Pad, Rocker-Pivot, Tilting-Pad Bearing in Load Between Pad Configuration,” *Proc. of ASME Turbo Expo 2008*, Paper GT2008-50069, June 9-13, Berlin, Germany.

[23] Harris, J., and Childs, D., 2008, "Static Performance Characteristics and Rotordynamic Coefficients for a Four-Pad Ball-In-Socket Tiling Pad Journal Bearing," *Proc. of ASME Turbo Expo 2008*, Paper GT2008-50063, June 9-13, Berlin, Germany.

[24] Delgado, A., Ertas, B., Drexel M., Naldi, L., and Vannini, G., 2010, “Identification and Prediction of Force Coefficients in a Five-Pad and Four-Pad Tilting Pad Bearing for Load-on-Pad and Load-Between-Pad Configurations,” *Proc. of ASME Turbo Expo 2010*, Paper GT2010-23802, June 14-18, Glasgow, UK.

[25] Kulhanek, C., 2010, “Dynamic and Static Characteristics of a Rocker-Pivot, Tilting-Pad Bearing with 50% and 60% Offsets,” M.S. Thesis, Mechanical Engineering, Texas A&M University, College Station, TX.

[26] Kulhanek, C., and Childs, D., 2011, “Measured Static and Rotordynamic Coefficient Results for a Rocker-Pivot, Tilting-Pad Bearing with 50 and 60% Offsets,” *Proc. of ASME Turbo Expo 2011*, Paper GT2011-45209, June 6-10, 2011, Vancouver, Canada.

[27] Rouvas, C., and Childs, D., 1993, “A Parameter Identification Method for the Rotordynamic Coefficients of a High Reynolds Number Hydrostatic Bearing,” ASME J. of Vibration and Acoustics, **115**, pp. 264-270.

[28] Reinhardt, E., and Lund, J., 1975, “The Influence of Fluid Inertia on the Dynamic Properties of Journal Bearings,” ASME J. Lub. Tech., ASME Trans., **97F**(2), pp. 159–167.

[29] Dmochowski, W., 2006, “Dynamic Properties of Tilting-Pad Journal Bearings: Experimental and Theoretical Investigation of Frequency Effects Due to Pivot Flexibility,” *Proc. of ASME Turbo Expo 2006*, Paper GT2006-90280, May 8-11, Barcelona, Spain.

[30] Pettinato, B., and De Choudhury, p., 1999, “Test Results of Key and Spherical Pivot Five-Shoe Tilt Pad Journal Bearings Part I: Performance Measurements,” Trib. Trans., **42**(3), pp. 541-547.

[31] Pettinato, B., and De Choudhury, p., 1999, “Test Results of Key and Spherical Pivot Five-Shoe Tilt Pad Journal Bearings Part II: Dynamic Measurements,” Trib. Trans., **42**(3), pp. 675-680.

[32] Al-Ghasem, A., and Childs, D., 2006, “Rotordynamic Coefficients Measurements Versus Predictions for a High-Speed Flexure-Pivot Tilting-Pad Bearing (Load-Between-Pad Configuration),” ASME J. Eng. Gas Turbines Power, **128**(4), pp. 896-906.

[33] Rodriguez, L., 2006, “Frequency Dependency of Measured and Predicted Rotordynamic Coefficients for a Load-on-Pad Flexible-Pivot Tilting-Pad Bearing,” ASME J. Trib., **128**(2), pp. 388-395.

[34] Hensley, J., 2006, “Rotordynamic Coefficients for a Load-Between-Pad Flexible-Pivot Tilting Pad Bearing at High Loads,” M.S. Thesis, Mechanical Engineering, Texas A&M University, College Station, TX.

[35] Al Jughaiman, B., 2006, “Static and Dynamic Characteristics for a Two-Axial-Groove Bearing and a Pressure-Dam Bearing,” M.S. Thesis, Mechanical Engineering, Texas A&M University, College Station, TX.

[36] Adams, M., and Payandeh, S., 1983, “Self-Excited Vibration of Statically Unloaded Pads in Tilting-Pad Journal Bearings,” ASME J. Lub. Tech., **105**, pp. 377-384.

[37] Sabnavis, G., 2005, “Test Results for Shaft Tracking Behavior of Pads in a Spherical Pivot Type Tilting Pad Journal Bearing,” M.S. Thesis, Mechanical Engineering, Virginia Polytechnic Institute and State University, Blacksburg, VA.

[38] Wilkes, J., 2011, “Measured and Predicted Transfer Functions between Rotor Motion and Pad Motion for a Rocker-Back Tilting-Pad Bearing in LOP Configuration,” *Proc. of ASME Turbo Expo 2011*, Paper GT2011-46510, June 6-10, 2011, Vancouver, Canada.

[39] Warner, R. and Soler, A., 1975 "Stability of Rotor-Bearing Systems with Generalized Support Flexibility and Damping and Aerodynamic Cross-Coupling," ASME J. Lub. Tech., pp. 461-471, July.

[40] Wygant, K., Barrett, L., and Flack, R., 2001, “The Influence of Negative Preload and Non-Synchronous Excitations on the Performance of Tilting-Pad Journal Bearings,” Ph.D. Dissertation, Mechanical Engineering, University of Virginia, Charlottesville, VA.

[41] Deeg, E., 1992, “New Algorithms for Calculating Hertzian Stresses, Deformations, and Contact Zone Parameters,” AMP J. Tech., **2**, pp. 14-24.

[42] Branagan, L., and Barrett, L., 1988, “Thermal Analysis of Fixed and Tilting Pad Journal Bearings Including Cross-Film Viscosity Variations and Deformations,” ROMAC Report No. 276, UVa Report No. UVA/643092/MAE88/376.

[43] Deutschman, A., Michels, W., and Wilson, C., 1975, *Machine Design*, Macmillan Publishing Co., Inc., New York, pp. 862-863.

[44] Lund, J. W., and Thomson, K. K., 1978, “A Calculation Method and Data for the Dynamic Coefficients of Oil-lubricated Journal Bearings,” Topics in Fluid Journal Bearing and Rotor Bearing System, ASME, New York, pp. 1-28.

[45] Szeri, A., 1980, *Tribology: Friction, Lubrication, and Wear*, McGraw-Hill Publishing, New York, NY.

[46] Varela, A., and Santos, I., 2011, “Stability Analysis of an Industrial Gas Compressor Supported by Tilting-Pad Bearings under Different Lubrication Regimes,” *Proc. ASME Turbo Expo 2011*, Paper GT2011-46450, June 6-10, 2011, Vancouver, Canada.

[47] Dimond, T., Younan, A., and Allaire, P., 2011, “A Review of Tilting Pad Bearing Theory,” Intl. J. Rot. Mach., **2011**, pp. 1-23.

APPENDIX A

PERTURBED PAD EQUATIONS OF MOTION

The partitions shown in $\mathbf{U_{1,k}}$ and $\mathbf{F_{0,k}}$, denote the portion of each matrix assigned to a given submatrix . Note that partitions not shown in $\mathbf{M_k}$, $\mathbf{C_k}$, and $\mathbf{K_k}$ would occur after the second and sixth row and column of each matrix, and that the subscript *k* is neglected when referring to $\mathbf{M_{jj}}$ and $\mathbf{M_{bb}}$, which do not depend on the pad in question.

$$\mathbf{U_{1,k}} = \left\{ \begin{array}{c} \eta_{j1,k} \\ \xi_{j1,k} \\ \hline \phi_{1,k} \\ \eta_{c1,k} \\ \xi_{c1,k} \\ c_{p1,k} \\ \hline \eta_{b1,k} \\ \xi_{b1,k} \end{array} \right\} = \left\{ \begin{array}{c} \mathbf{U_{j1,k}} \\ \mathbf{U_{p1,k}} \\ \mathbf{U_{b1,k}} \end{array} \right\}, \quad \mathbf{F_{0,k}} = \left\{ \begin{array}{c} f_{\eta 0,k} \\ f_{\xi 0,k} \\ \hline r_{cp,k} f_{\eta 0,k} - f_{cz0,k} \\ -f_{\eta 0,k} + f_{c\eta 0,k} \\ -f_{\xi 0,k} + f_{c\xi 0,k} \\ f_{c_p 0,k} \\ \hline -f_{c\eta 0,k} \\ -f_{c\xi 0,k} \end{array} \right\} = \left\{ \begin{array}{c} \mathbf{F_{j0,k}} \\ \mathbf{F_{p0,k}} \\ \mathbf{F_{b0,k}} \end{array} \right\},$$

$$\mathbf{M_k} = \begin{bmatrix} m_j & 0 & 0 & 0 & 0 & 0 & 0 & 0 \\ 0 & m_j & 0 & 0 & 0 & 0 & 0 & 0 \\ 0 & 0 & I_{c,k} & -b_{\xi go,k} m_{p,k} & b_{\eta go,k} m_{p,k} & 0 & -b_{\xi go,k} m_{p,k} & b_{\eta go,k} m_{p,k} \\ 0 & 0 & -b_{\xi go,k} m_{p,k} & m_{p,k} & 0 & 0 & m_{p,k} & 0 \\ 0 & 0 & b_{\eta go,k} m_{p,k} & 0 & m_{p,k} & 0 & 0 & m_{p,k} \\ 0 & 0 & 0 & 0 & 0 & m_{c_p,k} & 0 & 0 \\ 0 & 0 & 0 & 0 & 0 & 0 & m_b & 0 \\ 0 & 0 & 0 & 0 & 0 & 0 & 0 & m_b \end{bmatrix},$$

$$\mathbf{C_k} = \begin{bmatrix} c_{\eta\eta,k} & c_{\eta\xi,k} & r_{cp,k}c_{\eta\eta,k} & -c_{\eta\eta,k} & -c_{\eta\xi,k} & -c_{\eta\xi,k}-c_{\eta c_p,k} & -c_{\eta\eta,k} & -c_{\eta\xi,k} \\ c_{\xi\eta,k} & c_{\xi\xi,k} & r_{cp,k}c_{\xi\eta,k} & -c_{\xi\eta,k} & -c_{\xi\xi,k} & -c_{\xi\xi,k}-c_{\xi c_p,k} & -c_{\xi\eta,k} & -c_{\xi\xi,k} \\ r_{cp,k}c_{\eta\eta,k} & r_{cp,k}c_{\eta\xi,k} & r_{cp,k}^2c_{\eta\eta,k}+c_{cz,k} & -r_{cp,k}c_{\eta\eta,k} & -r_{cp,k}c_{\eta\xi,k} & -r_{cp,k}\left(c_{\eta\xi,k}+c_{\eta c_p,k}\right) & -r_{cp,k}c_{\eta\eta,k} & -r_{cp,k}c_{\eta\xi,k} \\ -c_{\eta\eta,k} & -c_{\eta\xi,k} & -r_{cp,k}c_{\eta\eta,k} & c_{\eta\eta,k}+c_{c\eta,k} & c_{\eta\xi,k} & c_{\eta\xi,k}+c_{\eta c_p,k} & c_{\eta\eta,k} & c_{\eta\xi,k} \\ -c_{\xi\eta,k} & -c_{\xi\xi,k} & -r_{cp,k}c_{\xi\eta,k} & c_{\xi\eta,k} & c_{\xi\xi,k}+c_{c\xi,k} & c_{\xi\xi,k}+c_{\xi c_p,k} & c_{\xi\eta,k} & c_{\xi\xi,k} \\ -c_{c_p\eta,k} & -c_{c_p\xi,k} & -r_{cp,k}c_{c_p\eta,k} & c_{c_p\eta,k} & c_{c_p\xi,k} & c_{c_p\xi,k}+c_{c_pc_p,k} & c_{c_p\eta,k} & c_{c_p\xi,k} \\ 0 & 0 & 0 & -c_{c\eta,k} & 0 & 0 & 0 & 0 \\ 0 & 0 & 0 & 0 & -c_{c\xi,k} & 0 & 0 & 0 \end{bmatrix},$$

$$\mathbf{K_k} = \begin{bmatrix} k_{\eta\eta,k} & k_{\eta\xi,k} & r_{cp,k}k_{\eta\eta,k} & -k_{\eta\eta,k} & -k_{\eta\xi,k} & -k_{\eta\xi,k}-k_{\eta c_p,k} & -k_{\eta\eta,k} & -k_{\eta\xi,k} \\ k_{\xi\eta,k} & k_{\xi\xi,k} & r_{cp,k}k_{\xi\eta,k} & -k_{\xi\eta,k} & -k_{\xi\xi,k} & -k_{\xi\xi,k}-k_{\xi c_p,k} & -k_{\xi\eta,k} & -k_{\xi\xi,k} \\ r_{cp,k}k_{\eta\eta,k} & r_{cp,k}k_{\eta\xi,k} & r_{cp,k}^2k_{\eta\eta,k}+k_{cz,k} & -r_{cp,k}k_{\eta\eta,k} & -r_{cp,k}k_{\eta\xi,k} & -r_{cp,k}\left(k_{\eta\xi,k}+k_{\eta c_p,k}\right) & -r_{cp,k}k_{\eta\eta,k} & -r_{cp,k}k_{\eta\xi,k} \\ -k_{\eta\eta,k} & -k_{\eta\xi,k} & -r_{cp,k}k_{\eta\eta,k} & k_{\eta\eta,k}+k_{c\eta,k} & k_{\eta\xi,k} & k_{\eta\xi,k}+k_{\eta c_p,k} & k_{\eta\eta,k} & k_{\eta\xi,k} \\ -k_{\xi\eta,k} & -k_{\xi\xi,k} & -r_{cp,k}k_{\xi\eta,k} & k_{\xi\eta,k} & k_{\xi\xi,k}+k_{c\xi,k} & k_{\xi\xi,k}+k_{\xi c_p,k} & k_{\xi\eta,k} & k_{\xi\xi,k} \\ -k_{c_p\eta,k} & -k_{c_p\xi,k} & -r_{cp,k}k_{c_p\eta,k} & k_{c_p\eta,k} & k_{c_p\xi,k} & k_{c_p\xi,k}+k_{c_pc_p,k}+k_{sc_p,k} & k_{c_p\eta,k} & k_{c_p\xi,k} \\ 0 & 0 & 0 & -k_{c\eta,k} & 0 & 0 & 0 & 0 \\ 0 & 0 & 0 & 0 & -k_{c\xi,k} & 0 & 0 & 0 \end{bmatrix},$$

(102)

APPENDIX B

ADDITIONAL CONSIDERATIONS IN A ROCKER-PIVOT TPJB

For the case of a rocker-pivot TPJB, it may be necessary to account for the effect of pad tilt on the actual contact location about which moments are summed in writing the static and dynamic equations for pad tilt ϕ. In general, this transverse change in contact location has the effect of changing the pad's offset. Figure 67 shows a schematic representing the transverse movement of the contact location, η_{f_c}, as the pad tilts.

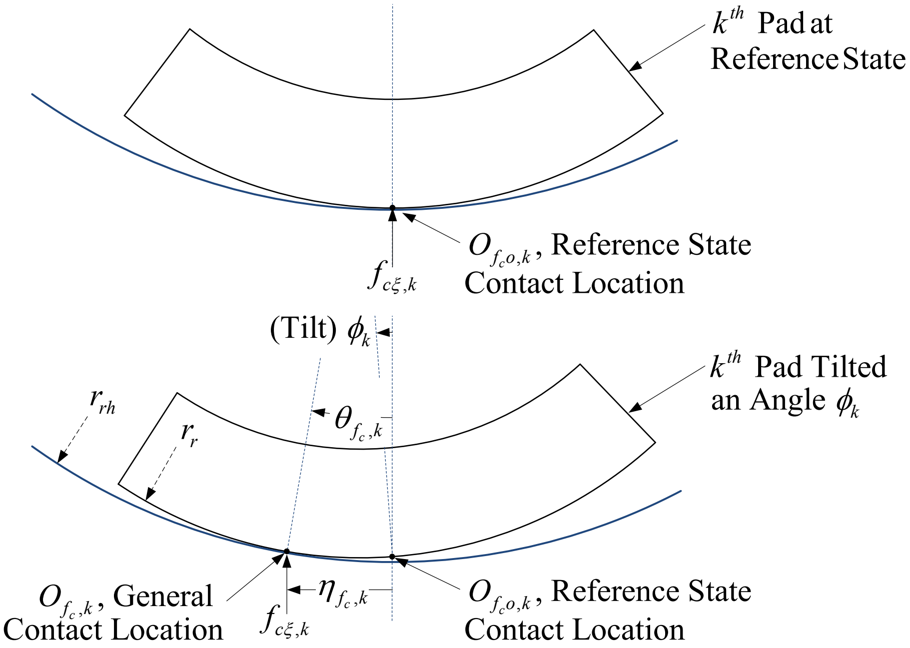

Figure 67: Change in contact location for a rocker-pivot TPJB

Note that Figure 67 uses $O_{fc,k}$ to denote the actual contact location (location where the pivot's radial reaction force is applied to the pad), which is different from the aforementioned pivot location ($O_{c,k}$) shown in Figure 11. $O_{c,k}$ denotes the translation of the reference state pivot location (contact location) in the inertial frame as given in Eq. (32) and is the location about which moments are summed in the pad's EOMs. Thus changes noted here are consistent with the previous derivation of pad dynamics.

Assuming that pad tilt is small, the effect of changes in $O_{f_c,k}$ should have a second order impact on pad dynamics with one exception; the moment created by the radial pivot force $f_{c\xi 0,k}$ (resulting from the zeroth order pressure field) passing through the new contact location $O_{f_c,k}$. This moment is given by

$$M_{\eta f_c,k} = -f_{c\xi 0,k}\eta_{f_c,k}\,. \tag{103}$$

Assuming that the rocker with radius r_r is rolling-without-slipping on the housing with radius r_{rh}, the kinematic constraint relating pad tilt (ϕ_k) to $\theta_{f_c,k}$, the angle from $\theta_{f_co,k}$ to $\theta_{f_c,k}$ about the center of curvature of the housing, is given by

$$\theta_{f_c,k} = \frac{r_r}{r_{rh} - r_r}\phi_k\,. \tag{104}$$

Note that depending on the bearing design, r_{rh} may not necessarily correspond to the contact radius r_c shown in Figure 4. It may be selected to achieve some specific radial pivot stiffness, or perhaps an insert may be used in the housing to improve pivot wear. From Eq. (104), it can be seen that

$$\eta_{f_c,k} = r_{rh}\sin\left(\theta_{f_c,k}\right) = r_{rh}\sin\left(\frac{r_r}{r_{rh} - r_r}\phi_k\right) \tag{105}$$

Thus the moment on the pad resulting from the application of a rolling-without-slipping constraint between the rocker and housing consists of a zeroth order component given by

$$M_{\eta f_c,k} = -f_{c\xi 0,k}r_{rh}\sin\left(\frac{r_r}{r_{rh} - r_r}\phi_{0,k}\right) \tag{106}$$

which should be added to the right hand side of the first relation in Eq. (54), and a first order component given by

$$M_{\eta f1_c,k} = -f_{c\xi 0,k}\frac{r_r\, r_{rh}}{r_{rh} - r_r}\cos\left(\theta_{f_c,k}\right)\phi_{1,k} \tag{107}$$

which should be added to the right hand side of the first relation in Eq. (60). Note that the reaction moment resulting from the application of a rolling-without-slipping constraint between a rocker-pivot and housing is proportional to the pad's tilt angle, thus it acts similar to the angular pivot stiffness in a flexure-pivot TPJB, which can increase the magnitude of destabilizing cross-coupled stiffness coefficients. Though the angular pivot stiffness resulting from a pivot rolling-without-slipping on a housing is likely insignificant for most bearings, Eq. (107) suggests that the magnitude of this stiffness increases in proportion to the factor $r_r r_{rh}$, and inversely proportional to the difference $r_{rh} - r_r$. This implies that rocker-pivot TPJBs having large rocker and housing radii that are very similar in magnitude could potentially have large destabilizing cross coupled stiffness coefficients.

APPENDIX C

STEADY STATE DATA

This appendix contains steady state data recorded during each dynamic test.

Table 13: Steady state data at 4400 rpm at various unit loads

Speed	**rpm**	4523.4	4437.8	4407.0	4371.2	4445.7
Load	**kPa**	-1.2	814.3	1583.1	2363.1	3153.0
P_{in}	**kPa**	114.7	115.6	116.6	117.7	119.2
NDE P_{out}	**kPa**	-0.1	-0.1	-0.1	-0.1	-0.1
DE P_{out}	**kPa**	-0.1	-0.1	-0.1	-0.1	-0.1
T_{in}	**°C**	36.5	36.5	36.4	36.3	36.4
NDE T_{out}	**°C**	39.9	40.0	40.2	40.1	40.6
DE T_{out}	**°C**	37.1	37.6	37.8	38.0	38.2
T_{pad} 1	**°C**	41.1	47.3	51.1	53.6	55.9
T_{pad} 2	**°C**	46.4	55.4	60.5	63.8	67.4
T_{pad} 3	**°C**	49.4	59.7	65.4	69.2	73.1
T_{pad} 4	**°C**	52.8	64.6	71.2	74.8	78.1
T_{pad} 5	**°C**	50.7	58.4	61.3	61.7	62.0
T_{pad} 6	**°C**	43.4	41.9	41.4	41.2	42.0
T_{pad} 7	**°C**	52.6	53.6	54.4	56.0	59.1
T_{pad} 8	**°C**	56.7	58.5	60.1	62.3	66.2
T_{pad} 9	**°C**	55.1	56.9	58.4	60.2	63.4
T_{pad} 10	**°C**	55.2	56.5	57.8	59.5	62.5
T_{pad} 11	**°C**	53.7	46.2	44.2	43.1	43.1
T_{pad} 12	**°C**	43.5	40.2	39.4	38.8	39.1
T_{pad} 13	**°C**	44.0	41.9	41.2	40.6	40.6
T_{pad} 14	**°C**	55.7	49.4	47.7	46.6	46.4
T_{pad} 15	**°C**	43.7	49.2	50.3	51.3	53.2
T_{pad} 16	**°C**	53.8	58.1	60.2	62.4	65.8
T_{pad} 17	**°C**	55.2	59.2	61.7	64.1	67.6
T_{pad} 18	**°C**	52.9	56.0	58.1	59.9	62.7
T_{pad} 19	**°C**	53.0	56.7	58.7	60.7	63.6

Table 14: Steady state data at 7300 rpm at various unit loads

Speed	**rpm**	7157.8	7219.8	7209.4	7241.4	7264.3
Load	**kPa**	-2.6	780.8	1570.3	2363.6	3160.7
P_{in}	**kPa**	116.3	117.8	120.7	121.1	122.9
NDE P_{out}	**kPa**	-0.2	-0.1	-0.2	-0.2	-0.2
DE P_{out}	**kPa**	-0.2	-0.2	-0.2	-0.2	-0.2
T_{in}	**°C**	36.5	36.4	36.5	36.9	37.0
NDE T_{out}	**°C**	45.1	45.1	45.5	45.8	45.9
DE T_{out}	**°C**	37.4	37.6	39.1	40.1	42.2
T_{pad} 1	**°C**	41.6	47.4	54.4	59.2	62.0
T_{pad} 2	**°C**	49.5	60.6	69.5	75.0	79.3
T_{pad} 3	**°C**	55.0	68.3	77.7	84.2	89.4
T_{pad} 4	**°C**	60.8	76.5	87.3	94.1	98.6
T_{pad} 5	**°C**	57.9	67.3	71.6	72.4	72.1
T_{pad} 6	**°C**	46.1	44.6	43.6	43.2	43.5
T_{pad} 7	**°C**	60.4	62.5	63.2	64.3	66.8
T_{pad} 8	**°C**	67.0	70.8	72.6	74.5	78.1
T_{pad} 9	**°C**	65.3	68.8	70.5	72.6	75.0
T_{pad} 10	**°C**	63.6	66.5	68.0	69.6	71.9
T_{pad} 11	**°C**	62.6	54.7	51.5	50.2	49.4
T_{pad} 12	**°C**	48.0	43.9	42.4	42.2	41.9
T_{pad} 13	**°C**	48.1	46.1	45.1	44.9	44.6
T_{pad} 14	**°C**	63.9	57.5	55.2	54.2	53.5
T_{pad} 15	**°C**	46.6	54.5	56.4	57.7	59.3
T_{pad} 16	**°C**	63.2	68.7	70.9	73.6	77.4
T_{pad} 17	**°C**	66.0	71.2	74.0	77.2	81.3
T_{pad} 18	**°C**	62.6	66.2	68.6	71.4	74.3
T_{pad} 19	**°C**	62.6	67.2	69.5	72.3	75.5

Table 15: Steady state data at 10200 rpm at various unit loads

Speed	**rpm**	10354.8	10227.4	10108.8	10096.1	10213.6
Load	**kPa**	-3.4	762.8	1586.5	2360.6	3155.8
P_{in}	**kPa**	156.0	155.7	156.5	157.2	158.3
NDE P_{out}	**kPa**	-0.2	-0.1	-0.2	-0.2	-0.2
DE P_{out}	**kPa**	-0.2	-0.2	-0.2	-0.2	-0.2
T_{in}	**°C**	36.7	36.7	36.7	36.8	36.7
NDE T_{out}	**°C**	44.8	45.8	46.4	46.8	47.2
DE T_{out}	**°C**	45.6	43.3	43.6	44.0	44.8
T_{pad} 1	**°C**	42.3	46.6	53.8	59.6	61.2
T_{pad} 2	**°C**	52.6	63.3	74.3	81.2	85.9
T_{pad} 3	**°C**	61.3	74.9	86.3	93.8	100.5
T_{pad} 4	**°C**	69.8	86.4	99.5	107.9	114.5
T_{pad} 5	**°C**	64.6	73.6	78.2	78.7	78.6
T_{pad} 6	**°C**	47.8	47.0	45.8	45.3	45.1
T_{pad} 7	**°C**	68.1	70.3	70.3	71.2	73.4
T_{pad} 8	**°C**	386.8	243.8	231.4	136.8	89.9
T_{pad} 9	**°C**	75.1	77.9	79.2	81.2	83.7
T_{pad} 10	**°C**	71.1	74.3	75.3	76.8	79.0
T_{pad} 11	**°C**	70.9	62.6	57.8	56.1	55.1
T_{pad} 12	**°C**	50.9	46.8	44.8	44.5	44.3
T_{pad} 13	**°C**	52.6	50.2	48.4	47.8	47.8
T_{pad} 14	**°C**	72.4	65.3	61.5	60.0	59.5
T_{pad} 15	**°C**	50.4	58.2	61.4	62.5	64.2
T_{pad} 16	**°C**	73.1	78.4	80.0	82.3	86.3
T_{pad} 17	**°C**	77.8	82.1	84.2	87.3	92.0
T_{pad} 18	**°C**	72.2	74.7	76.4	78.7	81.9
T_{pad} 19	**°C**	71.9	75.4	77.0	79.5	83.4

Table 16: Steady state data at 13200 rpm at various unit loads

Speed	**rpm**	13253.1	13074.2	13342.1	13309.8	13253.8
Load	**kPa**	-3.9	780.8	1565.8	2334.4	3131.9
P_{in}	**kPa**	153.2	155.0	155.5	152.8	154.3
NDE P_{out}	**kPa**	-0.3	-0.3	-0.2	-0.3	-0.3
DE P_{out}	**kPa**	-0.3	-0.3	-0.2	-0.3	-0.3
T_{in}	**°C**	36.6	36.7	36.5	37.0	36.8
NDE T_{out}	**°C**	48.8	49.5	50.4	52.3	52.2
DE T_{out}	**°C**	48.9	47.9	48.5	49.1	47.9
T_{pad} 1	**°C**	43.0	46.9	52.2	58.4	61.8
T_{pad} 2	**°C**	54.9	64.1	73.9	82.5	88.1
T_{pad} 3	**°C**	65.5	78.0	88.9	98.2	105.9
T_{pad} 4	**°C**	76.1	91.9	105.7	116.0	124.8
T_{pad} 5	**°C**	70.0	79.2	84.4	87.0	87.0
T_{pad} 6	**°C**	51.9	52.8	50.2	49.9	48.7
T_{pad} 7	**°C**	74.7	76.6	77.1	78.7	79.4
T_{pad} 8	**°C**	356.5	213.1	98.6	95.4	97.9
T_{pad} 9	**°C**	83.2	85.0	87.7	90.3	91.6
T_{pad} 10	**°C**	77.5	79.5	81.9	83.8	84.9
T_{pad} 11	**°C**	79.9	71.3	68.1	66.6	64.5
T_{pad} 12	**°C**	56.4	51.7	50.3	51.1	50.1
T_{pad} 13	**°C**	59.7	57.1	56.1	56.2	55.4
T_{pad} 14	**°C**	81.6	74.8	72.2	70.5	68.2
T_{pad} 15	**°C**	56.7	62.9	65.9	68.9	70.2
T_{pad} 16	**°C**	80.5	83.7	86.3	89.5	92.6
T_{pad} 17	**°C**	86.5	89.4	92.5	95.7	100.0
T_{pad} 18	**°C**	79.3	81.1	83.7	86.7	89.7
T_{pad} 19	**°C**	80.0	82.2	85.0	87.7	91.0

Table 17: Locations of pad thermocouples

	Pad	Angle (°) Relative to Pivot	Depth from Surface (mm)
T_{pad} 1	1	-27	3.225
T_{pad} 2	1	-9	3.225
T_{pad} 3	1	6	3.225
T_{pad} 4	1	15	3.225
T_{pad} 5	1	27	3.225
T_{pad} 6	2	-27	3.225
T_{pad} 7	2	6	3.225
T_{pad} 8	2	15	3.225
T_{pad} 9	2	27	3.225
T_{pad} 10	2	17	11.163
T_{pad} 11	3	-27	3.225
T_{pad} 12	3	15	3.225
T_{pad} 13	4	-27	3.225
T_{pad} 14	4	15	3.225
T_{pad} 15	5	-27	3.225
T_{pad} 16	5	6	3.225
T_{pad} 17	5	15	3.225
T_{pad} 18	5	27	3.225
T_{pad} 19	5	17	11.163

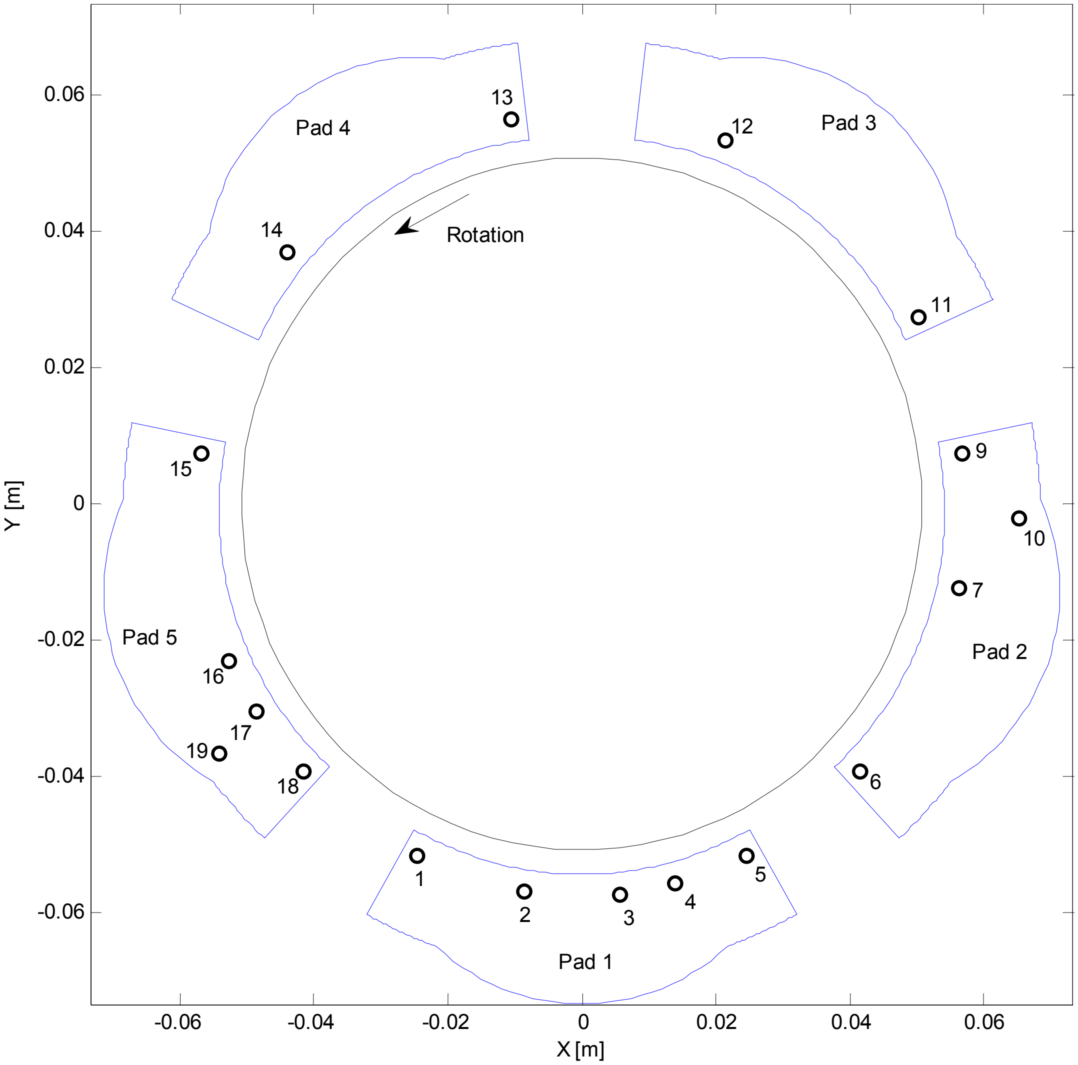

Figure 68: Location of pad thermocouples (pad 1 is the loaded pad)

APPENDIX D

JOURNAL VS. BEARING IMPEDANCES AT 10200 rpm, 783 kPa

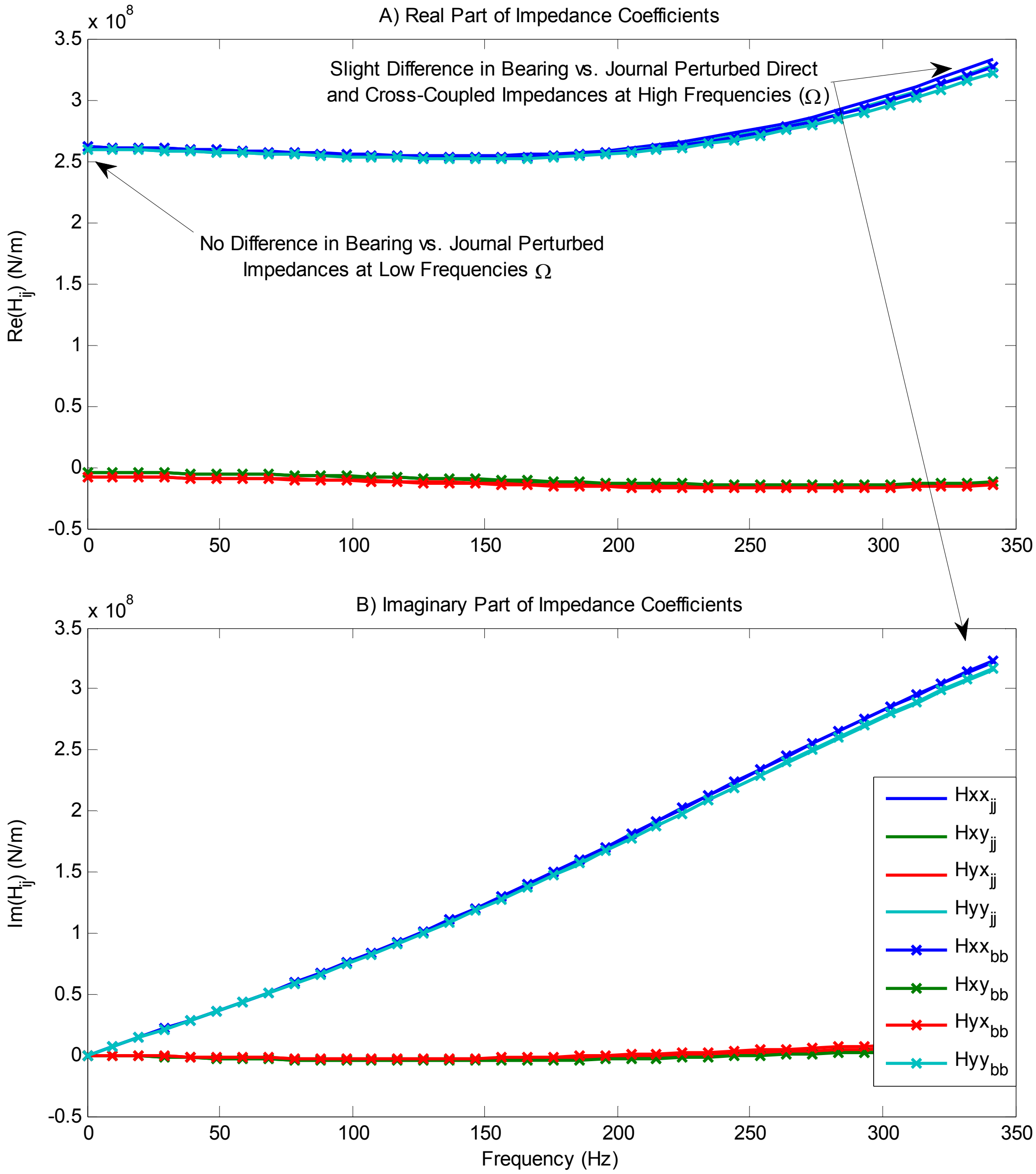

Figure 69: Real and imaginary bearing impedances predicted relative to perturbations of the journal (jj) and bearing (bb) at 10200 rpm 783 kPa

VITA

Name: Jason Christopher Wilkes

Address: Texas A&M Turbomachinery Laboratory
Texas A&M University, Mail Stop 3123
College Station, TX 77843-3123

Email: jasonwilkes@gmail.com

Education: Ph.D., Mechanical Engineering, Texas A&M University, December 2011.
M.S., Mechanical Engineering, Texas A&M University, August 2008.
B.S., Mechanical Engineering, Texas A&M University, August 2005.

Interests: Professional interests include research in fluid film bearing lubrication modeling and testing, with an emphasis on pad motion in tilting-pad journal bearings, as well as dry-friction whip and whirl. Additional interests include spending time with my wife and kids, woodworking, home remodeling, and biking.